9-2012

Porous Metal Oxide Materials Through Novel Fabrication Procedures

Nicholas Hendricks
University of Massachusetts Amherst, nicholas.hendricks@gmail.com

POROUS METAL OXIDE MATERIALS THROUGH NOVEL FABRICATION PROCEDURES

A Dissertation Presented

by

NICHOLAS RAYMOND HENDRICKS

Submitted to the Graduate School of the
University of Massachusetts Amherst in partial fulfillment
of the requirements for the degree of

Doctor of Philosophy

September 2012

Polymer Science and Engineering

POROUS METAL OXIDE MATERIALS THROUGH NOVEL FABRICATION PROCEDURES

A Dissertation Presented

by

NICHOLAS RAYMOND HENDRICKS

Approved as to style and content by:

_____
James J. Watkins, Co-Chair

_____
Kenneth R. Carter, Co-Chair

_____
Mark T. Tuominen, Member

_____
David A. Hoagland, Department Head
Polymer Science and Engineering

DEDICATION

To the Hendricks Family.

ACKNOWLEDGMENTS

I would like to acknowledge all of the people that made my graduate school experience what it was, for better or for worse, and the memories that I will have for a lifetime. I would like to first thank my dissertation advisors, Prof. James J. Watkins and Prof. Kenneth R. Carter, to whom I owe a tremendous amount of gratitude for helping develop myself to the scientist I am today. I was extremely fortunate during my dissertation to have the opportunity to attend conferences, experience research at an international university, perform industrial research through an internship and work on top-level research at the University of Massachusetts Amherst, none of which would have been possible without Jim and Ken. I would specifically like to acknowledge Jim, for it was his research group that I gravitated towards during my dissertation. The honest feedback that Jim provided to me, as well as the diversity of our discussions, will always be remembered. I would also like to thank my committee member, Prof. Mark T. Tuominen, for his attention to details and challenging questions.

I would like to acknowledge the past and present members of the Watkins and Carter research groups. I would especially like to acknowledge the following Watkins research group members: Christos Karanikas, Curran Chandler, Chris Ziegler, Todd Crosby, Alvin Romang, Dan Miranda, Eric Anderson and Michael "Ruosty" Beaulieu. This group of people made coming to lab a real enjoyment and many friendships were forged that will last a lifetime. I would specially like to thank Ruosty for his friendship during graduate school, I am truly grateful our paths crossed here in the Watkins research group.

I would also like to acknowledge the staff of the Center for Hierarchical Manufacturing, past and present: Barbara Bou, Jo-Ann Bourguignon, Trouble “Erin” Mandeson, Mary Ann Mish, Jeff Morse, Paul Clark and Bob Stevens. Without their service, the Center for Hierarchical Manufacturing would not operate as smoothly as it does. I would specifically like to acknowledge the Center for Hierarchical Manufacturing Nanotechnology Cleanroom Lab Manager, John Nicholson, who first introduced me to and taught me about cleanroom techniques and protocols. John also has an active life away from the university and I will remember our fruitful discussions regarding energy, electric vehicles and politics.

I would like to thank the Polymer Science and Engineering front office staff: Lisa Groth, Ann Brainerd, Maria Farrington, Lisa McNamara and Jessica Skrocki. I specially would like to thank Lisa Groth for all of her hardwork in reminding the graduate students of important deadlines and dealing with the perils of paperwork. Without Lisa’s help, there would have been many more frustrating days and nights experienced by myself and many other students.

I would like to thank the facilities directors within the Polymer Science and Engineering Department, past and present: Jack Hirsch, Sekar Thirunavukkarasu, Lou Raboin, Alex Ribbe and Wim de Jeu. From this collective group of people, I was able to absorb an immense amount of knowledge regarding characterization techniques and use of equipment, and for this, I am extremely grateful. I would also like to thank Prof. Mike Jercinovic of the Geology Department at the University of Massachusetts Amherst. His knowledge of electron microscopy is vast and I only wish I had more time to work with him.

I would like to thank the Center for UMass / Industry Research on Polymer (CUMIRP) personnel Alyssa Walder and former director Jim Capistran. The CUMIRP events each year were executed flawlessly and provided an excellent opportunity for students to present their research while also networking with industrial and government representatives. I would like to specifically thank Jim Capistran for taking time out of his day to review resumes, not only mine but countless others, and for providing crucial feedback.

I would like to thank Greg Dabkowski for organizing the various education and outreach volunteer opportunities for the Polymer Science and Engineering Department. I will never forget the experiences I had with the ASPIRE and OUTREACH programs. The work that Greg does to motivate K-12 students about polymers, and science in general, is inspirational.

I would like to thank the Polymer Science and Engineering class of 2007. We had a wonderful group of people and we were able to have many memorable experiences together, not only within the walls of the Conte Polymer Research Center but also extracurricular activities such as softball and holiday gatherings. I specifically would like to acknowledge Yuri Ebata for her friendship over the years and I hope we are able to stay in contact over the years to come. I would also like to thank the original group of housemates I had at 24 Summer Street: Bugra Toga, Scott Christensen, Eric Anderson and Sam Pendergraph. The discussions and experiences that we had within this house were epic and I will never forget them.

I would like to thank my family for their constant support of decisions I have made through my life. The choices I have made in my life, as well as future choices,

have been a direct result of the influence they have had on me and I am truly grateful to have such wonderful, caring people in my life.

Perhaps the most important outcome of my time here at the University of Massachusetts Amherst is that I was able to meet an incredible young lady named Caroline. She has been everything to me since the day we first met and I hope we have a long and exciting life together.

ABSTRACT

POROUS METALOXIDE MATERIALS THROUGH NOVEL FABRICATION PROCEDURES

SEPTEMBER 2012

NICHOLAS RAYMOND HENDRICKS, B.S., WRIGHT STATE UNIVERSITY

M.S., UNIVERSITY OF MASSACHUSETTS AMHERST

Ph.D., UNIVERISTY OF MASSACHUSETTS AMHERST

Directed by: Professor Kenneth R. Carter and Professor James J. Watkins

Porous metal oxide materials, particularly those comprised of silica or titania, find use in many applications such as low-k dielectric materials for microelectronics as well as chemical sensors, micro/nanofluidic devices, and catalyst substrates. For this dissertation, the focus will be on the processing of porous metal oxide materials covering two subjects: hierarchical porosity exhibited over two discrete length scales and incorporation of functional nanomaterials.

To generate the porous silica materials, the technique of supercritical carbon dioxide infusion ($scCO_2$) processing was heavily relied upon. Briefly, the $scCO_2$ infusion processing utilizes phase selective chemistries within a pre-organized amphiphilic block copolymer template using $scCO_2$ as the reaction medium to selectively hydrolyze and condense silica precursors to yield mesoporous materials. To further develop the $scCO_2$ infusion processing technique, hierarchically porous silica materials were generated on unique substrates. Hierarchically structured silica nanochannels were created using a combination of $scCO_2$ infusion processing and nanoimprint lithography (NIL) patterned sacrificial polymer templates to yield mesopores and airgap structures respectively.

Hierarchically porous silica materials were also generated on alternative substrates, in the form of cellulose filter paper, which were used to host the amphiphilic block copolymer template to yield tri-modal porosity silica materials.

To extend the applicability of mesoporous silica generated from $scCO_2$ infusion processing, functional nanomaterials, in the form of pre-synthesized gold nanoparticles, fullerene derivatives, and polyhedral oligomeric silsequioxanes (POSS) were embedded within the mesoporous silica to produce unique composite materials. The functional nanomaterials were able to impart specific properties, typically only afforded to the functional nanomaterials, upon the mesoporous silica thin film with an example being enhanced thermal and hydrothermal properties of mesoporous silica doped with POSS molecules.

To continue research with functional nanomaterials, nanoparticle composite materials, comprised of crystalline metal oxide nanoparticles and binder/filler materials, either organic or inorganic, were also evaluated as novel NIL resist materials. Patterning of the nanoparticle composite materials, specifically, but not limited to, titanium dioxide based materials, into two dimensional, arbitrarily shaped, sub-micron features was readily achieved on either rigid or flexible substrates. True three-dimensional structures, based on nanoparticle composite materials, were fabricated by utilizing release layers and pre-patterned substrates.

TABLE OF CONTENTS

Page

LIST OF TABLES

Table **Page**

LIST OF FIGURES

CHAPTER 1

INTRODUCTION

1.1. Overview

The research objective presented within this dissertation is to fabricate unique metal oxide materials which exhibit hierarchical porosity and/or consist of dopant materials by using novel fabrication procedures. The hierarchically porous metal oxide materials exhibit two discrete length scales, often referred to as domain level features and device level features where the former is smaller than the latter. The dopant materials consist of functional nanomaterials, in the form of pre-synthesized nanoparticles as well as small molecules.

In this introductory chapter, typical fabrication methods used to create device level structures will be discussed, with a particular focus on the imprint lithography technique. An introduction to block copolymers, sol-gel chemistry of metal oxide materials, and supercritical carbon dioxide ($scCO_2$) will be presented along with a detailed description of the procedure to create mesoporous metal oxide materials through $scCO_2$ infusion processing. Finally, a general description of the characterization instruments and techniques used for this dissertation will be discussed.

The second chapter will describe the formation of hierarchically structured silica nanochannels through the combination of mesopores and airgap structures, created by $scCO_2$ infusion processing and nanoimprint lithography (NIL) respectively. The effect of the airgap structure on the electrical and mechanical properties of the mesoporous silica is evaluated by capacitance measurements and nanoindentation.

Chapter three describes the synthesis of mesoporous silica doped with functional materials, ranging from pre-synthesized nanoparticles to commercially available nanomaterials, using $scCO_2$ infusion processing. The loading of the functional nanomaterials is evaluated along with the capability of the mesoporous silica to accommodate the functional nanomaterial while maintaining a long-range ordered mesopore structure. The influence of the functional nanomaterial on the mesoporous silica is evaluated based on the specific properties afforded to the functional nanomaterial.

The fourth chapter discusses the fabrication of mesoporous silica on alternative substrates, specifically cellulosic materials, to generate a hierarchically porous structure. The processing conditions, in terms of $scCO_2$ infusion processing, porosity, and thermal degradation temperatures, are extensively evaluated.

Chapter five describes the nanopatterning of nanoparticle composites, with a particular focus on metal oxide nanoparticles, into arbitrary geometries with a critical dimension less 1 μm and more often less than 500 nm. The physical properties of planar and patterned nanoparticle composites are evaluated. The fabrication of true three-dimensional nanostructures, constructed from nanoparticle composites, via release layers and/or transfer printing will be discussed.

The final chapter will provide a summary of the research performed within this dissertation, continuation / future work opportunities regarding the research projects presented here, and finally, a brief description of research projected initiated here that are truly in the initial phases as well as collaborative research efforts.

1.2. Motivation

Metal oxide materials offer functionalities and properties that are often not provided by other materials such as photoactivity, semiconductivity, mechanical strength, thermal stability, and high, tunable surface area, to name several. With such functionalities and properties, metal oxide materials are used in numerous applications including catalysis, separations, alternative energy (photovoltaics and fuel cells), microelectronics, optics (antireflection coatings (ARCs) and photonics), environmental remediation, and drug delivery.

The dissertation presented here has two main themes within; the first theme is to further extend the capabilities of generating mesoporous metal oxide materials, particularly mesoporous silica, through the use of $scCO_2$ infusion processing techniques, which were previously developed in the research labs of Professor James J. Watkins. The second theme presented intends to develop the additive driven process of functional metal oxide nanostructures through the use of pre-synthesized nanoparticles and unique lithography techniques, based on imprint lithography and photolithography.

1.3. Device Level Fabrication Methods

Nano and microscale features may be created via numerous methods such as photolithography, electron beam lithography, soft lithography, scanning probe techniques, and self-assembly of various techniques. Of the previously mentioned lithography techniques, the most established are photolithography and electron beam lithography. Current photolithography techniques are able to pattern features to a resolution of several tens of nanometers but this resolution comes at a tremendously

expensive capital cost. Electron beam lithography has terrific resolution and remarkable versatility but often suffers from extended processing times. While the established lithography techniques have a large percentage of the lithography market, there have been many non-conventional lithography techniques introduced over the past decade such as imprint lithography, micro-contact printing (μCP), micromolding in capillaries (MIMIC), and dip-pen lithography to name several. The semiconductor industry, which relies heavily on lithography to create next generation microelectronics, commonly refers to these alternative patterning techniques as next generation lithography (NGL) techniques along with other alternative lithography techniques such as extreme ultraviolet (UV) lithography (EUV), X-ray lithography, large area electron beam lithography, and focused ion beam lithography. Of all the alternative lithography techniques, imprint lithography seems to have the greatest potential as a future nanoscale patterning method due to the ability to quickly reproduce nanoscale features over large areas at low capital cost and high throughput capabilities.

1.4. Imprint Lithography

Imprint lithography, also referred to as nanoimprint lithography (NIL), has garnered tremendous interest from the lithography community since the invention of this technique by Chou et al. in 1995[1–3] due to the simplicity, high throughput, high resolution, and low cost that is offered from this technique. Two general methods of imprint lithography to produce nanoscale features are thermal nanoimprint lithography (TNIL) and ultraviolet-assisted nanoimprint lithography (UV-NIL). Figure 1.1 shows the typical processing steps for both TNIL and UV-NIL.

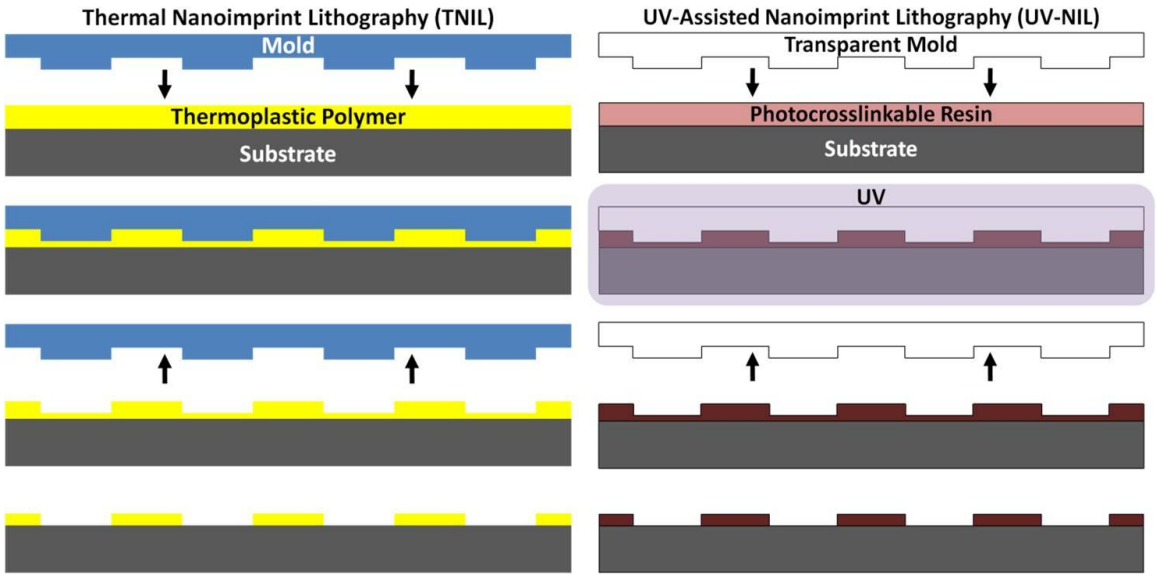

Figure 1.1. Typical processing steps for TNIL (left) and UV-NIL (right).

TNIL, sometimes referred to as hot embossing lithography (HEL), was the first reported nanoimprint lithography technique as described by Chou and co-workers in 1995[1–3]. The basic principles of TNIL have origins in HEL (e.g. LIGA, a German acronym for Lithographie, Galvanoformung, and Abformung, which translates to English as Lithography, Electroplating, and Molding) with the difference being that the TNIL process is performed at the sub-100 nm scale. The process of TNIL requires a hard mold, typically fabricated from silicon, silicon dioxide, or silicon nitride, with predetermined nanoscale features, to be brought into contact with a film of thermoset polymeric material on a substrate by means of external force (controlled temperature and/or pressure). It is important to note that the mold is treated with a low-surface energy material prior to being used in the TNIL process to ensure a successful separation of the mold and polymeric material after processing. The mold embosses the polymeric layer and displaces material three-dimensionally during the imprint due to the high temperature, typically 20 °C or greater above the glass transition temperature (Tg) of the polymeric

material, and/or pressure exerted on the mold during the imprinting procedure, usually within the range of 10s to 1000s of psi. Once the polymeric material has been embossed with the nanoscale features of the mold, the temperature is reduced below the Tg of the polymeric material, while maintaining the elevated pressure, to lock-in the embossed nanoscale features present in the polymeric material. The elevated pressure will then be released and the mold and the substrate, containing the polymeric material, will be separated.

Typically, a residual polymeric layer remains within the region where the mold depresses furthest towards the substrate which prevents the hard mold from making contact with the underlying substrate. Depending on the intended application of the patterned material, the residual polymeric layer may need to be removed via a subtractive etch process, such as an anisotropic oxygen plasma reactive ion etch (RIE) process, to expose the underlying substrate for further processing.

Developments in ultraviolet-assisted nanoimprint lithography (UV-NIL), or photocurable nanoimprint lithography (PNIL), quickly followed TNIL and the earliest description of this technique was first reported by the Philips Research Laboratories in 1996[4]. The UV-NIL process requires a transparent mold, typically fabricated from glass or quartz, with predefined nanoscale features to be applied by pressure to a UV-curable precursor liquid and cured by UV-radiation to a solid material for pattern replication. The mold typically is treated with a low-surface energy material to ensure release after curing while the substrate is usually chemically treated to enable adhesion of the patterned photopolymer. Like TNIL, in order to facilitate pattern transfer to the underlying substrate, a post-imprint RIE process is usually required to remove the

residual layer connecting the nanoscale features and to expose the underlying substrate to further processing by either wet or dry etching techniques.

A variation of the UV-NIL process was developed by Willson et al. in 1999 and is known as Step and Flash Imprint Lithography (SFIL)[5]. SFIL is modeled after stepper and scanner technology used in photolithography and takes the advantages afforded to UV-NIL with the capability of repeating the process over a large area wafer substrate due to the step and repeat mechanism employed. Just as in UV-NIL, SFIL utilizes a surface treated, transparent mold, usually quartz, to perform the pattern transfer. The mold is brought into proximity of the substrate, with the possibility of optical alignment due to the transparency, and a low viscosity, photocurable material is introduced to the gap between the mold and substrate. Capillary forces fill the surface structures of the mold with the photocurable material. The mold can be brought into closer contact with the substrate by the application of low pressure and, once intimate contact is made between the mold and the substrate, the structure is irradiated with UV-light through the mold to cure and solidify the photocurable material. Once the irradiation is complete, the mold and substrate are separated and a replication of the mold is transferred to the substrate. The amount of residual material can be controlled by selecting exceptionally low viscosity resist formulations and dispensing precise amounts of resist upon imprint, for example, through the use of ink-jet heads. After one imprint cycle, the wafer can be moved to imprint a new field and the cycle is repeated until the entire wafer has been imprinted.

1.5. Sol-Gel Chemistry of Metal Oxide Materials

To begin the discussion of sol-gel chemistry, several definitions need to be established, as according to the book "Sol-Gel Science: The Physics and Chemistry of Sol-Gel Processing" by C. Jeffrey Brinker and George W. Scherer[6]. The sol is defined as a colloidal suspension of solid particles in a liquid where as a gel is defined as when a single molecule extends through the entire solution. Sol-gel chemistry may be described by three simple processing steps: the preparation of a sol, the gelation of the sol, and the removal of the solvent[6]. The use of sol-gel chemistry generates ceramic materials, which are created by the precursors that are capable of undergoing hydrolysis, which is the reaction of water with the precursor to create hydroxyl groups on the precursor, and condensation, which is the reaction between two precursors that have undergone hydrolysis. After the condensation of the hydrolyzed precursors, the metal oxide material may be either porous or dense, depending on the post-synthesis processing experienced by the metal oxide material.

To create the porosity of porous metal oxide material, the porogen material must be removed. When the porogen material is a solvent, a drying process is required by either evaporation under standard conditions, to yield a xerogel, or supercritical drying, to yield an aerogel. For the case of template assisted formation of porosity for porous metal oxide materials, the template material must be removed by either solvent extraction or thermal degradation at elevated temperatures. To undergo further condensation of the metal oxide matrix, and impart greater mechanical integrity, the dried metal oxide gel will undergo aging or high temperature thermal processing. To generate a dense metal oxide material, the dried porous metal oxide gel must undergo a severe thermal process,

known as sintering, such that the pores collapse and densification occurs. A large number of metal oxide materials have been synthesized by sol-gel processing, such as aluminum oxide, titanium dioxide, and cerium dioxide, but the most studied metal oxide created by sol-gel chemistry is that of silicon dioxide.

1.6. Block Copolymer Templates

Block copolymers consist of multiple blocks, i.e. two or more, of polymer segments that are covalently attached to one another. Multiple architectures are afforded to block copolymers, which are based on the number of blocks, i.e. diblock, triblock, etc., and the positioning of the blocks, i.e. linear, star, graft, etc. The simplest form of block copolymers is the linear diblock copolymer, which is comprised of a single covalent attachment point between the two polymer segments. A unique aspect of block copolymers is the ability to phase separate to form periodically structured morphologies, which is dictated by the total molecular weight of the block copolymer, i.e. degree of polymerization (N), volume fraction of each polymer segment, f_A or f_B (which is the degree of polymerization of the respective block divided by the total degree of polymerization for the block copolymer), and segment-segment interaction parameter, better known as the Flory-Huggins parameter or χ (chi)[7]. The simplest mean to determine the type of morphology a block copolymer will provide is through the use of a phase diagram. An example of a phase diagram, as well as the most commonly observed phase separated morphologies for a linear diblock copolymer, is provided in Figure 1.2. Each parameter that controls the phase separation of block copolymers, i.e. N, f_A, and χ, is responsible for the morphological properties of the block copolymer in the following

manner: N controls the domain size of the periodic structure, f_A controls the morphology, and χ, in combination with N, controls the segregation strength between segment A and segment B of an A-B linear diblock copolymer.

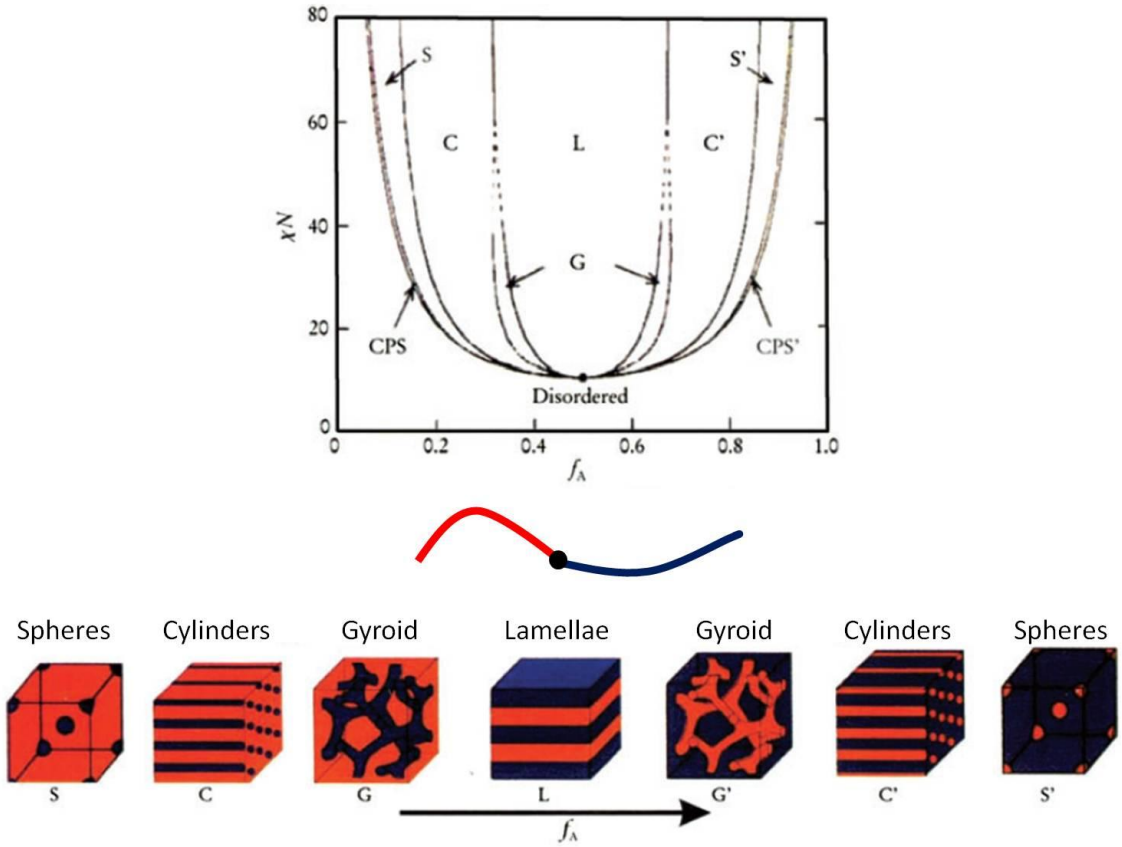

Figure 1.2. Standard phase diagram for a linear diblock copolymer and the representative morphologies provided by the phase separation of linear diblock copolymers[8].

1.7. Supercritical Fluids (SCFs)

A supercritical fluid (SCF) is a material that has been heated and pressurized to conditions at or above the critical temperature (Tc) and the critical pressure (Pc) of the material respectively. The intersection of the critical temperature and the critical pressure on a pressure-temperature phase diagram is known as the critical point, which is the point where the material becomes supercritical and exhibits a combination of gas-like and liquid-like behavior. An example of a phase diagram for a common supercritical fluid,

carbon dioxide, is shown in Figure 1.3. To further elaborate on the gas-like and liquid-like behavior of supercritical fluids, Table 1.1 compares various properties between gases, liquids, and supercritical fluids.

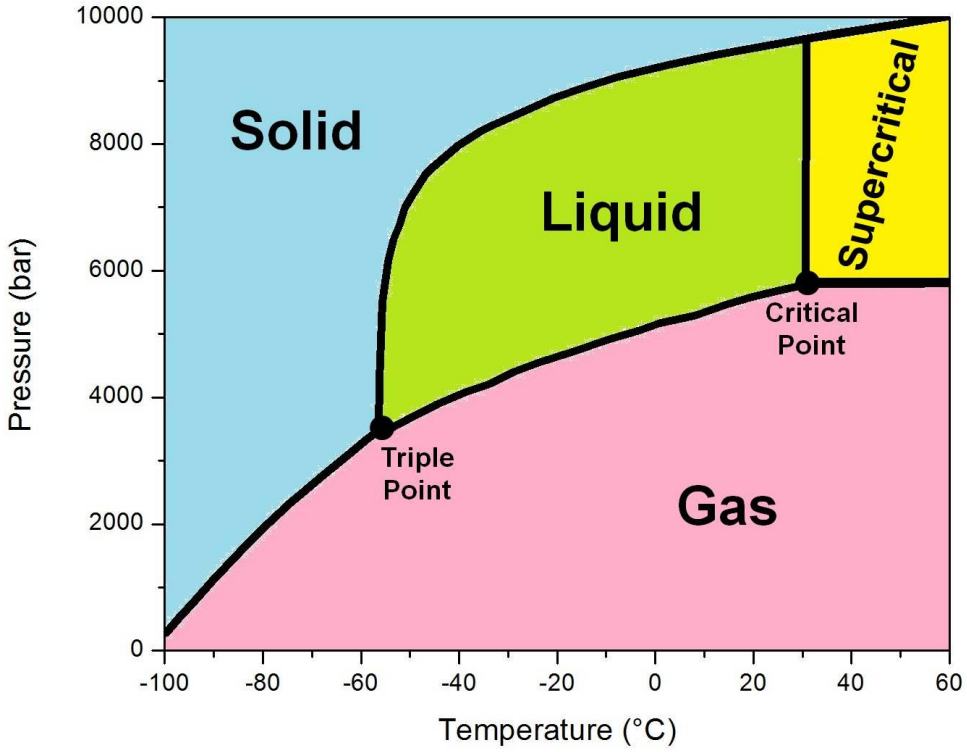

Figure 1.3. Phase diagram for carbon dioxide.

Table 1.1. Comparison of typical properties between gases, liquids, and supercritical fluids.

Property / Substance	Surface Tension (dyn/cm)	Density (g/cm^3)	Viscosity (Pa·s)	Diffusivity (cm^2/s)
Liquid	10 – 60	0.8 – 1.2	10^{-3}	10^{-5}
Supercritical Fluid	0	0.1 – 1.2	10^{-4} – 10^{-5}	10^{-3}
Gas	0	10^{-3}	10^{-5}	0.1

One of the most widely used supercritical fluids, as well as the supercritical fluid used primarily for the research presented within this dissertation, is that of carbon dioxide. Carbon dioxide has an easily accessible critical point, where the Tc is 31.1 °C and the Pc is 7.39 MPa (1071.8 psi), and several other advantages such as nonflammable, nontoxic, ability to swell polymeric materials, environmentally benign when compared to organic solvents, and tunable solvent parameters. Supercritical fluids can be designated as "designer" solvents due to the ability to tune the density of the fluid through processing conditions, i.e. temperature and pressure, as shown in Figure 1.4 for the example of carbon dioxide. By having the ability to tune the solvating capability of the solvent, supercritical fluids, specifically carbon dioxide, are capable of dilating polymeric materials to enhance the diffusion of small molecules within the polymeric material[9]. Finally, the use of carbon dioxide as the supercritical fluid allows one to completely remove the solvent once the processing is complete by simply depressurizing the reaction vessel.

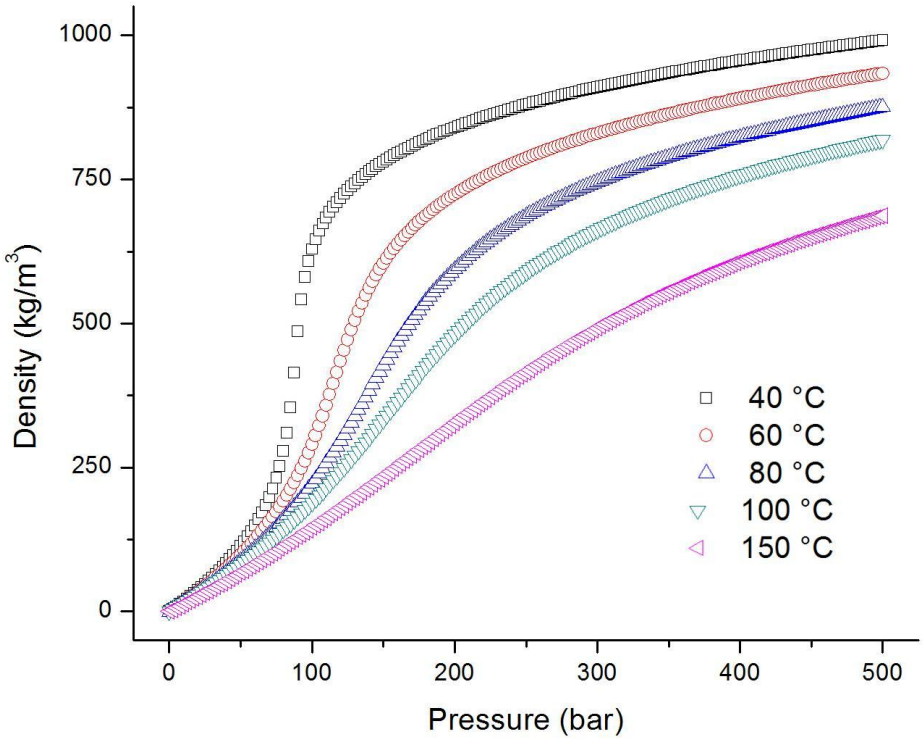

Figure 1.4. Density of carbon dioxide at various temperatures[10].

1.8. Supercritical Carbon Dioxide Infusion Processing

The $scCO_2$ infusion process to create mesoporous metal oxide thin films through the three-dimensional replication of ordered block copolymer templates was developed by Watkins et al. in 2004[11]. In this report, a well-ordered amphiphilic block copolymer was replicated by silica through the selective deposition of silica precursors in one domain of the template using $scCO_2$ as the reaction medium to create measoporous silica. To control the deposition of the metal oxide precursor, the chemistry of the replication process must be limited to one domain of the block copolymer template. To perform selective chemistries, a block copolymer template consisting of hydrophobic and hydrophilic domains was selected. The condensation of the metal oxide precursor is

promoted by the addition of a catalytic amount of acid to the block copolymer template / solvent solution. This catalytic amount of the acid will preferentially partition to the hydrophilic domain of the block copolymer due to the inherent hydrophilicity of the acid.

For a high fidelity replication of a block copolymer template, the ordered domains must remain ordered during the replication process. The use of $scCO_2$ allows for the domains to remain well-ordered while being slightly dilated, which allows the metal oxide precursor to permeate into the block copolymer domains for replication. Even though the metal oxide precursor was able to permeate into both domains of the block copolymer template, the replication only proceeds within the hydrophilic domain due to the acid catalyst being hydrophilic in nature, thus selectively condensing the metal oxide precursor in the hydrophilic domain. This is how the condensation of the metal oxide precursor is selective to a single domain of the block copolymer template. The reaction by-product and un-reacted metal oxide precursor were readily removed upon de-pressurization of the carbon dioxide.

To ultimately recover the mesoporous metal oxide structure, the block copolymer template must be removed by either thermal or plasma degradation. The typical degradation technique used was a thermal degradation (calcination) at a temperature of 400 °C, however, the option of organic template removal through elevated temperatures and alternating oxygen / hydrogen plasmas was available as well. Through the $scCO_2$ infusion process, a multitude of mesoporous metal oxide structures can be replicated via the self-assembly of amphiphilic block copolymer templates into periodic structures as well as lithographically defined structures[12–16]. The utility of this technique has been demonstrated by the replication of mesoporous silica, but is should be noted that the

$scCO_2$ infusion technique is not limited to silica precursors. This technique is a viable option to create titanium dioxide, cerium dioxide, and other novel metal oxide mesoporous thin films.

1.9. Characterization Instruments and Techniques

To perform a complete and thorough characterization of the fabricated metal oxide materials, a vast amount of characterization tools were required. Knowledge of the following characterization techniques was necessary:

1.9.1. Scanning Electron Microscopy (SEM)

Scanning electron microscopy (SEM) is a characterization technique to determine the surface structure and composition of samples at or near the surface. SEM gathers information from the samples by scanning the sample with a focused beam of electrons in a raster method. The interaction between the electron beam and the surface of the sample generates signals, most commonly in the form of secondary electrons, back-scattered electrons, and characteristic X-rays, which generates images and compositional maps of the sample by detecting and processing each of the signals. Each one of the signals is produced from interactions between the electron beam and the surface of the sample in the form of either inelastic scattering, where kinetic energy is not conserved, or elastic scattering, where kinetic energy is conserved. From the inelastic scattering of primary electrons, i.e. electrons from the electron beam source, the signals of secondary electrons and characteristic X-rays are produced. Secondary electrons, i.e. electrons generated (ejected) from the transfer of energy from the primary electrons to the surface of the sample, are used as the primary signal to generate three-dimensional images of the

surface structure of the sample. Characteristic X-rays are another product of the inelastic scattering between the primary electron and the surface of the sample. Characteristic X-rays are generated from a release of energy when a higher energy electron replaces the vacancy created by the emission of a secondary electron from an inner orbital shell. Compositional maps, or elemental analysis, is able to be collected from characteristic X-rays because each element in the periodic table generates a specific X-ray, hence the name of characteristic X-rays.

The signal of back-scattered electrons is generated from the elastic scattering of primary electrons from the surface of the sample. The back-scattered electron signal is extremely sensitive to the mass of elements, i.e. heavier elements have a stronger back-scattered electron signal, and is able to qualitatively provide elemental analysis information from the surface of the sample. An excellent reference on scanning electron microscopy is provided by Goldstein et al. titled Scanning Electron Microscopy and X-Ray Microanalysis[17].

1.9.2. Transmission Electron Microscopy (TEM)

Transmission electron microscopy (TEM) is a characterization technique where a beam of electrons is transmitted through a specimen to, most commonly, collect crystallographic information and/or capture an image. TEMs regularly operate at extremely high voltages, on the order of 100s of kV, due to the various elastic and inelastic scattering that may occur when the electrons interact with the sample. It should be stated here that the TEM collects information and generates data based on the electron density differences, i.e. scattering. Along this premise, to collect useful and informative images, the TEM samples must have a thickness less than several hundred nanometers

due to the contrast present in TEM being from the differences in electron densities, i.e. thicker regions of the sample will appear darker than thinner regions. Within the path of the electron beam, there are three important planes present: the object plane, the back focal plane, and the image plane. The object plane is where the specimen under investigation is placed. Placement of the specimen within the object plane determines the type of information that will be collected such that the back focal plane provides crystallographic information while the image plane provides images of the specimen. In the back focal plane, all the electrons that are scattered at the same angle are collected in one specific point such that the scattered electrons form the diffraction pattern which is used for determining the crystal lattice. Farther down the electron column and away from the back focal plane is the image plane and this is where all the electrons scattered from a specific point in the object plane are collected in a common point and thus form a generic picture of the object. To collect more specific images from TEM, adjustments to where the scattering electrons are collected may be performed such that one can obtain images from either phase contrast or amplitude contrast.

Phase contrast arises from the electrons interacting with the specimen on the atomic scale such that as the electrons are passing through the specimen, diffraction occurs and causes the phase of the electrons to be altered. For the amplitude contrast mechanism, there are two modes: diffraction contrast and mass-thickness contrast. In diffraction contrast mode there are two means to obtain contrast, either by bright field diffraction contrast or dark field diffraction contrast. For bright field diffraction contrast, the crystalline regions of the sample will appear dark due to the use of the objective aperture, which is essential a small hole that limits the scattering angle to which the

electrons are allowed to proceed down the electron column to form an image. Due to the position of the objective aperture, only un-scattered electrons are allowed to proceed to form the image such that scattered electrons are shielded and the crystalline material present in the sample appears dark. The opposite is true for the description of dark field diffraction contrast. The objective aperture is positioned in such a manner to allow only scattered electrons to continue down the electron column to form the image, thus, the crystalline portions of the sample will appear bright and the rest of the image will appear dark.

For the mass-thickness contrast, the amount of scattering increases with increasing sample thickness. The mass-thickness contrast produces an image based on diffuse scattering of electrons and scattering increases with increased atomic number and local density of the sample.

1.9.3. Atomic Force Microscopy (AFM)

Atomic force microscopy (AFM) is part of the scanning probe family which includes scanning tunneling, magnetic force, and electrostatic force microscopes. The AFM has many capabilities for analysis at the nanometer scale such as imaging and manipulation of materials or even atoms. AFM is a near nondestructive technique and is capable of measuring surfaces of solids and liquids. The imaging technique of AFM is different from other microscopy methods in that the AFM uses no lenses or light in order to build an image. The heart of the AFM is a device called a cantilever, which is best described as a plate spring that is fixed at one end. The free end of the cantilever has a pointed tip that can interact with the surface of the sample and register information as the cantilever is deflected upon changes to the sample surface such as height variations and

interactions between the tip and the sample surface. Images are collected by the AFM through various modes of operations, which are often divided into two categories, static mode (often referred to as constant mode) and dynamic mode. Constant mode is comprised of constant force and constant height techniques while dynamic mode is comprised of non-contact mode and tapping mode techniques.

For the constant mode operation, the cantilever tip is essentially pulled across the surface of the sample either at constant force or constant height, and defections of the cantilever record information of the sample surface. The more commonly used mode of operation for AFM is the dynamic mode, specifically tapping mode, which relies on the oscillation of the cantilever tip for interaction with the sample surface. The value of interest for dynamic mode is the amplitude of the cantilever beam after interaction with the sample surface. Non-contact mode depends on the van der Waals force present near the surface of the sample to deflect the cantilever for construction of the image. Tapping mode measures the topology of the surface by oscillating the cantilever and intermittingly touching the sample surface such that as the oscillation amplitude of the cantilever is altered by the sample surface. To regain the desired oscillation amplitude of the cantilever, the cantilever height is adjusted and an image is constructed, i.e. changes in the oscillation amplitude produce the required deflection of the cantilever to create an image. Images in tapping mode may be constructed from height variations as well as phase variations. Phase imaging depends on the phase of the cantilever oscillation after interacting with the sample surface and will provide information that compliments the height image such as material properties, i.e. adhesion and viscoelasticity.

Besides the common recording of topography, the AFM is capable of other applications such as lithography where AFM has been used to manipulate individual molecules into arbitrary geometries. The AFM is also capable of recording information regarding mechanical, electrostatic, electrical, or magnetic properties of a sample surface by simply modifying the cantilever tip.

1.9.4. Spectroscopic Ellipsometry (SE)

Ellipsometry is often used to characterize the thickness of thin films, i.e. from several angstroms in thickness to several microns, as well as determine optical constants, such as refractive index. To determine such physical properties, ellipsometry simply measures two parameters, delta (Δ) and psi (Ψ). Delta measures the phase difference of light that is perpendicular and parallel to the plane of incidence before and after reflection from the surface of interest. Along with the phase shift before and after reflection, the light undergoes a reduction of amplitude, which is measured by the value of psi. It should be noted here that ellipsometry only measures the values of delta and psi, not the thickness or optical constants. The physical properties of the sample are calculated on models based from the measured delta and psi.

Ellipsometry is comprised of two complementary techniques, single-wavelength ellipsometry (SWE) and spectroscopic ellipsometry (SE). SWE often employees a monochromatic light source, i.e. a single wavelength visible laser, and is only able to measure a single set of delta and psi values, which makes measuring multiple layers and thick films difficult. Spectroscopic ellipsometry is capable of measuring delta and psi values for wavelengths ranging from the ultraviolet region, through the visible spectrum, to the near infrared (NIR) region. Through these multiple wavelengths of measurement,

complex models can be built to analyze multiple layers and determine physical properties of each of layer. Several great references on ellipsometry are provided here[18,19].

1.9.5. X-Ray Diffraction (XRD)

X-ray diffraction (XRD) is a powerful tool to determine the structure of well-ordered solid phase crystals, i.e. domain spacing and crystallographic phase. The contrast mechanism that XRD relies on is the differences in electron densities. The principle of XRD depends on the interaction of X-rays with electrons, or charged particles, and the response of the electrons to the X-ray irradiation. The interaction between the X-ray and the electrons will lead to either constructive or destructive interference of the scattered X-ray, such that only the constructive interference of the scattered X-rays will produce diffraction. Constructive interference occurs when a well-ordered structure is present, such as the arrangement of atoms in a crystal and is often defined by Bragg's law in Equation 1.1:

Equation 1.1 $$\lambda = 2d \sin\theta$$

where λ is the X-ray wavelength, d is the domain spacing, and θ is the incidence angle. XRD is typically performed in practice with incidence angles between 0.5 ° to 85 ° but when performing XRD at angles less than 10 °, the technique is often referred to as low-angle X-ray diffraction (LAXRD).

1.9.6. Small Angle and Wide Angle X-Ray Scattering (SAXS and WAXS)

X-ray scattering is a technique used to determine the structure of materials on the scale of nanometers to 100s of nanometers. The contrast for X-ray scattering relies on variations of electron density difference within a specimen. The principle behind X-ray

scattering is the interaction of the X-ray with the specimen, which, with the appropriate contrast, i.e. electron density difference present within the specimen, will result in the elastic scattering of the X-rays. The elastic scattering of the X-rays corresponds to the regularity of the electron density difference, according to Bragg's law, Equation 1.1. The angles of interest for small angle X-ray scattering (SAXS) are in the range of 0.1 ° to 1 °, while the wide angle X-ray scattering has a range of 5 ° to 60 °.

1.9.7. Spectroscopy Techniques

Spectroscopy is the study of interaction between radiation and matter[20]. The type of radiation used for spectroscopy may vary from electromagnetic to particle radiation and the interactions undergone by matter due to irradiation include absorption, emission, and scattering of photons when the energy is altered[20]. In general, spectroscopy deals with three types of motion: translational, rotational, and vibrational. Translational motion is the movement of a molecule from one position to another with a characteristic velocity composed of the three Cartesian components: x, y and z. Rotational motion is the rotation of a molecule about one of the three Cartesian axes. Vibrational motion is the repeated stretching and contraction of bonds between atoms.

1.9.7.1. Fourier Transform Infrared Spectroscopy (FT-IR)

Infrared (IR) spectroscopy is a common absorption technique used to characterize specific chemical bonds present in a molecule. IR is a common form of electromagnetic radiation used for spectroscopy because most vibrational motions of molecules have transitional energies that occur in the IR regime of the electromagnetic spectrum[21]. The IR regime of the electromagnetic spectrum is subdivided into three divisions: far (~ 15

cm^{-1} - ~ 120 cm^{-1}), mid (~ 120 cm^{-1} - ~ 5000 cm^{-1}), and near IR (~ 5000 cm^{-1} - ~ 12500 cm^{-1}). For a molecule to be IR active, one stipulation must be met and that is the absorption of radiation by a vibrational mode must change the electric dipole moment of the molecule when the atoms are displaced relative to one another[20].

Most modern IR spectrometers are Fourier transform infrared (FT-IR) spectrometers which employee an interferometer to analyze the sample. Most interferometers are comprised of a beam splitter and a set of mirrors, one stationary and one mobile. The beam splitter splits the incident radiation into two equal beams, one beam is sent to the stationary mirror and one beam is sent to the mobile mirror. The two separate beams will recombine to form one beam with either constructive interference or destructive interference, which depends on the phase shift at the point of recombination. This recombination signal is sent to the sample where the signal will be absorbed and/or reflected by the sample or transmitted to the detector. The signal that passes on to the detector will be converted into an interferogram. The interferogram is then converted to a spectrum by performing a Fourier transformation on the interferogram which is then presented in the form of intensity, either absorbance or transmittance, versus frequency.

1.9.7.2. Ultraviolet-Visible Spectroscopy (UV-Vis)

Ultraviolet-visible spectroscopy (UV-Vis) has the same basic principles to infrared spectroscopy except that the electromagnetic radiation used in UV-Vis is comprised of the ultraviolet and visible spectra, which correspond to the wavelength range of 100 nm to 800 nm. UV-Vis spectroscopy primarily encounters absorption or reflectance of the electromagnetic radiation within the UV-Vis range.

1.9.8. Interferometry and Profilometry

Interferometry is a simple characterization technique typically used to determine thickness of films as well as optical constants. The principle behind interferometry is the phase difference between the combinations of electromagnetic waves and, for purposes here, the electromagnetic radiation is visible light. The phase difference is generated in interferometry through reflections of the visible light from the top and the bottom interfaces of a film. The phase difference is either represented by constructive or destructive interference, often referred to as in phase or out of phase respectively, and will be seen as reflection maximums or reflection minimums, i.e. oscillations, when reflectance is plotted against wavelength. With reflectance data acquired for a specific wavelength region, the data will be fitted against a model based on the structure properties of the film material, i.e. refractive index.

Profilometry is a technique that measures the surface properties of samples such as profiles and roughness. Measurements are conducted by scanning a probe tip, typically less than 25 μm in diameter, across the surface of the sample and collecting the height variations, that the probe tip experiences from the sample surface, with respect to the distance traveled by the probe tip.

1.9.9. Thermal Gravimetric Analysis (TGA)

Thermal gravimetric analysis (TGA) measures the change in mass of a sample under well controlled conditions, such as temperature, temperature ramp rates, and atmosphere. TGA measurements are typically performed to determine the thermal stability of a material with respect to temperature and atmosphere, i.e. inert or air environments.

1.9.10. Differential Scanning Calorimetry (DSC)

Differential scanning calorimetry (DSC) is one of the most important characterization tools used to understand the thermal behavior of polymeric materials. Many polymers are semicrystalline and consist of a crystalline region and an amorphous region, with each region having a characteristic thermal behavior. The types of thermal transitions that are experienced by polymers consist of a crystalline melting temperature, T_m, and a glass transition temperature, T_g[22]. The T_m is best described as the melting temperature of the crystalline regions and T_g is best described as the temperature at which the amorphous regions become brittle and stiff[22]. Below the T_g, the polymer attains a brittle, glassy-like nature while above the T_g, the polymer becomes more flexible and rubber-like. This transition in the polymer is due to the existence of long range motion or segmental motion[23]. This type of motion arises from the rotation of bonds at the end of a segment of a polymer chain and becomes more prevalent as temperature increases[23]. It should be noted that only segmental motion is occurring and that the whole polymer chain is not experiencing motion. Upon further heating, the entire polymer will begin to have motion and the T_m transition will be observed.

The basis of DSC operation is to measure the heat capacity of a sample as a function of temperature. This analysis is performed by measuring the heat flow required to maintain a zero temperature differential between an inert reference material and the polymeric sample[22]. As the polymeric material goes through a thermal transition, the heat capacity of the polymer will be altered. This change in heat capacity will be quantified by the change in heat flow required to maintain zero temperature difference

between the reference material and the polymer sample. Typical DSC results plot heat flow versus temperature.

1.9.11. Nanoindentation

Nanoindentation is an important technique for measuring the mechanical properties of thin films. The mechanical properties of thin films are determined by indenting a specimen with a probe, constructed from a hard material, i.e. diamond, which has known properties, such as mechanical and geometric dimensions. The geometry of the probe tip is typically a three-sided pyramid, which is often referred to as a Berkovich tip. The probe will apply a specific load to the specimen through a program which has a defined load ramp rate, maximum load, hold time for the maximum load, and unload ramp rate, all while precisely monitoring the penetration depth of the probe.

The two most common mechanical properties that are measured through nanoindentation are hardness and modulus, which are products of load-displacement curves. The hardness is primarily dependent on the maximum load placed on the specimen and the displacement of the specimen due to the probe geometry, which is determined by Equation 1.2:

Equation 1.2
$$H = \frac{P_{max}}{A}$$

where H is the calculated hardness, P_{max} is the maximum load placed on the specimen (determined from the load-displacement curve), and A is the area of the indent. The modulus of the specimen is determined from the displacement of the specimen by the probe as well as the stiffness of the contact made between the probe and the specimen, which is shown in Equation 1.3:

Equation 1.3 $$E_r = \frac{1}{\beta}\frac{\sqrt{\pi}}{2}\frac{S}{\sqrt{A}}$$

where E_r is the reduced modulus, β is a correction factor for geometry, S is the contact stiffness between the probe and the specimen (determined by the slope of the unload region from the load-displacement curve), and A is the area of the indent. It should be noted that for high-quality data to be obtained from nanoindentation, the contributions from the substrate need to be minimized. The mechanical response from the substrate is removed by simply sampling a limited region of the specimen, i.e. nanoindentation is only performed such that the maximum indentation depth is no more than 10 % of the entire film thickness. Another important note regarding the quality of nanoindentation data is that the probe, specifically the Berkovich tip, must reach a minimum indentation depth (this depth is dependent on the instrument being used) such that intimate contact is established between the probe and the specimen.

1.10. References

(1) Chou, S. Y.; Krauss, P. R.; Renstrom, P. J. *Applied Physics Letters* **1995**, *67*, 3114-3116.

(2) Chou, S. Y.; Krauss, P. R.; Renstrom, P. J. *Science* **1996**, *272*, 85-87.

(3) Chou, S. Y.; Krauss, P. R.; Zhang, W.; Guo, L.; Zhuang, L. *Journal of Vacuum Science & Technology B: Microelectronics and Nanometer Structures* **1997**, *15*, 2897-2904.

(4) Haisma, J.; Verheijen, M.; van den Heuvel, K.; van den Berg, J. *Journal of Vacuum Science & Technology B: Microelectronics and Nanometer Structures* **1996**, *14*, 4124-4128.

(5) Colburn, M.; Johnson, S.; Stewart, M.; Damle, S.; Bailey, T.; Choi, B.; Wedlake, M.; Michaelson, T.; Sreenivasan, S. V.; Ekerdt, J.; Willson, C. G. *Proceedings of SPIE* **1999**, *3676*, 379-389.

(6) Brinker, C. J.; Scherer, G. W. *Sol-Gel Science: The Physics and Chemistry of Sol-Gel Processing*; Academic Press: San Diego, 1990.

(7) Bates, F. S.; Fredrickson, G. H. *Annual Review of Physical Chemistry* **1990**, *41*, 525-57.

(8) Bates, F. S.; Fredrickson, G. H. *Physics Today* **1999**, *52*, 32.

(9) Gupta, R. R.; RamachandraRao, V. S.; Watkins, J. J. *Macromolecules* **2003**, *36*, 1295-1303.

(10) Linstrom, P. J.; Mallard, W. G. National Institute of Standards and Technology Chemistry WebBook http://webbook.nist.gov (accessed Sep 3, 2008).

(11) Pai, R. A.; Humayun, R.; Schulberg, M. T.; Sengupta, A.; Sun, J.-N.; Watkins, J. J. *Science* **2004**, *303*, 507-510.

(12) Nagarajan, S.; Bosworth, J. K.; Ober, C. K.; Russell, T. P.; Watkins, J. J. *Chemistry of Materials* **2008**, *20*, 604-606.

(13) Nagarajan, S.; Li, M.; Pai, R. A.; Bosworth, J. K.; Busch, P.; Smilgies, D.-M.; Ober, C. K.; Russell, T. P.; Watkins, J. J. *Advanced Materials* **2008**, *20*, 246-251.

(14) Chen, H.-T.; Crosby, T. A.; Park, M.-H.; Nagarajan, S.; Rotello, V. M.; Watkins, J. J. *Journal of Materials Chemistry* **2009**, *19*, 70.

(15) Ell, J. R.; Crosby, T. A.; Peterson, J. J.; Carter, K. R.; Watkins, J. J. *Chemistry of Materials* **2010**, *22*, 1445-1451.

(16) Hendricks, N. R.; Watkins, J. J.; Carter, K. R. *Journal of Materials Chemistry* **2011**, *21*, 14213-14218.

(17) Goldstein, J.; Newbury, D. E.; Joy, D. C.; Lyman, C. E.; Echlin, P.; Lifshin, E.; Sawyer, L.; Michael, J. *Scanning Electron Microscopy and X-Ray Microanalysis*; 3rd ed.; Springer: New York, 2003.

(18) Tomkins, H. G. *A User's Guide to Ellipsometry*; 1st ed.; Academic Press: San Diego, 1992.

(19) Tomkins, H. G.; McGahan, W. A. *Spectroscopic Ellipsometry and Reflectometry*; John Wiley & Sons, Inc.: New York, 1999.

(20) Atkins, P.; de Paula, J. *Physical Chemistry*; 7th ed.; W. H. Freeman and Company: New York, 2002.

(21) White, R. *Handbook of Industrial Infrared Analysis*; 1st ed.; Plenum Press: New York, 1964.

(22) Odian, G. *Principles of Polymerization*; 4th ed.; John Wiley & Sons, Inc.: Hoboken, New Jersey, 2004.

(23) Bahadur, P.; Sastry, N. V. *Principles of Polymer Science*; 1st ed.; Alpha Science International Ltd.: Pangbourne, England, 2002.

CHAPTER 2

FORMATION OF HIERARCHICAL SILICA NANOCHANNELS THROUGH NANOIMPRINT LITHOGRAPHY

2.1. Introduction

The fabrication of mesoporous silica nanochannels with hierarchical structure has attracted increasing interest for applications such as ultra-low-k dielectric materials for microelectronics[1–4], separations media, catalyst substrates[5,6], chemical sensors[7,8], and micro/nanofluidic devices[9]. These applications benefit from the hierarchical structure, which exhibit features at two distinct length scales. At the domain level, the film contains well defined pores, generally of discrete size distributions with diameters in the range of 3 to 10 nm, although larger pores are possible. At the device level, channel structures on the order of 25 to 500 nm provide increased porosity and fluid flow capabilities. Several approaches have previously been taken to create embedded nanochannels. These include the combinations of electron-beam (e-beam) lithography, reactive ion etching (RIE), wet etching[10,11], or focused-ion beam (FIB) milling techniques to create the template and channel isolation with wafer bonding procedures, sacrificial material templates[12], directed self assembly of nanoparticles[13], nanoimprint lithography[14–17], buried channel technology[18], and surface nanomachining[19].

Of particular interest to the semiconductor community is the formation of airgap structures for use as an ultra-low-k (ULK) interlayer dielectric (ILD). As the size of interconnects continues to decrease, the capacitance that resides between metallic interconnects continues to increase. The objective is to diminish the capacitance between

interconnects for decreased resistive-capacitive (RC) delay and reduced power consumption. The materials approach to reduce the dielectric constant of ILDs is to incorporate air into the ILD, by either porosity or airgaps, effectively replacing a higher dielectric constant materials, for example, silicon dioxide, with a dielectric constant of ~ 3.9, with air, which has a dielectric constant of ~ 1. Common methods to create airgaps are through sacrificial material removal and non-conformal chemical vapor deposition (CVD)[20–22]. An alternative, efficient route for the fabrication of embedded nanochannels within a mesoporous film is through a combination of supercritical carbon dioxide ($scCO_2$) infusion processing, to yield the mesopore structure, with nanoimprint lithography (NIL), to yield the airgap structure. The combination of these two techniques enables precise design of both domain level and device level structures.

2.2. Experimental

2.2.1. Materials

[3-(methacryloyloxy)propyl] trimethoxysilane (98%, Aldrich), ethoxylated-bisphenol A dimethacrylate esters (Sartomer), trimethylolpropane triacrylate (tech. grade, Aldrich), propylene glycol methyl ether acetate (≥ 99.5%, Aldrich), Pluronic® F127 and Pluronic® F108 block copolymers (BASF), para-toluene sulfonic acid (99%, Acros Organics), poly(acrylic acid) (1.8k Mw, Aldrich), tetraethyl orthosilicate (99.999%, Sigma-Aldrich), and carbon dioxide (Merrian Graves, bone-dry grade) were used as received without further purification. Silicon wafers of (100) orientation (p-type, boron dopant) were obtained from University Wafer.

2.2.2. Silicon Wafer Preparation

Silicon substrates (2.5 cm x 2.5 cm) were coated with a self-assembled monolayer (SAM) of [3-(methacryloyloxy)propyl] trimethoxysilane that was anchored to the silicon substrate to serve as an adhesion promoter. The chemical structure of the adhesion promoter is shown in Figure 2.1.

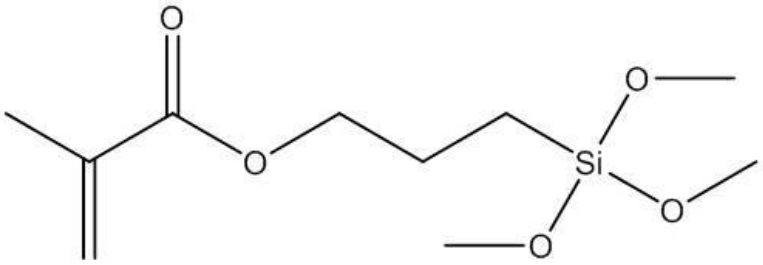

Figure 2.1. Chemical structure of the adhesion promotion molecule [3-(methacryloyloxy)propyl] trimethoxysilane.

The silicon wafer surface must be modified with an adhesion promoter to adjust the surface energies of the substrate to be compatible with the ultraviolet (UV)-curable resist, which allows a uniform thin film to be spin-coated. The silicon wafer pieces were rinsed with acetone and isopropanol (IPA), dried under a stream of nitrogen (N_2) and then etched with an oxygen (O_2) plasma with an inductively coupled plasma (ICP) etcher (30 W, 100 mTorr) for 15 minutes to remove any surface contamination. The silicon wafers were then rinsed with water and ethanol, dried under a stream of N_2 and immediately placed in a 1 vol. % solution of 3-(trimethoxysilyl)propyl methacrylate in dry toluene at 80 °C for 2 hours. Upon removal from the adhesion promotion solution, the silicon wafers were rinsed with IPA and dried under a stream of N_2. A static water contact angle measurement of 81 ± 2 ° was reported for the 3-(trimethoxysilyl)propyl methacrylate SAM surface.

2.2.3. Mold Fabrication

2.2.3.1. Fluorination of Master Molds

Polycarbonate and silicon master molds were used in the fabrication of replica, i.e. daughter, molds for the NIL procedure. Depending on the master mold being used, either silicon or polycarbonate, there was a separate procedure to apply the release layer to the surface of the master mold. For the silicon master molds, the molds were rinsed with acetone and IPA then dried under a stream of N_2. The rinsed silicon master molds were then etched in an ICP etcher with O_2 plasma (30 W, 100 mTorr) for 1 minute to generate reactive functional groups on the surface. To provide a release layer for the polycarbonate master molds, the molds were initially rinsed with acetone, ethanol and IPA and dried under a stream of N_2. To provide an anchoring site for the release layer, a thin layer, ~ 10 nm, of silicon monoxide (99.9%, Kurt J. Lesker) was deposited via thermal evaporation. Once the silicon monoxide layer was deposited on the polycarbonate master mold, an O_2 plasma etch was performed from an inductively coupled plasma (ICP) etcher (30 W, 100 mTorr) for 1 minute to activate the surface with silanol groups for further functionalization.

With the surfaces of the silicon and polycarbonate master molds populated with reactive functional groups, the molds were exposed to a 1 vol. %, with respect to the reactor volume, of (heptadecafluoro-1,1,2,2-tetrahydrodecyl) dimethyl chlorosilane (Gelest) at 80 °C for 24 - 48 hours to generate the fluorinated release layer self assembled monolayer (SAM). The chemical structure of (heptadecafluoro-1,1,2,2-tetrahydrodecyl) dimethyl chlorosilane is shown in Figure 2.2.

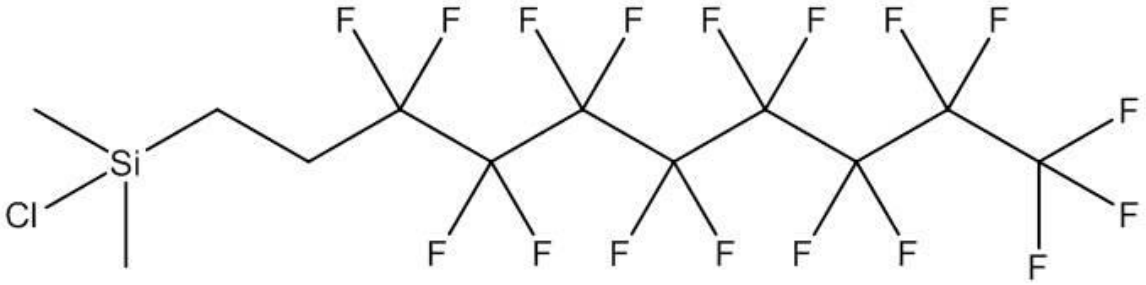

Figure 2.2. Chemical structure of (heptadecafluoro-1,1,2,2-tetrahydrodecyl) dimethyl chlorosilane.

For both the silicon and polycarbonate master molds, the static contact angle measurement for the fluorinated replica molds was ~ 135°. The master molds with the fluorinated release layer applied were ready for replication. The process to apply the fluorinated release layer to a silicon master mold is shown in Figure 2.3 and the process to apply the fluorinated release layer to a polycarbonate master mold is shown in Figure 2.4.

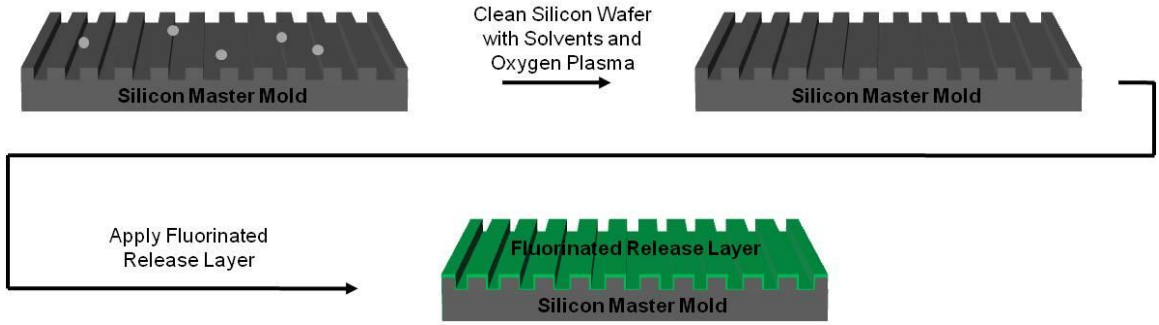

Figure 2.3. Process to apply fluorinated release layer to a silicon master mold.

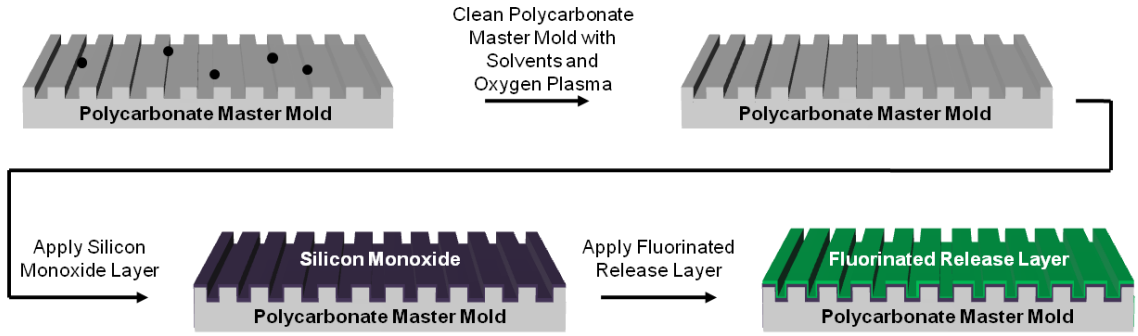

Figure 2.4. Process to apply fluorinated release layer to a polycarbonate master mold.

2.2.3.2. Replication of Fluorinated Master Molds

The replication of the fluorinated master molds began by applying the adhesion promoter molecule to the surface of a glass slide. The process to apply the SAM of the adhesion promoter to the glass slide was identical to the process used for applying the SAM of the adhesion promoter to the silicon wafer. With the adhesion promoted glass slides and fluorinated master molds available, a microscopic amount, on the order of several microliters, of the UV-curable photoresist, comprised of ethoxylated-bisphenol A dimethacrylate, trimethylolpropane triacrylate, and 2,2-dimethoxy-2-phenylacetophenone, was applied to the center of a fluorinated master mold. The actual amount of the UV-curable photoresist needed depends on the size of the fluorinated master mold that was being replicated. The adhesion promoted glass slide was then gently placed on top of the fluorinated master mold and exposed to 365 nm UV-radiation (12.7 mW/cm^2) in a N_2 environment for 15 minutes. The replicated mold was then manually de-molded from the fluorinated master mold with the aid of a razor blade and compressed air. The process of mold replication is shown in Figure 2.5.

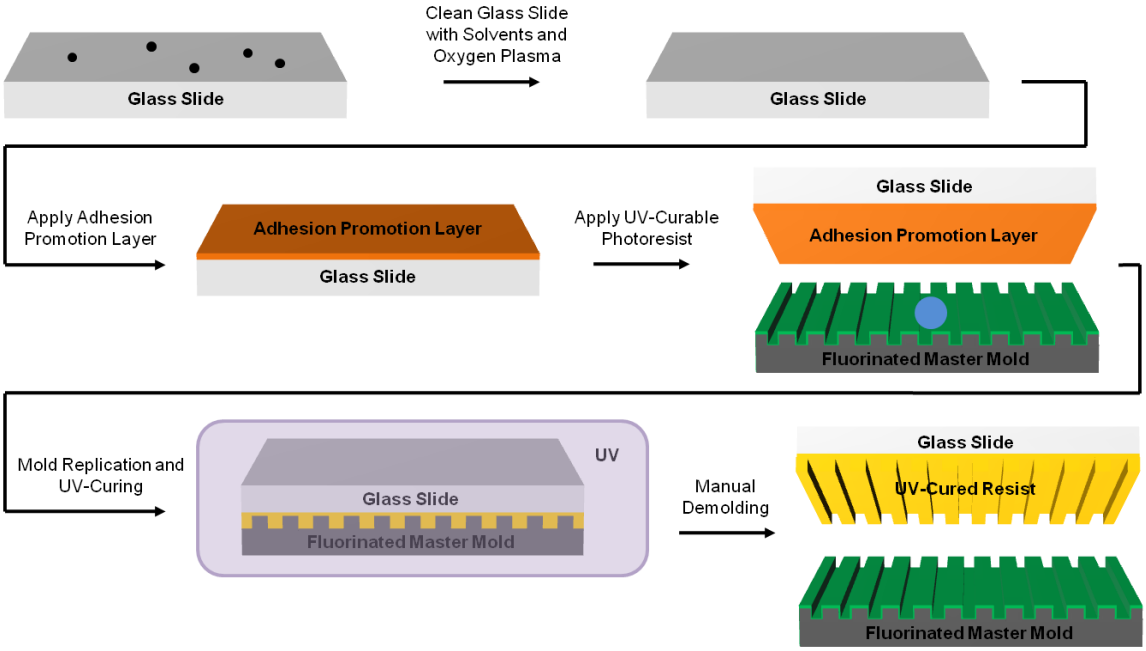

Figure 2.5. Process of mold replication.

A release layer must be applied to the replicated mold prior to use in the NIL process. The SAM of the release layer was applied to the replicated mold via the same process that was used for the fluorination of the polycarbonate master molds (see Figure 2.4). The fluorinated replica mold was then ready for use in the NIL process.

2.2.4. Nanoimprint Lithography

A UV-curable photopolymer solution comprised of ethoxylated-bisphenol A dimethacrylate, trimethylolpropane triacrylate, and 2,2-dimethoxy-2-phenylacetophenone dissolved in propylene glycol methyl ether acetate (PGMEA) was spin-coated at 3000 rpm for 15 seconds on the adhesion promoted substrate. The components of the photopolymer are shown in Figure 2.6.

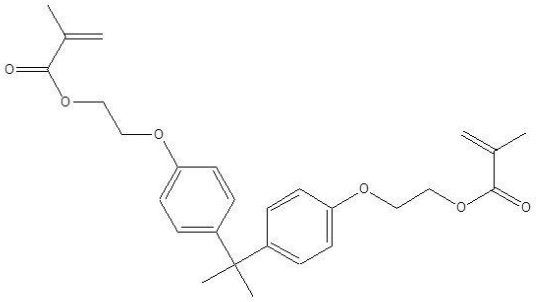

Ethoxylated Bisphenol-A Dimethacrylate Esters (~75%) [Difunctional Monomer]

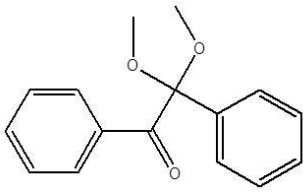

2,2-dimethoxy-2-phenylacetophenone (~2%) [Photoinitiator]

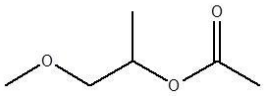

Propylene Glycol Methyl Ether Acetate (PGMEA) [Solvent]

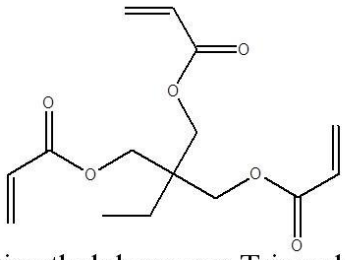

Trimethylolpropane Triacrylate (~23%) [Crosslinker]

Figure 2.6. UV-curable photoresist composition.

The concentration of the photoresist solution determined the film thickness from spin-coating, where typical concentrations ranged from 1 wt. % to 20 wt. % to yield film thicknesses from ~ 25 nm to ~ 400 nm. Thin films of the UV-curable photoresist were patterned with transparent, fluorinated molds using a Nanonex NX-2000 Nanoimprinter tool with the following conditions: the pre-imprint was made at 25 °C and 0.86 MPa (125 PSI) for 30 seconds, the imprint was made at 25 °C and 1.38 MPa (200 PSI) for 60 seconds with the last 30 seconds of the imprint time irradiating the sample with 365 nm UV-light from a Dymax Bluewave® 200 UV-light source (upon exposure to 365 nm UV light, the UV-curable resist undergoes a crosslinking polymerization), and then the pressure was released. The fluorinated mold and sample was then manually separated with the assistance of a razor blade and compressed air.

2.2.5. Anisotropic Etching

Following NIL replication, the thin residual layer connecting the features was removed using dry etching. An inductively coupled plasma reactive ion etch (ICP-RIE, Trion Technology Inc., Phantom III) with O_2 plasma (150 W ICP, 30 W RIE, 250 mTorr, 49 sccm O_2) was applied for 30 seconds and resulted in free-standing structures.

2.2.6. Supercritical Carbon Dioxide Infusion Processing

Mesoporous silica films were generated by exposing amphiphilic block copolymer templates to a solution of tetraethyl orthosilicate (TEOS) in scCO_2 within a high pressure reactor at 60 °C and 12.41 MPa (1800 psi). The high pressure reactor, ~ 160 mL in volume, was constructed from two stainless steel opposed ended hubs sealed with a graphite ring (55 ft-lb torque) purchased from Grayloc® Products. Heating bands (Watlow®) were connected to the outside of the reactor walls to control the gas temperature. The top reactor hub was drilled to have 4 ports; one to measure internal pressure, one to measure internal temperature, one for gas inlet, and one for gas outlet. For the Pluronic® surfactant solutions (Pluronic® F127 or Pluronic® F108) containing 40 wt. % PAA (1.8k Mw, with respect to Pluronic F127® or Pluronic F108®) and 3 wt. % pTSA (with respect to solid material), TEOS (6 – 10 μL) was directly placed within the high pressure reactor along with 500 μL of reverse osmosis (RO) water prior to sealing. Once the reactor was sealed and heated to a gas temperature of 60 °C, carbon dioxide (CO_2) was injected with a high pressure syringe pump (ISCO, Model 500 HP) at a rate of 2 – 3 mL/minute. Once the desired pressure was reached, a soak time of 2 hours at 60 °C and 12.41 MPa (1800 psi) was employed. The reactor was then de-pressurized

overnight to room pressure. Samples were thermally degraded at 400 °C for various times with a ramp rate of 1.56 °C/minute.

2.2.7. Capacitance Measurements

The hierarchically structured silica nanochannels were fabricated on low-resistivity silicon wafers (0.001 – 0.005 Ω-cm, University Wafers) to minimize the capacitance associated with the silicon wafer. The samples were directly taken from the thermal degradation, i.e. calcination, oven to a 150 °C pre-heated hexamethyldisilazane (HMDS) vapor prime oven (YES LP-III vapor prime oven) for hydrophobic treatment. This was done to minimize the uptake of atmospheric water by the mesoporous silica. The top contact for the capacitance measurements was deposited by evaporation of ~ 100 nm of aluminum (99.999%, Ted Pella, Inc.) by electron-beam evaporation (CHA SE-600 electron beam evaporator) using a shadow mask consisting of 1 mm, 1.5 mm, and 2 mm diameter pads. Capacitance measurements were conducted with a Keithley 4200 Semiconductor Characterization System coupled with a Wentworth MP-2300 probe station. A frequency of 100 kHz was used with a sweep voltage from 0 V to -5 V using a step size of 0.1 V.

2.2.8. Characterization

Water contact angle measurements were conducted using a VCA Optima surface analysis/goniometry system with a 0.5 μL drop. Atomic force microscopy (AFM) images were collected with a Digital Instruments Nanoscope IIIA in tapping mode under ambient conditions. Thermogravimetric analysis (TGA) was conducted with a DuPont TGA 2950 using a ramp rate of 1.56 °C/minute and holding at 400 °C for 6 hours under an air

environment. Attenuated total reflectance Fourier transform infrared (ATR-FT-IR) measurements were collected on a Nicolet 6700 FT-IR spectrometer equipped with a Harrick grazing angle ATR accessory (GATR) with a liquid N_2 cooled photovoltaic detector (LN-MCT). Sample preparation by FIB was performed with a FEI Strata 400 DualBeam which was also used for the collection of the cross-sectional SEM images. The procedure requires the deposition of ~ 1.3 μm of platinum as the protection layer followed by FIB etching of ~ 5 μm. The images were collected at an angle of 52 °. Film thickness was measured with a Filmetrics F20 Thin Film Measurement System and reported values were an average of 5 measurements over the entire surface with a deviation of ± 5 nm. Silicon wafers were cleaned via a Harrick Scientific Corp. plasma cleaner/sterilizer (Model PDC-001) operating at ICP strength of 30 W and 100 mTorr of O_2. A Phantom III ICP reactive ion etch (RIE) tool from Trion Technology Inc. was used for etching the NIL patterned substrates to generate free-standing nanostructures. Transmission electron microscopy (TEM) samples were prepared by scraping mesoporous silica from the substrate, grinding via mortar and pestle, suspended with ethanol and transferred to a carbon-coated copper grid to be analyzed with a JEOL 2000FX II operating at 200 kV. Variable angle spectroscopic ellipsometry (VASE) was performed with a Sopra GES-5 Variable Angle Spectroscopic Ellipsometer (VASE).

2.3. Results and Discussion

To produce the desired hierarchical nanochannels, a seven step approach was developed. The procedure is outlined in Figure 2.7.

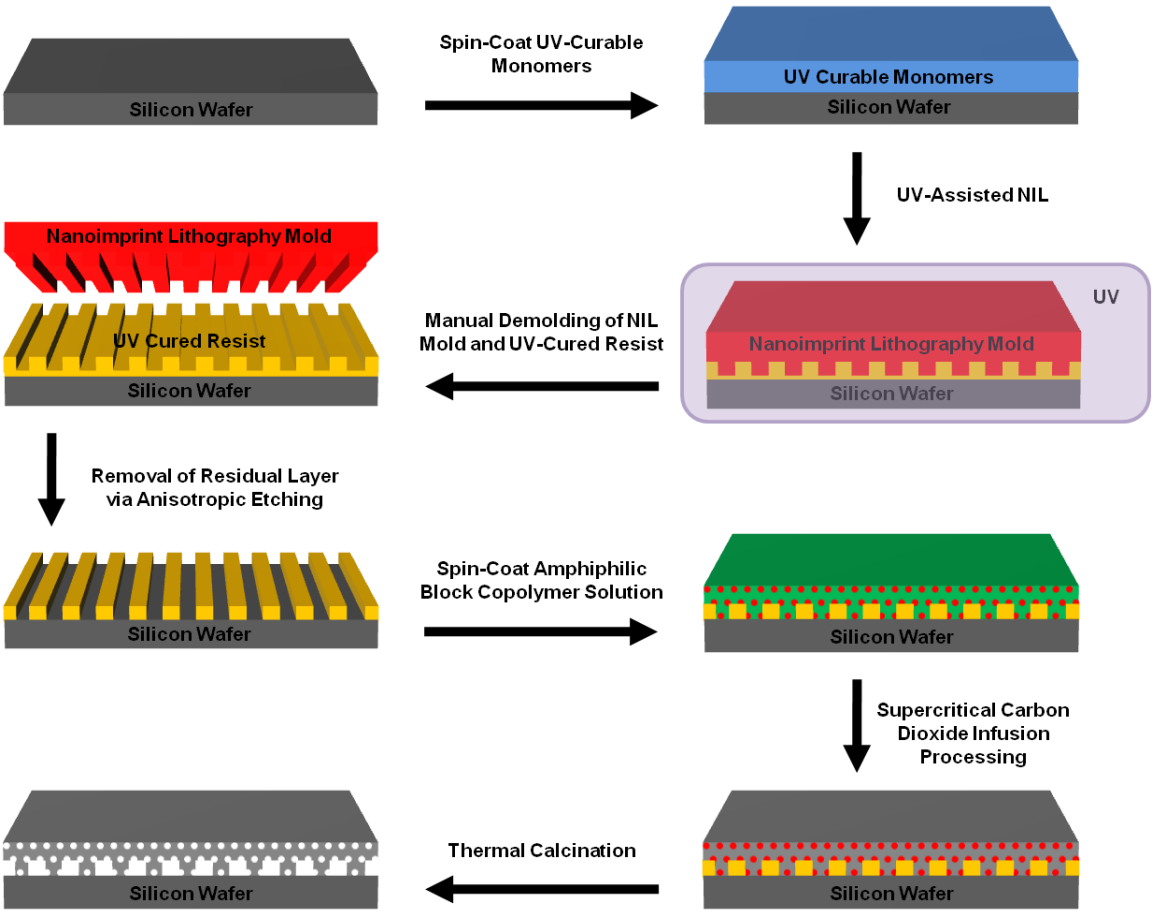

Figure 2.7. Schematic showing the procedure to fabricate hierarchical silica nanostructures with domain and device level features.

The process began by making uniform thin films of UV-curable monomers by spin-coating a solution of ~ 75 wt. % ethoxylated-bisphenol A dimethacrylate, ~ 23 wt. % trimethylolpropane triacrylate and ~ 2 wt. % 2,2-dimethoxy-2-phenylacetophenone dissolved in propylene glycol methyl ether acetate (PGMEA) onto a 3-(trimethoxysilyl)propyl methacrylate treated silicon wafer surface at 3000 rpm for 15 seconds in the presence of air. Typical concentrations ranged from 1 wt. % to 20 wt. % which yielded film thicknesses from ~ 25 nm to ~ 400 nm. The surface of the silicon wafer was treated with [3-(methacryloyloxy)propyl] trimethoxysilane to avoid dewetting of the UV-curable monomer solution and to adjust the surface of the silicon wafer with a

functionality that allows for participation in the crosslinking via UV-exposure. To begin the fabrication of hierarchical silica nanochannels, an initial device level pattern consisting of a test pattern with various pattern geometries and pattern densities, with both positive and negative tones, was patterned into the photopolymer composition. Characterization of the test pattern master mold with scanning electron microscopy and optical microscopy is provided in Figure 2.8.

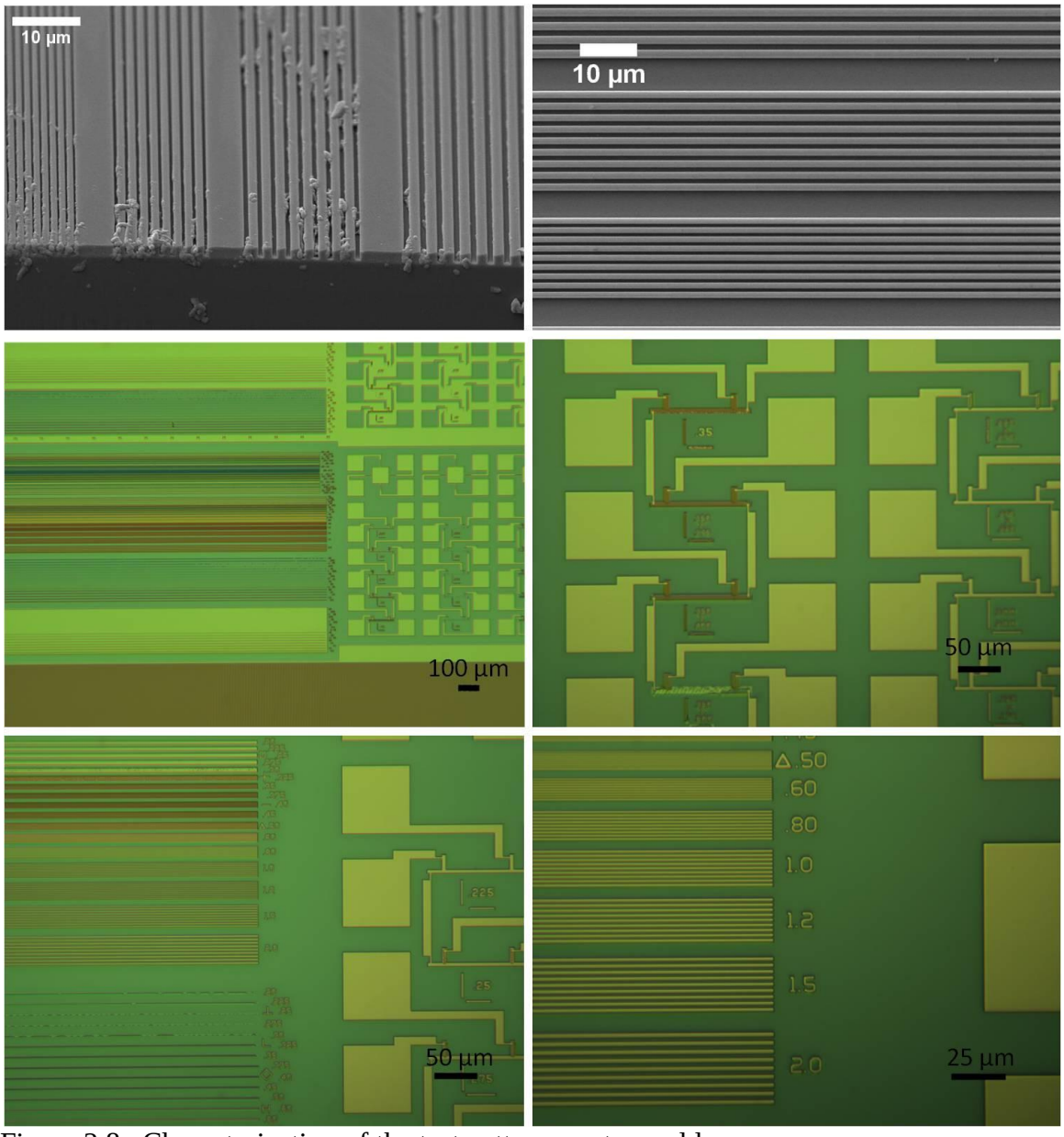

Figure 2.8. Characterization of the test pattern master mold.

To pattern the device level features, a thin film of ~ 400 nm from a 20 wt. % solution of the UV-curable photopolymer was spin-coated at 3000 rpm for 15 seconds in the presence of air. UV-assisted NIL was then performed with a transparent mold containing the device level features to create a replication of the mold into the UV-curable photopolymer. Upon exposure to 365 nm UV-light, the UV-curable resist undergoes a crosslinking polymerization . A film thickness of ~ 400 nm yielded a minimal residual layer while achieving complete filling of the mold features. Swelling of the UV-cured photopolymer was monitored in $scCO_2$ by variable angle spectroscopic ellipsometry (VASE) to check for pattern fidelity. It was determined that the UV-cured photopolymer swelled a marginal amount of ~ 4 % in the presence of $scCO_2$ at 12.41 MPa (1800 psi) and 60 °C. This minimal amount of swelling should not disrupt the dimensions of the polymer template.

Following NIL replication, the thin residual layer connecting the features was removed using dry etching. An ICP-RIE with O_2 plasma was applied to create free-standing structures. The plasma treatment resulted in a surface modificaiton and yielded a more hydrophilic surface on the patterned silicon wafer. To monitor the depth of the O_2 plasma ICP-RIE etch, optical microscopy was performed after each step and is detailed in Figure 2.9. The ICP-RIE etch was determined successful once the silicon wafer was observed, i.e. the brighter regions within the optical microscopy images were exposed. The structure of the original NIL template ultimately dictates the dimensions of the embedded nanochannels and thus the device level feature of the hierarchical structure.

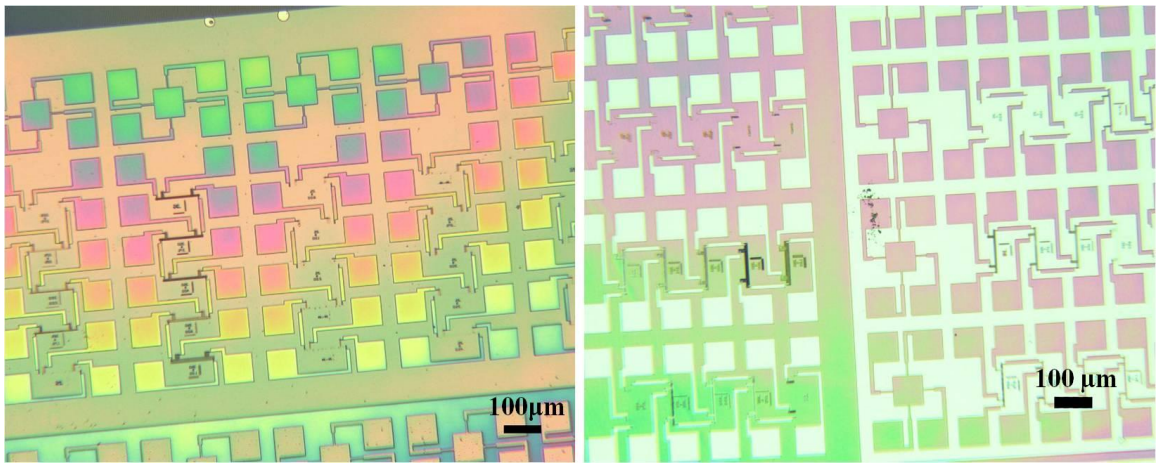

Figure 2.9. Optical microscopy images of imprinted (left) and etched (right) samples patterned with the test pattern structure.

With the silicon substrate exposed between the free-standing structures, the amphiphilic block copolymer used in the $scCO_2$ infusion processing was deposited. The amphiphilic block copolymers selected to template the domain level features, i.e. mesopores were the commercially available members of the BASF Pluronic® family. The Pluronic® family of block copolymer templates is based on triblock copolymers of poly(ethylene oxide)-b-poly(propylene oxide)-b-poly(ethylene oxide) [PEO-b-PPO-b-PEO]. The coding for the Pluronic® trade name of triblock copolymers begins with a letter, which represents the physical state of the material at room temperature, i.e. P = paste, F = flake (solid), L = liquid, followed by a series of digits, either two or three numbers in length. The first digit of the number or the first two digits of the three digit number represents the approximate molecular weight of the poly(propylene oxide) block multipled by 300. The last digit of the number represents the weight percent of the poly(ethyelene oxide) block multipled by 10. An example of the Pluronic® coding is Pluronic® F127, which is a flake (solid) at room temperature with 3600 Mw poly(propylene oxide) and 70 % poly(ethylene oxide). The number of Pluronic®

derivatives is vast and is easily summarized by the Pluronic® grid, which is provided in Figure 2.10.

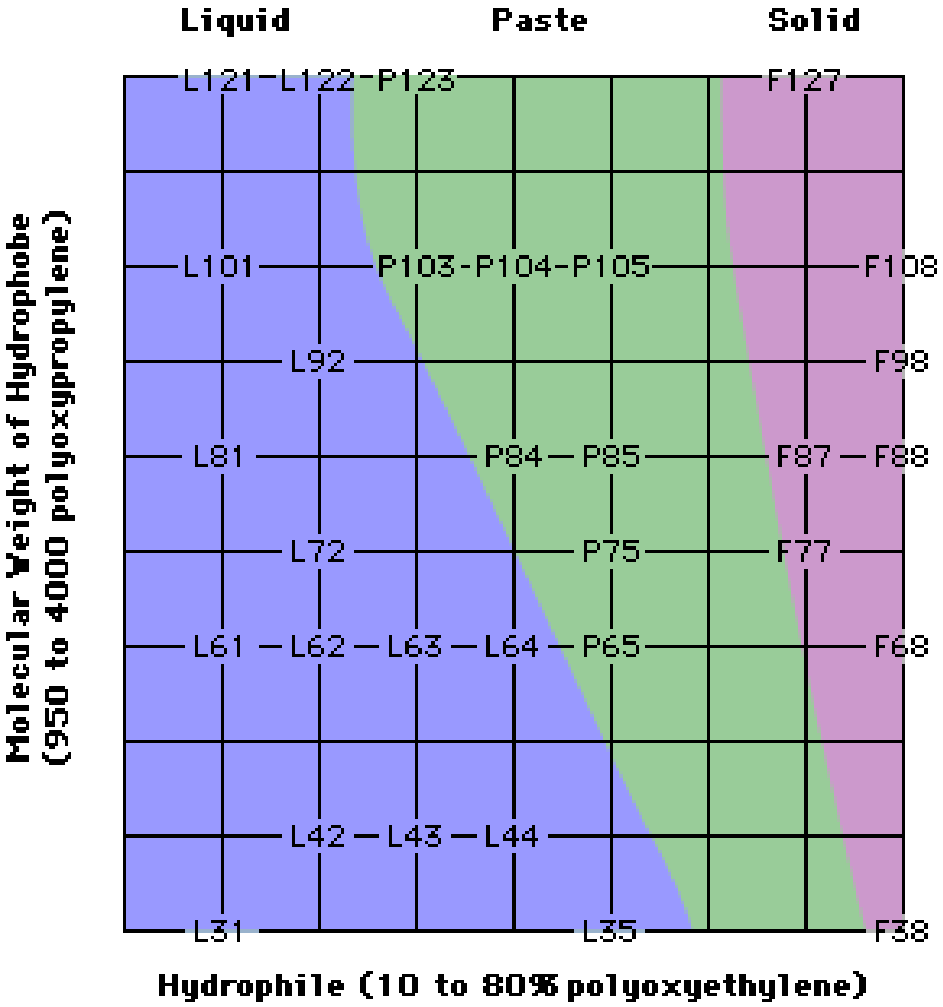

Figure 2.10. The Pluronic® grid.

Two triblock copolymers were chosen as templates from the Pluronic® series; Pluronic® F127, PEO_{106}-b-PPO_{70}-b-PEO_{106}, which phase separates into a cylindrical morphology during the template process and Pluronic® F108, PEO_{127}-b-PPO_{48}-b-PEO_{127}, which phase separates into a spherical morphology. An organic acid catalyst, p-toluene sulfonic acid (pTSA), was added to the amphiphilic block copolymer solution to promote the hydrolysis and condensation of the silica network. The template also contains a

hydrophilic homopolymer such as poly(acrylic acid) (PAA) or poly(4-hydroxystyrene) (PHOST) to help promote template phase segregation and long-range order of the domain level features[23–25]. A 10 wt. % solution of either Pluronic F127® or Pluronic F108® was prepared in a 50:50 ethanol:deionized (DI) water solution with 40 wt. % PAA (1.8k Mw, with respect to Pluronic F127® or Pluronic F108®) and 3 wt. % pTSA (with respect to solid material). The solution was then directly spin-coated in an air environment, through a 0.2 μm poly(tetrafluoroethylene) (PTFE) filter, on the NIL patterned surface for 15 seconds at 3000 rpm forming a film of ~ 1 μm thick.

The next step was to transform the template into mesoporous silica. The block copolymer coated NIL template was exposed to a silicon alkoxide precursor, tetraethyl orthosilicate (TEOS), solution in humidified $scCO_2$ at 60 °C and 12.41 MPa (1800 psi) for 2 hours. Upon exposure to $scCO_2$, both the block copolymer template and the NIL template swell slightly allowing the TEOS to diffuse within both templates. As stated in Chapter 1, the acid catalyst, pTSA, selectively segregates to the hydrophilic segment of the block copolymer template within which hydrolysis and condensation of TEOS occurs. Little to no condensation of TEOS occurs within the hydrophobic segment of the block copolymer and the NIL template due to no acid catalyst being present. To ultimately form the hierarchical silica nanochannels, the polymer templates from both the block copolymer and NIL pattern were removed through thermal degradation. Accordingly, the substrates were placed in a calcination oven heated at a 1.56 °C/minute ramp rate from room temperature to 400 °C for 6 hours and a ramp rate of 1.56 °C/minute back to room temperature.

The degradation of the polymer templates is of importance as to ensure that the nanochannel dimensions are transferred into the mesoporous silica with high accuracy and to avoid the nanochannel collapsing. To determine the thermal degradation pathway of the polymer templates, thermogravemetic analysis (TGA) was performed and is provided in Figure 2.11. From the TGA data, it was determined that the block copolymer template was removed first followed by the removal of the NIL template. This order of template removal should provide highly accurate replication into the mesoporous silica due to the porosity imparted by the block copolymer template[26], which would provide a pathway for the degradation products of the NIL template to escape and yield crack-free films.

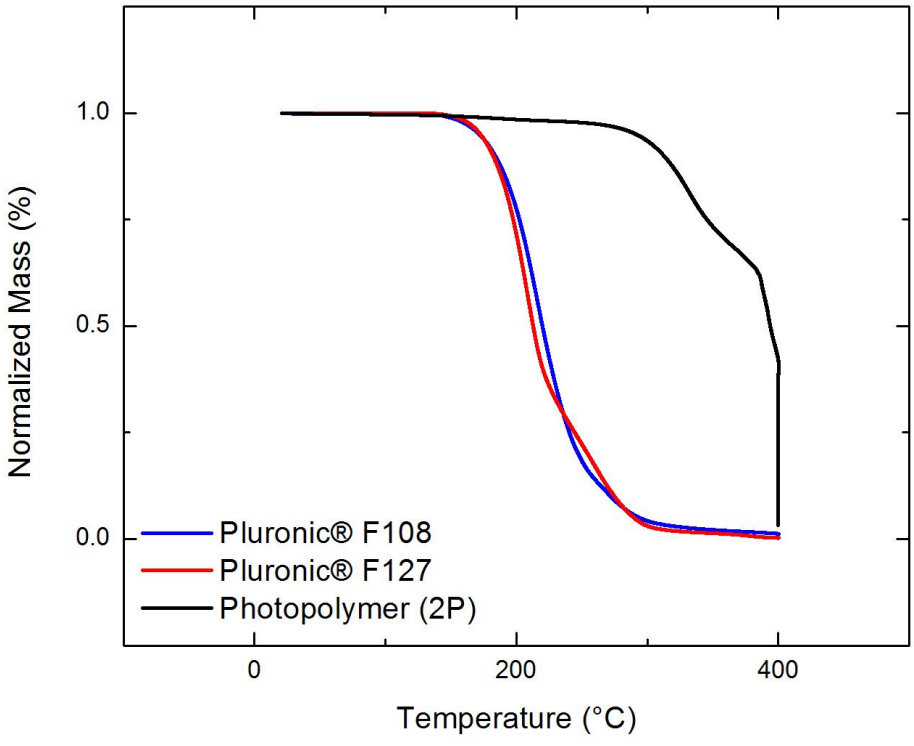

Figure 2.11. Thermogravimetric analysis (TGA) of polymers templates: Pluronic® F108, Pluronic® F127, and photopolymer (2P).

Transmission electron microscopy (TEM) images of the domain level features for Pluronic® F127, Figure 2.12 (left), and Pluronic® F108, Figure 2.12 (right), templates show mesopore morphologies of cylinders and spheres respectively with diameters of ~ 4 - 5 nm.

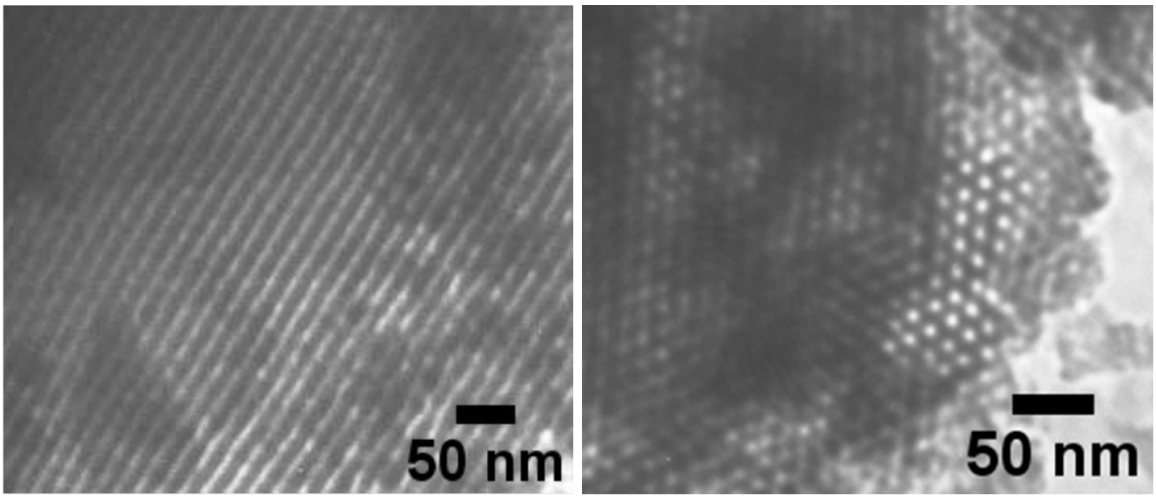

Figure 2.12. Transmission electron micrographs showing the domain level features of the hierarchical silica nanochannel for Pluronic® F127 (left) and Pluronic® F108 (right).

To determine the fidelity of the device level structure, optical microscopy and scanning electron microscopy (SEM) were obtained. For the test pattern structures, severe defects, in the form of cracks, were present through the entire film, as shown in Figure 2.13. Attempts to eliminate the defects consisted of adjusting the thermal degradation cycling parameters, i.e. ramp rates and hold times, as well as adjusting the thickness of the mesoporous silica film from the $scCO_2$ infusion process. Variations of the thermal degradation procedure were adjusted such that the range of the ramp rate (0.39 - 6.25 °C / min.) and the range of hold time (4 - 12 hrs.) were attempted without any success in removing the defects. The thickness of the mesoporous silica film was adjusted from 500 nm to 1.4 μm without any success in removing the defects as well.

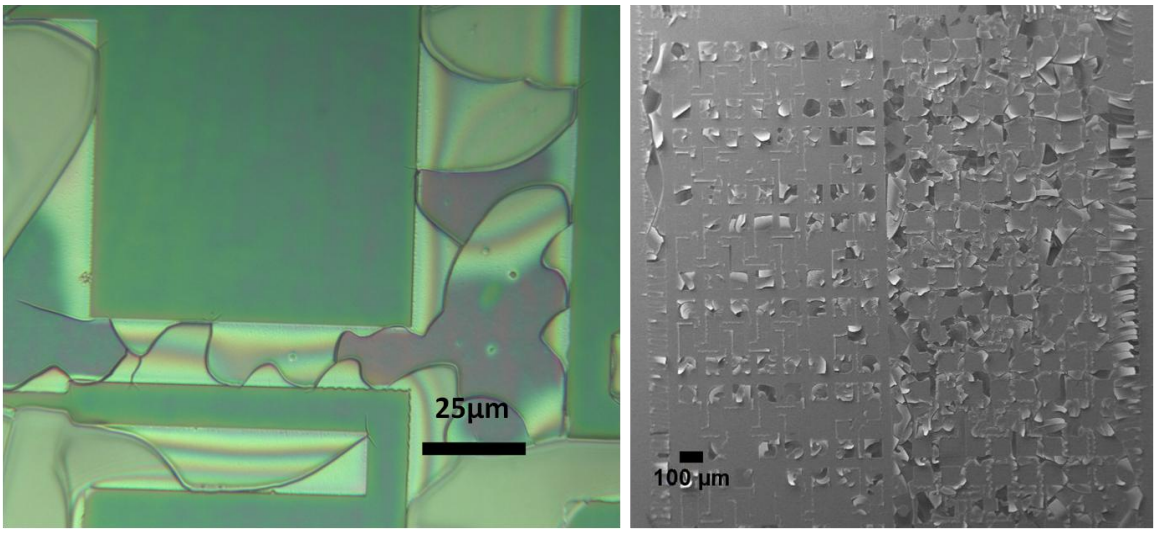

Figure 2.13. Optical microscopy and scanning electron microscopy images of the hierarchical silica structures with device level structures from the test pattern mold.

From the adjustments that were attempted to remove the defects within the mesoporous silica film, the conclusion was made that the dimensions of the device level structure must be adjusted such that the device level structure would be a structure that was uniform with reduced dimensions. The uniform structure would remove any defects that would be caused from mechanical failure, i.e. due to the poor mechanical strength of the mesoporous silica film and/or spanning over large gaps, and the reduced dimensions would remove any defects that would be caused from an explosive removal of excess material. A suitable master mold that has such requirements was found from an everyday material, a digital versatile disc (DVD) made of polycarbonate. The DVD structure consisting of a line array of ~ 650 nm wide, ~ 800 nm periodicity and ~ 200 nm tall lines. To pattern the device level features of a DVD, a thin film of ~ 90 nm from a 6 wt. % solution of the UV-curable photopolymer was spin-coated at 3000 rpm for 15 seconds in the presence of air. Processing of the DVD device level structures was performed in an identical manner as to the test pattern device level structure. To remove the residual layer

which connects the features to one another, an O_2 plasma ICP-RIE etch was performed. To monitor the depth of the O_2 plasma ICP-RIE etch, atomic force microscopy (AFM) was performed after each step and is detailed in Figure 2.14. After the O_2 plasma ICP-RIE etch, the DVD line array dimensions were reduced to ~ 500 nm wide, ~ 750 nm periodicity and ~ 150 nm tall.

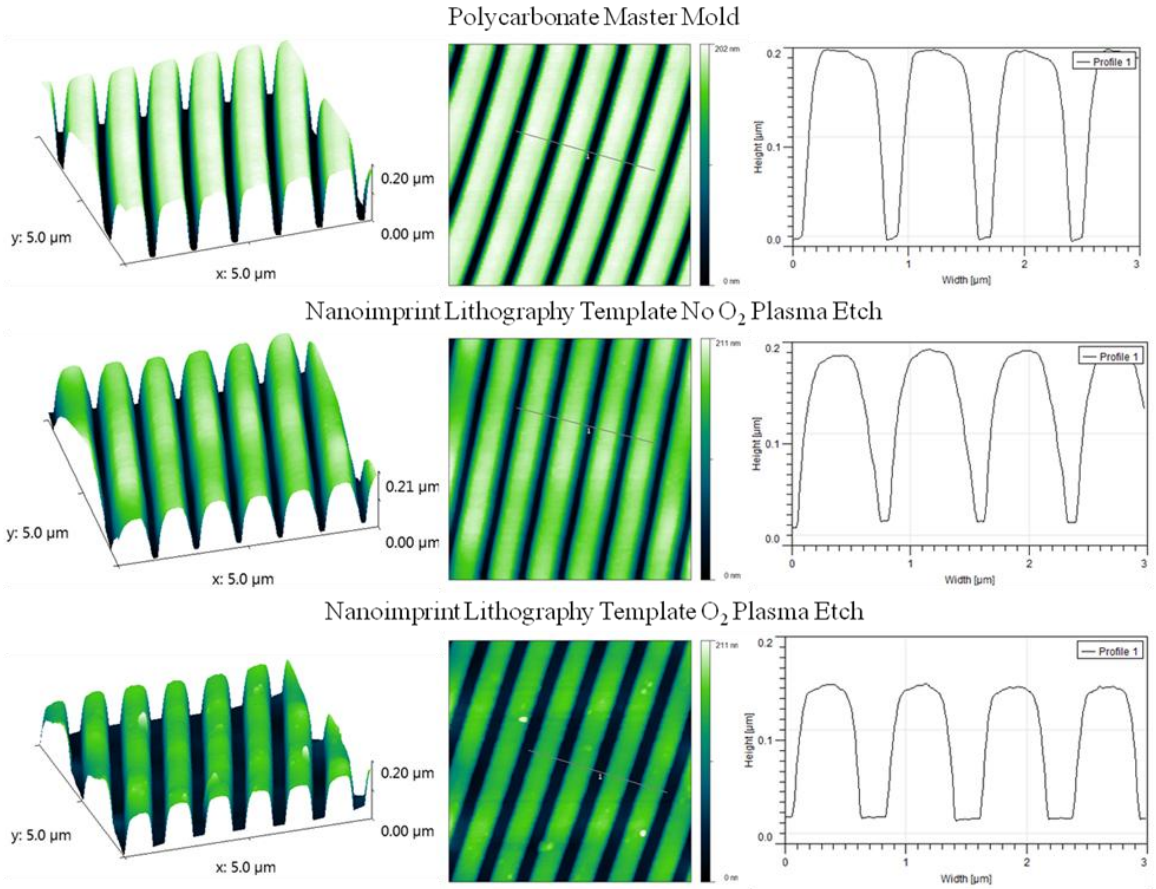

Figure 2.14. Progress of ICP-RIE O_2 plasma etch to yield free-standing nanostructures.

To determine the fidelity of the device level structure from the DVD mold, optical microscopy and focused ion beam scanning electron microscopy (FIB-SEM) was utilized. From the optical microscopy image, Figure 2.15, it was observed that the cracking defect was eliminated by adjusting the device level structure uniformity and dimensions.

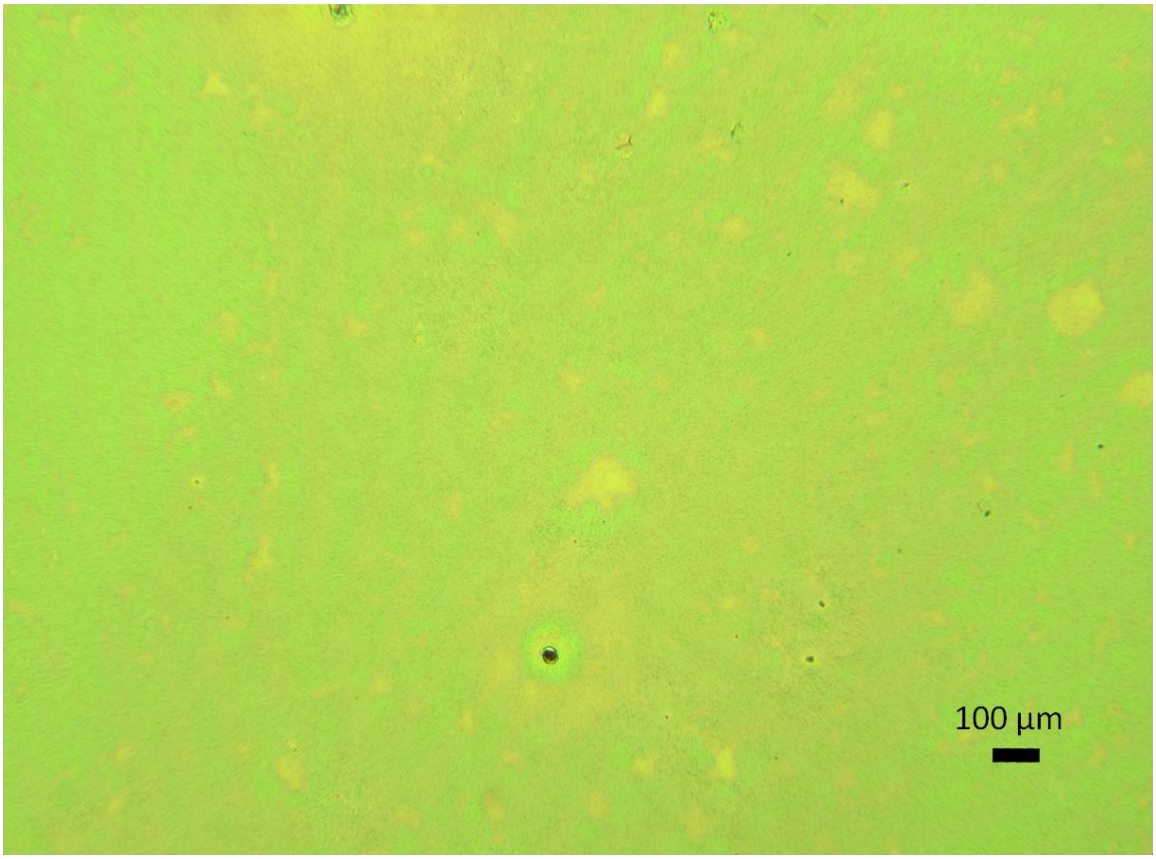

Figure 2.15. Optical microscopy image of hierarchical silica structures with device level structures from the DVD master mold.

The fidelity of the device level structure was characterized via cross-sectional SEM images as well as FIB-SEM images, taken at an angle of 52 °, which are shown in Figure 2.16. It should be noted that the defects visible in the silica film arise from the FIB-SEM sample preparation process and were considerably larger than the mesopores identified through TEM. The dimensions of the nanochannel, shown in Figure 2.14, were nearly identical to that of the polymer template prior to the $scCO_2$ infusion processing.

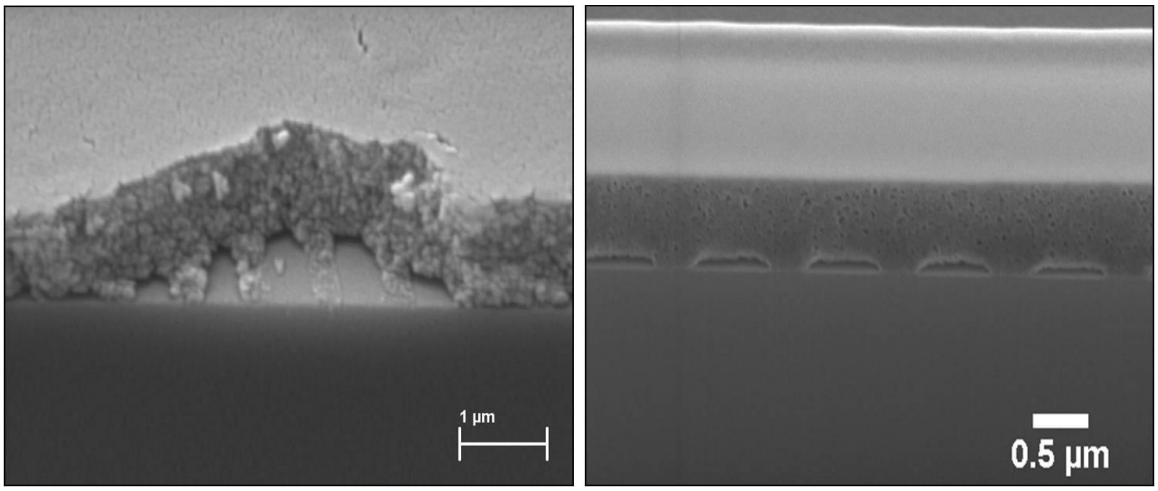

Figure 2.16. Cross-sectional scanning electron microscopy image (left) and FIB-SEM image (right) showing the nanochannel dimension of the hierarchical silica nanochannel.

To confirm the removal of polymeric templates from the hierarchical silica nanochannel, attenuated total reflectance Fourier transform infrared spectroscopy (ATR-FT-IR) was performed and the results are provided in Figure 2.17.

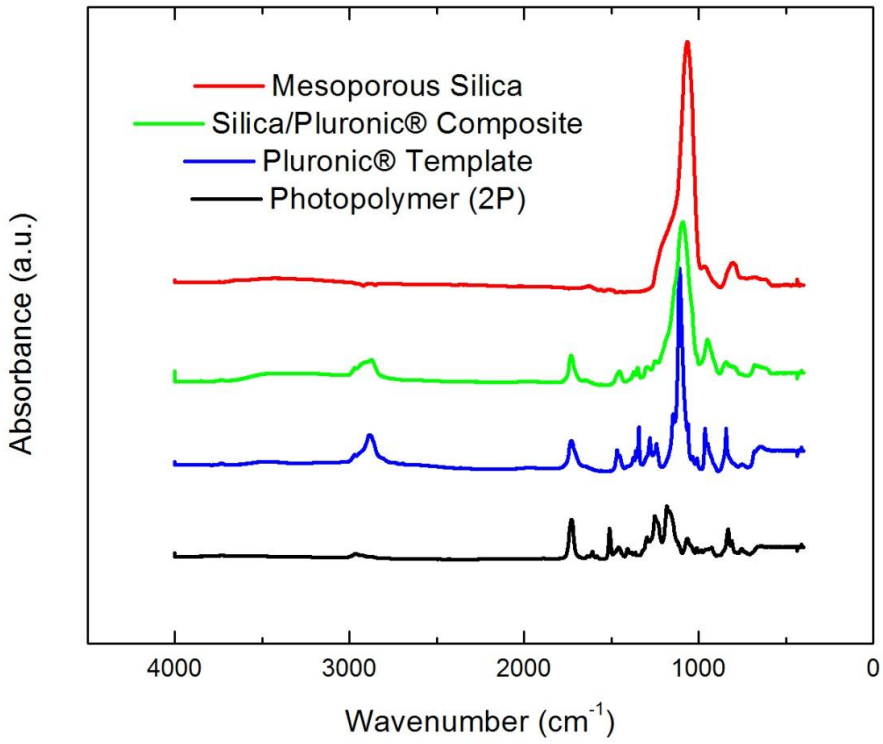

Figure 2.17. Attenuated total reflectance Fourier transform infrared (ATR-FT-IR) spectroscopy for the fabrication of hierarchical silica nanochannels.

From the combination of the TGA and the ATR-FT-IR data, the polymeric templates from both the block copolymer and NIL pattern appear to be greater than 98 percent removed.

To demostrate the utility of the hierarchical silica nanochannel structure, capacitance measurements were performed. The structure chosen for capacitance measurements was the metal-insulator-semiconductor (MIS) technique, as shown in Figure 2.18. The equation for capacitance is provided in Equation 2.1:

Equation 2.1 $$C = {\kappa\varepsilon_o A}/{T_{oxide}}$$

where C is capacitance, κ is the dielectric constant, ε_o is the permittivity of free space, A is the area of the electrode overlap, and T_{oxide} is the thickness of the dielectric material under investigation. Capacitance measurements were performed on device level features shown in Figure 2.16 while the domain level features were synthesized using the Pluronic® F127 template with a silica precursor mixture of 60:40 TEOS:MTES (methyl triethoxysilane, Gelest). The TEM image of the Pluronic® F127 template with 60:40 TEOS:MTES is shown in Figure 2.19.

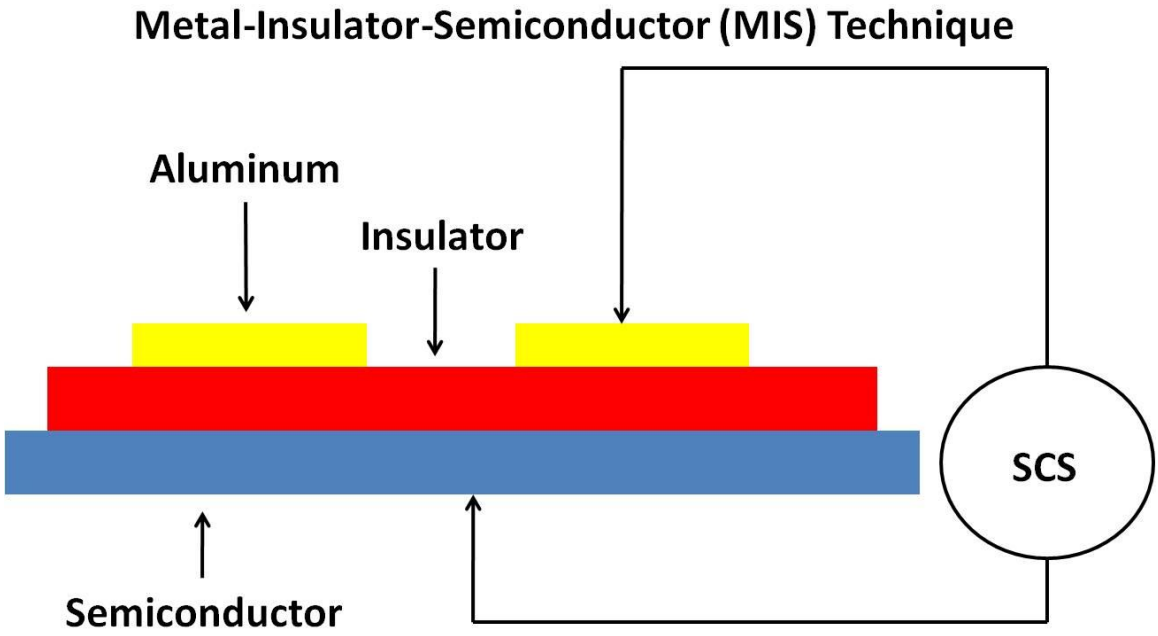

Figure 2.18. Schematic of the metal-insulator-semiconductor (MIS) technique used for capacitance measurements.

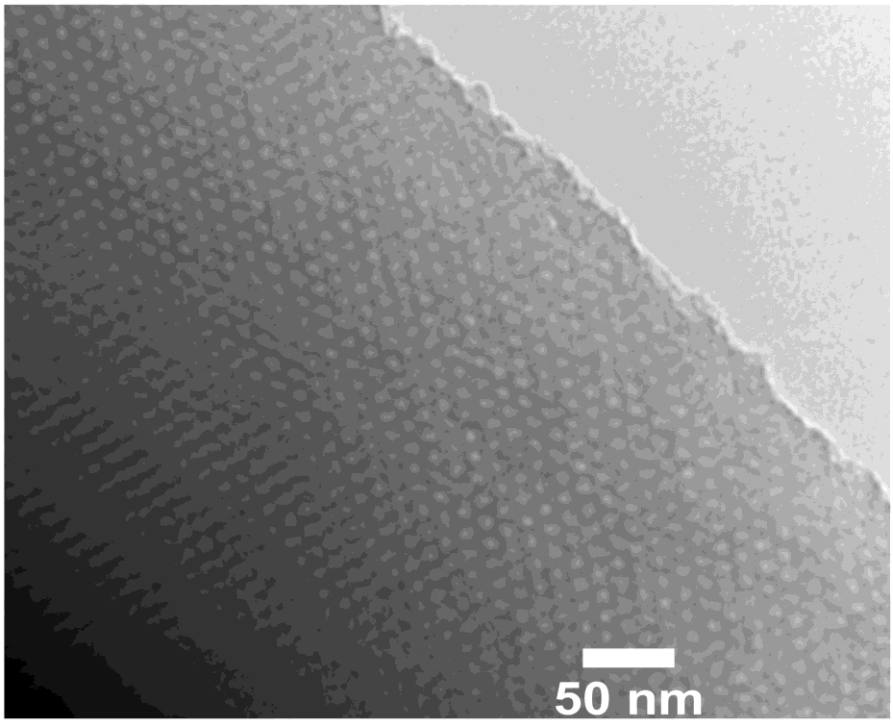

Figure 2.19. TEM image of the Pluronic® F127 template with 60:40 TEOS:MTES.

The choice of this silica precursor, a combination of TEOS and MTES, introduces a hydrophobic methyl group into the silica matrix which makes the silica template more hydrophobic and less capable of absorbing water while providing the desired spherical morphology. The dielectric constant of the non-airgap sample yielded a dielectric constant of 2.1, which was accurate with the reported value in literature[27]. The airgap sample yielded a dielectric constant of 2.0, which, based on the porosity and dimensions of the airgap sample, was the theoretical value that should have been expected, as shown schematically in Figure 2.20. It is recognized that the dimensions of the airgap sample described within this dissertation chapter are not ideal for first level ILDs, however, this type of structure could be useful in the upper levels of the microprocessor architecture as well as for active onboard cooling systems.

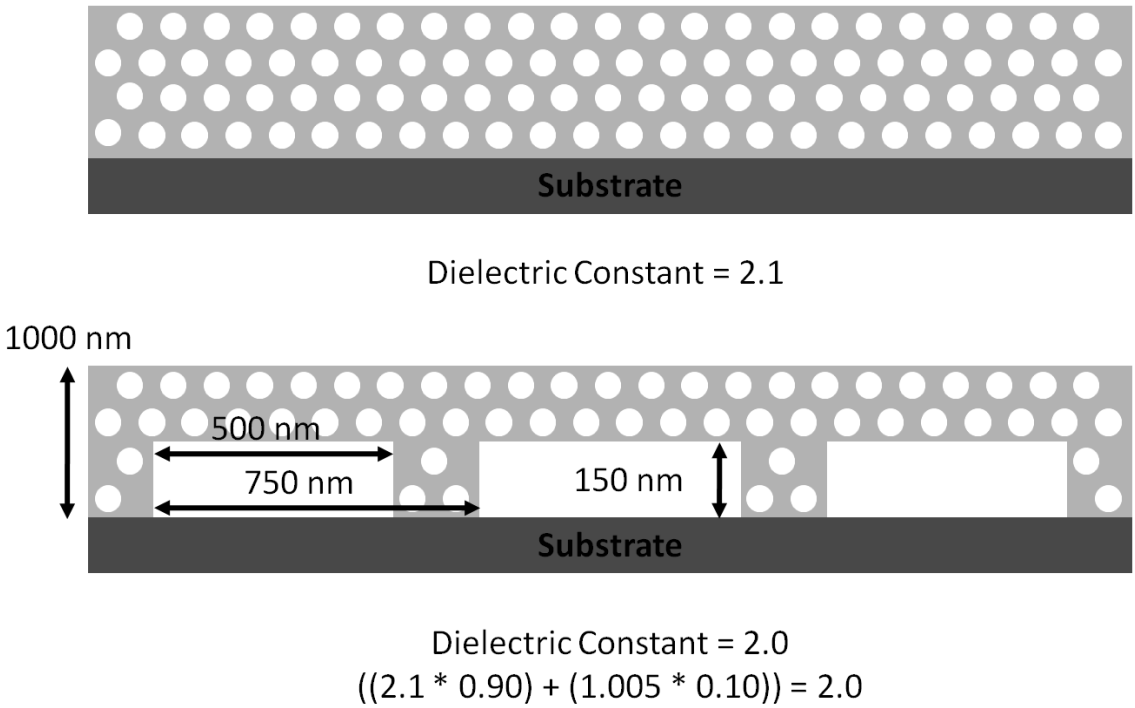

Figure 2.20. Schematic showing the theoretical value of the dielectric constant for the hierarchically structured silica nanochannels.

The mechanical properties of the hierarchically structured silica nanochannels were measured through nanoindentation. The use of nanoindentation to measure the mechanical properties of thin films requires that the thickness of the film under investigation to be a sufficient thickness such that the nanoindentation measurement was not affected by the presence of the substrate, i.e. a minimum of 500 nm thickness was required for the film under investigation. The samples that were measured via nanoindentation had a minimum thickness of 1 μm. The control samples of mesoporous silica without an airgap structure reported a hardness value of 0.65 ± 0.04 GPa while the hierarchically structured silica nanochannel exhibited a hardness value of 0.63 ± 0.02 GPa. The hardness values for both the control sample and the hierarchically structured silica nanochannel were within the error of each other which suggests that the presence of the nanochannel has no effect on the mechanical property of the film. This conclusion

can be rationalized by the dimensions of the airgap structure used as the device level structure, i.e. the DVD mold, which has a maximum height of ~ 150 nm, well below the sampling depth of the nanoindentation probe.

2.4. Conclusions

In summary, the combination of $scCO_2$ infusion processing and NIL allows for hierarchical silica nanochannels to be fabricated. The hierarhically structured silica nanochannels were investigated for use as a low-k dielectric material with a dielectric constant of 2.0 reported for channel dimensions of ~ 500 nm wide, ~ 750 nm periodicity and ~ 150 nm tall created by NIL. Domain level features with a diameter of ~ 4 - 5 nm of either spherical or cylindrical morphology were created by $scCO_2$ infusion processing. Domain level and device level features, if desired, may be adjusted through modifications of the block copolymer template and NIL mold respectively. The number of feature combinations that can be achieved are immense due to the availability of device level features afforded by NIL.

2.5. Acknowledgements

FIB-SEM images were obtained from the Cornell Center for Materials Research (CCMR, DMR-0552782) with the assistance of Malcolm Thomas. Dr. Stephan Cohen, of IBM Thomas J. Watson Research Center is acknowledged for the useful discussions regarding capacitance measurements.

2.6. References

(1) Hedrick, J. L.; Miller, R. D.; Hawker, C. J.; Carter, K. R.; Volksen, W.; Yoon, D. Y.; Trollsås, M. *Advanced Materials* **1998**, *10*, 1049-1053.

(2) Nguyen, C. V.; Carter, K. R.; Hawker, C. J.; Hedrick, J. L.; Jaffe, R. L.; Miller, R. D.; Remenar, J. F.; Rhee, H.-W.; Rice, P. M.; Toney, M. F.; Trollsås, M.; Yoon, D. Y. *Chemistry of Materials* **1999**, *11*, 3080-3085.

(3) Baskaran, S.; Liu, J.; Domansky, K.; Kohler, N.; Li, X.; Coyle, C.; Fryxell, G. E.; Thevuthasan, S.; Williford, R. E. *Advanced Materials* **2000**, *12*, 291-294.

(4) Wirnsberger, G.; Yang, P.; Scott, B. J.; Chmelka, B. F.; Stucky, G. D. *Spectrochimica Acta. Part A, Molecular and Biomolecular Spectroscopy* **2001**, *57*, 2049-60.

(5) Corma, A. *Chemical Reviews* **1997**, *97*, 2373-2420.

(6) Stein, A. *Advanced Materials* **2003**, *15*, 763-775.

(7) Innocenzi, P.; Martucci, A.; Guglielmi, M.; Bearzotti, A.; Traversa, E.; Pivin, J. C. *Journal of the European Ceramic Society* **2001**, *21*, 1985-1988.

(8) Innocenzi, P.; Martucci, A.; Guglielmi, M.; Bearzotti, A.; Traversa, E. *Sensors and Actuators B: Chemical* **2001**, *76*, 299-303.

(9) Chen, H.-T.; Crosby, T. A.; Park, M.-H.; Nagarajan, S.; Rotello, V. M.; Watkins, J. J. *Journal of Materials Chemistry* **2009**, *19*, 70.

(10) Seidel, H.; Csepregi, L.; Heuberger, A.; Baumgäterl, H. *Journal of The Electrochemical Society* **1990**, *137*, 3612-3626.

(11) Seidel, H.; Csepregi, L.; Heuberger, A.; Baumgäterl, H. *Journal of The Electrochemical Society* **1990**, *137*, 3626-3632.

(12) Li, W.; Tegenfeldt, J. O.; Chen, L.; Austin, R. H.; Chou, S. Y.; Kohl, P. A.; Krotine, J.; Sturm, J. C. *Nanotechnology* **2003**, *14*, 578-583.

(13) Xia, D.; Gamble, T. C.; Mendoza, E. A.; Koch, S. J.; He, X.; Lopez, G. P.; Brueck, S. R. J. *Nano Letters* **2008**, *8*, 1610-8.

(14) Cao, H.; Yu, Z.; Wang, J.; Tegenfeldt, J. O.; Austin, R. H.; Chen, E.; Wu, W.; Chou, S. Y. *Applied Physics Letters* **2002**, *81*, 174-176.

(15) Guo, L. J.; Cheng, X.; Chou, C.-F. *Nano Letters* **2004**, *4*, 69-73.

(16) Liang, X.; Morton, K. J.; Austin, R. H.; Chou, S. Y. *Nano Letters* **2007**, *7*, 3774-80.

(17) Ell, J. R.; Crosby, T. A.; Peterson, J. J.; Carter, K. R.; Watkins, J. J. *Chemistry of Materials* **2010**, *22*, 1445-1451.

(18) de Boer, M. J.; Tjerkstra, R. W.; Berenschot, J. W.; Jansen, H. V.; Burger, G. J.; Gardeniers, J. G. E.; Elwenspoek, M.; van den Berg, a. *Journal of Microelectromechanical Systems* **2000**, *9*, 94-103.

(19) Perry, J. L.; Kandlikar, S. G. *Microfluidics and Nanofluidics* **2005**, *2*, 185-193.

(20) Noguchi, J.; Sato, K.; Konishi, N.; Uno, S.; Oshima, T.; Ishikawa, K.; Ashihara, H.; Saito, T.; Kubo, M.; Tamaru, T.; Yamada, Y.; Aoki, H.; Fujiwara, T. *IEEE Transactions on Electron Devices* **2005**, *52*, 352-359.

(21) Hoofman, R.; Caluwaerts, R.; Michelon, J.; Herrerobernabe, P.; Gueneaudemussy, J.; Bruynseraede, C.; Lee, J.; List, S.; Bancken, P.; Beyer, G. *Microelectronic Engineering* **2006**, *83*, 2150-2154.

(22) Pantouvaki, M.; Humbert, A.; Vanbesien, E.; Camerotto, E.; Travaly, Y.; Richard, O.; Willegems, M.; Volders, H.; Kellens, K.; Daamen, R. *Microelectronic Engineering* **2008**, *85*, 2071-2074.

(23) Tirumala, V. R.; Pai, R. A.; Agarwal, S.; Testa, J. J.; Bhatnagar, G.; Romang, A. H.; Chandler, C.; Gorman, B. P.; Jones, R. L.; Lin, E. K.; Watkins, J. J. *Chemistry of Materials* **2007**, *19*, 5868-5874.

(24) Tirumala, V. R.; Romang, A.; Agarwal, S.; Lin, E. K.; Watkins, J. J. *Advanced Materials* **2008**, *20*, 1603-1608.

(25) Tirumala, V. R.; Daga, V.; Bosse, A. W.; Romang, A.; Ilavsky, J.; Lin, E. K.; Watkins, J. J. *Macromolecules* **2008**, *41*, 7978-7985.

(26) Vogt, B. D.; Pai, R. A.; Lee, H.-J.; Hedden, R. C.; Soles, C. L.; Wu, W.-li; Lin, E. K.; Bauer, B. J.; Watkins, J. J. *Chemistry of Materials* **2005**, *17*, 1398-1408.

(27) Pai, R. A.; Humayun, R.; Schulberg, M. T.; Sengupta, A.; Sun, J.-N.; Watkins, J. J. *Science* **2004**, *303*, 507-510.

CHAPTER 3

MESOPOROUS SILICA DOPED WITH FUNCTIONAL NANOMATERIALS

3.1. Introduction

Nanomaterials, specifically nanoparticles, which are particles that have one or more dimensions less than 100 nm in size, exhibit a number of interesting catalytic, magnetic, mechanical, electrical, and optical properties that are often not observed in their bulk material counterparts[1]. One of the earliest uses of nanoparticles was the use of gold nanoparticles as a colorant for glasses and ceramics with the best known example being the Lycurgus Cup from the 5th to 4th century B.C. The Lycurgus Cup was capable of manipulating light such that transmitted light would appear red and reflected light would appear green due to the presence of the gold nanoparticles and the unique surface plasmon absorption provided by the nanometer dimensions of the particle[2]. The use of nanoparticles, particularly for consumer products, has increased in popularity over the last twenty years and products that contain nanoparticles can be found in everyday items such as titanium dioxide or zinc oxide in sunblocks and sunscreens, silver in antimicrobial and antibacterial products, and carbon nanotubes (CNTs) in sporting equipment, i.e. golf clubs and tennis racquets[3].

A significant challenge of incorporating nanoparticles into meaningful products is the tendency of the nanoparticles to agglomerate or aggregate, which severely hinders the properties given to the nanoparticles. To take full advantage of the unique properties afforded to nanoparticles, novel composite materials are being developed to incorporate uniformly dispersed, functional nanoparticles into various host matrices, such as

polymers[4–10], block copolymers[11–13], and metal oxides[14–18]. The focus of this dissertation chapter will be on the use of metal oxide materials as the host matrix for the composite material.

The use of metal oxides as host matrices for nanoparticles provides a suitable host material with a significant temperature resilience, considerable mechanical properties, substantial material options, i.e. non-conductive, semiconductive, and/or photoactive to name several, and potential for porosity with long-range order and high surface areas. A composite material comprised of nanoparticles within a metal oxide host matrix may be created by several methods[19]. Pre-synthesized nanoparticles may be complimented by the metal oxide matrix by synthesizing / forming the metal oxide matrix around the nanoparticles via hydrolysis and/or polycondensation reactions. Pre-synthesized nanoparticles may also be deposited within pre-synthesized porous metal oxide matrix materials. Another option is to form the nanoparticles within the pre-formed metal oxide matrix via impregnation of nanoparticle precursors. The nanoparticles and metal oxide matrix may also be co-established such that the metal oxide matrix is formed first followed by formation of the nanoparticle. The most popular technique of establishing the metal oxide matrix from the aforementioned method is through the use of sol-gel chemistry.

Recently the Watkins' research group has developed a simple approach to provide enhanced, long-range order to otherwise disordered block copolymer templates by incorporating hydrogen bonding additives, i.e. homopolymers[20–22], block copolymers[23], and small molecules[24]. This has been extended to the preparation of well-ordered block copolymer/nanoparticle composites through the concept of additive-driven self-

assembly[12,13]. This concept uses multipoint, enthalpically favorable interactions between nanoparticles containing hydrogen bond donating ligands with hydrogen bond accepting block copolymer segments. These enthalpically favorable interactions allow typically disordered block copolymer templates to form ordered block copolymer morphologies. To take advantage of the well order hybrid materials, a metal oxide host matrix must be incorporated to compliment the functional nanoparticles present in the block copolymers. The metal oxide host matrix material of choice is silica due to being one of the most studied metal oxide materials to date, favorable material properties (amorphous, optically transparent), and simple surface functionalization. A technique based on phase selective chemical reactions performed within an amphiphilic block copolymer template, utilizing a reaction medium of supercritical carbon dioxide ($scCO_2$), is used to create the mesoporous silica network.

The functional nanomaterials of interest for this research consist of pre-synthesized gold nanoparticles, fullerene molecules, and polyhedral oligomeric silsesquioxane (POSS). The chemical structures of these nanomaterials are shown in Figure 3.1. The aforementioned functional nanomaterials were selected based on the ability to selectively interact with the hydrophilic segment of an amphiphilic block copolymer template through the ligands present on the surface of the functional nanomaterials. The chosen functional nanoparticles also exhibit unique properties such as conductivity, activity upon exposure to specific electromagnetic radiation, and enhanced mechanical and thermal properties. To compliment the functional nanomaterials, a silica matrix will be established around the functional nanomaterials

through $scCO_2$ infusion processing to generate a nanocomposite material comprised of mesoporous silica doped with functional nanomaterials.

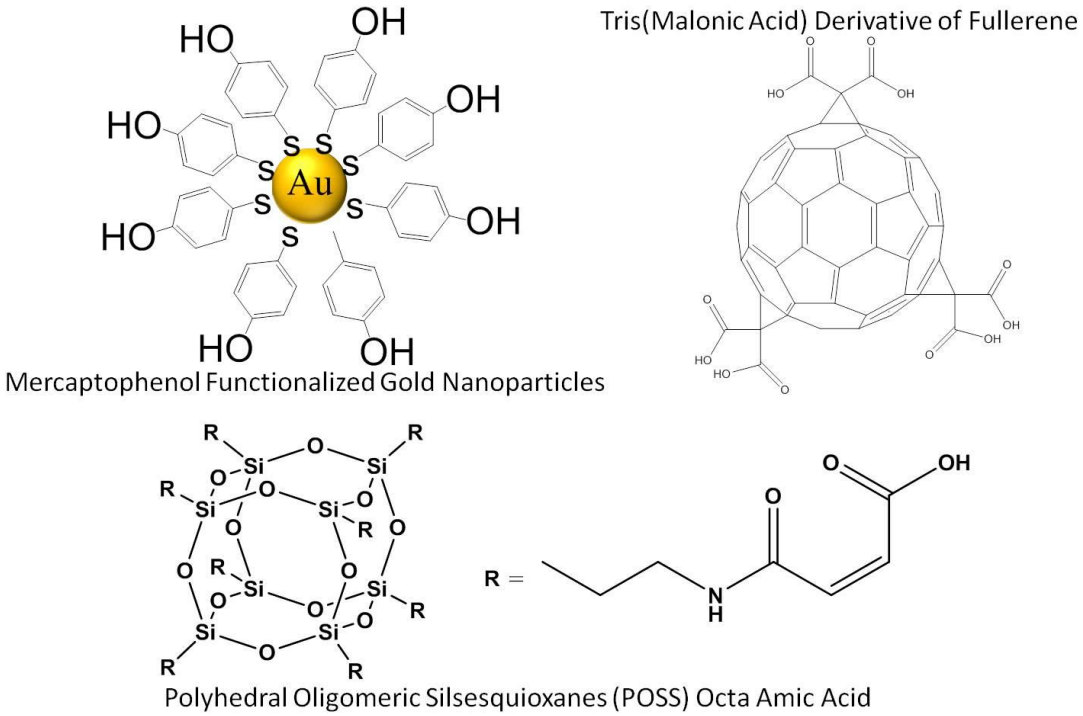

Figure 3.1. Functional nanomaterials of interest.

3.2. Experimental

3.2.1. Materials

Hydrogen tetrachloroaurate trihydrate (ACS Grade, MP Biomedical), para-mercaptophenol (99%, Acros Organic), acetic acid (Glacial, Fisher Scientific), sodium borohydride (Venpure SF, Aldrich), fullerene (Nano-C), diethyl bromomalonate (92 %, Aldrich), 1,8-diazobicyclo[5,4,0]undec-7-ene (98 %, Aldrich), toluene (ACS Grade, Fisher Scientific), hexane (ACS Grade, Fisher Scientific), polyhedral oligomeric silsesquioxane octa maleamic acid (POSS-OAA) (Hybrid Plastics), Pluronic® F127 (PEO_{106}-PPO_{70}-PEO_{106}) block copolymer (BASF), para-toluene sulfonic acid (99%, Acros Organics), tetraethyl orthosilicate (99.999%, Sigma-Aldrich), de-ionized water

(Optima, Fisher Scientific), methanol (ACS Grade, Fisher Scientific and/or BDH), dimethylformamide (ACS Grade, BDH), tetrahydrofuran (ACS Grade, Fisher Scientific), and carbon dioxide (CO_2, Merriam Graves, bone-dry grade) were used as received without further purification. Silicon wafers of (100) orientation (p-type, boron dopant) were obtained from University Wafer.

3.2.2. Gold Nanoparticle Synthesis

Para-mercaptophenol functionalized gold nanoparticles, with a diameter of ~ 2 nm, were synthesized according to a modified Brust method[25]. The standard synthesis consisted of dissolving hydrogen tetrachloroaurate trihydrate (300 mg, 0.762 mmol) and para-mercaptophenol (690 mg, 5.468 mmol) in chilled methanol (300 mL). Acetic acid (10 mL) was then added as one portion to avoid deprotonation of the para-mercaptophenol. A freshly made 0.4 mol/L solution of sodium borohydride was prepared and 90 mL was added as one portion to the solution carefully and under strong stirring. The solution was allowed to stir under ambient conditions for 3 hours. The solution was dried under a continuous stream of nitrogen (N_2) overnight to remove the solvent. Ethyl ether was then added to the nanoparticles which were then centrifuged at 10000 rpm for 20 minutes three separate times. An identical centrifuge step was performed with de-ionized water. Around ~ 400 mg of gold nanoparticles decorated with para-mercaptophenol were obtained.

3.2.3. Tris(Malonic Acid) Fullerene Synthesis

Synthesis of the tris(malonic acid) fullerene were performed according to the reference of Lamparth and Hirsch[26,27] with slight modifications. Diethyl bromomalonate

was added to a solution of C60 in toluene followed by the addition of 1,8-diazobicyclo[5,4,0]undec-7-ene (diazabicycloundecene, DBU). After stirring for several days, the solvent was removed by rotary evaporation and chromatography was performed with silica gel and various volume ratios of toluene and hexane as the eluent. The volume ratio of toluene:hexane was 1:1 which would elute the unreacted C60 followed by the diester. The eluent was changed to a volume ratio of 4:1 toluene:hexane and isomers of the tetraester were collected. The eluent was changed to a volume ratio of 9:1 toluene:hexane to provide the D3 isomer of the hexaester. Finally, pure toluene was passed through the column to collect a combination of C3 and D3 isomers of the hexaester. The D3 isomer was collected by evaporating the solvent with rotary evaporation. To generate the tris(malonic acid) derivative of fullerene, hydrolysis was performed by adding acetic acid and hydrochloric acid to a toluene solution of the collected D3 isomer and refluxed for 24 hours. The tris(malonic acid) derivative of fullerene was collected by removing the solvent via rotary evaporation.

3.2.4. Silicon Wafer Preparation

Silicon substrates (2.5 cm x 2.5 cm) were cleaned by ultrasonication in concentrated sulfuric acid (H_2SO_4, ACS Grade, Fisher Scientific) for 15 minutes followed by rinsing with acetone (ACS Grade, Fisher Scientific and/or BDH) and isopropyl alcohol (ACS Grade, Fisher Scientific and/or BDH) and dried under a stream of N_2.

3.2.5. Supercritical Carbon Dioxide Infusion Process for Mesoporous Silica Doped with Pre-Synthesized Gold Nanoparticles

Mesoporous silica films doped with hydrophilic gold nanoparticles were generated by exposing the amphiphilic block copolymer templates to a solution of tetraethyl orthosilicate (TEOS) in supercritical carbon dioxide ($scCO_2$) within a high pressure reactor at 60 °C and 125 bar. The high pressure reactor, ~ 160 mL in volume, was constructed from two stainless steel opposed ended hubs sealed with a graphite ring (55 ft-lb torque) purchased from Grayloc® Products. Heating bands (Watlow®) were connected to the outside of the reactor walls to control the gas temperature. The top reactor hub was drilled to have 4 ports; one to measure internal pressure, one to measure internal temperature, one for gas inlet, and one for gas outlet. For the Pluronic® F127 solution containing pre-synthesized gold nanoparticles, 8 µL of TEOS, for each sample, was directly placed within the high pressure reactor along with 300 µL of de-ionized water, each in separate Vespel® containers, prior to sealing. Once the reactor was sealed and heated to a specific gas temperature, either 40 °C or 60 °C, the CO_2 was injected with a high pressure syringe pump (ISCO, Model 500 HP) at a rate of 2 - 3 mL/minute. Once the correct pressure was reached, a reaction time of 14 hours at 60 °C and 125 bar was observed. The reactor was then de-pressurized within 20 minutes to ambient pressure. Samples were thermally degraded at an elevated temperature within the range of 200 °C to 400 °C for 6 hours with a ramp rate of 1.56 °C/minute.

3.2.6. Supercritical Carbon Dioxide Infusion Process for Mesoporous Silica Doped with Fullerene

For the preparation of mesoporous silica doped with fullerene, solutions containing Pluronic® F127, tris(malonic acid) fullerene, and para-toluene sulfonic acid (PTSA) in a solvent of tetrahydrofuran (THF) were prepared. Thin films of the fullerene

containing Pluronic® F127 solutions were spin-coated on silicon wafers (2.5 cm x 2.5 cm) at 3000 rpm for 15 seconds under ambient conditions. The thin film samples were loaded into the high pressure reactor, along with 300 µL of de-ionized water and 8 µL of TEOS per 2.5 cm x 2.5 cm thin film sample, and the system was heated to a gas temperature of 60 °C prior to introducing CO_2. The CO_2 was introduced to the high pressure reactor through a high pressure syringe pump (ISCO, Model 500 HP) at a rate of 2 - 3 mL/minute until a final pressure of 125 bar was reached. A reaction time of 14 hours was observed and the reactor was then depressurized to ambient pressure over a period of 20 minutes. Samples were thermally degraded at 400 °C for 6 hours with a ramp rate of 1.56 °C/minute in an air environment.

3.2.7. Supercritical Carbon Dioxide Infusion Process for Polyhedral Oligomeric Silsesquioxane (POSS)

For the preparation of mesoporous silica doped with POSS, solutions containing Pluronic® F127, POSS-OAA, and para-toluene sulfonic acid (PTSA) in dimethylformamide (DMF) were prepared. Thin films of the POSS-OAA containing Pluronic® F127 solutions were spin-coated on silicon wafers (2.5 cm x 2.5 cm) at 3000 rpm for 60 seconds under high humidity conditions. The thin film samples were loaded into the high pressure reactor, along with 300 µL of de-ionized water and 1 µL of TEOS per 2.5 cm x 2.5 cm thin film sample, and the system was heated to a gas temperature of 60 °C prior to introducing CO_2. An additional 7 µL of TEOS per 2.5 cm x 2.5 cm thin film sample was introduced with the CO_2 via a high pressure syringe pump (ISCO, Model 500 HP) at a rate of 2 - 3 mL/minute until a final pressure of 125 bar was reached. A reaction time of 2 hours was observed and the reactor was then depressurized to

ambient pressure over a 20 minute time period. Samples were thermally degraded at various final temperatures with a ramp rate of 1.56 °C/minute in an air environment.

3.2.8. Characterization

Film thicknesses were measured with a Filmetrics F20 Thin Film Measurement System and reported values were an average of 5 measurements over the entire surface with a deviation of ± 5 nm. Transmission electron microscopy (TEM) samples were prepared by scraping mesoporous silica from the substrate, grinding via mortar and pestle, suspended with ethanol, and transferred to a carbon-coated copper grid to be analyzed with a JEOL 2000FX II operating at 200 kV. High resolution TEM (HRTEM) was performed with a JEOL 2010 operating at 200 kV. Field Emission Scanning Electron Microscope (FESEM), operating in scanning transmission electron microscopy (STEM) mode, was performed with a FEI Magellan 400 operating at 5 kV. X-ray diffraction (XRD) and low-angle XRD (LAXRD) were performed on a PANalytical X'Pert diffractometer, using copper (Cu) Kα X-rays (0.1542 nm) operating at 45 kV and 40 mA. Ultraviolet-visible (UV-Vis) spectra were obtained on an Agilent 8453 UV-Vis spectrometer and collected with an integration time of 0.5 seconds and intervals of 1 nm. Variable angle spectroscopic ellipsometry (VASE) was performed with a Sopra GES-5 Variable Angle Spectroscopic Ellipsometer.

3.3. Results and Discussion

3.3.1. Mesoporous Silica Doped with Pre-Synthesized Gold Nanoparticles

3.3.1.1. Introduction

Composite materials of gold nanoparticles with silica as the host matrix have attracted interest for use in catalysis[28], sensors[29], and optoelectronic devices[30]. Previous research efforts have incorporated gold nanoparticles into the pores of mesoporous silica by the in-situ reduction of gold precursors through thermal, chemical, and photo reduction methods. Others have investigated the surface modification of mesoporous silica with functional groups, i.e. amines, to attract pre-synthesized gold nanoparticles to the mesoporous silica surface[31] as well as building the sol-gel network of the silica matrix around pre-synthesized gold nanoparticles[32,33]. Another approach focused on the transport properties of pre-synthesized gold nanoparticles within the mesoporous silica and then depositing the gold nanoparticles through the addition of an anti-solvent[34]. While these previous research efforts have successfully incorporated gold nanomaterials, either in-situ or pre-synthesized, the gold nanoparticles were incorporated within the pore of the mesoporous silica, which would hinder the transport of materials through the mesoporous silica, and/or lacked the presence of a true mesoporous structure, which are useful for applications such as catalysis and sensors.

The effort of this dissertation section was to fabricate well-ordered mesoporous silica that has pre-synthesized gold nanoparticles present within the matrix of the silica, i.e. not in the mesopore. The use of $scCO_2$ infusion processing, which allows the separation of template formation from silica condensation, was used to generate the mesoporous silica matrix.

3.3.1.2. Results and Discussion

The Pluronic® family of block copolymers are amphiphilic tri-block copolymers that consist of poly(ethylene oxide) (PEO) and poly(propylene oxide) (PPO), where the

latter corresponds to the hydrophilic block while the former corresponds to the hydrophobic block. To incorporate pre-synthesized gold nanoparticles (~ 2 nm in diameter, TEM image shown in Figure 3.2) into the Pluronic® block copolymer, a favorable interaction between the gold nanoparticle and Pluronic® PEO segment must be established.

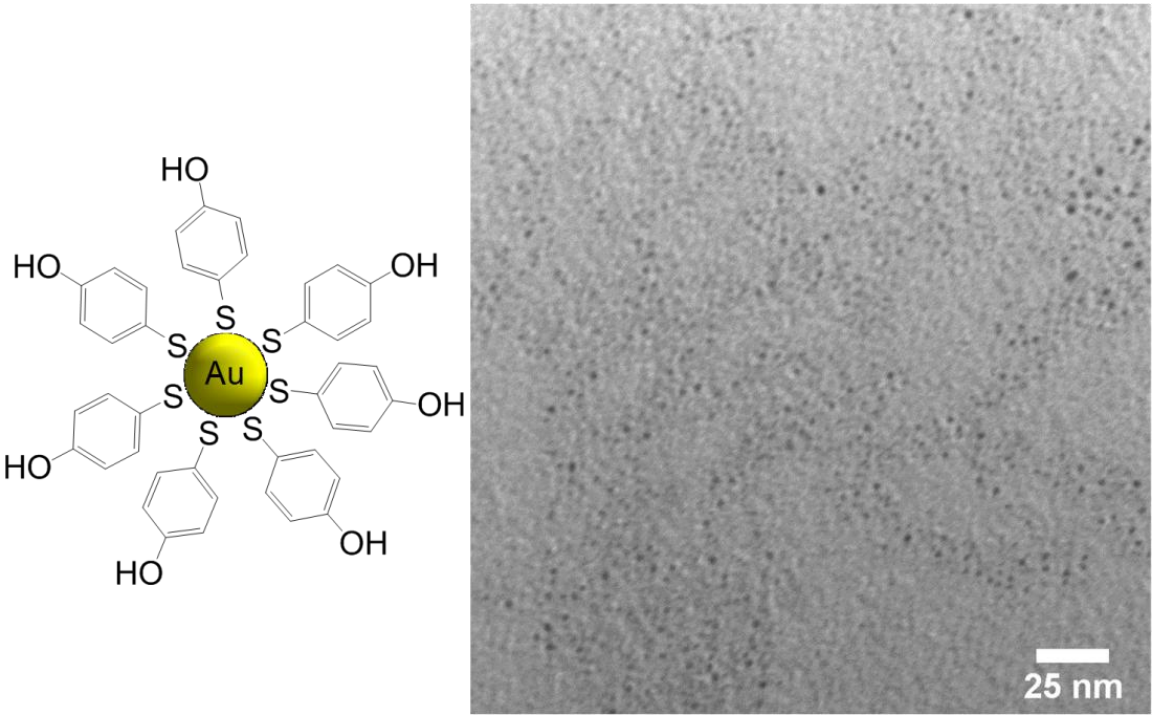

Figure 3.2. Cartoon depicting the gold nanoparticle decorated with para-mercaptophenol ligands (left). TEM image of the as synthesized gold nanoparticles functionalized with para-mercaptophenol ligands (right).

A previous research report by Lin et al. showed that gold nanoparticles decorated with the hydrogen bond donating group of para-mercaptophenol exhibited the highest degree of ordering for the disordered Pluronic® block copolymer template while also incorporating the largest amount of pre-synthesized gold nanoparticles[12]. The use of Pluronic® F127, PEO_{106}-b-PPO_{70}-b-PEO_{106}, template was an ideal candidate for the incorporation of pre-synthesized gold nanoparticles because this template was known to

phase separate into a cylindrical morphology, both in bulk[21,22] and thin film samples[20,35–37]. Fabrication of mesoporous silica through the $scCO_2$ infusion processing has also been characterized to show that an interpenetrating network (IPN) structure is formed from the micropores created during the thermal degradation of the PEO blocks[38]. These characteristics of the mesoporous silica created through $scCO_2$ infusion processing, once doped with pre-synthesized gold nanoparticles, make for unique substrates that would be ideal for use in catalysis and sensing applications.

Figure 3.3 shows an illustration of how the desired mesoporous silica doped with pre-synthesized gold nanoparticles were produced. The process began by spin-coating a solution of gold nanoparticles with Pluronic® F127 and para-toluene sulfonic acid (PTSA), which is a strong organic acid used to promote the hydrolysis and condensation of the silica network, to create a 400 - 500 nm thin film. The solutions consisted of 10 wt. % solids (Pluronic® F127, pre-synthesized gold nanoparticles and PTSA) and were prepared in a co-solvent of 50:50 ethanol:de-ionized water, for lower concentrations of gold nanoparticles, i.e. 5 wt. %, or tetrahydrofuran (THF) for higher concentrations of gold nanoparticles, i.e. 25 wt. %. Concentration of the pre-synthesized gold nanoparticles ranged from 5 wt. % to 25 wt. % with respect to Pluronic® F127 while the concentration of the PTSA was held constant at 15 wt. % with respect to all solid materials. The solutions were stirred at room temperature for 15 minutes to ensure the components were sufficiently mixed. The solutions were then directly spin-coated in an air environment, through a 0.2 μm poly(tetrafluoroethylene) (PTFE) filter, on a cleaned silicon wafer for 30 seconds at 3000 rpm. The thin films showed no signs of crystallization, dewetting, or macrophase separation.

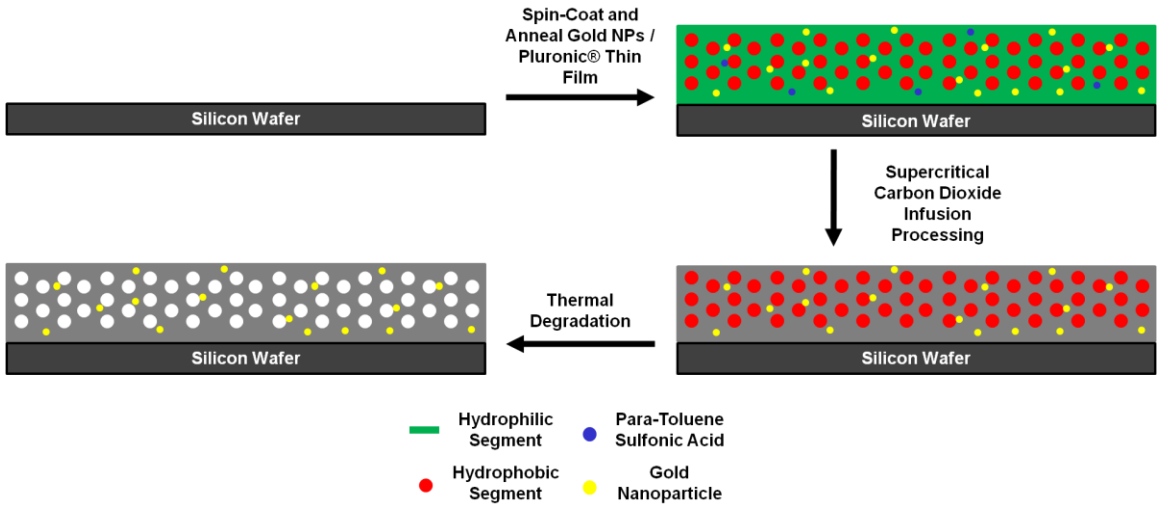

Figure 3.3. Illustration showing the fabrication steps to create mesoporous silica doped with gold nanoparticles.

To template the mesoporous silica around the pre-synthesized gold nanoparticles, the thin film samples were exposed to a humidified solution of $scCO_2$ containing the silicon alkoxide precursor of tetraethyl orthosilicate (TEOS) at 60 °C and 125 bar for 14 hours. The unique aspect of templating mesoporous silica through the use of $scCO_2$ infusion processing is that the thin film block copolymer template formation is separated from the hydrolysis and condensation of the silica precursor. This allows the block copolymer template to retain the morphology created during the spin-coating and annealing steps and remain unperturbed during the formation of the silica network. To ultimately form the mesoporous silica doped with pre-synthesized gold nanoparticles, the organic material present in the samples must be removed by thermal degradation. The thermal degradation was performed with a 1.56 °C/minute ramp rate from room temperature to an elevated temperature, within the range of 200 °C to 400 °C, hold at the final temperature for 6 hours, and brought back to room temperature with a ramp rate of 1.56 °C/minute.

Mesoporous silica samples containing pre-synthesized gold nanoparticles of 5 wt. % and 25 wt. %, with respect to the Pluronic® F127 template, were created. To confirm the presence of the gold nanoparticles within the mesoporous silica, electron microscopy was utilized. Figure 3.4 shows the successful incorporation of pre-synthesized gold nanoparticles into mesoporous silica while maintaining the presence of mesopores with a diameter of 4 - 5 nm for both mesoporous silica samples containing either 5 wt. % or 25 wt. % of pre-synthesized gold nanoparticles. The darkest areas of the electron micrographs correspond to the gold nanoparticles, while the lighter gray areas correspond to the silica, and the lightest gray areas correspond to the mesopores. A high-resolution TEM (HRTEM) is provided in Figure 3.5 to show the crystallinity, i.e. crystal lattices, of the gold nanoparticles. From the electron microscopy images, the gold nanoparticles appear to be present both in the walls and the pores of the mesoporous silica. The observation was made that the gold nanoparticles maintaining diameters approximate to the as-synthesized diameter of ~ 2 nm were preserved within the walls of the mesoporous silica while the gold nanoparticles that experienced growth, i.e. several nanometers greater in diameter than the as-synthesized diameter, were pushed into the pores of the mesoporous silica. Further explanation for the gold nanoparticle growth is provided later on in this dissertation section. It should be noted here that electron microscopy images provided are simple two-dimension images and overlaying of several sections of the gold nanoparticle doped mesoporous silica was possible and may explain the positioning of several of the gold nanoparticles.

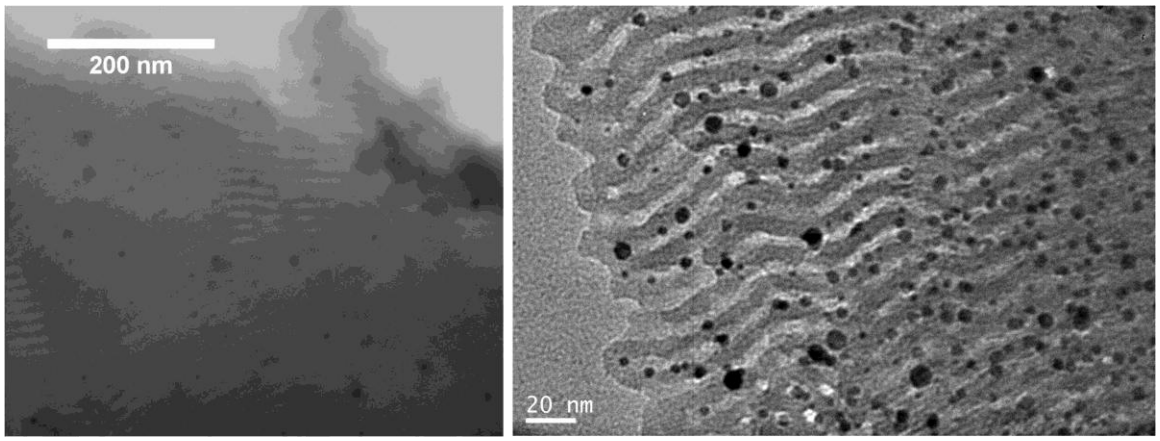

Figure 3.4. Scanning transmission electron microscopy (STEM) image of mesoporous silica created from Pluronic® F127 containing 5 wt. % pre-synthesized gold nanoparticles (left) and TEM image of mesoporous silica created from Pluronic® F127 containing 25 wt. % pre-synthesized gold nanoparticles (right).

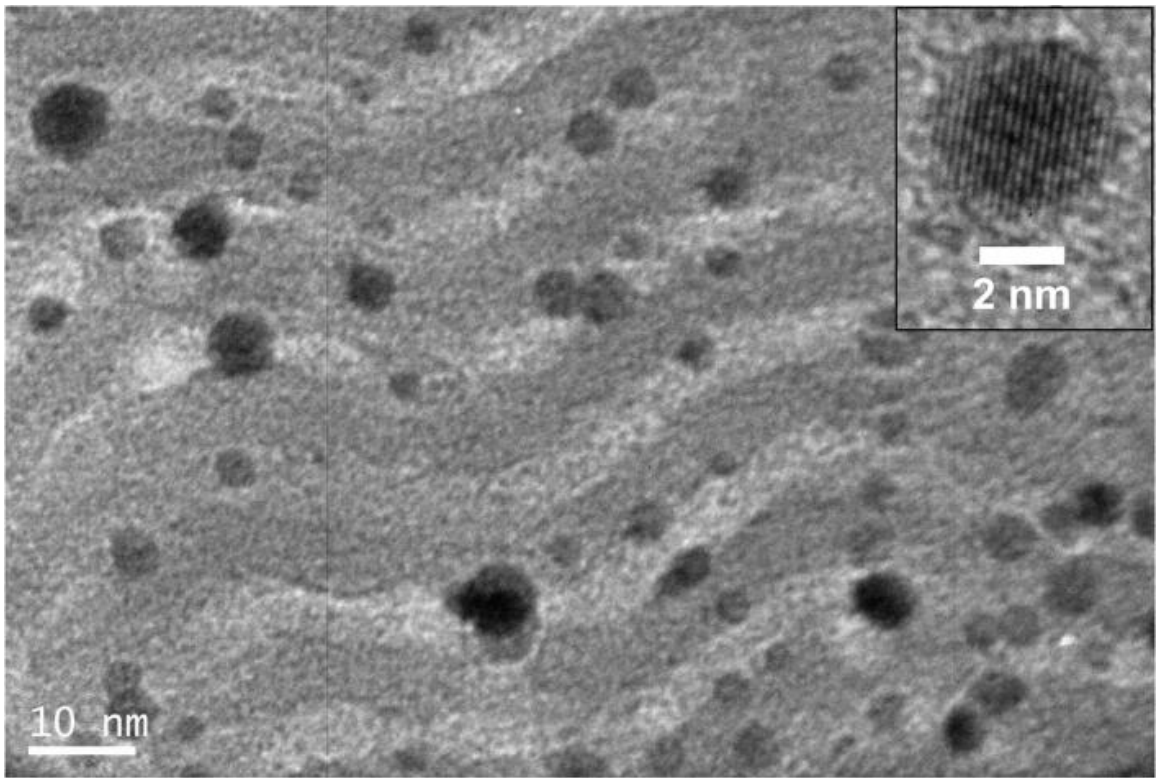

Figure 3.5. HRTEM of the mesoporous silica doped with pre-synthesized gold nanoparticles. Insert: HRTEM of an individual gold nanoparticle.

To further confirm the presence of the gold nanoparticles within the mesoporous silica, X-ray diffraction (XRD) was collected and is shown in Figure 3.6. From the XRD

results, the presence of the characteristic gold crystalline peaks further confirm the presence of the gold in the mesoporous silica thin film. As the concentration of the gold nanoparticles increased, the intensity of the gold crystalline peaks increased as well. Another observation from the XRD was the narrowing of the crystalline peaks, i.e. growth of the gold nanoparticles to larger diameters, from two circumstances; exposure to elevated temperatures and incorporation of gold nanoparticles at higher concentrations. This observation may be explained through the growth of the gold nanoparticles at elevated temperatures (sintering or Ostwald ripening) and/or closer proximities of nanoparticles to themselves at increased concentrations (migration and coalescence), both of which arise due to nanoparticle instability from high surface energies and/or large surface curvatures. For the system investigated in this report, both Ostwald ripening and coalescence may be occurring simultaneously at the higher loading of gold nanoparticles[39].

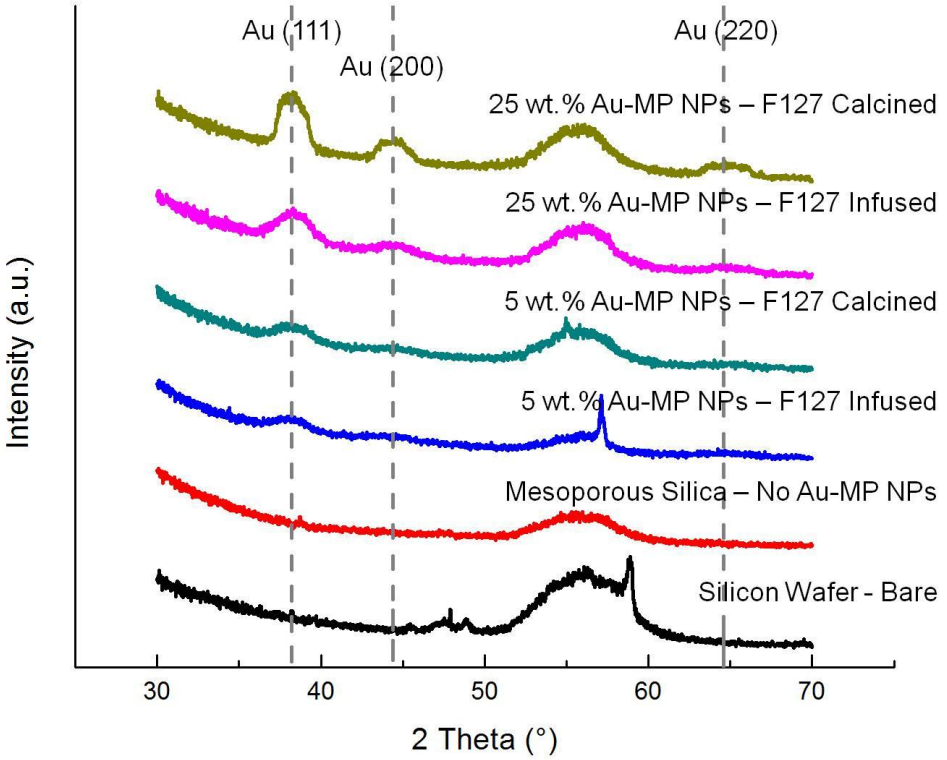

Figure 3.6. X-ray diffraction (XRD) of mesoporous silica doped with pre-synthesized gold nanoparticles. Weight percents of gold nanoparticles was with respect to Pluronic® F127. The terms of infused and calcined refer to the presence of organic materials (infused) and to the presence of no organic material (calcined).

To monitor the growth of the gold nanoparticles within the mesoporous silica thin film, UV-Vis spectra were collected and shown in Figure 3.7. Due to the size of the nanoparticles being ~ 2 nm, the typical surface plasmon resonance (SPR) or plasmon absorbance, typically between 500 nm and 550 nm, depending on size and shape of the gold nanoparticle, was not present[40] and will maintain a brown color while in solution or thin film. If the ~ 2 nm gold nanoparticles were to become larger than 3 nm, the plasmon absorbance would be detected.

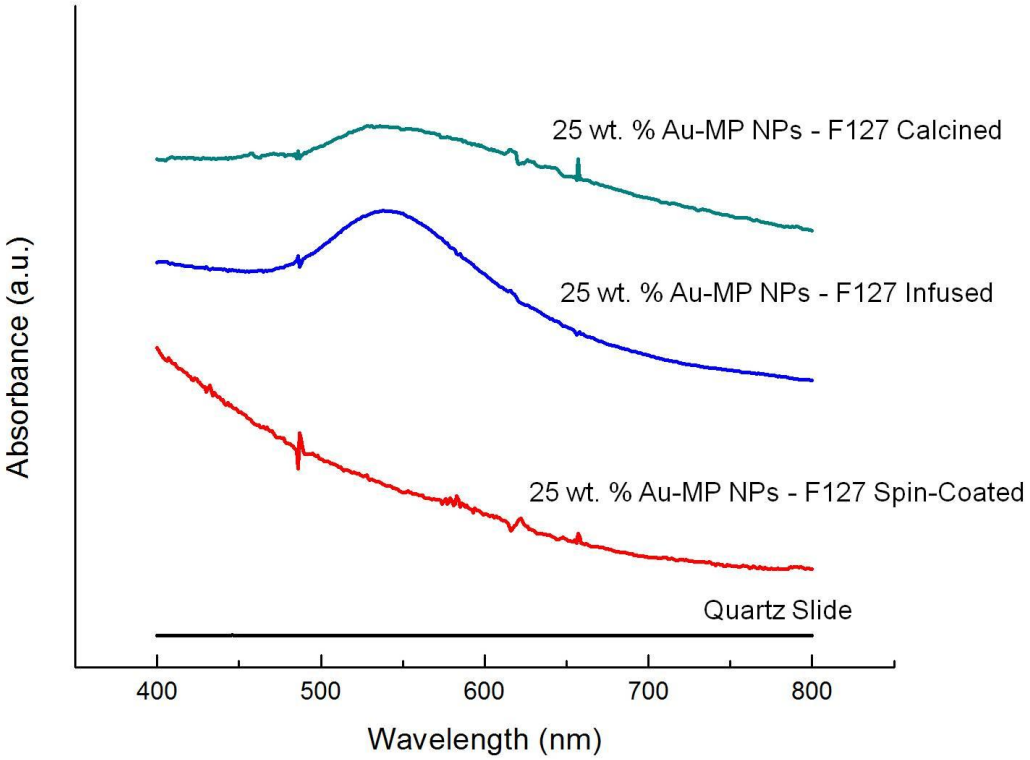

Figure 3.7. UV-Vis spectra acquired during the fabrication of mesoporous silica doped with pre-synthesized gold nanoparticles. The $scCO_2$ infusion processing temperature was 60 °C. The terms of infused and calcined refer to the presence of organic materials (infused) and to the presence of no organic material (calcined).

From the UV-Vis spectra, the gold nanoparticles kept an average size of ~ 2 nm before generation of the silica network via $scCO_2$ infusion processing due to the lack of a plasmon absorbance in the 500 nm to 550 nm range. However, at an elevated temperature of 60 °C during the $scCO_2$ infusion processing step, the gold nanoparticles have grown to be larger than 3 nm as explained by the presence of the plasmon absorbance in the 535 nm to 540 nm range. The plasmon resonance of the gold nanoparticles greater than 3 nm was still present after thermal degradation at 400 °C

under an air environment. This phenomenon was observed through photographs after each processing step as well, which is shown in Figure 3.8.

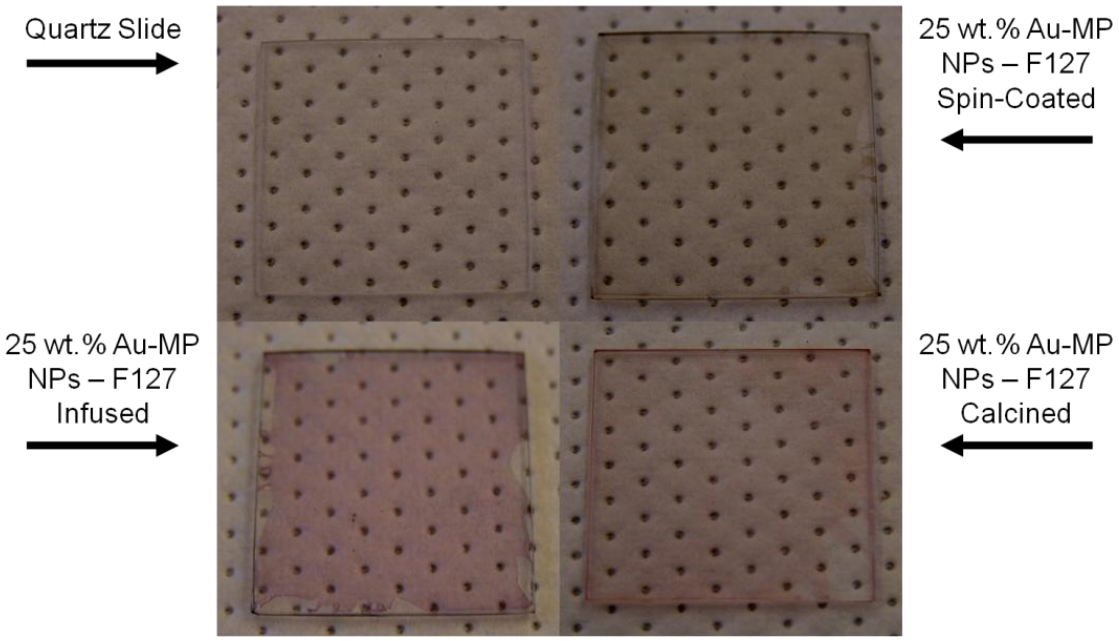

Figure 3.8. Photo of each processing step for Pluronic® F127 doped with 25 wt. % gold nanoparticles decorated with para-mercaptophenol ligands. The terms of infused and calcined refer to the presence of organic materials (infused) and to the presence of no organic material (calcined). $scCO_2$ infusion processing was performed at 60 °C for 14 hours while the thermal degradation was performed at 400 °C for 6 hours in an air environment.

To avoid pre-mature gold nanoparticle growth, the $scCO_2$ infusion processing temperature was reduced to 40 °C and the UV-Vis spectra was compared in Figure 3.9 to the $scCO_2$ infusion processing temperature of 60 °C. By reducing the $scCO_2$ infusion processing temperature by 20 °C, the gold nanoparticles maintained a size less than 3 nm.

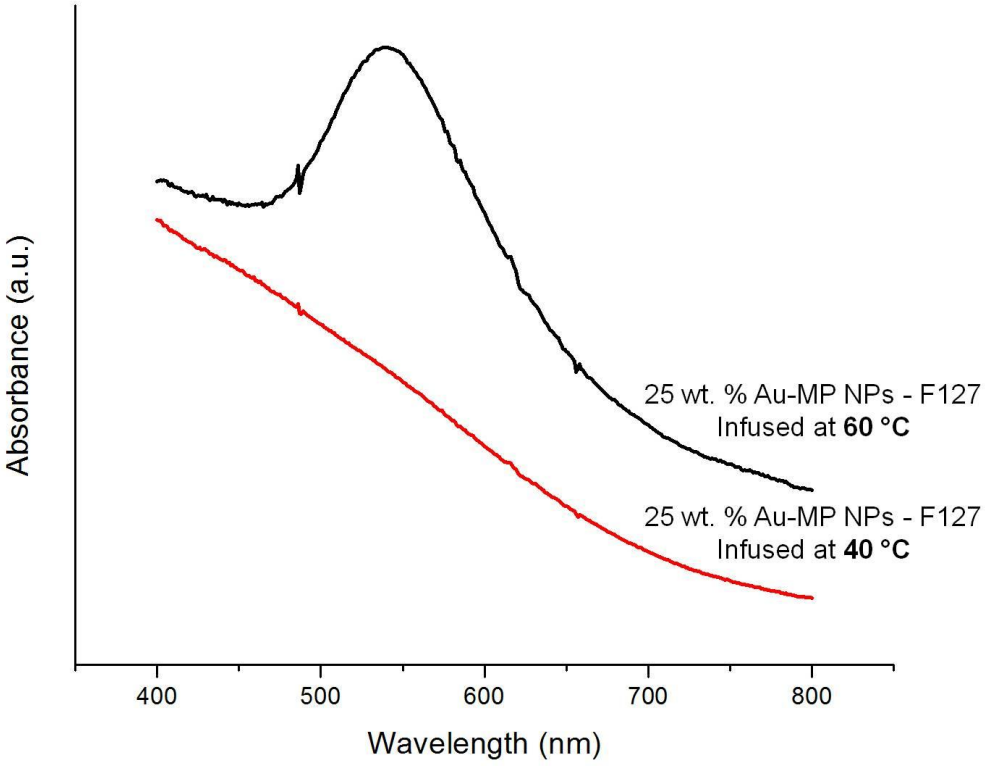

Figure 3.9. Comparison of plasmon absorbance for various $scCO_2$ infusion processing temperatures.

However, even by reducing the $scCO_2$ infusion processing temperature to 40 °C, the gold nanoparticles continued to grow to a size greater than 3 nm after thermal degradation at 400 °C in an air environment, as shown in Figure 3.10.

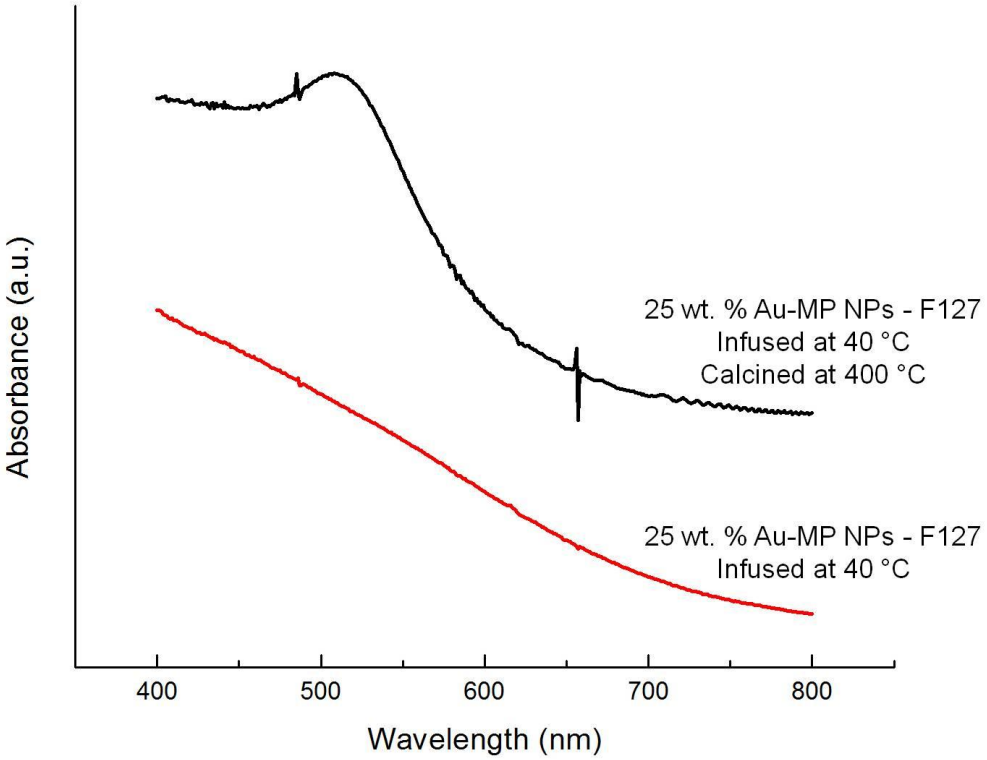

Figure 3.10. Comparison of plasmon absorbance for Pluronic® F127 doped with 25 wt. % gold nanoparticles decorated with para-mercaptophenol ligands processed at a $scCO_2$ infusion processing temperature of 40 °C and subsequent thermal degradation at 400 °C for 6 hours in an air environment.

Other efforts were used to reduce the growth of the gold nanoparticles at elevated temperatures such as reduction of the thermal degradation temperature to 200 °C in air, which will thermally degrade the Pluronic® template as well as the ligands present on the gold nanoparticles (UV-Vis spectra shown in Figure 3.11) as well as increasing the degree of silica condensation through additional processing steps prior to thermal degradation such as exposure to ammonium hydroxide (NH_4OH) vapor, hydrothermal conditions, and 254 nm UV-irradiation (UV-Vis spectra shown in Figure 3.12). Even

with the additional efforts to reduce the gold nanoparticle growth, the gold nanoparticles were able to grow to a size greater than 3 nm, as shown by the UV-Vis results.

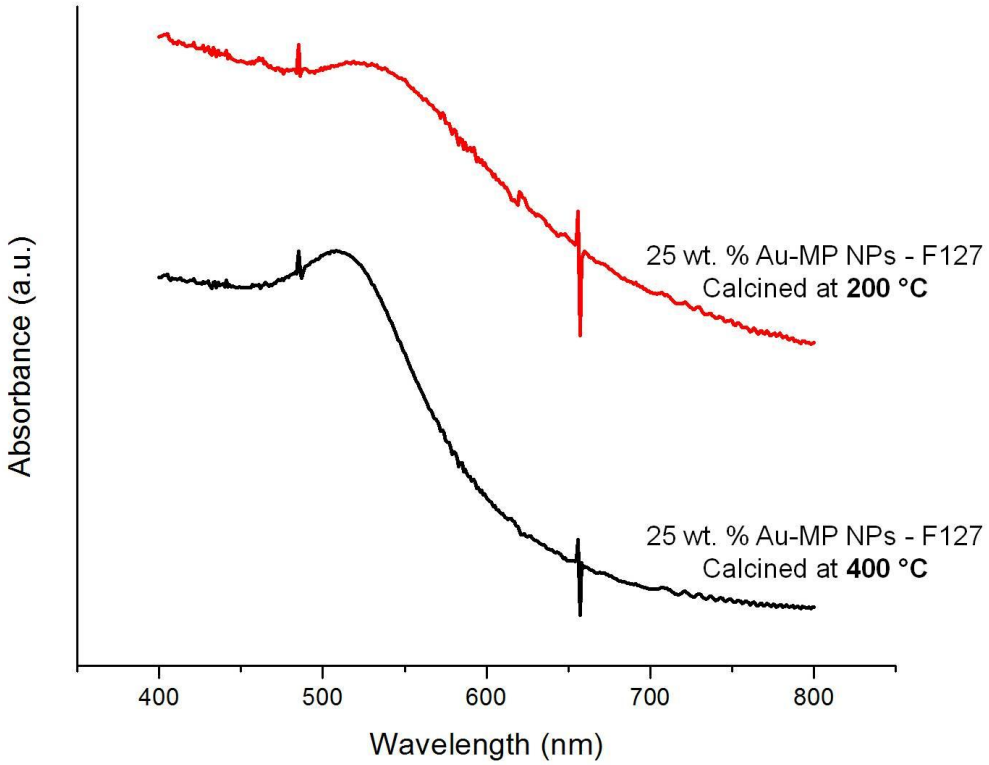

Figure 3.11. Comparison of plasmon absorbance for various thermal degradation temperatures.

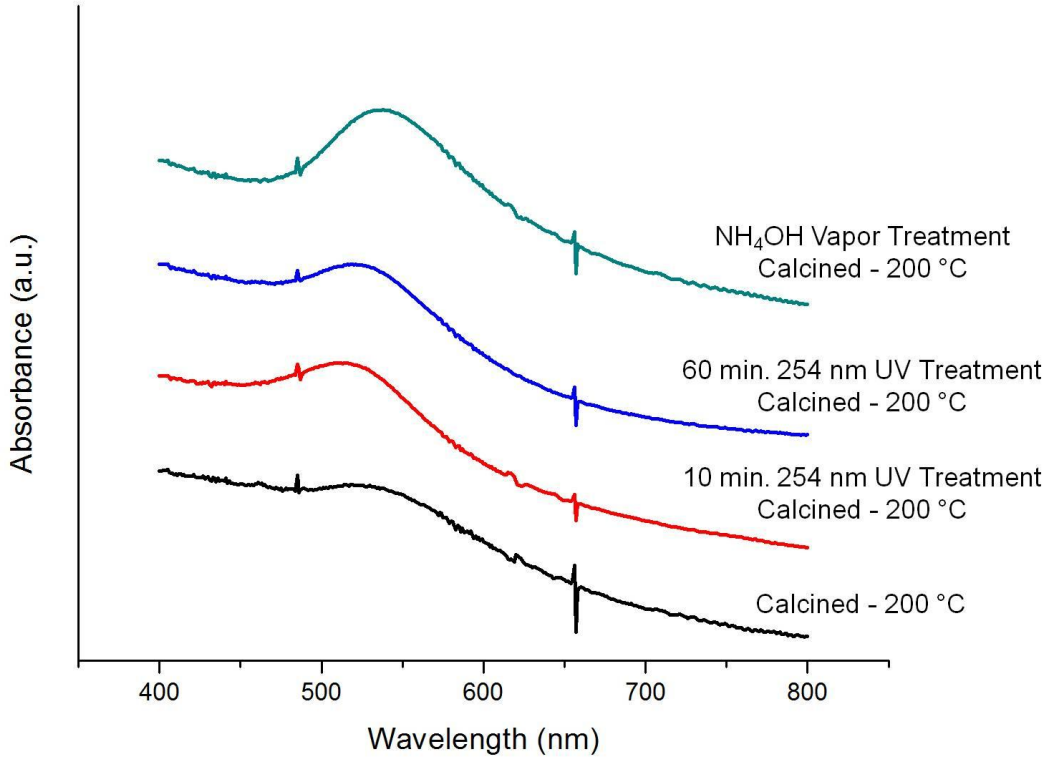

Figure 3.12. Comparison of plasmon absorbance for various processing steps to further condense the silica network prior to thermal degradation.

Low-angle X-ray diffraction (LAXRD) was used to evaluate the long-range order of the mesoporous silica doped with gold nanoparticles, which is shown in Figure 3.13. From the LAXRD data, the domain spacing, of both mesoporous silica samples containing pre-synthesized gold nanoparticles, remains constant at ~ 13.2 nm for the infused samples while the domain spacing for the calcined samples reduced to ~ 10.9 nm, which corresponded to a contraction, or shrinkage, of the mesopore by ~ 18 %. Also from the LAXRD data, the long-range order of the mesopore, according to the full width at half maximum (FWHM) of the primary peak, for the silica incorporated with 5 wt. % gold nanoparticles was significant while upon the addition of 25 wt. % pre-synthesized

gold nanoparticles, the long-range order of the mesopore was severally compromised, however, still present.

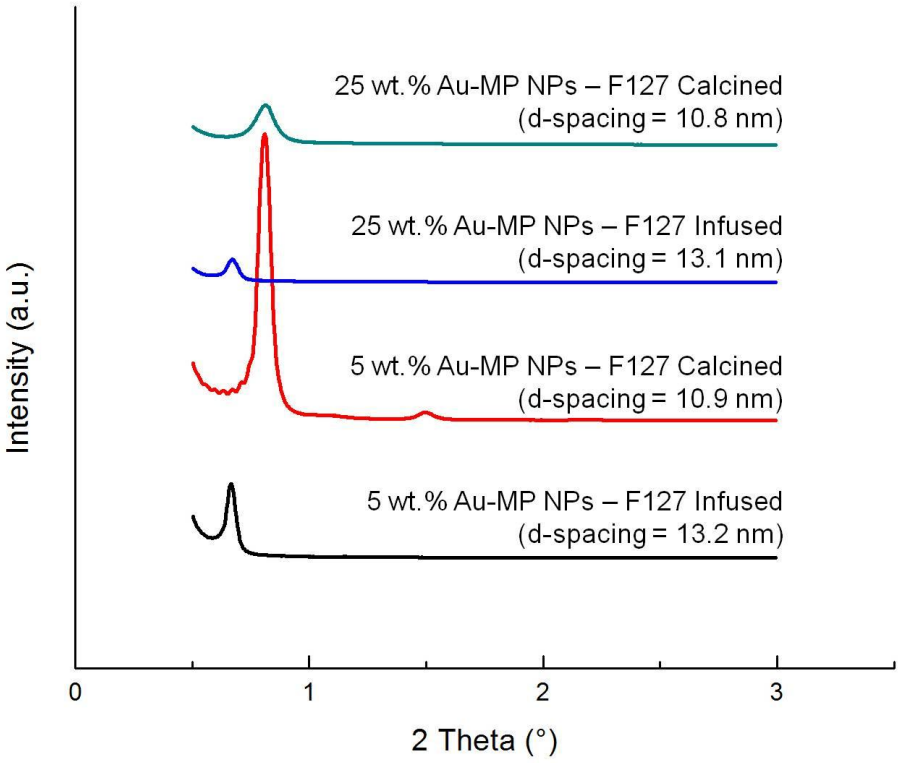

Figure 3.13. Low-angle X-ray diffraction (LAXRD) for mesoporous silica containing pre-synthesized gold nanoparticles. Weight percents of gold nanoparticles was with respect to Pluronic® F127. The terms of infused and calcined refer to the presence of organic materials (infused) and to the presence of no organic material (calcined).

It should be noted here that when pre-synthesized gold nanoparticles decorated with mercaptophenol ligands, were stored in solutions, rather than as dry powders, for long periods of time, 4 weeks or greater, the nanoparticles demonstrated aggregation, as shown in Figure 3.14, due to the mobility of the mercaptophenol ligands in solution. When using the aggregated gold nanoparticle solutions for the fabrication of mesoporous silica doped with pre-synthesized gold nanoparticles, the resulting mesoporous silica

demonstrated aggregation of the gold nanoparticles, for both infused (the presence of polymer template) and calcined (the absence of polymeric/organic materials) conditions within the mesoporous silica film, as shown in Figure 3.15. From the TEM images, the aggregation of the gold nanoparticles was severe and without the presence of a physical barrier to prevent growth of the gold nanoparticles at elevated temperatures, the aggregated gold nanoparticles were able to grow to diameters greater than 50 nm.

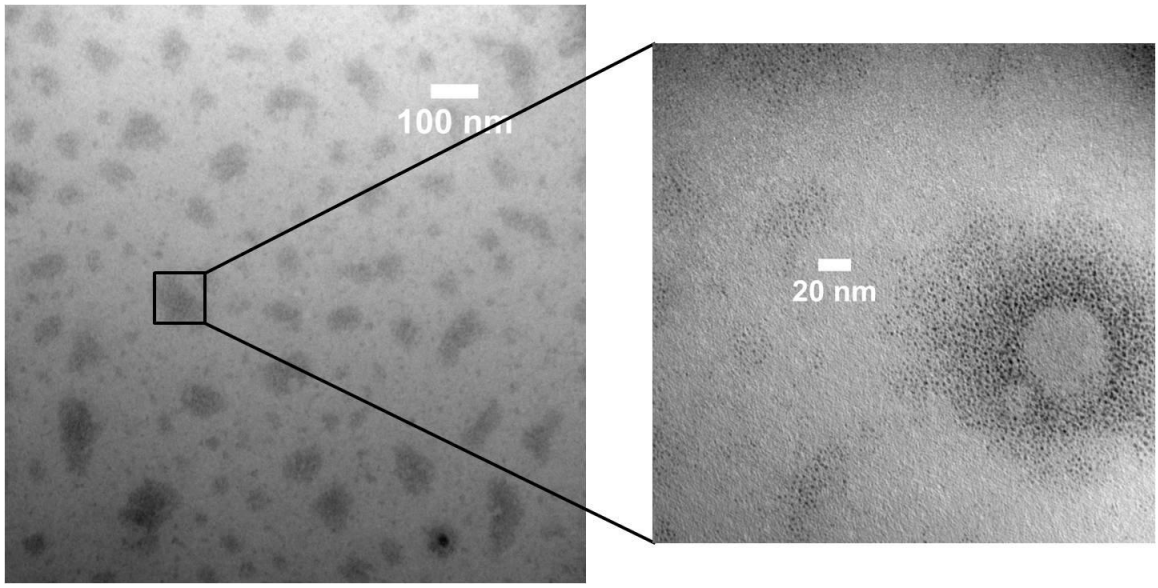

Figure 3.14. Aggregation of pre-synthesized gold nanoparticles with mercaptophenol ligands after storage in methanol for 4 weeks.

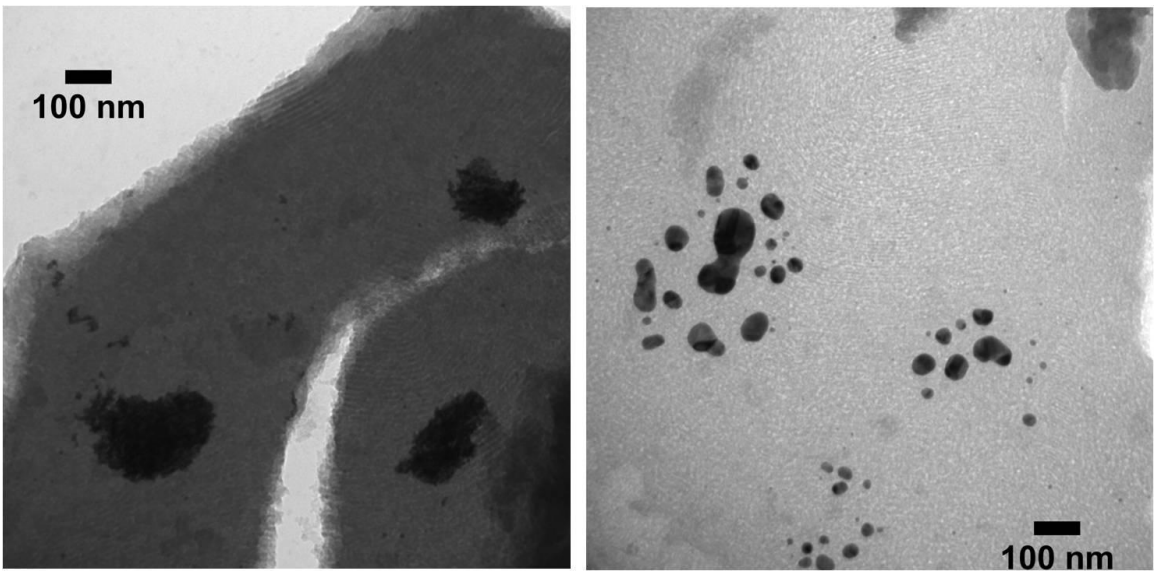

Figure 3.15. TEM images of the as infused condition (left) and as calcined condition (right).

The objective of presenting this information was to show the importance of how the pre-synthesized gold nanoparticles decorated with mercaptophenol ligands were stored and that the storage of the gold nanopartilces as a dry powder under ambient conditions was of great importance to successfully fabricate mesoporous silica doped with gold nanoparticles.

3.3.1.3. Conclusions

Within this dissertation section, a method for attaining functional nanoparticles within the walls of mesoporous silica was presented. The nanoparticle used here was that of ~ 2 nm gold nanoparticles decorated with para-mercaptophenol ligands to selectively hydrogen bond to the hydrophilic segment of Pluronic® F127. To generate the silica to encapsulate the gold nanoparticles within the walls of the mesopores, a three-dimensional replication technique utilizing block copolymer phase separation, phase selective chemistries, and $scCO_2$ infusion processing was used. The gold nanoparticles were

confirmed primarily within the walls of the mesoporous silica by electron microscopy, which would allow the mesopore to be free of obstruction for transport of materials. At a gold nanoparticle loading of 25 wt. % with respect to the Pluronic® template and a reduced $scCO_2$ infusion processing temperature of 40 °C, the gold nanoparticles were found to not grow significantly larger than 3 nm in diameter, which was characterized by UV-Vis spectroscopy. Through the combination of characterization techniques performed on the mesoporous silica doped with pre-synthesized gold nanoparticles, it appears that this type of material would be useful for applications that require access to gold nanoparticles that are hosted within the walls of mesoporous silica such as catalyst substrates and sensors. This procedure described here could be applied to any number of nanoparticles as long as the dimension of the nanoparticles remains below a critical value such that the amphiphilic block copolymer may accommodate the nanoparticle and that the correct hydrogen bonding ligands may be placed on the surface of the nanoparticle.

3.3.2. Mesoporous Silica Doped with Fullerene

3.3.2.1. Introduction

Fullerene molecules, also known as buckminsterfullerene, buckyballs, and/or C60, were first discovered in 1985 by Smalley et al.[41] and have received tremendous research attention over the last three plus decades. Much of this research interest is attributed to the unique physical properties (electronic, electrochemical, and photochemical)[42] offered by fullerene molecules. Such unique properties allow for a large number of potential applications where fullerene molecules are of use such as organic photovoltaics, polymer and organic electronics, biopharmaceuticals (antioxidants), catalysis, water purification, fuel cells, additives (rubber compounds), and

medical (magnetic resonance imaging (MRI) agents)[43]. As with most functional nanomaterials, the aggregation of fullerene molecules severely hinders the extraordinary properties afforded to this molecule and limits the applicability of fullerene. However, the surface of fullerene molecules is easily accessible to chemical functionalization, which may reduce the aggregation phenomena of fullerene and further increase the solubility of fullerene within solvents. Efforts to finely disperse fullerene molecules began with simply blending fullerenes with various materials[44] and then research activities became more sophisticated such that efforts were initiated to chemically functionalize the fullerene to increase the solubility of the material within polymeric materials and solvents. The fullerene derivates were then incorporated within a matrix, either polymeric or inorganic based. Of particular interest to this dissertation chapter is the use of inorganic matrix materials based on sol-gel and sol-gel like processing techniques to support fullerene molecules.

The use of inorganic matrix materials to host fullerene molecules allows for easy fabrication of nanocomposites containing fullerene in the form of solid state devices. Advantages of using matrix materials based on sol-gel chemistries include the complete entrapment of fullerene within the matrix, sufficient mechanical properties, enhanced thermal properties, and increased surface area. Initial trials to incorporate fullerene within metal oxide matrices involved the co-dispersion of a solution of fullerene molecules within a solvent, typically toluene or dichlorobenzene, with a solution of metal oxide precursors, typically silicon dioxide based[45,46]. However, this method of incorporating fullerene molecules within a metal oxide matrix suffered from low solubility of unmodified fullerene molecules in solvents resulting in low concentration of

fullerene within the metal oxide matrix, aggregation of the fullerene molecules, and poor quality of the thin films. The use of hybrid inorganic-organic matrices, where the metal oxide matrix is complimented by organic functionality, increased the concentration of fullerene molecules present in the metal oxide matrix by incorporating favorable organic functionality, i.e. phenyl groups, into the metal oxide matrix[47–50]. The hybrid inorganic-organic matrix allowed for greater concentrations of fullerene molecules to be incorporated within the matrix but aggregation of the fullerene molecules was observed.

Another method of placing fullerene molecules within a metal oxide matrix relied on the diffusion of fullerene molecules into pre-established, porous metal oxide matrices[51–53]. A uniform impregnation of the fullerene molecules within the porous metal oxide matrix was observed but the concentration of the fullerene molecule was extremely low.

To further increase the concentration of fullerene molecules, without aggregation, within metal oxide matrices, the use of fullerene derivatives was investigated. Several derivatives of fullerene have been created that incorporate functionality such that the properties afforded to the fullerene are preserved while increasing the solubility of the fullerene in common polar solvents, which are used for sol-gel processing. The functional groups present on the surface of the fullerene should be able to favorably interact with the metal oxide matrix as the matrix is being established through sol-gel processing, either through direct covalent reactions with the metal oxide matrix, i.e. alkoxide functionality[54,55], and/or intermolecular interactions, i.e. phenyl and amino groups[56–58].

The research described within this dissertation section is devoted to the incorporation of fullerene derivatives (tris(malonic acid) functionality) within the matrix of mesoporous silica produced from supercritical carbon dioxide ($scCO_2$) infusion processing. The selective hydrogen bonding between the tris(malonic acid) fullerene and the hydrophilic segment of the amphiphilic block copolymer allows for selective segregation of the fullerene molecule at high loadings. The compliment of the silica matrix allows for a mesoporous structure to be formed around the fullerene molecule, making the fullerene doped mesoporous silica an attractive substrate for catalysis applications[59,60].

3.3.2.2. Results and Discussion

To incorporate a significant amount of fullerene within a porous metal oxide matrix, while avoiding significant amounts of aggregation, a strong interaction between the fullerene molecule and the matrix material was required. By performing the condensation of the metal oxide matrix via $scCO_2$ infusion processing, the formation of the polymer template was separated from the condensation of the metal oxide matrix, which, for this dissertation chapter, was comprised of silica. The polymer template that was used to direct the phase selective condensation of silicon dioxide precursors was the Pluronic® F127 template, poly(ethylene oxide)-b-poly(propylene oxide)-b-poly(ethylene oxide) (PEO_{106}-b-PPO_{70}-b-PEO_{106}), which has a molecular weight of ~ 12.6 k and a composition of 70 % PEO, was known to phase separate into a cylindrical morphology upon condensation of silica precursors via $scCO_2$ infusion processing.

To achieve high-loadings of fullerene molecules within the Pluronic® F127 template, the establishment of a strong interaction between the poly(ethylene oxide)

(PEO) segment of the Pluronic® F127 and the surface of the fullerene molecule must be created. The use of hydrogen bond donating ligands on the fullerene molecule would provide an exclusive hydrogen bonding opportunity between the surface of the fullerene molecule and the PEO segment of the Pluronic® F127 template. The derivative of fullerene that appeared most appropriate for providing hydrogen bond donating ligands was the derivative of fullerene with the tris(malonic acid) functionality[61].

Two concentrations of tris(malonic acid) fullerene molecules were incorporated into the Pluronic® F127 template for condensation of the silica matrix, 20 wt. % and 50 wt. % with respect to the Pluronic® template, with a constant loading of para-toluene sulfonic acid (pTSA), as the acid catalyst, at 5 wt. % with respect to the Pluronic® template. Films of ~ 400 - 500 nm in thickness were generated on silicon wafer substrates and were absent of any defects such as cracking, dewetting, or macrophase separation. The transmission electron microscopy (TEM) images of the infused sample, i.e. containing organic materials, are provided in Figure 3.16.

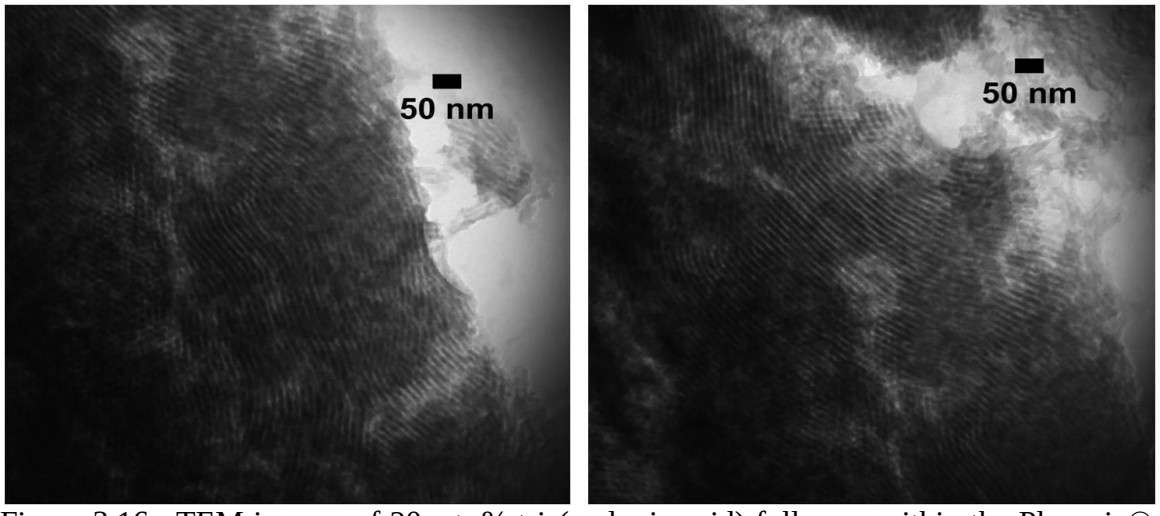

Figure 3.16. TEM images of 20 wt. % tris(malonic acid) fullerene within the Pluronic® F127 template after $scCO_2$ infusion processing.

From Figure 3.16, the presence of a cylindrical mesopore of ~ 4 - 5 nm in diameter was observed and this TEM image was characteristic of the type of result that was easily found within the TEM observation. However, from Figure 3.16, the organic material, i.e. the Pluronic® template, was present such that the contrast between the pore and matrix was not generated from the electron density differences between the fullerene doped silica matrix and pore, i.e. air, but rather from the electron density difference between the fullerene doped silica matrix and PPO domain. For comparison of the electron density difference between an undoped silica matrix and fullerene doped silica matrix, both in comparison to the poly(propylene oxide) (PPO) domain, Figure 3.17 is provided. The TEM images provided in Figure 3.17 were acquired under identical circumstances, i.e. accelerating voltage, aperture size, and were synthesized under identical circumstances such that the only difference between the two TEM images was the presence of the tris(malonic acid) fullerene molecule.

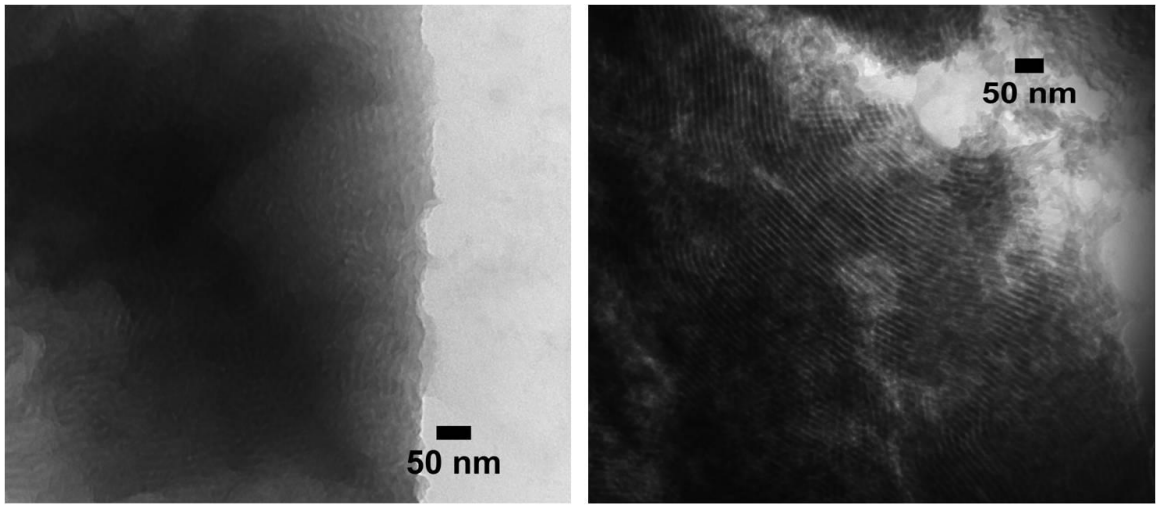

Figure 3.17. TEM images comparing the contrast between updoped silica matrix after $scCO_2$ infusion processing (left) and fullerene doped silica matrix after $scCO_2$ infusion processing (right).

From Figure 3.17, the difference in contrast between the two TEM images was significant and suggests the presence of the fullerene molecule within the silica matrix.

To generate an actual mesoporous material, the Pluronic® template must be removed and the preferred method for removing the Pluronic® template was through elevated temperatures under ambient conditions. The thermal degradation procedure proceeds by increasing the temperature at a ramp rate of 1.56 °C/minute to 400 °C from room temperature, holding at 400 °C for 6 hours, and decreasing the temperature at a ramp rate of 1.56 °C/minute to room temperature. Figure 3.18 shows the TEM images of the 20 wt. % fullerene doped mesoporous silica after thermal degradation, i.e. the Pluronic® template has been removed.

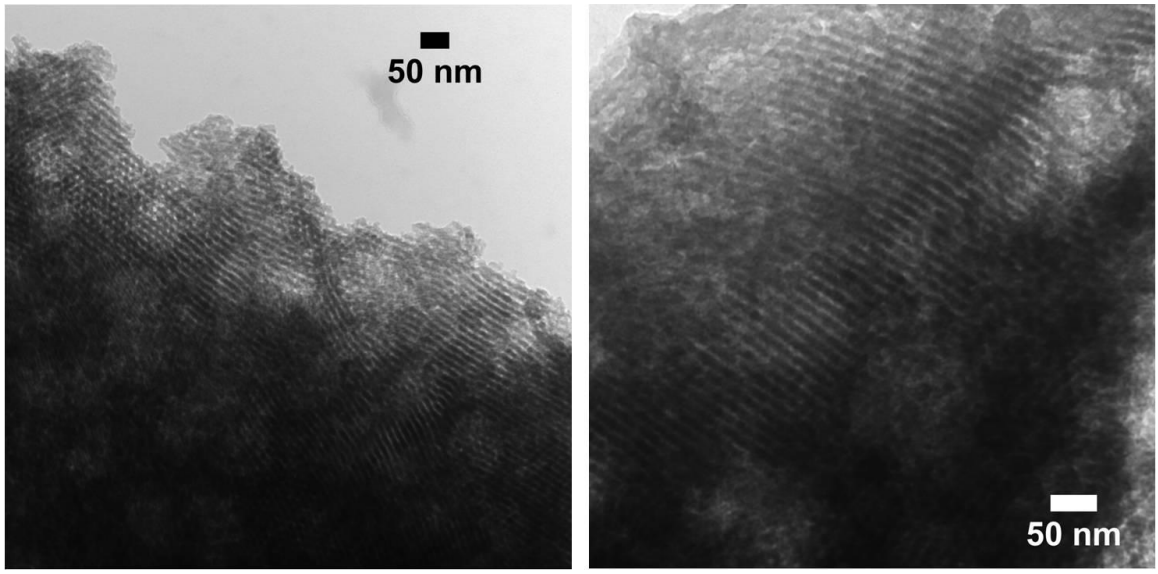

Figure 3.18. TEM images of 20 wt. % tris(malonic acid) fullerene within the Pluronic® F127 templated mesoporous silica after thermal degradation of the Pluronic® template, i.e. calcination.

From Figure 3.18, the presence of a cylindrical mesopore with a diameter of ~ 4 - 5 nm was shown where the mesopore was free of organic material. Due to the 400 °C temperature exhibited on the fullerene doped mesoporous silica thin films, the thermal

stability of the tris(malonic acid) fullerene molecule was evaluated by thermogravimetric analysis (TGA), performed with the identical procedure for the thermal degradation, and is shown in Figure 3.19. From the TGA data, it appears that the thermal stability of fullerene core was quite stable[62,63] for the tris(malonic acid) fullerene molecule where as it appears that the malonic acid functionality may be removed at elevated temperatures, which corresponds to ~ 30 - 31 weight percent of the tris(malonic acid) fullerene, which was the approximate amount of weight lose determined by TGA.

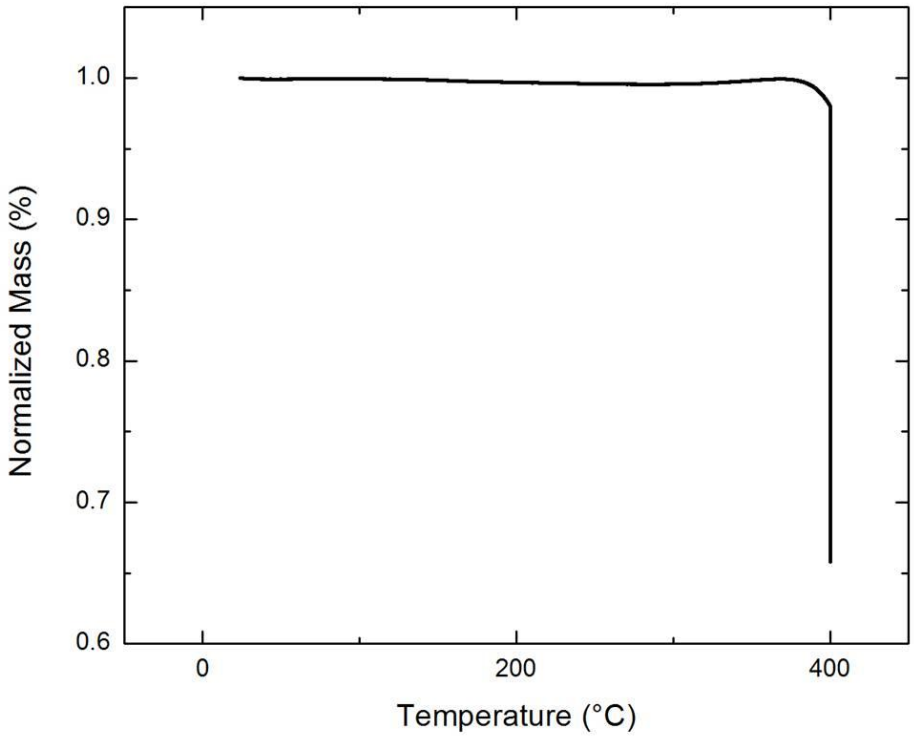

Figure 3.19. Thermogravimetric analysis (TGA) of tris(malonic acid) fullerene.

A higher concentration of 50 wt. % tris(malonic acid) fullerene, with respect to the Pluronic® template, was incorporated within the Pluronic® template with 5 wt. % PTSA, with respect to Pluronic® template, to be complimented by a silica matrix through

$scCO_2$ infusion processing. Figure 3.20 and Figure 3.21 shows the TEM images of the 50 wt. % fullerene doped silica matrix with and without the Pluronic® template present respectively. From the TEM images, a cylindrical mesopore of ~ 4 - 5 nm was preserved within the Pluronic® F127 templated mesoporous silica, even with the presence of 50 wt. % tris(malonic acid) fullerene.

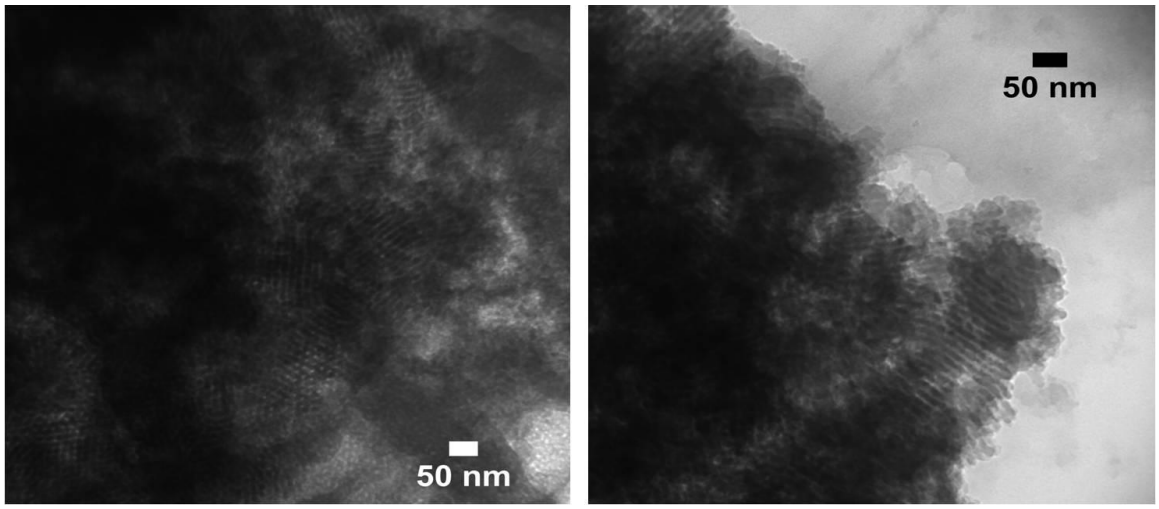

Figure 3.20. Transmission electron microscopy images of 50 wt. % tris(malonic acid) fullerene within the Pluronic® F127 template after $scCO_2$ infusion processing.

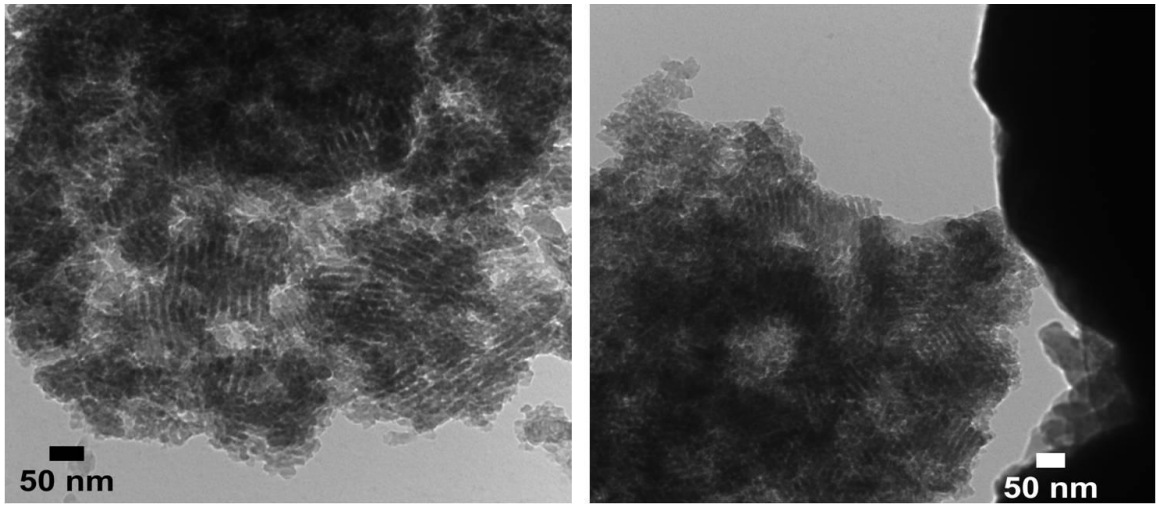

Figure 3.21. Transmission electron microscopy images of 50 wt. % tris(malonic acid) fullerene within the Pluronic® F127 templated mesoporous silica after thermal degradation of the Pluronic® template, i.e. calcination.

From the TEM images of mesoporous silica doped with 50 wt. % tris(malonic acid) fullerene, regardless of the presence of the Pluronic® template, the long-range order of the cylindrical mesopore has been severally hindered. To quantify the long-range order of the mesoporous silica doped with various concentrations of tris(malonic acid) fullerene, low-angle X-ray diffraction (LAXRD) was performed and is provided in Figure 3.22.

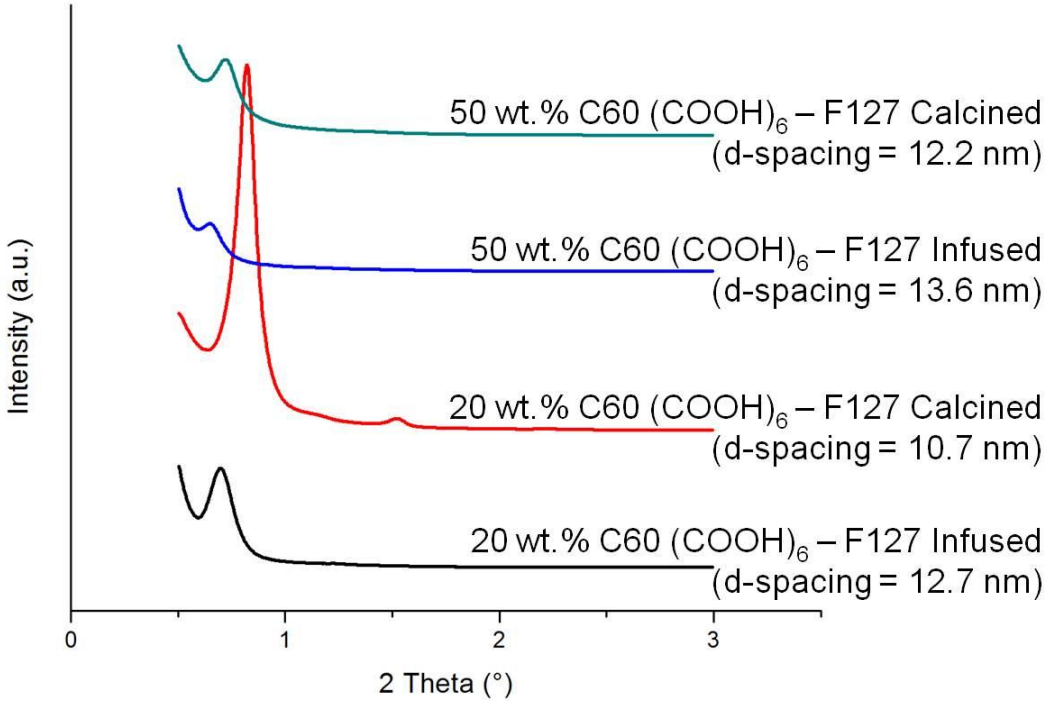

Figure 3.22. LAXRD of mesoporous silica doped with various concentrations of tris(malonic acid) fullerene. The terms of infused and calcined refer to the presence of the Pluronic® template (infused) and to the presence of no Pluronic® template (calcined).

The LAXRD data shows that the incorporation of the fullerene molecule does not disrupt the ordering of the mesopore silica structure templated by the Pluronic® template and generated by $scCO_2$ infusion processing. The LAXRD data was confirmed from the

TEM images where the long-range order of the cylindrical mesopore was reduced when increased concentrations of fullerene molecules were incorporated within the mesoporous silica matrix according to the intensity reduction of the primary peak as well as the increase in FWHM of the primary peak. The Pluronic® F127 template also appears to be stretching to greater lengths with the incorporation of increased concentrations of fullerene molecules, which was seen in the increased domain-spacing from the LAXRD data.

To further confirm the presence of the fullerene molecules within the mesoporous silica matrix, a multitude of characterization techniques have been attempted, however, with limited success. Transmission Fourier transform infrared (FT-IR) spectroscopy, electron diffraction, X-ray diffraction, photoluminescence (PL), and Raman spectroscopy were attempted but all suffered from signal to noise ratio and/or background issues involving either the silicon wafer and/or mesoporous silica matrix.

3.3.2.3. Conclusions

Within this dissertation section, a method for attaining functional nanomaterials in the form of fullerene within the walls of mesoporous silica was presented. The fullerene derivative used here was that of tris(malonic acid) functionality, which has the ability to selectively hydrogen bond to the hydrophilic segment of Pluronic® F127. To generate the silica to encapsulate the fullerene molecules within the walls of the mesopores, a three-dimensional replication technique utilizing block copolymer phase separation, phase selective chemistries, and $scCO_2$ infusion processing was used. The confirmation of the fullerene within the matrix of the mesoporous silica remains qualitative, at best, from the TEM images and the enhanced contrast that was exhibited in the TEM images

where the Pluronic® template was present. Through the combination of selective hydrogen bonding, between the functional nanomaterials and the hydrophilic domain of an amphiphilic block copolymer, i.e. PEO of Pluronic®, coupled with the condensation of silica through $scCO_2$ infusion processing, the concentration of fullerene molecules may easily be controlled and adapted to specific applications where nanocomposites comprised of fullerene and silica are of interest.

3.3.3. Mesoporous Silica Doped with Polyhedral Oligomeric Silsesquioxane (POSS)

3.3.3.1. Introduction

Porous silica has long been an interest of the catalysis and separations communities since the discovery of this material in the early 1970s[64,65]. The ability to control the pore size and architecture of the porous material followed two decades later by the development of Mobil Crystalline Material (MCM) from the Mobil Oil Corporation, often designated as M41S, based on either silicate or aluminosilicate (zeolites) frameworks with the most common set of M41S materials being MCM-41 and MCM-48[66–68]. Several other variations of porous silica materials were simultaneously being researched such as Santa Barbara Amorphous 15 (SBA-15)[69] and Korean Advanced Institute of Science and Technology 1 (KIT-1)[70] and others, which have exhibited unique properties such as wall thickness, tunable pore sizes to 30 nm in diameter, and mechanical stability. One property that has been thoroughly investigated to further improve upon has been the thermal and the hydrothermal stability of the mesoporous silica.

To make a truly mesoporous silica, the organic template that directs the structure must be removed to yield a mesopore. The most common method to remove the organic

template is through thermal degradation at elevated temperatures, however, other methods to remove the organic template have been successful such as solvent extraction. The physical response from mesoporous silica upon thermal degradation at elevated temperatures is shrinkage. During the thermal degradation procedure, the mesoporous silica will experience unique shrinkage phases with each phase corresponding to a specific temperature range. Through the initial phase (room temperature (RT) to 150 °C) of the thermal degradation, the physical absorbed water is removed and slight shrinkage is observed due to the increase of the surface energy[71]. Within the temperature range of 150 °C to 525 °C, the mesoporous silica undergoes weight loss from the removal of organic material and shrinkage from further condensation of the silica matrix (slight weight loss as well) and structural relaxation, i.e. bond restructuring and/or rearrangement. At temperatures greater than 525 °C, the mesoporous silica undergoes additional shrinkage through the combination of further condensation and structural relaxation until free energy of the mesoporous silica matrix has reached a minimum[71].

For several applications, particularly with catalysis, the mesoporous silica materials will regularly experience elevated temperatures and high humidity conditions. The previously described synthesis of mesoporous silica has been directed via surfactant templates (structure directing agents), either non-ionic, anionic, or cationic based and have suffered from poor thermal and hydrothermal stability. The initial M41S, which were synthesized with tetraethyl orthosilicate (TEOS), suffered from poor thermal and hydrothermal properties due to the pore walls being amorphous and thin. In general, mesoporous silica materials suffer from hydrothermal treatments at elevated temperatures and high relative humidities for prolonged periods of time, often leading to shrinkage

and/or collapse of the mesopore. The mesoporous silica matrix is hindered under these conditions due to the continuous silicate hydrolysis of the pore wall, i.e. the Si-O-Si bond, which will ultimately result in collapse of the mesoporous structure.

To improve upon the stability of the M41S mesoporous silica materials, adjustments to the synthesis process (use of different silica precursors, addition of organic[72–75] or inorganic salts[72,73,76], incorporation of heteroatoms such as aluminum) as well as post-processing (hydrothermal treatments at low temperatures and hydrophobization of the surface) have been attempted and have shown enhanced stability. Other efforts to increase the stability of mesoporous silica to thermal and hydrothermal conditions have consisted of increasing the pore wall thickness[77] and surface functionalization[78–80]. Observations have also been made that enhancing the local ordering of M41S materials as well as increasing the pore wall thicknesses showed greater stability under harsh conditions of thermal and hydrothermal processing.

To provide more stable mesoporous silica materials, others have created synthetic approaches that differ from the synthesis of M41S materials such that improvements were made to the pore wall thickness, choice of silica precursors, degree of silica condensation, and local ordering of the mesopores. The properties that determine the thermal and the hydrothermal stability of mesoporous silica materials have been thoroughly evaluated and has been determined that the thermal stability of mesoporous silica materials is directly related to the pore wall thickness (thicker the pore wall, greater thermal stability) as well as the choice of silica precursor. The hydrothermal stability of mesoporous silica materials has been correlated to the pore wall thickness (thicker pore well, greater

hydrothermal stability), the degree of condensation within the mesoporous silica matrix, and the affinity of water to the mesoporous silica matrix, i.e. hydrophobicity[81].

There have been many approaches to increase the stability of mesoporous silica materials under harsh conditions, through synthetic strategies or post-processing methods, and the research described within this dissertation section is built around the principle of incorporating a material within the mesoporous silica matrix to reinforce the stability of the mesoporous structure. The material of choice here is polyhedral oligomeric silsesquioxane (POSS) decorated with maleamic acid functionality. POSS has often been used to generate composite materials that are comprised of thermal, mechanical, and other chemical and physical properties that are intermediate between organic polymer materials and ceramics. The desire to use POSS for investigating thermal and hydrothermal properties of mesoporous silica generated from $scCO_2$ infusion processing is to take advantage of the intermediate properties afforded to POSS, i.e. the use of ligands with organic functionality to increase solubility and allow for preferential hydrogen bonding between the POSS molecules and amphiphilic block copolymer template. By incorporating the POSS molecule into the mesoporous silica matrix generated by the $scCO_2$ infusion processing, the ceramic nature of the silsesquioxane core should improve upon the thermal and the hydrothermal properties of the silica matrix.

3.3.3.2. Results and Discussion

To determine the incorporation of POSS-OAA molecules within the matrix of the mesoporous silica wall, attenuated total reflectance FT-IR (ATR-FT-IR) was performed on low-resistivity silicon wafers, which do not produce an infrared signal, throughout the processing steps and is shown in Figure 3.23. It should be noted that the noise shown in

Figure 3.23 between the wavenumber range of 1800 cm^{-1} to 1400 cm^{-1} was due to absorption of the diamond crystal used for ATR-FT-IR as well as absorption of atmospheric water, while the noise present in the wave number range of 750 cm^{-1} to 650 cm^{-1} and 2350 cm^{-1} was due to atmospheric carbon dioxide.

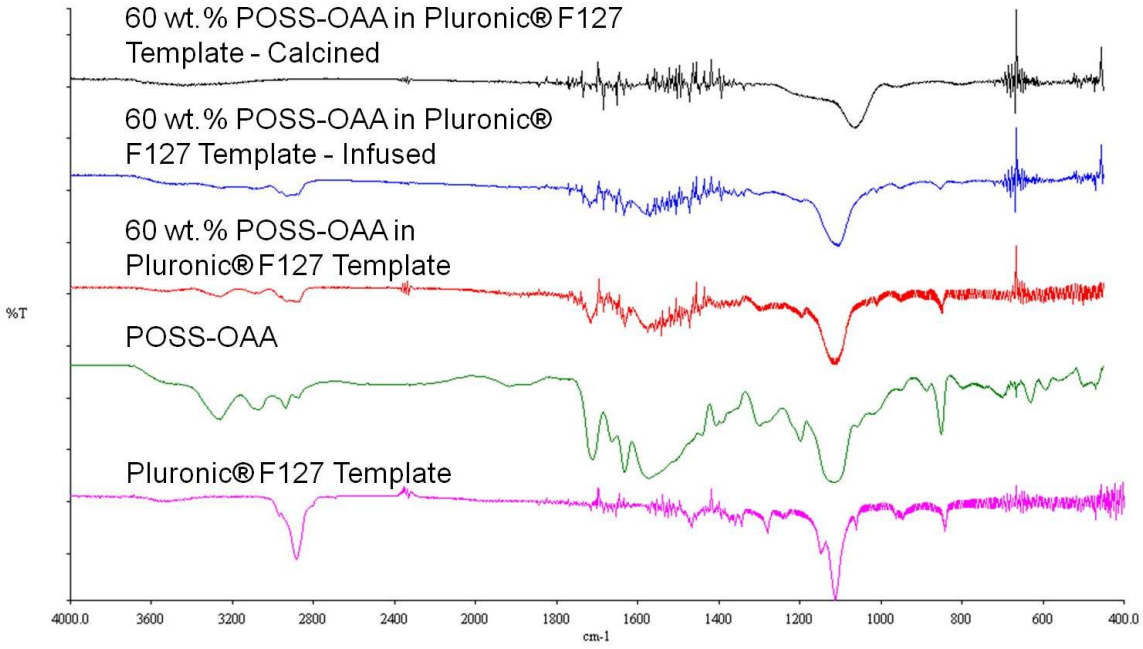

Figure 3.23. ATR-FT-IR spectroscopy for the fabrication of POSS-OAA doped mesoporous silica.

The infrared (IR) signals of interest for the Pluronic® template, POSS-OAA molecule, and mesoporous silica are shown in Table 3.1. From the ATR-FT-IR spectroscopy data, the presence of the POSS molecule was confirmed throughout the blending of the POSS molecule with the Pluronic® template as well as the $scCO_2$ infusion processing by monitoring the secondary amine and carbonyl IR signals. Upon thermal degradation at elevated temperatures, i.e. 650 °C, in an air environment, the organic material present within the POSS molecule and the Pluronic template were removed, as explained by the absence of any IR signals other than the IR signals

corresponding to the silica matrix. To confirm the removal of the POSS-OAA ligands, thermogravimetric analysis (TGA), Figure 3.24, was performed with a thermal degradation procedure of 1.56 °C/minute ramp rate to 650 °C and held at 650 °C for 6 hours. The percentage of mass remaining after this thermal degradation procedure was ~ 32 % which, with the POSS core equaling ~ 26 % of the POSS-OAA mass, corresponds to several percentage points of residual mass remaining that does not belong to the POSS core.

Table 3.1. IR Signals of Interest for Pluronic Templates, POSS-OAA Molecules, and Mesoporous Silica[82]

Functional Group	**Characteristic Absoprtion (cm^{-1})**	**Type of Vibration and Intensity**
Ether (C-O)	1300-1000 (1150-1070)	Stretching (Strong)
Carbonyl (C=O)	1820-1670	Stretching (Strong)
Alcohol (O-H)	3700-3200	Stretching (Strong and/or Broad)
Alcohol (C-O)	1150-1050	Stretching (Strong)
Secondary Amine (N-H)	3350-3310	Stretching (Weak)
Amine (N-H)	1650-1580	Bending (Medium/Strong)
Silicon-Oxygen (Si-O-Si)	1100-1000	Stretching (Strong)

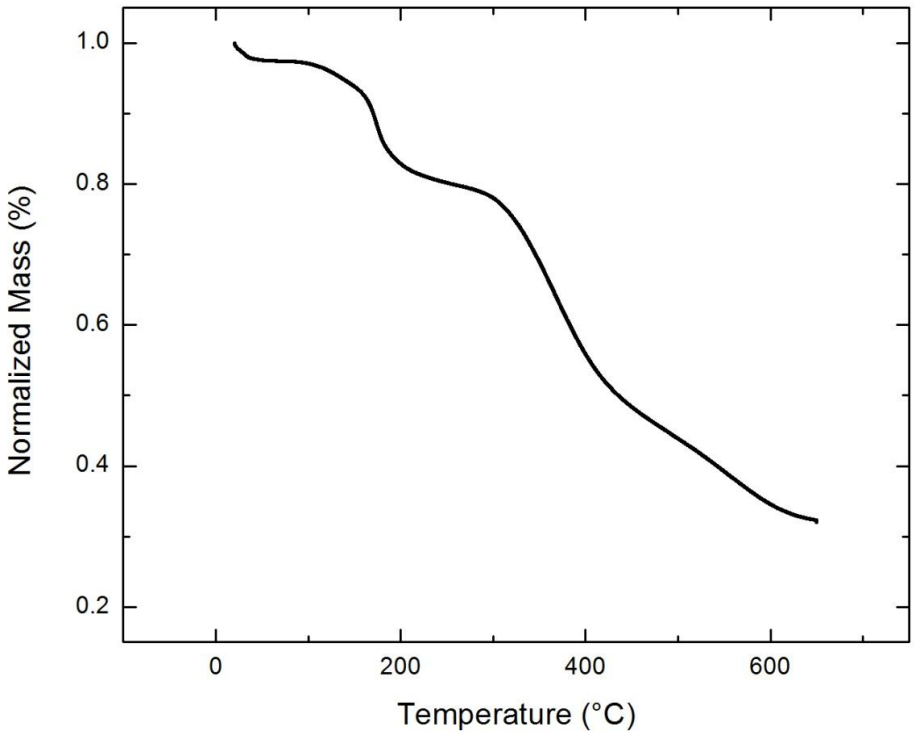

Figure 3.24. TGA of POSS-OAA following the thermal degradation procedure of 1.56 °C/minute ramp rate to 650 °C and hold at 650 °C for 6 hours.

Various loadings of POSS-OAA doped with mesoporous silica from $scCO_2$ infusion processing were evaluated for domain spacing, thermal stability, and hydrothermal stability. The loading of the POSS-OAA varied from 5 wt. % to 35 wt. %, with respect to the Pluronic® template, within the Pluronic® F127 template and the control sample was comprised of 20 wt. % 1.8 k Mw poly(acrylic acid) (PAA) doped Pluronic® F127. The domain spacing was evaluated by low-angle X-ray diffraction (LAXRD), provided in Figure 3.25, and was performed every 100 °C increment from 400 °C till 1000 °C was reached or a discernible domain spacing could not be determined from the LAXRD spectrum. A single sample for each of the various concentrations of POSS-OAA was

used for the evaluation, i.e. a single sample experienced a ramp rate of 1.56 °C/minute to 400 °C, hold for 6 hours, and ramp rate of 1.56 °C/minute to room temperature, then evaluation by LAXRD and spectroscopic ellispometry, this procedure was repeated for hold temperatures with increments of 100 °C till 1000 °C was reached.

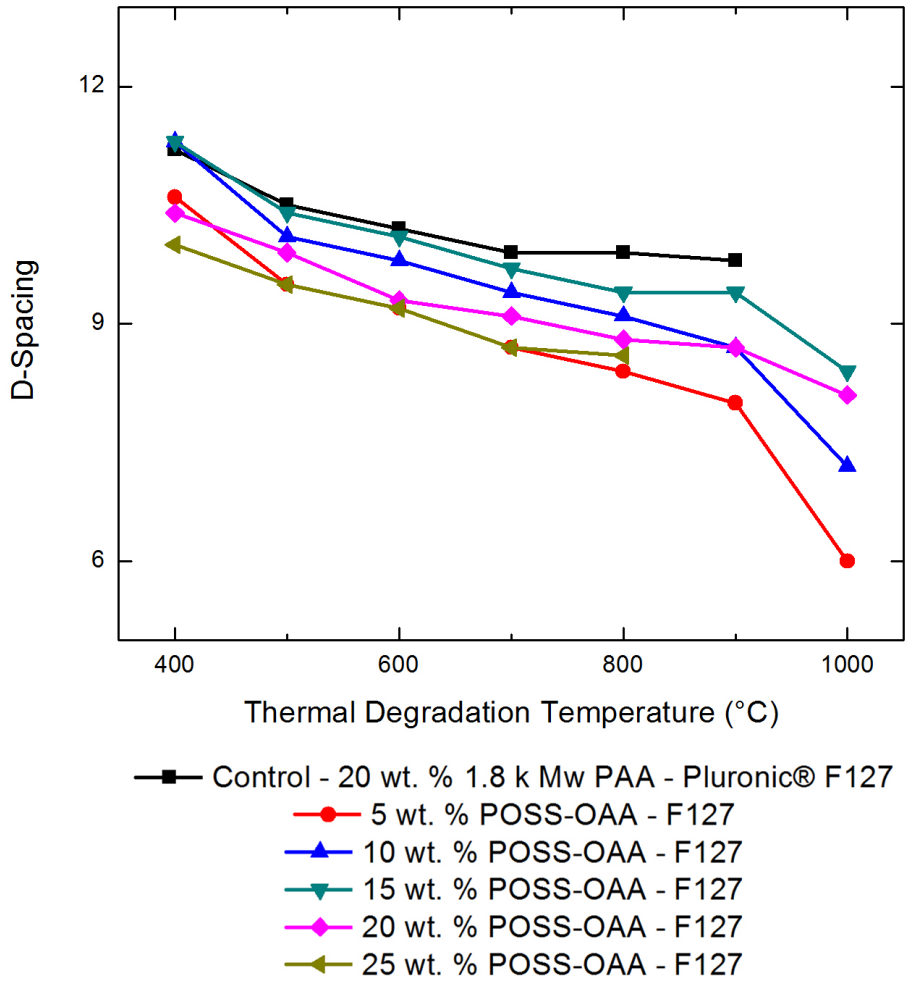

Figure 3.25. Low-angle X-ray diffraction (LAXRD) of various POSS-OAA loadings within mesoporous silica from Pluronic® F127 template and supercritical carbon dioxide infusion processing.

From the LAXRD, it is shown that the control sample of PAA doped Pluronic® F127 did not maintain a mesoporous structure at 1000 °C while the samples containing POSS-

OAA, in the loading range of 5 wt. % to 20 wt. %, were able to maintain a well-defined mesoporous structure. The loading of the POSS-OAA reached an upper limit of approximately 25 wt. % to maintain a discernible mesopore structure, i.e. the Pluronic® template with loadings of POSS-OAA greater than 25 wt. % did not show a well-defined mesoporous structure. Another observation from the LAXRD data was that as the loading of the POSS-OAA increased, the thermal stability increased of the well-defined mesopore structure, i.e. the mesopore contracted less with the addition of more POSS-OAA. The morphology of the 15 wt. % POSS-OAA doped mesoporous silica from the Pluronic® F127 template thermally degraded at various temperatures was confirmed from TEM images, which are provided in Figure 3.26.

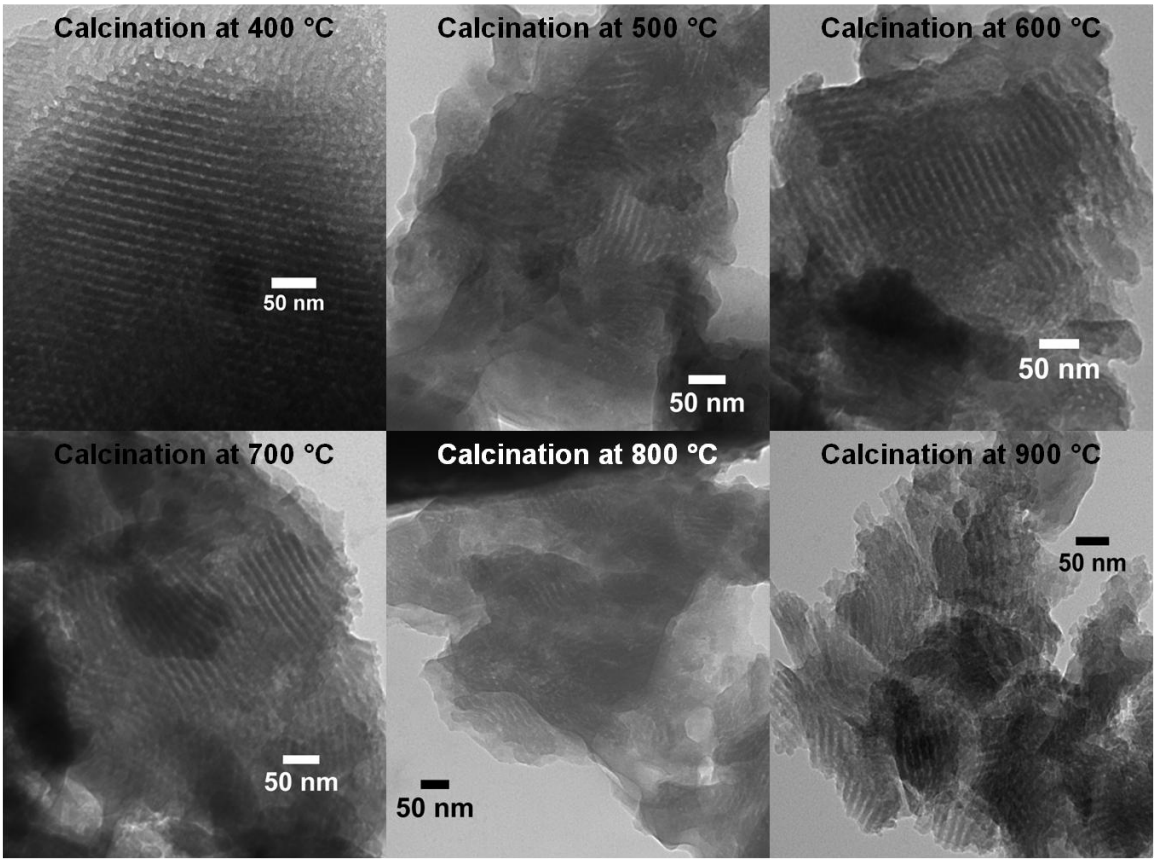

Figure 3.26. TEM images of 15 wt. % POSS-OAA doped mesoporous silica from the Pluronic® F127 template at various thermal degradation (calcination) temperatures.

Another method to determine the thermal stability of mesoporous silica materials was through the monitoring of the refractive index with spectroscopic ellipsometry. As the mesoporous silica becomes denser, the refractive index of the thin film will increase. For reference, the refractive index of dense silicon dioxide is ~ 1.538 when measured at the wavelength of 800 nm[83]. The refractive index of the mesoporous silica films from the Pluronic® F127 template doped with loadings of POSS-OAA from 5 wt. % to 35 wt. % were evaluated, as shown in Figure 3.27. It should be noted that the control sample has an additional porosity due to the presence of PAA which will yield a more porous silica film when compared to mesoporous silica from just the Pluronic® F127 template alone. Along this theory, the incorporation of higher amounts of POSS-OAA will yield more porous films due to the presence of organic material based side chains on the POSS cage and this trend was confirmed within the refractive index data. Another conclusion from the refractive index data was that the presence of a well-defined mesopore yielded thin films that were not as susceptible (5 wt. % through 20 wt. %) to densification as un-ordered mesopores were (25 wt. % through 35 wt. %).

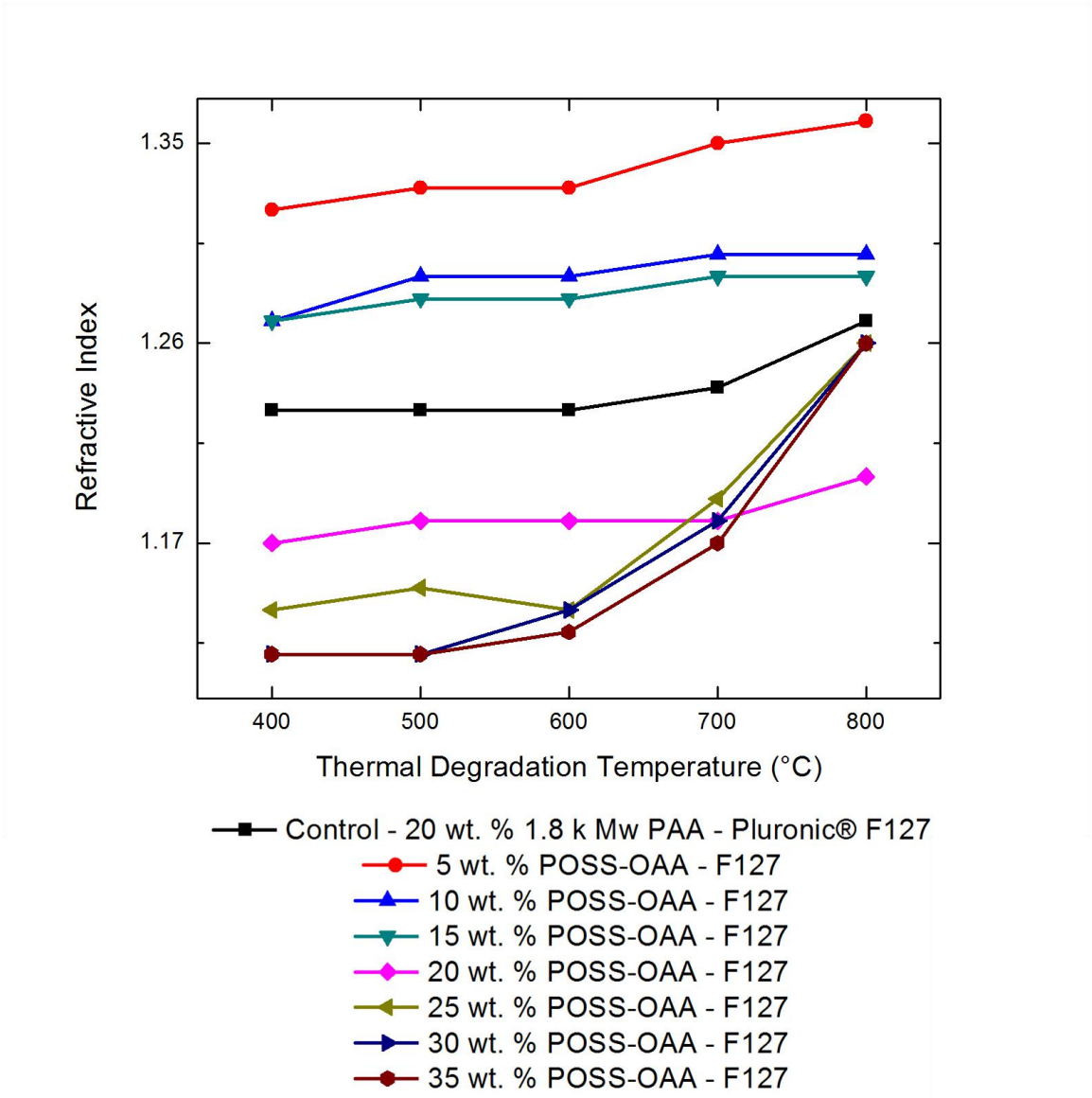

Figure 3.27. Refractive index values for various loadings of POSS-OAA within mesoporous silica from the Pluronic® F127 template.

The porosity of the thin films was also estimated from the spectroscopic ellipsometry data as well and is provided in Figure 3.28.

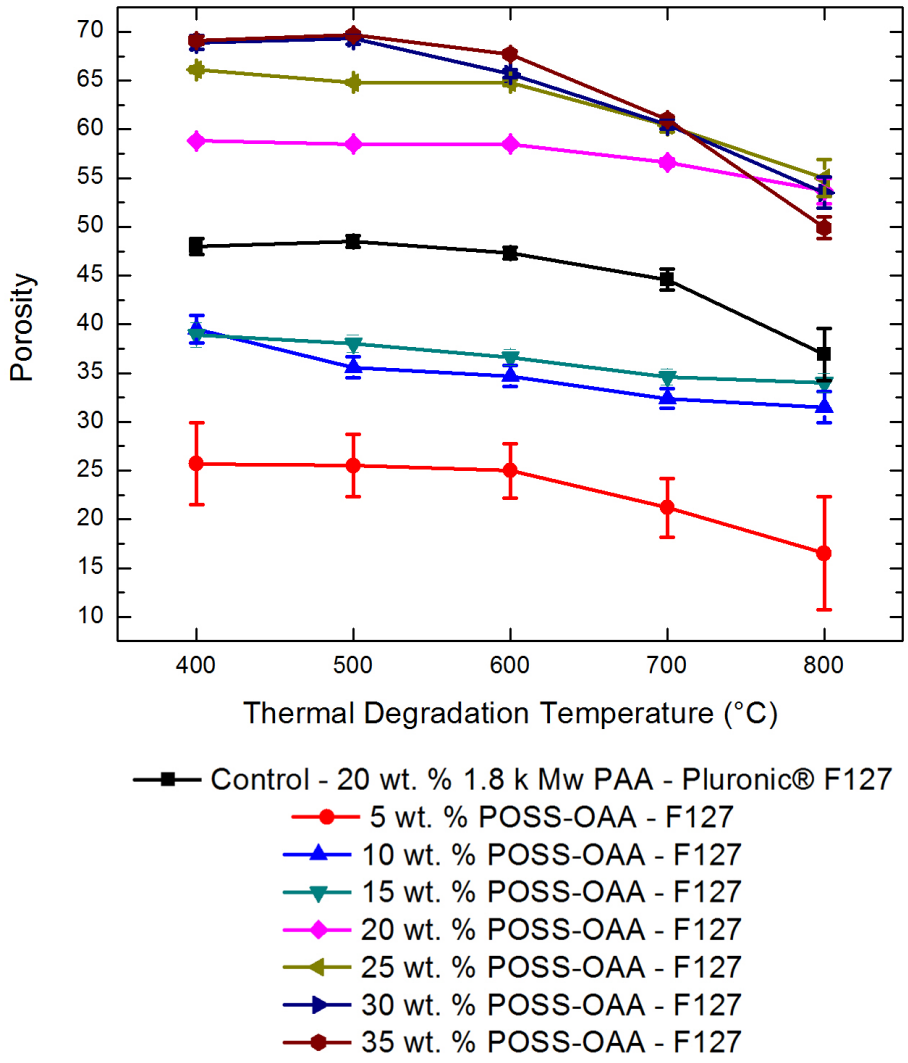

Figure 3.28. Porosity estimated from spectroscopic ellipsometry data for various loadings of POSS-OAA within mesoporous silica from the Pluronic® F127 template.

The porosity of the thin films was approximated using the WINELLI software developed by Sopra. The simulated mixing of dense silicon dioxide and void, i.e. air, was performed using Bruggeman's effective medium approximation and the regression method of Levenberg-Marquardt. From the estimated porosity from the spectroscopic ellipsometry, the trend of increased porosity for increased amounts of POSS-OAA molecules was observed.

The hydrothermal stability of the mesoporous silica doped with POSS-OAA was also evaluated under 100 % relative humidity at autogenous pressures from temperatures greater than 100 °C for prolonged periods of time, generally 24 hours. Mesoporous silica samples were placed in an autoclave with 5 mL of reverse osmosis (RO) water such that the sample was elevated to not be in direct contact with the water. The control sample was mesoporous silica from the Pluronic® F127 template doped with 20 wt. % 1.8k Mw PAA. From Figure 3.29, the hydrothermal stability of the control sample and mesoporous silica doped with 15 wt. % POSS-OAA were evaluated at two hydrothermal conditions, 24 hours at 120 °C in 100 % relative humidity and 24 hours at 150 °C in 100 % relative humidity. The domain spacing of the mesoporous structure was monitored for the various samples and the hydrothermal processing, even under extreme conditions such as 100 % relative humidity, the domain spacing remained unchanged (see Appendix I). In fact, the mesoporous silica doped with POSS-OAA has a greater intensity for the domain spacing peak from LAXRD after the hydrothermal processing when compared to the mesoporous silica without POSS-OAA additives (see Appendix I). Spectroscopic ellipsometry was performed as well where the properties of film thickness, refractive index, and estimated porosity were determined and shown in Figure 3.30. For the control sample, the film thickness was not severely hindered (less than 5 % shrinkage) and the porosity maintained values of 50 % for even the most severe hydrothermal treatment while the refractive index slightly increased. The 15 wt. % POSS-OAA doped mesoporous silica experiencing 400 °C calcination (thermal degradation) followed the identical trend observed by the control sample with the exception of overall porosity where 38 % porosity was obtained for the most severe hydrothermal treatment. The

spectroscopic ellipsometry data for the 15 wt. % POSS-OAA doped mesoporous silica experiencing 650 °C calcination was unable to be successfully modeled by the WINELLI software; however, the trend that was observed for the 15 wt. % POSS-OAA doped mesoporous silica experiencing 400 °C calcination would be expected. This assumption is strongly supported by the trend observed from the d-spacing of the 15 wt. % POSS-OAA doped mesoporous silica experiencing various calcination temperatures, shown in Figure 3.29.

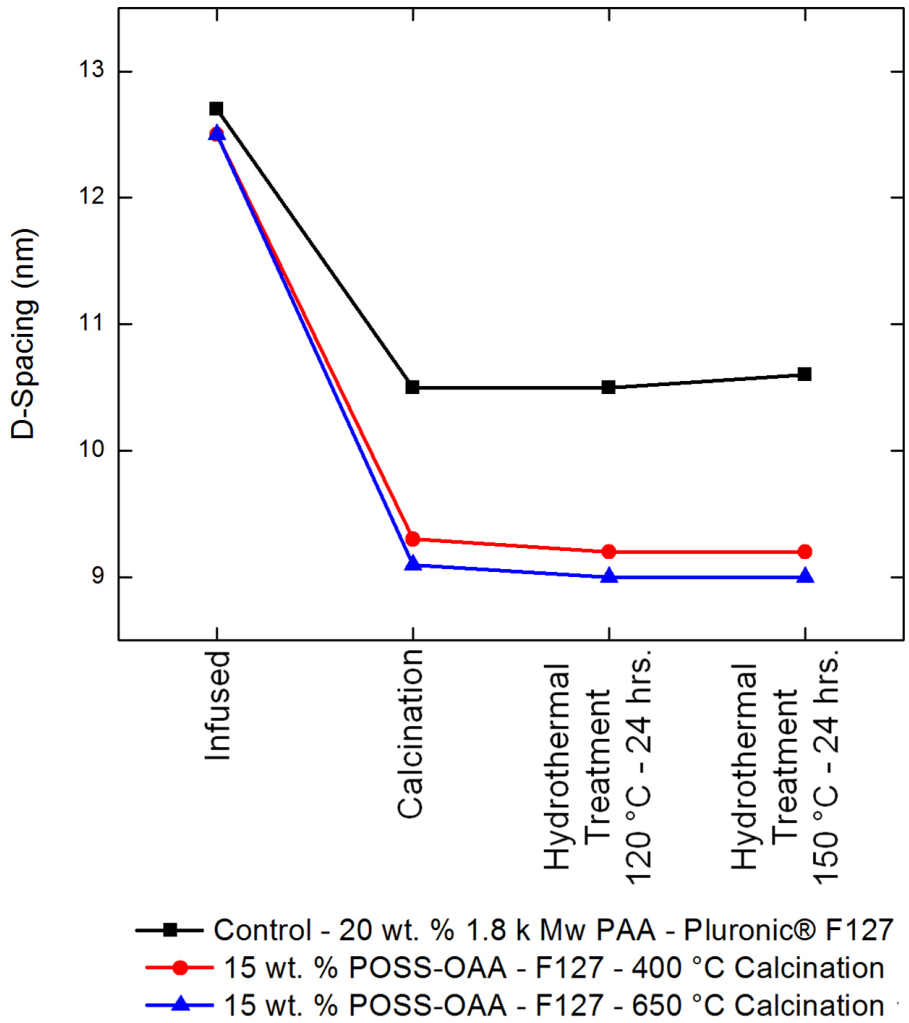

Figure 3.29. Hydrothermal treatment of mesoporous silica doped with POSS-OAA.

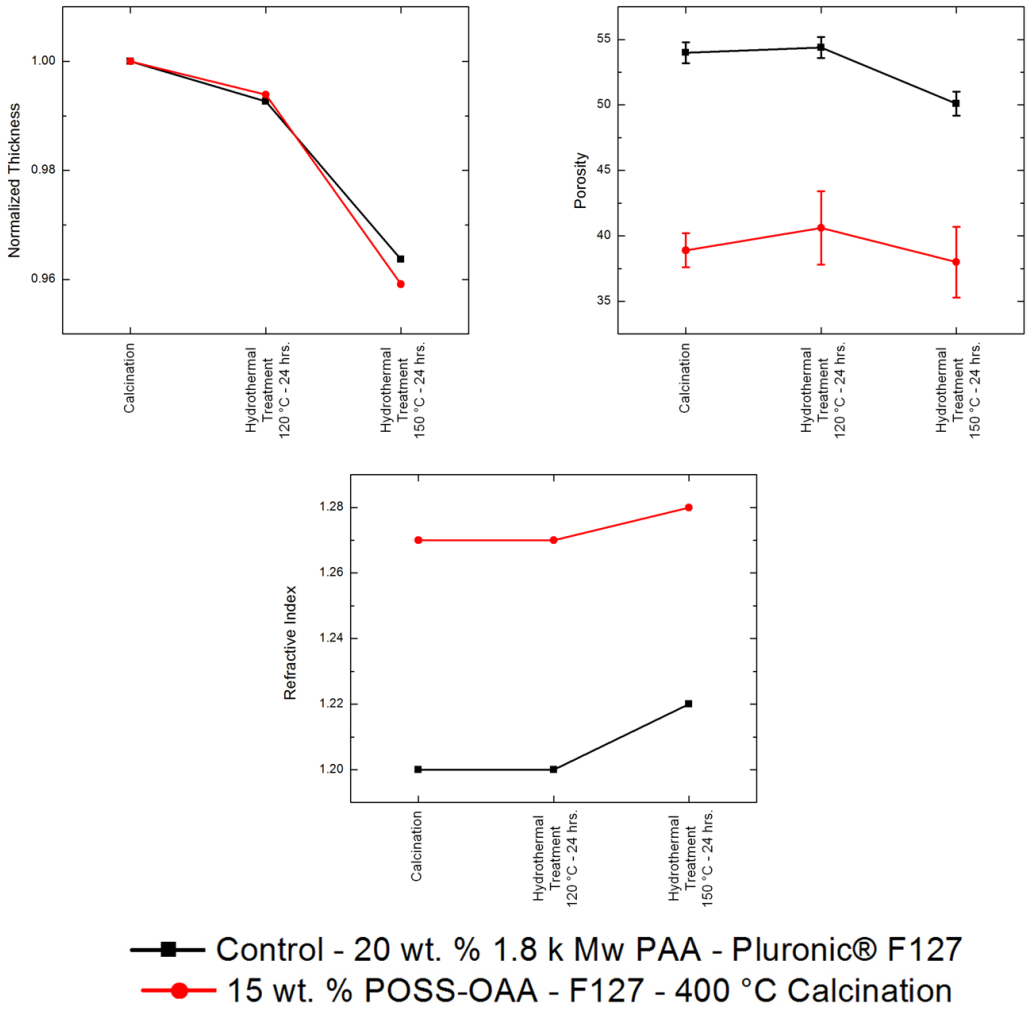

Figure 3.30. Spectroscopic ellipsometry data for the control sample of 20 wt. % 1.8 k Mw PAA doped Pluronic® F127 mesoporous silica and 15 wt. % POSS-OAA doped mesoporous silica experiencing 400 °C calcination under various hydrothermal treatments.

While performing the hydrothermal treatments, there was a concern that the amorphous mesoporous may undergo crystallization. To determine if a crystallization process was being performed, wide-angle X-ray diffraction (WXRD) was performed and shown in Figure 3.31. There were no observed diffraction peaks corresponding to crystallization of the amorphous silica.

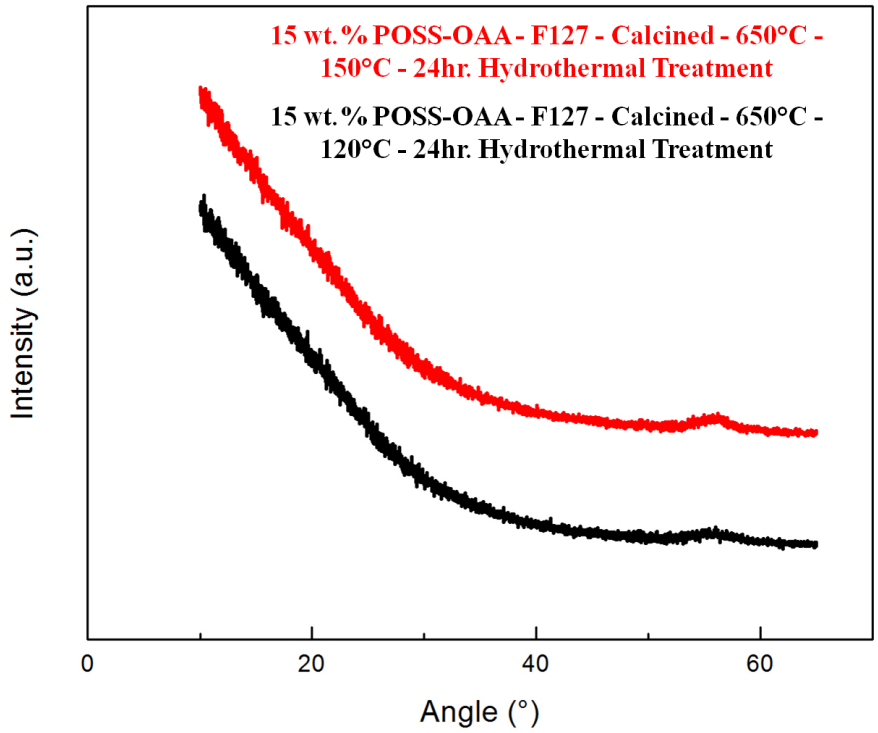

Figure 3.31. Wide-angle X-ray diffraction (WXRD) of mesoporous silica samples from Pluronic® F127 doped with POSS-OAA after undergoing hydrothermal treatments.

3.3.3.3. Conclusions

Within this dissertation section, a method for selectively adding functional polyhedral oligomeric silsesquioxane octa maleamic acid (POSS-OAA) within the walls of mesoporous silica through $scCO_2$ infusion processing has been achieved. The incorporation of POSS-OAA, at concentration less than 20 wt. % with respect to Pluronic® template, allowed for greater long-range ordered, as detected by LAXRD. The thermal properties of the POSS-OAA doped mesoporous silica were enhanced by 200 °C such that a mesopore was shown at thermal degradation temperatures up to 1000 °C for concentrations less than 25 wt. % POSS-OAA. The hydrothermal stability of the mesoporous silica doped POSS-OAA showed remarkable stability under harsh

conditions, such as 150 °C, 100 % relative humidity, and autogenous pressures. The incorporation of POSS molecules within mesoporous silica appears to be a unique fabrication method to enhance the thermal and the hydrothermal stability of mesoporous silica materials.

3.4. Conclusions

Functional nanomaterials, in the form of pre-synthesized gold nanoparticles, tris(malonic acid) fullerene derivatives, and polyhedral oligomeric silsesquioxane (POSS) molecules, have been successfully incorporated within mesoporous silica, which was synthesized from $scCO_2$ infusion processing. The ability to manipulate the mesoporous silica polymer template with additive functional materials was attributed to the unique synthetic strategy afforded to $scCO_2$ infusion processing which allows the polymer template formation to be separated from the silica condensation. Through the incorporation of functional nanomaterials, the properties afforded to the functional nanomaterial have been provided to the mesoporous silica, such as enhanced thermal and hydrothermal stability under extreme conditions. The research presented within this dissertation chapter has provided the framework for creating unique mesoporous materials that are capable of being functionalized with various nanomaterials. The technique is robust such that other novel functional nanomaterials may easily be inserted within mesoporous silica as long as there is functionality present on the nanomaterial that imparts an enthalpically favorable interaction between the nanomaterial and the polymer template.

3.5. Acknowledgements

HRTEM work was conducted in the labs of Professor Richard Tilley at the MacDiarmid Institute, Victoria University of Wellington, New Zealand. N. R. Hendricks would like to acknowledge assistance with HRTEM from Alec La Grow and with assistance for synthesizing gold nanoparticles and tris(malonic acid) fullerene from Dr. Ying Lin, postdoctoral fellow from Professor James J. Watkins research group.

3.6. References

(1) Burda, C.; Chen, X.; Narayanan, R.; El-Sayed, M. A. *Chemical Reviews* **2005**, *105*, 1025-1102.

(2) Daniel, M.-C.; Astruc, D. *Chemical Reviews* **2004**, *104*, 293-346.

(3) The Project on Emerging Nanotechnologies http://www.nanotechproject.org/ (accessed Jun 1, 2012).

(4) Usuki, A.; Kojima, Y.; Kawasumi, M.; Okada, A.; Fukushima, Y.; Kurauchi, T.; Kamigaito, O. *Journal of Materials Research* **1993**, *8*, 1179-1184.

(5) Kojima, Y.; Usuki, A.; Kawasumi, M.; Okada, A.; Fukushima, Y.; Kurauchi, T.; Kamigaito, O. *Journal of Materials Research* **1993**, *8*, 1185-1189.

(6) Liu, J.; Tanaka, T.; Sivula, K.; Alivisatos, A. P.; Fréchet, J. M. J. *Journal of the American Chemical Society* **2004**, *126*, 6550-6551.

(7) Gupta, S.; Zhang, Q.; Emrick, T.; Balazs, A. C.; Russell, T. P. *Nature Materials* **2006**, *5*, 229-233.

(8) Lee, J.-Y.; Zhang, Q.; Emrick, T.; Crosby, A. J. *Macromolecules* **2006**, *39*, 7392-7396.

(9) Ryan, K. M.; Mastroianni, A.; Stancil, K. A.; Liu, H.; Alivisatos, A. P. *Nano Letters* **2006**, *6*, 1479-1482.

(10) Gupta, S.; Zhang, Q.; Emrick, T.; Russell, T. P. *Nano Letters* **2006**, *6*, 2066-2069.

(11) Li, Q.; He, J.; Glogowski, E.; Li, X.; Wang, J.; Emrick, T.; Russell, T. P. *Advanced Materials* **2008**, *20*, 1462-1466.

(12) Lin, Y.; Daga, V. K.; Anderson, E. R.; Gido, S. P.; Watkins, J. J. *Journal of the American Chemical Society* **2011**, *133*, 6513-6516.

(13) Daga, V. K.; Anderson, E. R.; Gido, S. P.; Watkins, J. J. *Macromolecules* **2011**, *44*, 6793-6799.

(14) Ziolo, R. F.; Giannelis, E. P.; Weinstein, B. A.; O'Horo, M. P.; Ganguly, B. N.; Mehrotra, V.; Russell, M. W.; Huffman, D. R. *Science* **1992**, *257*, 219-223.

(15) Haruta, M.; Tsubota, S.; Kobayashi, T.; Kageyama, H.; Genet, M. J.; Delmon, B. *Journal of Catalysis* **1993**, *144*, 175-192.

(16) Hayashi, T.; Tanaka, K.; Haruta, M. *Journal of Catalysis* **1998**, *178*, 566–575.

(17) Zanella, R.; Giorgio, S.; Henry, C. R.; Louis, C. *The Journal of Physical Chemistry B* **2002**, *106*, 7634-7642.

(18) Sinha, A. K.; Seelan, S.; Tsubota, S.; Haruta, M. *Angewandte Chemie International Edition* **2004**, *43*, 1546-1548.

(19) Schubert, U. *Polymer International* **2009**, *58*, 317-322.

(20) Tirumala, V. R.; Pai, R. A.; Agarwal, S.; Testa, J. J.; Bhatnagar, G.; Romang, A. H.; Chandler, C.; Gorman, B. P.; Jones, R. L.; Lin, E. K.; Watkins, J. J. *Chemistry of Materials* **2007**, *19*, 5868-5874.

(21) Tirumala, V. R.; Daga, V.; Bosse, A. W.; Romang, A.; Ilavsky, J.; Lin, E. K.; Watkins, J. J. *Macromolecules* **2008**, *41*, 7978-7985.

(22) Tirumala, V. R.; Romang, A.; Agarwal, S.; Lin, E. K.; Watkins, J. J. *Advanced Materials* **2008**, *20*, 1603-1608.

(23) Anderson, E. R.; Daga, V. K.; Gido, S. P.; Watkins, J. J. *Submitted*.

(24) Daga, V. K.; Watkins, J. J. *Macromolecules* **2010**, *43*, 9990-9997.

(25) Brust, M.; Fink, J.; Bethell, D.; Schiffrin, D. J.; Kiely, C. *Journal of the Chemical Society, Chemical Communications* **1995**, 1655.

(26) Lamparth, I.; Hirsch, A. *Journal of the Chemical Society, Chemical Communications* **1994**, *7*, 1727.

(27) Dugan, L. L.; Turetsky, D. M.; Du, C.; Lobner, D.; Wheeler, M.; Almli, C. R.; Shen, C. K.; Luh, T. Y.; Choi, D. W.; Lin, T. S. *Proceedings of the National Academy of Sciences of the United States of America* **1997**, *94*, 9434-9.

(28) Wang, L.; Wang, H.; Hapala, P.; Zhu, L.; Ren, L.; Meng, X.; Lewis, J. P.; Xiao, F.-S. *Journal of Catalysis* **2011**, *281*, 30-39.

(29) Bai, Y.; Yang, H.; Yang, W.; Li, Y.; Sun, C. *Sensors and Actuators B: Chemical* **2007**, *124*, 179-186.

(30) Lu, Q.; Cui, F.; Dong, C.; Hua, Z.; Shi, J. *Optical Materials* **2011**, *33*, 1266-1271.

(31) Sen, T.; Jana, S.; Koner, S.; Patra, A. *The Journal of Physical Chemistry C* **2010**, *114*, 707-714.

(32) Kónya, Z.; Puntes, V. F.; Kiricsi, I.; Zhu, J.; Ager, J. W.; Ko, M. K.; Frei, H.; Alivisatos, P.; Somorjai, G. A. *Chemistry of Materials* **2003**, *15*, 1242-1248.

(33) Budroni, G.; Corma, A. *Angewandte Chemie International Edition* **2006**, *45*, 3328-31.

(34) Gupta, G.; Shah, P. S.; Zhang, X.; Saunders, A. E.; Korgel, B. A.; Johnston, K. P. *Chemistry of Materials* **2005**, *17*, 6728-6738.

(35) Pai, R. A.; Humayun, R.; Schulberg, M. T.; Sengupta, A.; Sun, J.-N.; Watkins, J. J. *Science* **2004**, *303*, 507-510.

(36) Chen, H.-T.; Crosby, T. A.; Park, M.-H.; Nagarajan, S.; Rotello, V. M.; Watkins, J. J. *Journal of Materials Chemistry* **2009**, *19*, 70.

(37) Hendricks, N. R.; Watkins, J. J.; Carter, K. R. *Journal of Materials Chemistry* **2011**, *21*, 14213-14218.

(38) Vogt, B. D.; Pai, R. A.; Lee, H.-J.; Hedden, R. C.; Soles, C. L.; Wu, W.-li; Lin, E. K.; Bauer, B. J.; Watkins, J. J. *Chemistry of Materials* **2005**, *17*, 1398-1408.

(39) Gabaldon, J. P.; Bore, M.; Datye, A. K. *Topics in Catalysis* **2007**, *44*, 253-262.

(40) Philip, D. *Spectrochimica Acta. Part A, Molecular and Biomolecular Spectroscopy* **2008**, *71*, 80-85.

(41) Kroto, H. W.; Heath, J. R.; O'Brien, S. C.; Curl, R. F.; Smalley, R. E. *Nature* **1985**, *318*, 162-163.

(42) Prato, M. *Journal of Materials Chemistry* **1997**, *7*, 1097-1109.

(43) Fullerene Applications http://www.nano-c.com/ (accessed Jun 3, 2012).

(44) Kost, A.; Tutt, L.; Klein, M. B.; Dougherty, T. K.; Elias, W. E. *Optics Letters* **1993**, *18*, 334-336.

(45) McBranch, D. W.; Mattes, B. R.; Koskelo, A.; Robinson, J. M.; Love, S. P. *Proceedings of SPIE* **1994**, *2284*, 15-20.

(46) Zhu, L.; Li, Y.; Wang, J.; Shen, J. *Chemical Physics Letters* **1995**, *239*, 393-398.

(47) Bentivegna, F.; Canva, M.; Georges, P.; Brun, A.; Chaput, F.; Malier, L.; Boilot, J.-P. *Applied Physics Letters* **1993**, *62*, 1721.

(48) Gvishi, R.; Bhawalker, J. D.; Kumar, N. D.; Ruland, G.; Narang, U.; Prasad, P. N.; Reinhardt, B. A. *Chemistry of Materials* **1995**, *7*, 2199-2202.

(49) Hasegawa, I.; Shibusa, K.; Kobayashi, S.; Nonomura, S.; Nitta, S. *Chemistry Letters* **1997**, 995-996.

(50) Hasegawa, I.; Nonomura, S. *Journal of Sol-Gel Science and Technology* **2000**, *19*, 297-300.

(51) Schell, J.; Ohlmann, D.; Hönerlage, B.; Levy, R.; Joucla, M.; Rehspringer, J. L.; Serughetti, J.; Bovier, C. *Carbon* **1998**, *36*, 671-674.

(52) Schell, J.; Brinkmann, D.; Ohlmann, D.; Hönerlage, B.; Levy, R.; Joucla, M.; Rehspringer, J. L.; Serughetti, J.; Bovier, C. *The Journal of Chemical Physics* **1998**, *108*, 8599.

(53) Schell, J.; Ohlmann, D.; Brinkmann, D.; Lévy, R.; Joucla, M.; Rehspringer, J. L.; Hönerlage, B. *The Journal of Chemical Physics* **1999**, *111*, 5929.

(54) Brusatin, G.; Guglielmi, M.; Bozio, R.; Meneghetti, M.; Signorini, R.; Maggini, M.; Scorrano, G.; Prato, M. *Journal of Sol-Gel Science and Technology* **1997**, *8*, 609-613.

(55) Kordatos, K.; Prato, M.; Menna, E.; Scorrano, G.; Maggini, M. *Journal of Sol-Gel Science and Technology* **2001**, *22*, 237-244.

(56) Gunji, T.; Ozawa, M.; Abe, Y.; West, R. *Journal of Sol-Gel Science and Technology* **2001**, *22*, 219-224.

(57) Wu, H.; Lin, Y.; Tang, J.; Gao, D.; Cai, R.; Zhao, D. *Bulletin of the Chemical Society of Japan* **2007**, *80*, 994-998.

(58) Klocek, J.; Henkel, K.; Kolanek, K.; Broczkowska, K.; Schmeisser, D.; Miller, M.; Zschech, E. *Thin Solid Films* **2012**, *520*, 2498-2504.

(59) Kyriakopoulos, J.; Tzirakis, M. D.; Panagiotou, G. D.; Alberti, M. N.; Triantafyllidis, K. S.; Giannakaki, S.; Bourikas, K.; Kordulis, C.; Orfanopoulos, M.; Lycourghiotis, A. *Applied Catalysis B: Environmental* **2012**, *117-118*, 36-48.

(60) Panagiotou, G. D.; Tzirakis, M. D.; Vakros, J.; Loukatzikou, L.; Orfanopoulos, M.; Kordulis, C.; Lycourghiotis, A. *Applied Catalysis A: General* **2010**, *372*, 16-25.

(61) Lin, Y.; Lim, J. A.; Wei, Q.; Mannsfeld, S. C. B.; Briseno, A. L.; Watkins, J. J. *Chemistry of Materials* **2012**, *24*, 622-632.

(62) Leifer, S.; Goodwin, D.; Anderson, M.; Anderson, J. *Physical Review B* **1995**, *51*, 9973-9978.

(63) Borodin, V. I.; Trukhacheva, V. A. *Technical Physics Letters* **2004**, *30*, 598-599.

(64) Le Page, M.; Beau, R.; Duchene, J. *US 3493341* **1970**, 3.

(65) Chiola, V.; Ritsko, J. E.; Vanderpool, C. D. *US 3556725* **1971**, 3.

(66) Beck, J. S. *US 5057296* **1991**, 20.

(67) Kresge, C. T.; Leonowicz, M. E.; Roth, W. J.; Vartuli, J. C.; Beck, J. S. *Nature* **1992**, *359*, 710-712.

(68) Beck, J. S.; Vartuli, J. C.; Roth, W. J.; Leonowicz, M. E.; Kresge, C. T.; Schmitt, K. D.; Chu, C. T. W.; Olson, D. H.; Sheppard, E. W. *Journal of the American Chemical Society* **1992**, *114*, 10834-10843.

(69) Zhao, D.; Feng, J.; Huo, Q.; Melosh, N.; Fredrickson, G. H.; Chmelka, B. F.; Stucky, G. D. *Science* **1998**, *279*, 548-552.

(70) Ryoo, R.; Kim, J. M.; Ko, C. H.; Shin, C. H. *The Journal of Physical Chemistry* **1996**, *100*, 17718-17721.

(71) Brinker, C. J.; Scherer, G. W. *Sol-Gel Science: The Physics and Chemistry of Sol-Gel Processing*; Academic Press: San Diego, 1990.

(72) Ryoo, R.; Jun, S. *The Journal of Physical Chemistry B* **1997**, *101*, 317-320.

(73) Kim, J. M.; Jun, S.; Ryoo, R. *The Journal of Physical Chemistry B* **1999**, *103*, 6200-6205.

(74) Das, D.; Tsai, C.-M.; Cheng, S. *Chemical Communications* **1999**, 473-474.

(75) Xia, Q.-H.; Hidajat, K.; Kawi, S. *Materials Letters* **2000**, *42*, 102-107.

(76) Jun, S.; Kim, J. M.; Ryoo, R.; Ahn, Y.-S.; Han, M.-H. *Microporous and Mesoporous Materials* **2000**, *41*, 119-127.

(77) Coustel, N.; Di Renzo, F.; Fajula, F. *Journal of the Chemical Society, Chemical Communications* **1994**, *41*, 967-968.

(78) McCullen, S. B.; Vartuli, J. C. Method for Stabilizing Synthetic Mesoporous Crystalline Material **1992**, 21.

(79) Koyano, K. A.; Tatsumi, T.; Tanaka, Y.; Nakata, S. *The Journal of Physical Chemistry B* **1997**, *101*, 9436-9440.

(80) Zhao, X. S.; Lu, G. Q. *The Journal of Physical Chemistry B* **1998**, *102*, 1556-1561.

(81) Cassiers, K.; Linssen, T.; Mathieu, M.; Benjelloun, M.; Schrijnemakers, K.; Van Der Voort, P.; Cool, P.; Vansant, E. F. *Chemistry of Materials* **2002**, *14*, 2317-2324.

(82) Silverstein, R. M.; Webster, F. X.; Kiemle, D. J. *Spectrometric Identification of Organic Compounds*; John Wiley & Sons, Inc.: Hoboken, New Jersey, 2005.

(83) Ghosh, G. *Optics Communications* **1999**, *163*, 95-102.

CHAPTER 4

ALTERNATIVE SUBSTRATES FOR MESOPOROUS SILICA

4.1. Introduction

Porous metal oxide materials, specifically porous silicon dioxide, have been researched extensively since the middle part of the 19th century[1]. The research efforts of this time were focused on generating porosity and were not concerned with the ordering of the porosity, i.e. well-ordered pores. The discovery of well-ordered pores, specifically micropores (pore diameters less than 2 nm) and mesopores (pore diameters between 2 nm and 50 nm), would not occur until the early 1990s through the template replication of liquid crystal structures from small surfactant molecules[2,3]. Soon after this template replication procedure was reported, several other uses of template replication were detailed that utilized layered silicates[4,5] and block copolymer surfactants[6–8] as well as continued research with small molecule surfactants[9–11]. While the synthesis of well-ordered micropores and mesopores has led to many advances in applications such as catalysis, separations, and filtration, there was a desire to further compliment the porosity from pores with diameters less than 50 nm with a macropore (pore diameters greater than 50 nm) to enhance properties such as diffusion[12]. This type of dual porosity structure is often referred to as a hierarchical structure due to the two discrete length scales present.

The initial research efforts to generate hierarchically porous structures consisted of two various pore sizes within the mesopore range, which were generated from approaches such as biomemetic synthesis[13], post-synthesis treatments[14], crosslinking reactions[15], and incorporation of synthetic additives[16–18]. The aforementioned approaches

were successful in fabricating dual scale mesoporosity but suffered from a lack of well-ordered porosity. To enhance the pore ordering, sol-gel processing was utilized with various templates, i.e. the combination of templates from small molecules and block copolymer surfactants. Hierarchically porous structures, involving the combination of micropores and mesopores[19,20] as well as micropores and macropores[21–23], have been investigated, however, the focus of this dissertation chapter will be on the combination of mesopores and macropores.

Hierarchically porous silica, fabricated with mesopores and macropores, have typically been fabricated by utilizing sol-gel processing techniques around an interconnecting three-dimensional structure of macro size. Popular templates for the macropore have been polystyrene beads or latex spheres[24–29], emulsions[30–33], polymeric membranes[34–37], biological skeletons[38], and inorganic salts[39]. By incorporating dual scale porosity within the silica template, the material exhibits the collective physical property advantages associated with both of the porosity scales, which is appropriate for many applications, such as separation, filtration, and catalysis. Several of the physical properties afforded to the dual scale porosity are high surface areas (mesopores), enhanced diffusion (macropores), and large pore volumes. To further build upon the advantages associated with dual scale porosity materials, a macropore template based on cellulose materials would be particularly advantageous for applications of filtration and separation.

Cellulose is one of the most abundant organic materials known and is capable of being found naturally or being chemically synthesized. The chemical and physical properties afforded to cellulose arise due to the glucose units that represent the backbone

structure of cellulose. The abundance of hydroxyl groups present on the surface of cellulose allows for intermolecular hydrogen bonding, which is responsible for the semi-crystalline nature of cellulose. The presence of surface hydroxyl groups also makes the cellulose surface hydrophilic and capable of being modified through appropriate condensation reactions. The surface hydroxyl groups will also increase the surface energy such that small molecule surfactants and/or amphiphilic block copolymers should readily adhere to the cellulose surface[40]. The presence of a structure directing template would allow for mesoporous silica to be selective deposited on the surface of the cellulose.

To avoid premature deposition and/or gradients of mesoporous silica on the surface of the cellulose template, the use of a supercritical fluid is required. The benefits of using supercritical fluids have been highlighted within Chapter 1 of this dissertation but several important qualities will quickly be mentioned here. Supercritical fluids offer zero surface tension, gas-like transport properties, complete removal of solvent upon depressurization, and, for the specific case of supercritical carbon dioxide ($scCO_2$), have easily accessible supercritical conditions. Supercritical fluids, i.e. $scCO_2$, has been used previously in a technique titled as "Nanoscale Casting" which replicates templates, such as carbon fiber, with metals and metal oxides to produce porous fibers of the respective material[41–44]. The research presented within this dissertation chapter builds upon the "Nanoscale Casting" method by investigating the fabrication of multi-scale porosity silica through the use of cellulose templates, i.e. filter paper, as the macropore template as well as host for the structure directing template for the mesopores through $scCO_2$ infusion processing.

4.2. Experimental

4.2.1. Materials

Pluronic® F127 (poly(ethylene oxide)-b-poly(propylene oxide)-b-poly(ethylene oxide) (PEO_{106}-PPO_{70}-PEO_{106})) block copolymer (BASF), para-toluene sulfonic acid (99%, Acros Organics), tetraethyl orthosilicate (99.999%, Sigma-Aldrich), ethanol (Fisher Scientific, ACS Grade), de-ionized water (Fisher Scientific, Optima), Whatman Qualitative Filter Paper, Grade No. 1, and carbon dioxide (CO_2, Merriam Graves, bone-dry grade) were used as received without further purification.

4.2.2. Sample Preparation

A solution of Pluronic® F127, typically 10 wt. %, with respect to solution, with para-toluene sulfonic acid (pTSA) at a concentration between 1 wt. % to 15 wt. %, with respect to the Pluronic® template, was prepared using a co-solvent of ethanol and water in a ratio of 1 to 1. A cellulose sample of filter paper, ~ 20 mm x ~ 20 mm, was placed in the Pluronic® solution for ~ 10 minutes prior to being removed and placed in a pre-heated oven of either ~ 80 °C or ~ 120 °C for ~ 30 minutes. The solution of Pluronic® was used for only one cellulose sample.

4.2.3. Supercritical Carbon Dioxide Infusion Process

Mesoporous silica films were generated by exposing the amphiphilic block copolymer coated cellulose filter paper templates to a solution of tetraethyl orthosilicate (TEOS) in supercritical carbon dioxide ($scCO_2$) within a high pressure reactor at 60 °C and 12.41 MPa (1800 psi). The high pressure reactor, ~ 160 mL in volume, was

constructed from two stainless steel opposed ended hubs sealed with a graphite ring (55 ft-lb torque) purchased from Grayloc® Products. Heating bands (Watlow®) were connected to the outside of the reactor walls to control the gas temperature. The top reactor hub was drilled to have 4 ports; one to measure internal pressure, one to measure internal temperature, one for gas inlet, and one for gas outlet. TEOS (350 µL to 500 µL) was directly placed within the high pressure reactor along with 500 µL of reverse osmosis (RO) water prior to sealing, each in separate Vespel® (polyimide) cups. Once the reactor was sealed and heated to a gas temperature of 60 °C, the carbon dioxide (CO_2) was injected with a high pressure syringe pump (ISCO, Model 500 HP) at a rate of 2 - 3 mL/minute. Once the correct pressure was reached, a soak time between 2 hours and 72 hours at 60 °C and 12.41 MPa (1800 psi) was observed. The reactor was then de-pressurized over 20 minutes to room pressure. Samples were exposed thermally degradation procedures at various temperatures (400 °C to 650 °C) for various times with a ramp rate of 1.56 °C/minute in an air environment.

4.2.4. Characterization

Water contact angle measurements were conducted using a VCA Optima surface analysis/goniometry system with a 0.5 µL drop. Attenuated total reflectance Fourier transform infrared (ATR-FT-IR) spectroscopy measurements were collected on a Nicolet 6700 FT-IR spectrometer equipped with a Harrick grazing angle ATR accessory (GATR) with a liquid nitrogen (LN_2) cooled photovoltaic detector (LN-MCT). Field emission scanning electron microscopy (FESEM) was performed on a FEI Magellan FESEM. Transmission electron microscopy (TEM) samples were prepared by grinding the hierarchically porous silica sample via mortar and pestle, suspended with ethanol, and

transferred to a carbon-coated copper grid to be analyzed with a JEOL 2000FX II operating at 200 kV. Thermogravimetric analysis (TGA) was conducted with a DuPont TGA 2950 using a ramp rate of 1.56 °C/minute and holding at a specific elevated temperature for 6 hours under an air environment.

4.3. Results and Discussion

To better understand the bare cellulose filter paper, scanning electron microscopy (SEM) images were acquired and are provided in Figure 4.1. The SEM images showed the expected macroporosity that would be expected for filter paper and the high-resolution image focused on an individual bundle of cellulose filter paper strands showed that the individual strands were tightly packed upon other individual strands of cellulose filter paper. Contact angle measurements were attempted; however, the water droplet was readily absorbed into the bare cellulose filter paper meaning that the surface of the cellulose filter paper was quite hydrophilic.

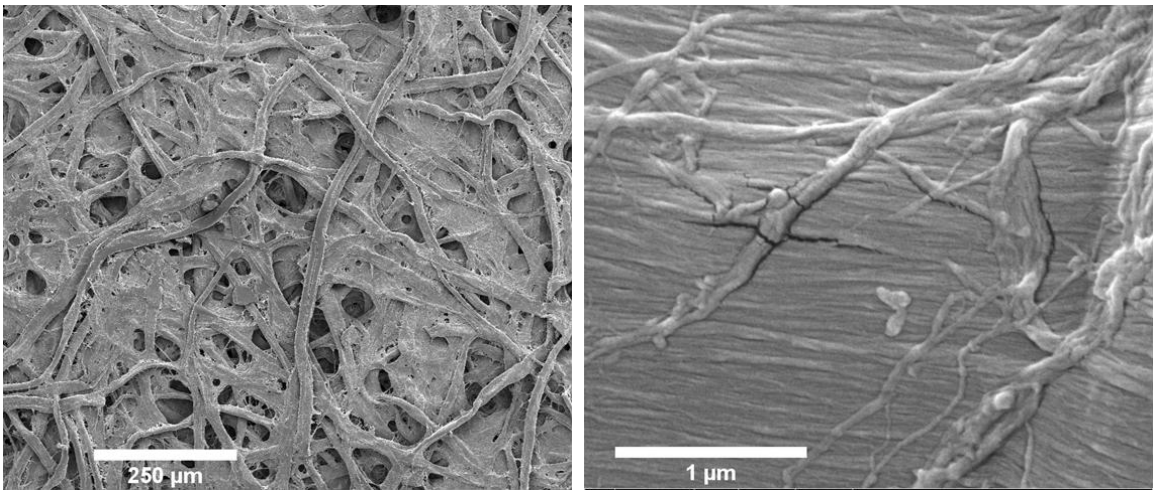

Figure 4.1. SEM evaluation of bare cellulose filter paper. Top-down image (left) and high-resolution image focused on an individual bundle of the cellulose filter paper strands (right).

The cellulose filter paper samples were then coated with Pluronic® F127 solution containing pTSA as the acid catalyst for condensation of the silica precursor and a co-solvent of ethanol and water at a 1 to 1 ratio. The Pluronic® F127 coated cellulose filter paper samples were placed in a pre-heated oven set at 120 °C for 30 minutes to remove the co-solvent. SEM evaluation was performed on the Pluronic® F127 coated cellulose filter paper and the images are provided in Figure 4.2. The coating of the Pluronic® solution does not appear to affect the macroporosity of the cellulose filter paper or show any other defects of any nature to the cellulose filter paper.

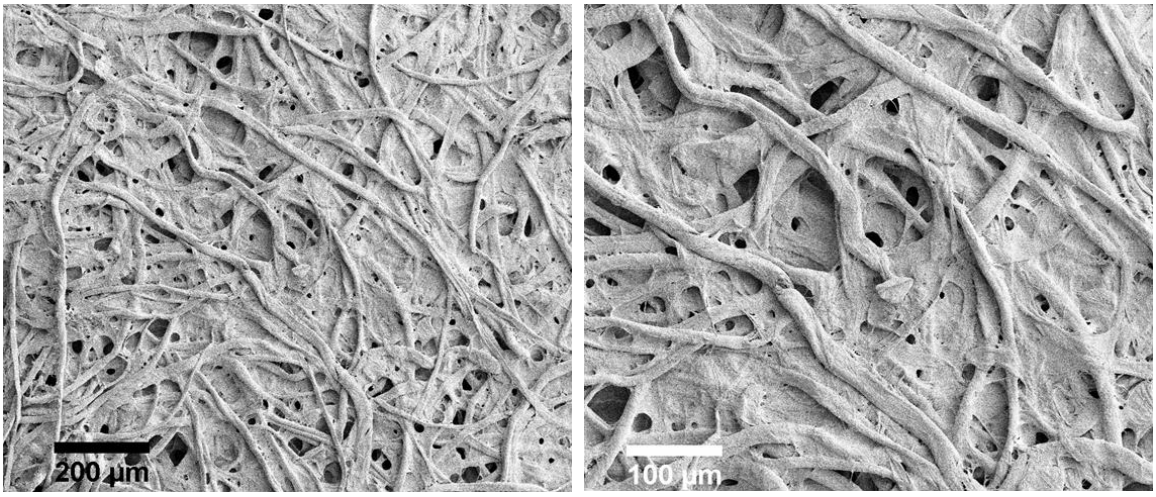

Figure 4.2. SEM evaluation of Pluronic® F127 coated cellulose filter paper.

The initial experiments to condense silica onto the Pluronic® F127 coated cellulose filter paper through the $scCO_2$ infusion processing kept the concentration of pTSA at 15 wt. %, with respect to the Pluronic® template, in the Pluronic® F127 solution. The silica precursor used throughout the $scCO_2$ infusion processing was tetraethyl orthosilicate (TEOS) and, for the initial experiments, was kept at 350 µL along with 350 µL of reverse osmosis (RO) water within the high-pressure reactor. SEM evaluation was performed after the $scCO_2$ infusion processing and the images are

provided in Figure 4.3. From the SEM images, the cellulose filter paper contained severe cracking defects in the regions between the cellulose fibers due to the premature growth of the silica matrix. The cracking defects have been observed before, in thin films samples, and was concluded that the overabundance of acid catalyst present in the sample was supporting the origination of the cracking defects. The amount of pTSA acid catalyst (15 wt. % with respect to the Pluronic® template) in the solution of the Pluronic® template was one of the largest concentrations of acid catalyst ever used for the $scCO_2$ infusion processing, which was a clear reason for the premature growth of the silica matrix. This phenomena is further explained by the abundance of the pTSA molecules at the interface of the Pluronic® coated cellulose filter paper and CO_2 which rapidly hydrolyzes and condenses the TEOS to form undesired dense silica. Another parameter that factors into the origination of the cracking defect was the method of $scCO_2$ infusion processing that was used. By placing the silica precursor directly in the high-pressure reactor prior to introducing CO_2, the silica precursor had an extended resonance time with the sample, at an elevated temperature of 60 °C, to react with the acid catalyst within the sample which promoted the premature growth of the silica matrix. (It should be noted here that the concentration of TEOS silica precursor and the ratio of TEOS to the Pluronic® template have been shown to contribute to the premature growth of the silica matrix[45], however, these parameters were not evaluated within this dissertation section.) The combination of high acid catalyst concentration and extended resonance time between the silica precursor and the sample resulted in the premature growth of the silica network. Approaches that were developed to overcome the cracking defects will be presented at a later time in this section of the dissertation.

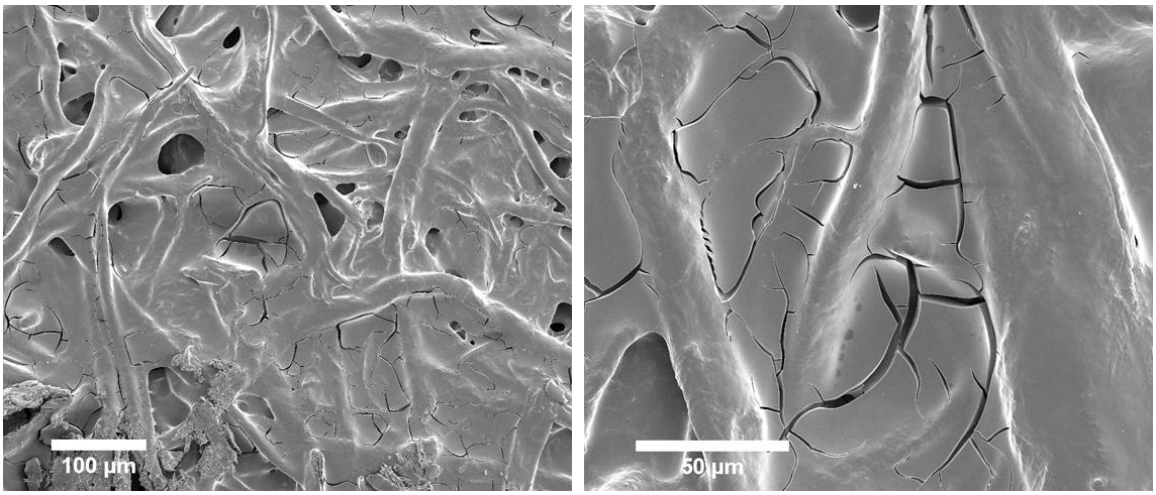

Figure 4.3. SEM evaluation of Pluronic® F127 coated cellulose filter paper after $scCO_2$ infusion processing.

With the establishment of the mesoporous silica network through $scCO_2$ infusion processing, the organic material templates must be removed to generate the hierarchically porous silica material. The method of removing the organic material templates, both the Pluronic® template as well as the cellulose filter paper, was thermal degradation at elevated temperatures, i.e. 400 °C, with a ramp rate of 1.56 °C/minute, and held for 6 hours, in an air environment. Thermogravimetric analysis (TGA) was performed on the organic material templates individually to understand the thermal degradation pathways of each as well as determining the amount of material remaining after thermal degradation. The TGA data is provided in Figure 4.4.

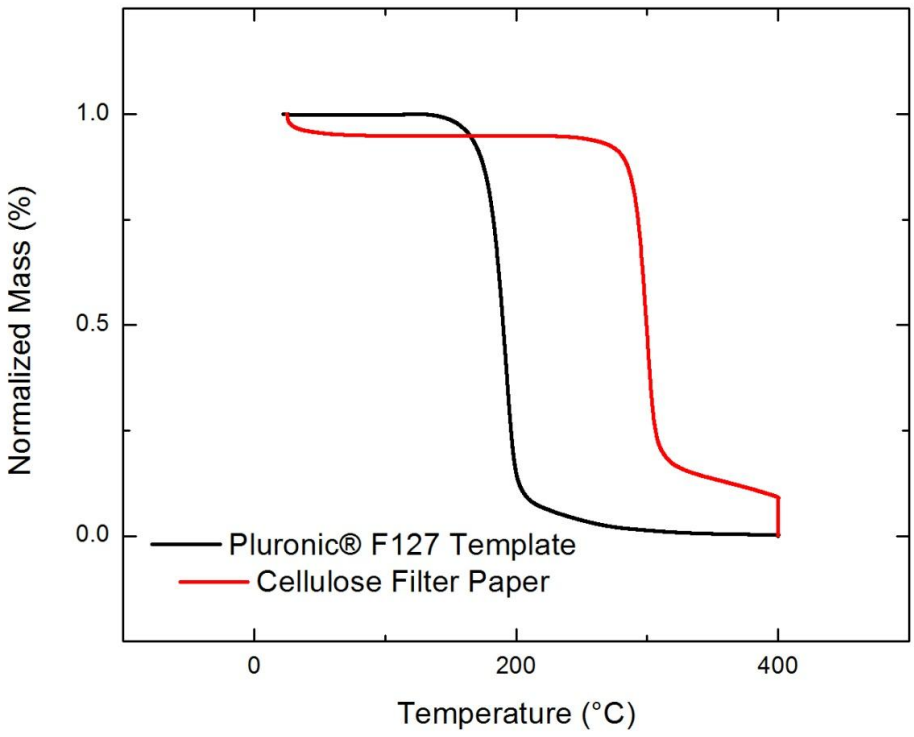

Figure 4.4. TGA data for organic material templates used in the fabrication of hierarchically porous silica materials.

From the TGA data, it showed that the Pluronic® template began to thermally degrade at ~ 165 °C while the cellulose filter paper does not experience degradation until ~ 288 °C. Both of the organic material templates exhibit complete removal under the thermal degradation procedure of 1.56 °C/minute ramp rate to 400 °C, held for 6 hours at 400 °C, and 1.56 °C/minute ramp rate to room temperature. With this knowledge of organic material template thermal degradation, the Pluronic® coated cellulose filter paper samples experiencing $scCO_2$ infusion processing will become hierarchically porous silica materials after undergoing the aforementioned thermal degradation procedure.

To further confirm the removal of the organic material templates, grazing angle attenuated total reflectance Fourier transform infrared (GATR-FT-IR) spectroscopy was

performed and is provided in Figure 4.5. The incorporation of silica was observed after $scCO_2$ infusion processing with the appearance of the asymmetric vibration of the silicon oxygen bond (Si-O) at 1035 cm^{-1}, the asymmetric vibration of the silicon hydroxyl bond (Si-OH) at 950 cm^{-1}, the symmetric vibration of Si-O at 795 cm^{-1}, and the broad peak between 1245 cm^{-1} and 1035 cm^{-1} that was attributed to various degrees of condensation of the silica matrix. Upon thermal degradation at elevated temperatures, the signature peaks corresponding to the organic material templates, i.e. the C-H stretching vibration around 2900 cm^{-1}, were not observable from the GATR-FT-IR spectrum, which equates to the removal of organic material from the hierarchically porous silica material.

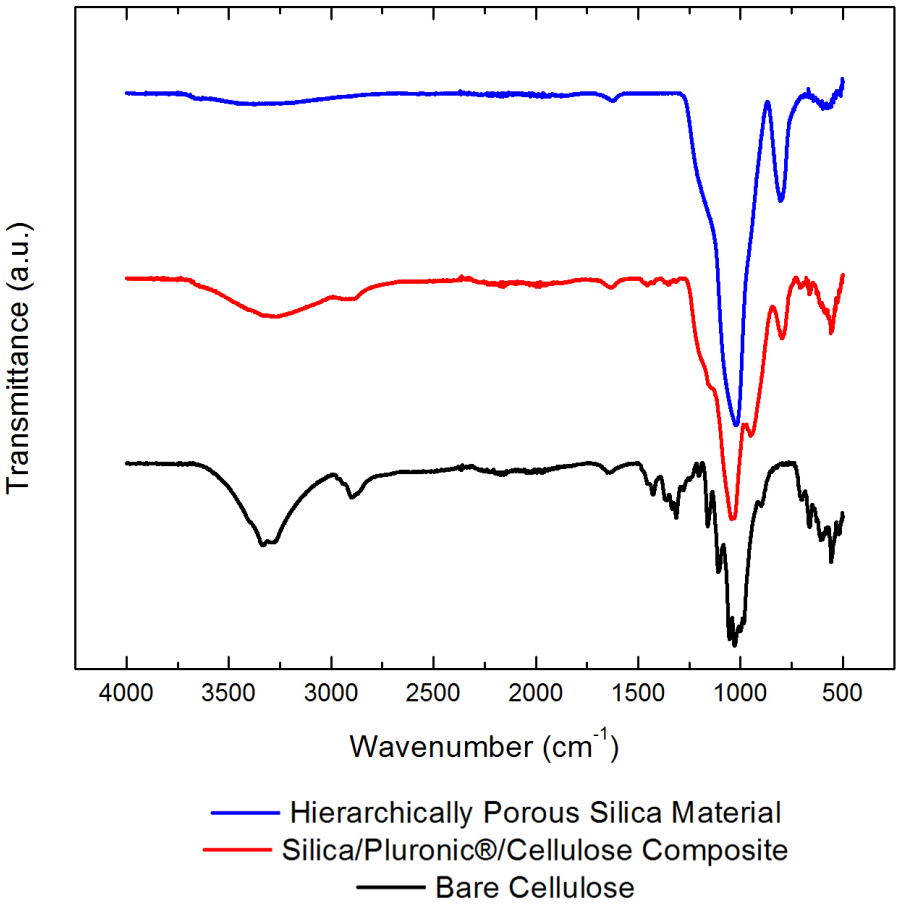

Figure 4.5. Systematic GATR-FT-IR spectroscopy of fabrication of hierarchically porous silica materials from Pluronic® coated cellulose filter paper and $scCO_2$ infusion processing.

To confirm the macroporosity and integrity of the hierarchically porous silica material, SEM was performed and is provided in Figure 4.6. The cracking defects that were observed after the $scCO_2$ infusion processing were present after the thermal degradation procedure and produced collapsed regions in the hierarchically porous silica material due to the shrinkage experienced from the silica material at elevated temperatures. The porosity generated from the presence of cellulose strands was present in the hierarchically porous silica material as well, which is shown in Figure 4.6.

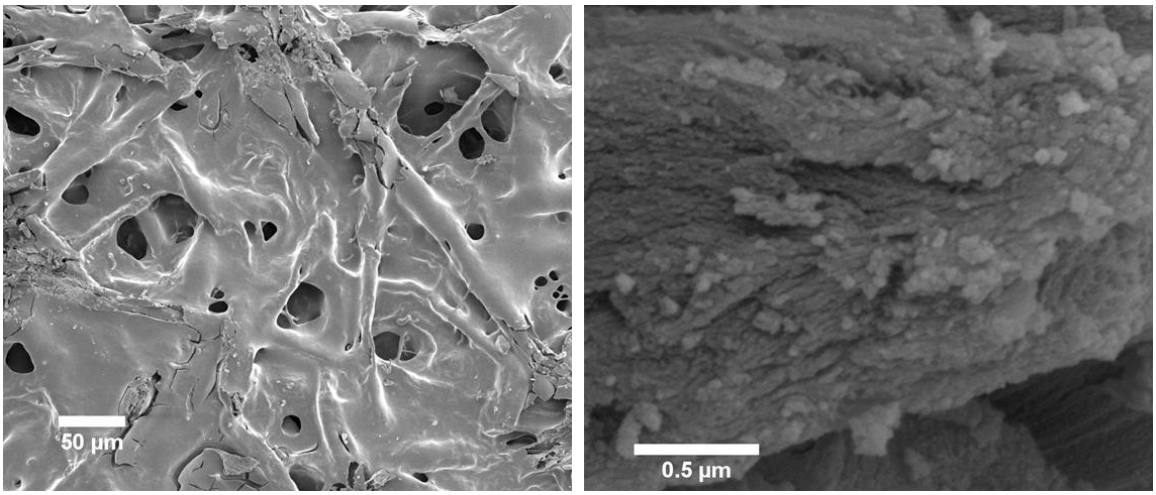

Figure 4.6. SEM evaluation of Pluronic® F127 coated cellulose filter paper after thermal degradation to remove the organic material templates. Top-down image (left) and image focused on porosity generated from the cellulose strands (right).

To confirm the mesoporosity of the hierarchically porous silica material as well as the porosity from the cellulose strands, transmission electron microscopy (TEM) was performed, which is provided in Figure 4.7. From the TEM images, the long-range order of the mesopores from the Pluronic® template was shown as well as the correct morphology of cylinders with a diameter of ~ 4 - 5 nm. The porosity from the cellulose strands was shown as well from the TEM images, which is the porosity that shows irregular organization and does not exhibit an exact morphology, which was shown for the mesoporosity generated from the Pluronic® template. The porosity attributed to the cellulose strands was unexpected and not originally accounted for in the proposal of this research project. With the understanding of mesoporosity being generated from the cellulose strands, as well as the mesoporosity from the Pluronic® template with the macroporosity of the overall cellulose filter paper structure, the hierarchically porous silica material may be considered a tri-modal porous structure.

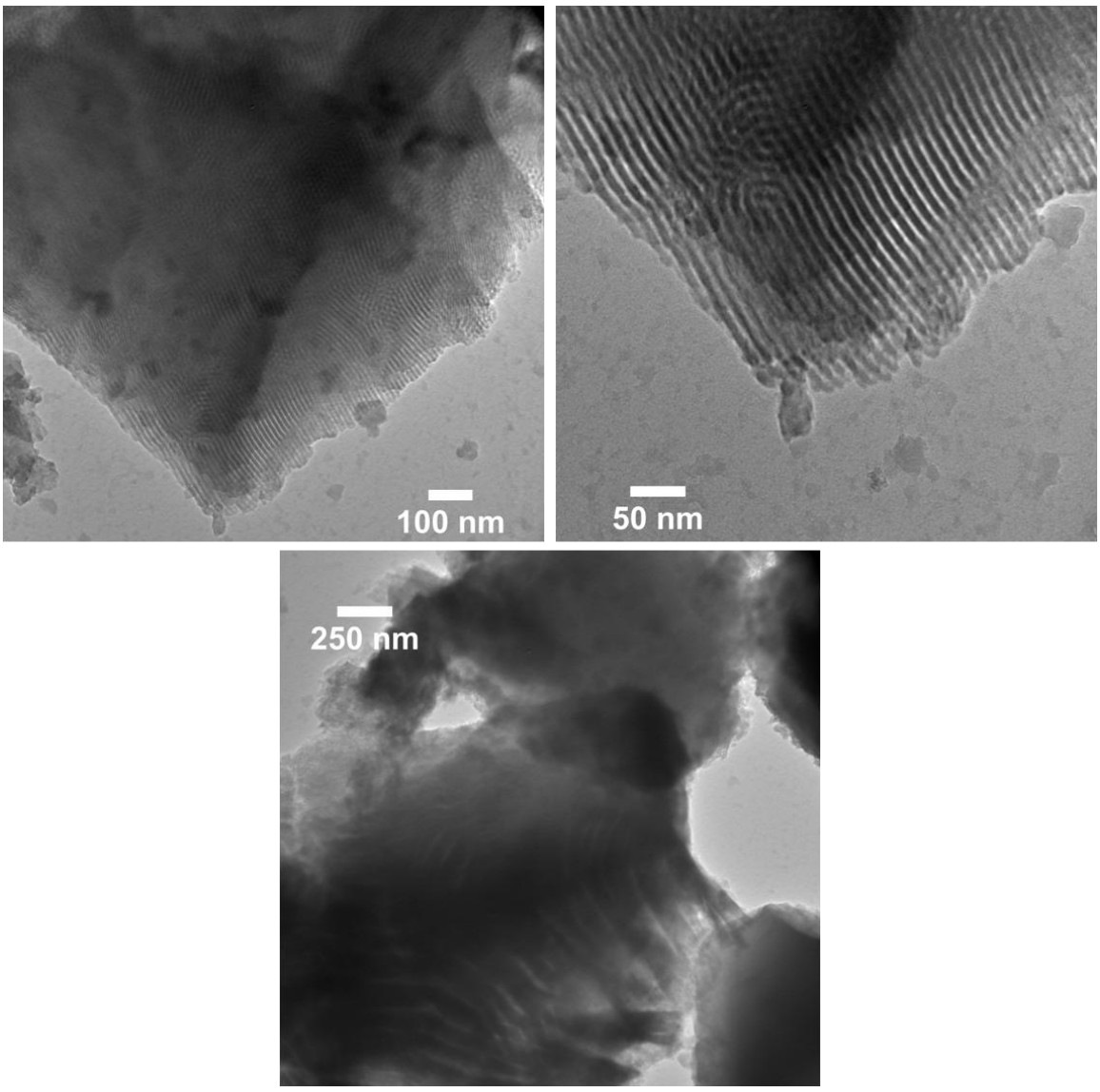

Figure 4.7. TEM images of mesoporosity generated from the Pluronic® template (upper two images) and the porosity generated from the cellulose strands (bottom image).

The reaction time for the $scCO_2$ infusion processing was adjusted for various times of 2, 5, 15, and 72 hours. The evaluation of the hierarchically porous silica materials by SEM and TEM showed that the cracking defects were persistent throughout the various reaction times and that the mesoporosity generated by the Pluronic® template, the cellulose bundles, and the cellulose strands were not dependent on the reaction times either.

From the SEM of the Pluronic® F127 coated cellulose filter paper after $scCO_2$ infusion processing, severe cracking defects were observed and accounted for by the premature condensation of TEOS into silica due to the high concentration of pTSA acid catalyst (~ 15 wt. % with respect to the Pluronic® template). To reduce the amount of cracking present on the cellulose filter paper after $scCO_2$ infusion processing, various concentrations of pTSA (with respect to the Pluronic® template) in the Pluronic® solution were attempted, with typical concentrations being less than 15 wt. %. The presence of the cracking defects were reduced by decreasing the pTSA concentration. Cracking issues equivalent to the cracking issues shown from the 15 wt. % pTSA were observed for Pluronic® solutions containing 10 wt. %, 5 wt. %, and 3 wt. % pTSA with respect to Pluronic® template. When the concentration of the pTSA was adjusted to 1 wt. %, with respect to the Pluronic® template, the cracking present within the sample was significantly reduced, as shown in Figure 4.8.

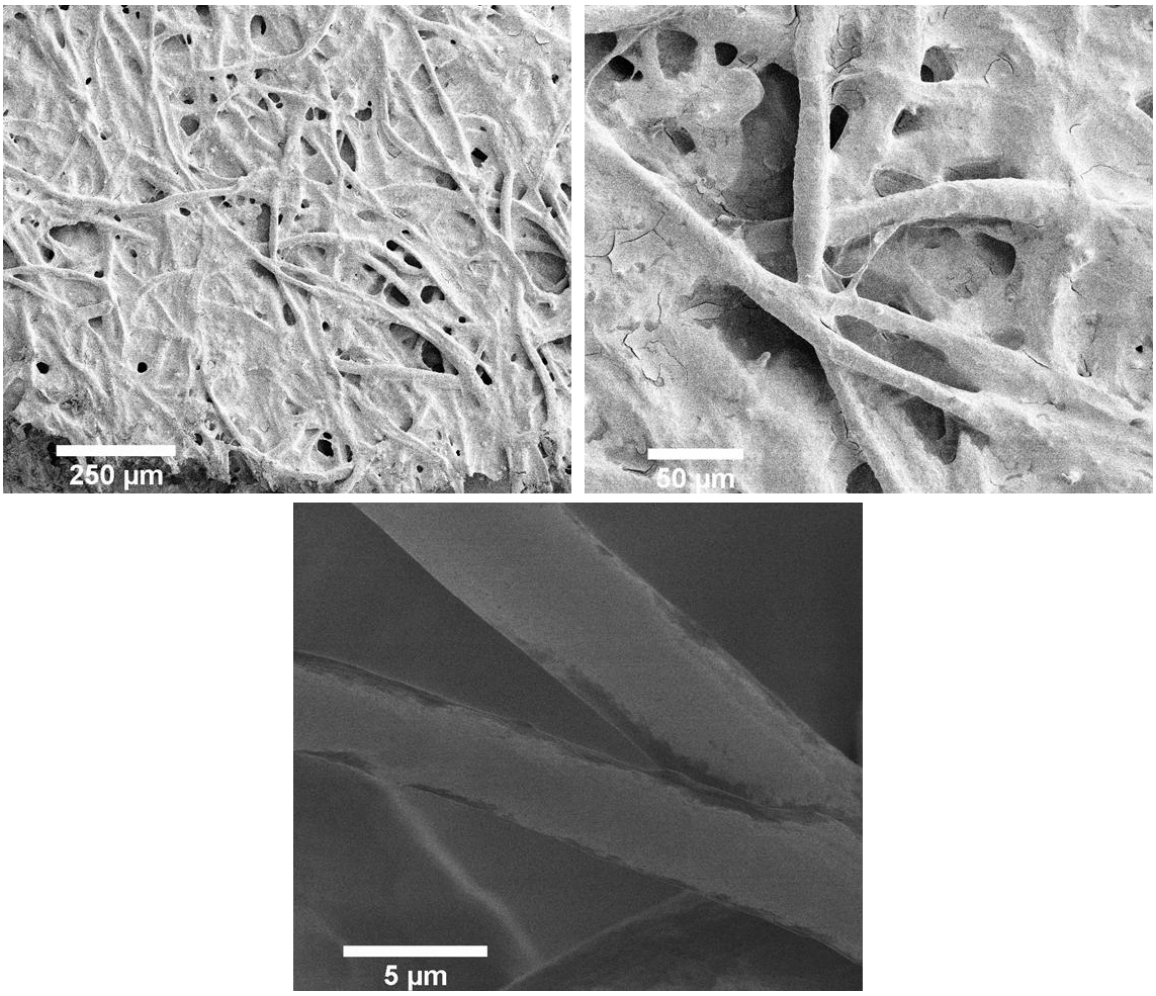

Figure 4.8. SEM evaluation of Pluronic® F127 coated cellulose filter paper with 1 wt. % pTSA, with respect to Pluronic® template, after $scCO_2$ infusion processing.

To confirm the structure of the Pluronic® coated cellulose filter paper, SEM was performed after the thermal degradation procedure and the SEM images are provided in Figure 4.9. The hierarchically porous silica material appeared to be replicated quite well, specifically the bundles of cellulose strands, without severe cracking defects. However, several cracking defects were observed between the bundles of cellulose strands due to the reduced amounts of silica condensation from the minimal amount of pTSA acid catalyst present. It was observed that as the amount of the acid catalyst was reduced, the amount of silica condensed was reduced as well. The lack of premature hydrolysis and

condensation of silica precursor, as well as the shrinkage observed at elevated temperatures from the thermal degradation procedure, would lead to an extremely susceptible area for cracking defects to generate.

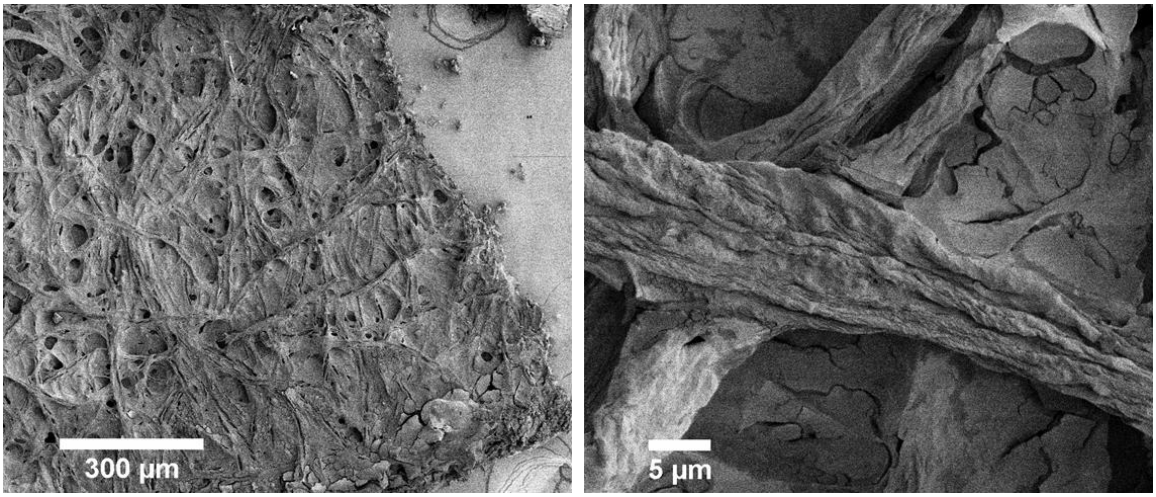

Figure 4.9. SEM evaluation of Pluronic® F127 coated cellulose filter paper containing 1 wt. % pTSA, with respect to Pluronic® template, after thermal degradation to remove the organic material templates

TEM images were acquired to determine the mesoporosity of the hierarchically porous silica material after performing the thermal degradation procedure. The TEM images are provided in Figure 4.10. The porosity generated from the cellulose whiskers, part of the crystalline structure of cellulose, had a diameter that was less than the diameter expected from the Pluronic® template as well as inherent roughness that was not observed in the porosity generated from the Pluronic® template. The mesoporosity from the Pluronic® template has the expected diameter of 4 - 5 nm and the expected cylindrical morphology with the exception of long-range order. The lack of long-range may be contributed to several sources such as the pTSA acid catalyst ordering the Pluronic® template and the lack of TEOS conversion to silica due to the low concentration of pTSA acid catalyst. The ordering of the Pluronic template may be

effected from the presence of the acid catalyst, which, at a concentration of 1 wt. %, may not be sufficient to increase the order of the Pluronic® template. The low concentration of pTSA acid catalyst may also not hydrolyze and condense the silica precursor of TEOS to silica as quickly such that the TEOS will not be able to influence the ordering of the Pluronic® template as well when compared to higher concentrations of pTSA acid catalyst. It should also be noted that the rate of hydrolysis for the conversion of TEOS to silicic acid increases in acid catalysts while the condensation reaction is slightly effected[46]. The presence of the silicic acid with four hydroxyl groups is expected to increase the order of Pluronic® template due to the selective hydrogen bonding between the poly(ethylene oxide) (PEO) segment of the Pluronic® template and the hydroxyl groups of the silicic acid, which is similar to previous research from the Watkins' research group[47]. The reduced concentration of pTSA may not hydrolyze the TEOS molecules as rapidly prior to condensation of the silicic acid to silica when compared to higher concentrations of pTSA therefore reducing the long-range order of the Pluronic® template.

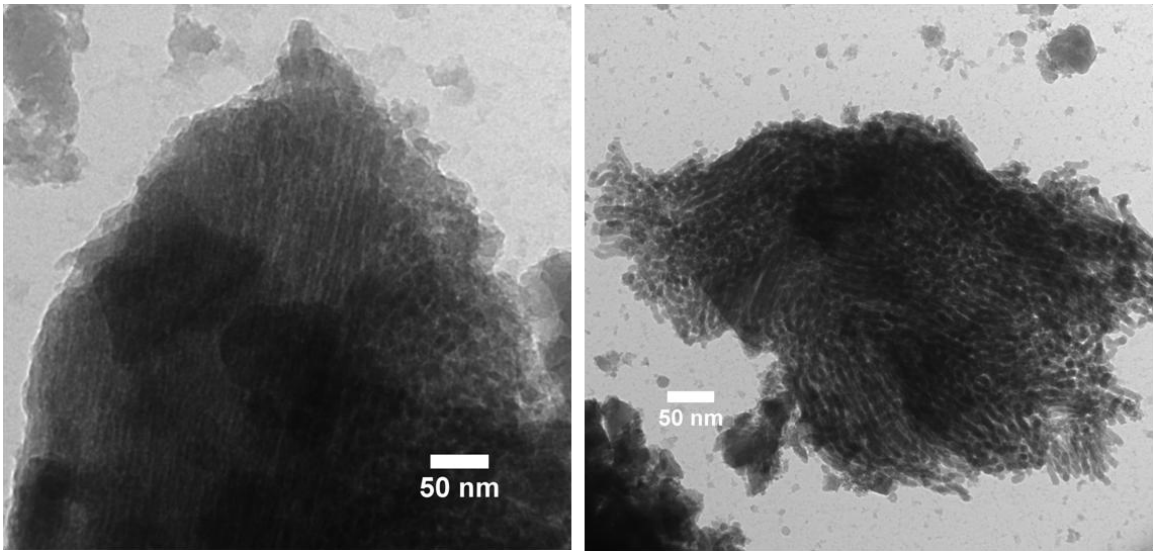

Figure 4.10. TEM images of mesoporosity generated from the cellulose strands (left) and porosity from the Pluronic® template (right).

Another method to reduce the premature deposition of silica through the $scCO_2$ infusion processing was to introduce the silica precursor to the reactor through a direct injection method rather than simply placing the silica precursor within the reactor from the beginning of the reaction. By reducing the exposure time of the TEOS silica precursor to the Pluronic® coated cellulose filter paper, the premature growth of the silica matrix was drastically reduced. Characteristic SEM images of Pluronic® coated cellulose filter paper after $scCO_2$ infusion processing with varying concentrations of pTSA acid catalyst are provided in Figure 4.11. The evidence of cracking from the premature growth of the silica network was absent from the direct injection method of $scCO_2$ infusion processing using 1 wt. % pTSA while the cracking defect were evident for the 3 wt. %, 6 wt. %, and 10 wt. % pTSA concentrations. When comparing the cracking defects present for the Pluronic® coated cellulose filter paper samples, with concentrations of pTSA greater than 1 wt. % were present, between the two $scCO_2$ infusion processing methods, placement of TEOS within the high-pressure reactor and direct injection of TEOS, the cracking defects in the $scCO_2$ infusion processing with direct injection were greatly reduced in number and severity.

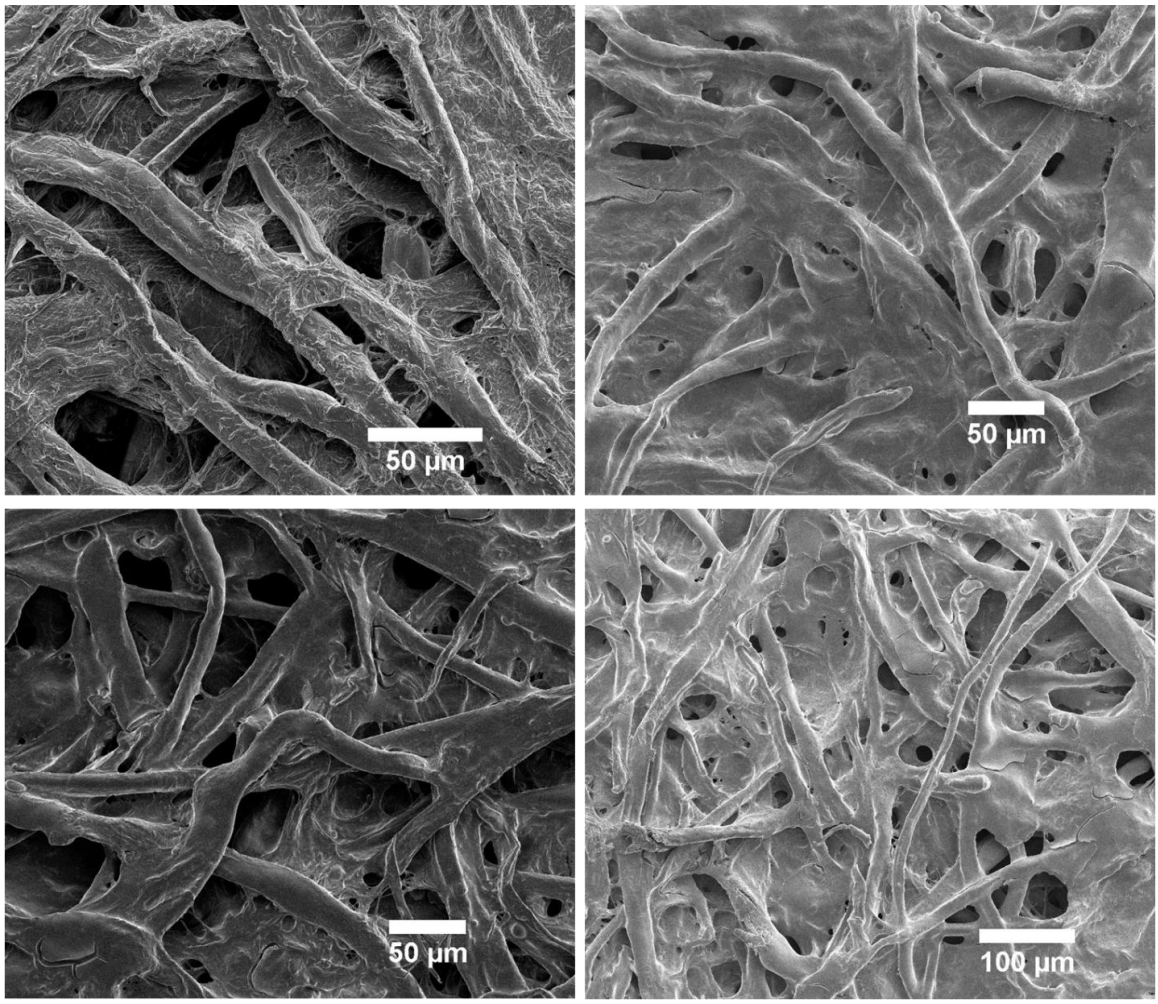

Figure 4.11. Various concentrations of pTSA acid catalyst (clockwise from top right image: 1 wt. %, 3 wt. %, 6 wt. %, and 10 wt. %, with respect to the Pluronic® template) after $scCO_2$ infusion processing using the direct injection of the TEOS silica precursor with the CO_2 method.

The Pluronic® coated cellulose filter paper samples that experienced the direct injection method of $scCO_2$ infusion processing underwent the typical thermal degradation procedure of 1.56 °C/minute ramp rate to 650 °C, held at 650 °C for 6 hours, and 1.56 °C/minute ramp rate to room temperature. The SEM images, provided in Figure 4.12, show that the cracking defects present after $scCO_2$ infusion processing were present after the thermal degradation procedure, where the severity of the cracking defects increased with increased concentrations of pTSA acid catalyst. To ensure the absence of cracking

defects, the combination of 1 wt. % pTSA acid catalyst concentration and the direct injection method of $scCO_2$ infusion processing was determined to be the appropriate fabrication method, however, at the expense of long-range order within the Pluronic® template.

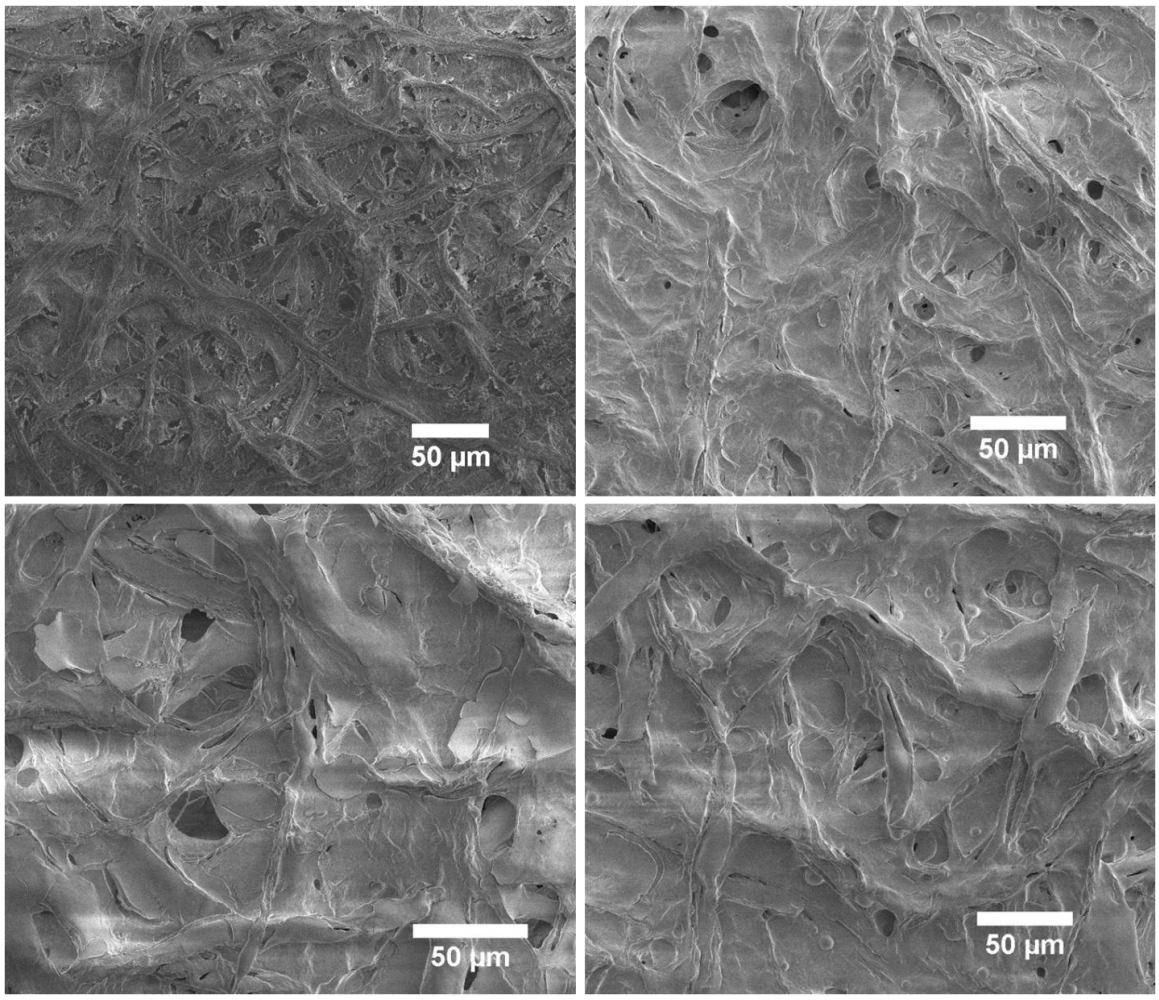

Figure 4.12. Various concentrations of pTSA acid catalyst (clockwise from top right image: 1 wt. %, 3 wt. %, 6 wt. %, and 10 wt. %, with respect to the Pluronic® template) after undergoing the thermal degradation procedure of 1.56 °C/minute ramp rate to 650 °C, held at 650 °C for 6 hours.

From the TGA data presented in Figure 4.4, a significant difference between the onset of degradation for the organic material templates of Pluronic® and cellulose filter paper was observed and the hypothesis of selectively degrading the Pluronic® template,

while maintaining the cellulose filter paper template, was proposed. The thermal degradation procedure required to degrade the Pluronic® template while keeping the cellulose filter paper template intact involved a ramp rate of 1.56 °C/minute to 200 °C, which was above the onset degradation temperature for Pluronic® F127 (~ 165 °C) but below the onset degradation temperature for the cellulose filter paper template (~ 288 °C), hold at 200 °C for 6 hours, and back to room temperature with a ramp rate of 1.56 °C/minute. The TGA data for the reduced temperature thermal degradation procedure is provided in Figure 4.13.

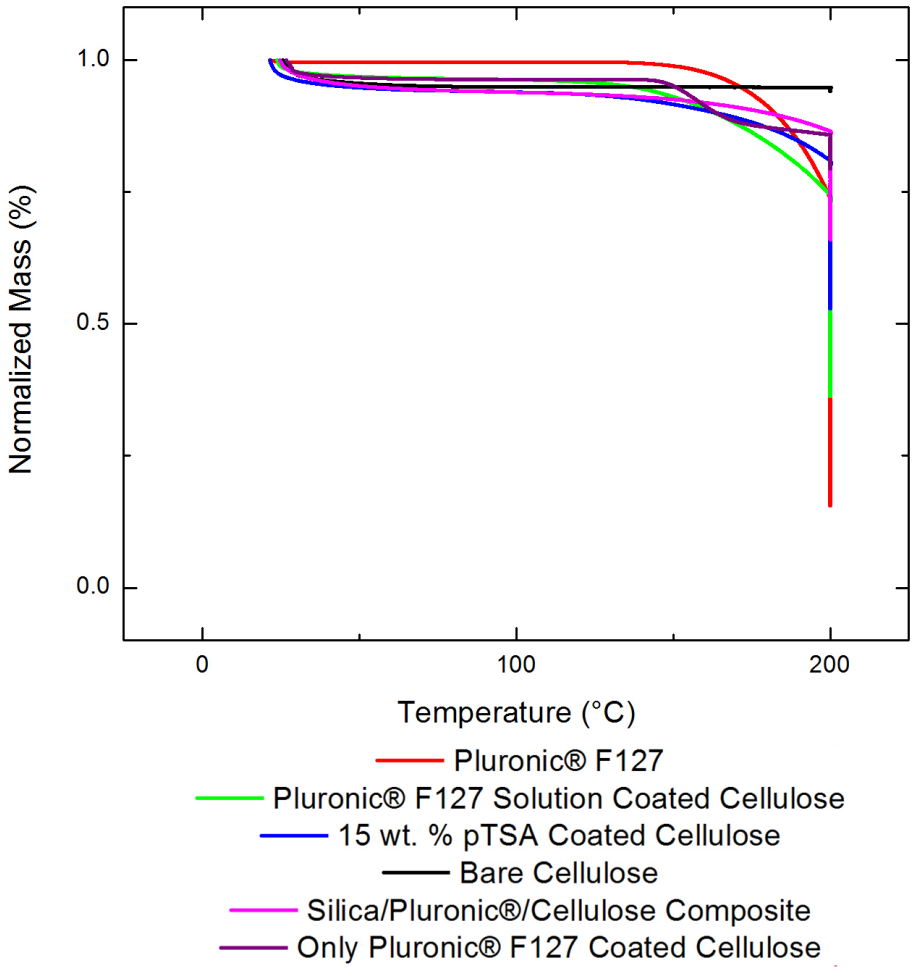

Figure 4.13. TGA data for the 200 °C thermal degradation procedure.

The cellulose filter paper template was extremely robust at 200 °C for prolonged periods of time, however, it was observed that the incorporation of the acid catalyst for the $scCO_2$ infusion processing caused the thermal stability of the cellulose filter paper to be severely hindered. The stability issues of the cellulose filter paper in the presence of strong acids was explained by the acid-catalyzed hydrolysis degradation of cellulose at elevated temperatures, which was confirmed through the literature as being the source of the problem[48,49].

4.4. Conclusions

The use of an alternative substrate, in the form of cellulose filter paper, to host mesoporous silica, generated from $scCO_2$ infusion processing, has been successfully demonstrated. The ability to create hierarchically porous silica materials was afforded from the mesoporosity produced from the Pluronic® amphiphilic block copolymer surfactants as well as the cellulose bundles and cellulose strands present within the filter paper, which complimented the macroporosity of the cellulose filter paper. The Pluronic® material was able to coat the cellulose filter paper without any issues and the $scCO_2$ infusion processing was able to generate mesoporous silica through phase selective chemistries, which was able to facilitate silica precursor materials through the complex geometry of the cellulose filter paper due to the inherent properties afforded to supercritical fluids, i.e. gas-like diffusion. Cracking defects were observed for initial experiments but were alleviated by decreasing the amount of acid catalyst present within the Pluronic® solution as well as introducing the silica precursor through the direct

injection method of $scCO_2$ infusion processing. The resulting hierarchically porous silica material exhibited tri-modal porosity: two scales of mesoporosity from the combination of Pluronic template® and bundles/strands of cellulose present within the cellulose filter paper and one scale of macroporosity from the cellulose filter paper.

4.5. Acknowledgments

This research project is currently being continued by Rohit Kothari, who will guide this research project to further frontiers. Rohit is also acknowledged for his research efforts on the direct injection method of silica precursor during the $scCO_2$ infusion processing.

4.6. References

(1) Graham, T. *Journal of the Chemical Society* **1864**, *17*, 318–327.

(2) Kresge, C. T.; Leonowicz, M. E.; Roth, W. J.; Vartuli, J. C.; Beck, J. S. *Nature* **1992**, *359*, 710–712.

(3) Beck, J. S.; Vartuli, J. C.; Roth, W. J.; Leonowicz, M. E.; Kresge, C. T.; Schmitt, K. D.; Chu, C. T. W.; Olson, D. H.; Sheppard, E. W. *Journal of the American Chemical Society* **1992**, *114*, 10834–10843.

(4) Inagaki, S.; Fukushima, Y.; Kuroda, K. *Journal of the Chemical Society, Chemical Communications* **1993**, 680–682.

(5) Galarneau, A.; Barodawalla, A.; Pinnavaia, T. J. *Nature* **1995**, *374*, 529–531.

(6) Bagshaw, S. A.; Prouzet, E.; Pinnavaia, T. J. *Science* **1995**, *269*, 1242–1244.

(7) Zhao, D.; Feng, J.; Huo, Q.; Melosh, N.; Fredrickson, G. H.; Chmelka, B. F.; Stucky, G. D. *Science* **1998**, *279*, 548–552.

(8) Zhao, D.; Huo, Q.; Feng, J.; Chmelka, B. F.; Stucky, G. D. *Journal of the American Chemical Society* **1998**, *120*, 6024–6036.

(9) Tanev, P. T.; Chibwe, M.; Pinnavaia, T. J. *Nature* **1994**, *368*, 321–323.

(10) Huo, Q.; Margolese, D. I.; Ciesla, U.; Feng, P.; Gier, T. E.; Sieger, P.; Leon, R.; Petroff, P. M.; Schüth, F.; Stucky, G. D. *Nature* **1994**, *368*, 317–321.

(11) Tanev, P. T.; Pinnavaia, T. J. *Science* **1995**, *267*, 865–867.

(12) Tsubaki, N.; Zhang, Y.; Sun, S.; Mori, H.; Yoneyama, Y.; Li, X.; Fujimoto, K. *Catalysis Communications* **2001**, *2*, 311–315.

(13) Bagshaw, S. A. *Chemical Communications* **1999**, 1785–1786.

(14) Yuan, Z.-Y.; Blin, J.-L.; Su, B.-L. *Chemical Communications* **2002**, 504–505.

(15) Sun, J.; Shan, Z.; Maschmeyer, T.; Moulijn, J. A.; Coppens, M.-O. *Chemical Communications* **2001**, 2670–2671.

(16) Wang, X.; Dou, T.; Xiao, Y. *Chemical Communications* **1998**, 1035–1036.

(17) El Haskouri, J.; Ortiz de Zárate, D.; Guillem, C.; Latorre, J.; Caldés, M.; Beltrán, A.; Beltrán, D.; Descalzo, A. B.; Rodríguez-López, G.; Martínez-Máñez, R.; Marcos, M. D.; Amorós, P. *Chemical Communications* **2002**, 330–331.

(18) Okabe, A.; Niki, M.; Fukushima, T.; Aida, T. *Journal of Materials Chemistry* **2005**, *15*, 1329.

(19) Xiao, F.-S. *Catalysis Surveys from Asia* **2004**, *8*, 151–159.

(20) Pérez-Pariente, J.; Díaz, I.; Agúndez, J. *Comptes Rendus Chimie* **2005**, *8*, 569–578.

(21) Huang, L.; Wang, Z.; Sun, J.; Miao, L.; Li, Q.; Yan, Y.; Zhao, D. *Journal of the American Chemical Society* **2000**, *122*, 3530–3531.

(22) Wang, Y. J.; Tang, Y.; Ni, Z.; Hua, W. M.; Yang, W. L.; Wang, X. D.; Tao, W. C.; Gao, Z. *Chemistry Letters* **2000**, 510–511.

(23) Dong, A.; Wang, Y.; Tang, Y.; Zhang, Y.; Ren, N.; Gao, Z. *Advanced Materials* **2002**, *14*, 1506–1510.

(24) Yang, P.; Deng, T.; Zhao, D.; Feng, P.; Pine, D.; Chmelka, B. F.; Whitesides, G. M.; Stucky, G. D. *Science* **1998**, *282*, 2244–2246.

(25) Velev, O. D.; Jede, T. A.; Lobo, R. F.; Lenhoff, A. M. *Chemistry of Materials* **1998**, *10*, 3597–3602.

(26) Antonietti, M.; Berton, B.; Göltner, C.; Hentze, H.-P. *Advanced Materials* **1998**, *10*, 154–159.

(27) Holland, B. T.; Abrams, L.; Stein, A. *Journal of the American Chemical Society* **1999**, *121*, 4308–4309.

(28) Holland, B. T.; Blanford, C. F.; Do, T.; Stein, A. *Chemistry of Materials* **1999**, *11*, 795–805.

(29) Vaudreuil, S.; Bousmina, M.; Kaliaguine, S.; Bonneviot, L. *Advanced Materials* **2001**, *13*, 1310–1312.

(30) Sen, T.; Tiddy, G. J. T.; Casci, J. L.; Anderson, M. W. *Chemical Communications* **2003**, 2182–2183.

(31) Zhang, H.; Hardy, G. C.; Rosseinsky, M. J.; Cooper, A. I. *Advanced Materials* **2003**, *15*, 78–81.

(32) Carn, F.; Colin, A.; Achard, M.-F.; Deleuze, H.; Sellier, E.; Birot, M.; Backov, R. *Journal of Materials Chemistry* **2004**, *14*, 1370–1376.

(33) Sen, T.; Tiddy, G. J. T.; Casci, J. L.; Anderson, M. W. *Microporous and Mesoporous Materials* **2005**, *78*, 255–263.

(34) Caruso, R. A.; Antonietti, M. *Advanced Functional Materials* **2002**, *12*, 307–312.

(35) Huerta, L.; Guillem, C.; Latorre, J.; Beltrán, A.; Beltrán, D.; Amorós, P. *Chemical Communications* **2003**, 1448–1449.

(36) Maekawa, H.; Esquena, J.; Bishop, S.; Solans, C.; Chmelka, B. F. *Advanced Materials* **2003**, *15*, 591–596.

(37) Giunta, P. R.; Washington, R. P.; Campbell, T. D.; Steinbock, O.; Stiegman, A. E. *Angewandte Chemie* **2004**, *43*, 1505–1507.

(38) Davis, S. A.; Burkett, S. L.; Mendelson, N. H.; Mann, S. *Nature* **1997**, *385*, 420–423.

(39) Zhao, D.; Yang, P.; Chmelka, B. F.; Stucky, G. D. *Chemistry of Materials* **1999**, *11*, 1174–1178.

(40) Zhang, Y.; Liu, X.; Huang, J. *ACS Applied Materials & Interfaces* **2011**, *3*, 3272–3275.

(41) Fukushima, Y.; Wakayama, H. *The Journal of Physical Chemistry B* **1999**, *103*, 3062–3064.

(42) Wakayama, H.; Fukushima, Y. *Chemical Communications* **1999**, 391–392.

(43) Wakayama, H.; Fukushima, Y. *Chemistry of Materials* **2000**, *12*, 756–761.

(44) Wakayama, H.; Itahara, H.; Tatsuda, N.; Inagaki, S.; Fukushima, Y. *Chemistry of Materials* **2001**, *13*, 2392–2396.

(45) Vogt, B. D. Diblock Copolymers Swollen with Compressible Fluids: Fundamentals and Applications, 2003, p. 203.

(46) Fardad, M. A. *Journal of Materials Science* **2000**, *35*, 1835–1841.

(47) Daga, V. K.; Watkins, J. J. *Macromolecules* **2010**, *43*, 9990–9997.

(48) Garves, K. *Journal of Wood Chemistry and Technology* **1988**, *8*, 121–134.

(49) Mok, W. S.-L.; Antal, M. J.; Varhegyi, G. *Industrial & Engineering Chemistry Research* **1992**, *31*, 94–100.

CHAPTER 5

PATTERNED NANOPARTICLE COMPOSITE STRUCTURES

5.1. Introduction

The catalysis behind innovations in nanotechnology has been the rapid development of nanoparticles, which are particles that have one or more critical dimensions less than 100 nm. Nanoparticles exhibit a number of interesting properties, such as catalytic, magnetic, mechanical, electrical, and optical properties, that are either not observed in their bulk material counterparts or exhibit enhancement when isolated as a nanoparticle[1]. To further increase the effectiveness of nanoparticles, unique composites are being created. The compliment composite material to the nanoparticles may be in the form of a matrix, i.e. majority, or in the form of a binder, i.e. minority. The matrix materials may be polymeric, either as a homopolymer or as a block copolymer or inorganic templates while the binder materials may be based on either organic or inorganic components.

To incorporate nanoparticles into composites, there are two general approaches that need to be considered, in-situ formation of nanoparticles within the composite or blending pre-synthesized nanoparticles with composite materials. The fabrication of composites from the in-situ formation of nanoparticles may be accomplished by either physical or chemical methods[2]. The use of in-situ reactions often involves harsh processing conditions, which could be detrimental to the composite materials, and/or require post-composite formation processing steps, such as thermal treatment, plasma treatment, or electromagnetic irradiation, to generate the desired nanoparticle. When

creating nanoparticle composites from pre-synthesized nanoparticles, the disadvantages associated with in-situ nanoparticle generation are removed by performing the synthesis of the nanoparticle in a separate reaction prior to incorporation into the composite. The separation of nanoparticle formation from composite formation allows for the nanoparticle to retain advantageous properties, such as crystallinity, without performing additional post-composite formation steps, such as crystallization procedures of either high-temperature thermal treatment and/or hydrothermal treatment.

To take full advantage of the properties afforded to nanoparticle composites, for example conductivity and refractive index, one must have the ability to pattern the composite materials in specific areas and into specific arbitrary geometries. Several lithography methods have been used to pattern nanoparticle polymer composites such as photolithography[3–6], electron beam lithography[7–9], soft lithography (micro molding in capillaries (MIMIC) and micro transfer molding (μTM))[10], and ink-jet printing[11–13] to name a few techniques. The aforementioned lithography techniques are well established and/or extremely novel, which offers specific and unique advantages, but one lithography technique that has garnered tremendous interest from the lithography community, due to the simplistic nature of the technique, is that of nanoimprint lithography (NIL).

NIL offers the capability of providing nanometer resolution, large area patterning, and sufficient throughput. Two general methods of imprint lithography to produce nanoscale features are thermal nanoimprint lithography (TNIL) and ultraviolet-assisted nanoimprint lithography (UV-NIL). The initial use of imprint lithography began in 1995 with the pioneering research of Professor Stephen Chou where TNIL was used to pattern 25 nm features through standard lift-off and metal deposition processing[14–16]. For a more

detailed description of NIL, the reader is directed to the first chapter of this dissertation. Since the preliminary research of imprint lithography in the middle of the 1990s, it has flourished as a lithography technique, not only for standard lift-off and deposition processing but also for the patterning of functional materials such as nanoparticle polymer composites[12,17–23]. An additional aspect of patterning functional materials with imprint lithography will be discussed within this dissertation chapter through a novel patterning concept to create sub-micron structured nanoparticle composite materials.

5.2. Experimental

5.2.1. Materials

Titanium dioxide (TiO_2, anatase phase) nanoparticle (5 - 30 nm average particle size (APS)) dispersions in water (15 wt. %, Nanostructured & Amorphous Materials, Inc.), cerium dioxide (CeO_2) nanoparticle (10 - 20 nm APS) dispersions in water (20 wt. %, Nyacol Nano Technologies, Inc.), Norland Optical Adhesive 60 (NOA60), *N*-methyl-2-pyrrolidone (NMP, ReagentPlus® 99 %, Sigma-Aldrich), methanol (ACS Grade, Fisher Scientific), titanium diisopropoxide (bis-2,4-pentanedionate) (75 % in isopropyl alcohol (2-propanol, IPA), Gelest), (heptadecafluoro-1,1,2,2-tetrahydrodecyl) dimethyl chlorosilane (Gelest), Sylgard 184 silicone elastomer kit (polydimethylsiloxane (PDMS), Ellsworth Adhesive), 1.8 k Mw poly(acrylic acid) (PAA, Aldrich), 45 k Mw polystyrene (PS, Scientific Polymer Products, Inc.), and poly(ethylene terephthalate) (PET) films (Melinex 535, DuPont) were used as received without further purification. Silicon wafers of (100) orientation (p-type, boron dopant) were obtained from University Wafer. Flexible glass was kindly donated from Schott.

5.2.2. Solvent Exchange of Water Based Nanoparticle Dispersions

A standard solvent exchange for the nanoparticle dispersions, from water to more usable solvents, was required. As received nanoparticle dispersions in water were dried under a constant flow of air for prolonged durations of time, typically several days, till the majority of the water was removed. Desired solvents, typically the combination of a polar aprotic solvent and a polar protic solvent, with the usual combination being methanol and NMP respectively, were added to make dispersion concentrations ~ 10 - 30 % nanoparticles by weight, however, lower concentrations were possible as well. Vortexing and ultrasonication of the solvent exchanged nanoparticle dispersions was required and once thoroughly blended, the solvent exchanged nanoparticle dispersions were ready for use. The solvent exchanged nanoparticles dispersions were stable for durations of several months.

5.2.3. Nanoparticle Based Composite Formation

Composite materials comprised of nanoparticles as the matrix material and binder materials based on organic, negative tone photoresist as well as inorganic sol-gel precursors were prepared. Solutions of solvent exchange nanoparticle dispersions and binder materials were made such that concentrations, based on weight percentages, were equal. Various amounts of the equal concentration solutions were mixed with each other to make the final nanoparticle based composite solution.

5.2.4. Sylgard 184 PDMS Mold Fabrication

Silicon master molds were used in the fabrication of replica, i.e. daughter, molds for the NIL procedure. A release layer was applied to the surface of the silicon master

mold to reduce the surface energy and for ease of removal between the master mold and the daughter mold. To apply the release layer, the silicon master molds were rinsed with acetone and IPA then dried under a stream of nitrogen (N_2). The rinsed silicon master molds were then etched in an inductively couple plasma (ICP) etcher with oxygen (O_2) plasma (30 W, 100 mTorr) for 1 minute to generate reactive functional groups on the surface. With the surfaces of the silicon master molds populated with reactive functional groups, the molds were exposed to a 1 vol. %, with respect to the reactor volume, of (heptadecafluoro-1,1,2,2-tetrahydrodecyl) dimethyl chlorosilane at 80 °C for 24 - 48 hours to generate the fluorinated release layer. The silicon master molds with the fluorinated release layer applied were ready for replication.

The replica molds used for the NIL processing were made from Sylgard 184 PDMS and the standard fabrication method of generating Sylgard 184 PDMS replica molds was used. The fabrication of Sylgard 184 PDMS molds were achieved by mixing the two components of the Sylgard 184 elastomer kit, the base and the curing agent, at a ratio of 10 to 1. Mixing was performed with a combination of hand mixing and vortexing. With the two components of the Sylgard 184 elastomer kit thoroughly mixed with one another, the mixture was degassed by using a vacuum oven till the air trapped within the mixture was removed, i.e. the trapped air moved to the surface. The degassed Sylgard 184 PDMS was poured over the fluorinated silicon master molds in a 100 mm polystyrene (PS) petri dish such that 4 mm of Sylgard 184 PDMS covered the silicon master mold. The Sylgard 184 PDMS covered fluorinated silicon master molds were degassed in the vacuum over for an additional 10 minutes. The degassed Sylgard 184 PDMS covered fluorinated silicon master molds was then cured in an 85 °C pre-heated

oven for 3 hours. The Sylgard 184 PDMS mold replica was removed from the oven and allowed to rest at room temperature for ~ 20 minutes prior to separation from the fluorinated silicon master mold, which was aided by the use of a scalpel and a razor blade. At this time, the Sylgard 184 PDMS replica molds were ready for use.

5.2.5. Patterning of Nanoparticle Based Resists

The process for generating nanostructures from the composite materials required the spin-coating of a uniform thin film, on a substrate of either silicon wafer or a flexible substrate (PET or glass), for short durations of time, typically less than 30 seconds, such that residual solvent was present within the nanoparticle based thin film. Spin-coating was performed at 3000 rpm for short periods of time, approximately 10 - 30 seconds (depending on the composite solution), in an inert environment of N_2 which had been purged for approximately 5 - 15 minutes prior to applying the composite solution. After the spin-coating, the Sylgard 184 PDMS mold was placed on the nanoparticle composite thin film and capillary forces brought the Sylgard 184 PDMS mold into intimate contact with the substrate. The nanoparticle composite was then exposed to 365 nm UV-light through the Sylgard 184 PDMS mold to achieve an energy per area of ~ 11.5 - 22.5 J/cm^2. The Sylgard 184 PDMS mold was then removed by hand to yield a sub-micron patterned nanoparticle composite structure.

5.2.6. Characterization

Atomic force microscopy (AFM) images were collected with either a Digital Instruments Nanoscope IIIA or an Asylum MFP3D in tapping mode under ambient conditions. Attenuated total reflectance Fourier transform infrared (ATR-FT-IR)

spectroscopy measurements were collected on a Nicolet 6700 FT-IR spectrometer equipped with a Harrick grazing angle ATR accessory (GATR) with a liquid N_2 cooled photovoltaic detector (LN-MCT). Film thickness measurements were performed with a Veeco Dektak 150 Surface Profilometer and an average of 5 measurements were made for the reported film thickness values. Silicon wafers and silicon master molds were cleaned and/or activated via a Harrick Scientific Corp. plasma cleaner/sterilizer (Model PDC-001) operating at an inductively coupled plasma (ICP) strength of 30 W and 100 mTorr of oxygen (O_2). UV-Vis-NIR spectroscopy was performed on a Shimadzu UV-3600 UV-Vis-NIR Spectrophotometer. Refractive indices and film thickness measurements were measured by variable angle spectroscopic ellipsometry (VASE) with a Sopra GES-5 Variable Angle Spectroscopic Ellipsometer. Modeling of the VASE data was performed with Winelli, commercial software available from Sopra. Field emission scanning electron microscopy (FESEM) was performed on a FEI Magellan FESEM. Photocuring of the nanoparticle composite materials was monitored by photo differential scanning calorimetry (photoDSC) with a TA Instruments Q2000 DSC equipped with a photocalorimeter accessory (PCA).

5.3. Results and Discussion

The first nanoparticle based composite system to be extensively evaluated was comprised of titanium dioxide nanoparticles and an organic, negative tone, photoresist material known as Norland Optical Adhesive 60 (NOA60). To begin the nanostructuring of nanoparticle based composite materials, the properties of the planar films were first evaluated. The surface roughness of the planar films was investigated with AFM. The

reported root-mean-square (RMS) roughness was calculated for an area of 2.5 µm x 2.5 µm dimensions from the AFM height images after data processing (plane leveling, facet leveling, height leveling, and horizontal scar correction) with Gwyddion software. Composites consisting of 50 wt. % titanium dioxide nanoparticles and increasing to 100 wt. %, with increments of 10 wt. %, were analyzed for roughness, which the RMS roughness values are provided in Table 5.1 and the 50 wt. % and the 100 wt. % titanium dioxide nanoparticles AFM images shown in Figure 5.1.

Table 5.1. RMS roughness values for various concentrations (wt. %) of titanium dioxide nanoparticles

wt. % TiO_2 Nanoparticles	50	60	70	80	90	100
RMS Roughness (nm)	5.41	5.10	4.85	4.70	4.97	4.68

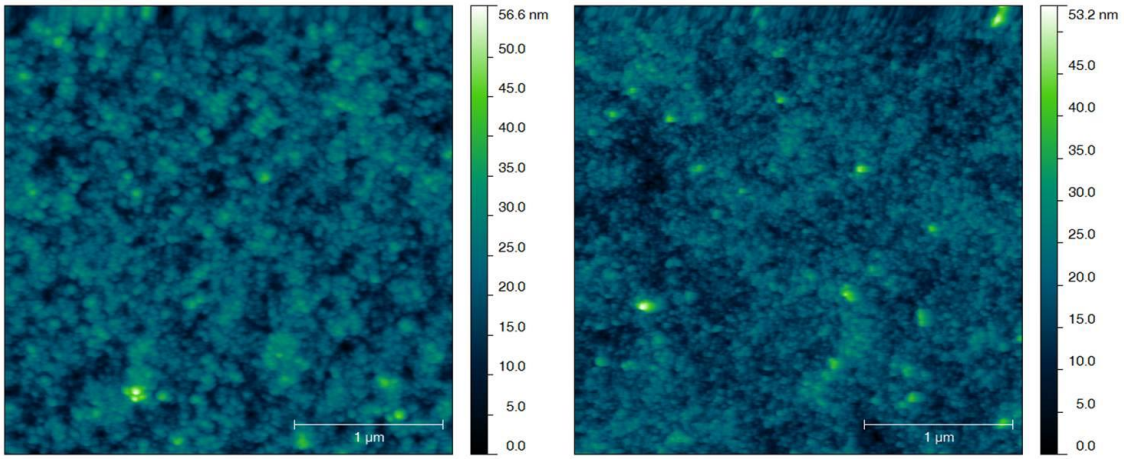

Figure 5.1. AFM height images of 50 wt. % (left) and 100 wt. % (right) of titanium dioxide nanoparticle films.

From the AFM images, it was determined that the RMS roughness of the titanium dioxide nanoparticle composite films was between 4.5 and 5.5 nm and without the presence of large spikes in height variations, which is confirmed in Figure 5.1. For reference, the RMS roughness of a silicon wafer was ~ 0.2 nm while the RMS roughness for a planarized PET film was ~ 5 nm. Additional AFM images for the composite comprised of titanium dioxide nanoparticle and NOA60 are provided in the appendix, Figure S5.1.

The use of pre-synthesized nanoparticles allows for the nanoparticles to impart utility upon the composite material without the composite material experiencing additional, and potentially harsh, processing conditions. One such utility imparted on the composite material was crystallinity. The crystallinity of the composites containing titanium dioxide nanoparticles, of the anatase phase, was evaluated through XRD, which is shown in Figure 5.2.

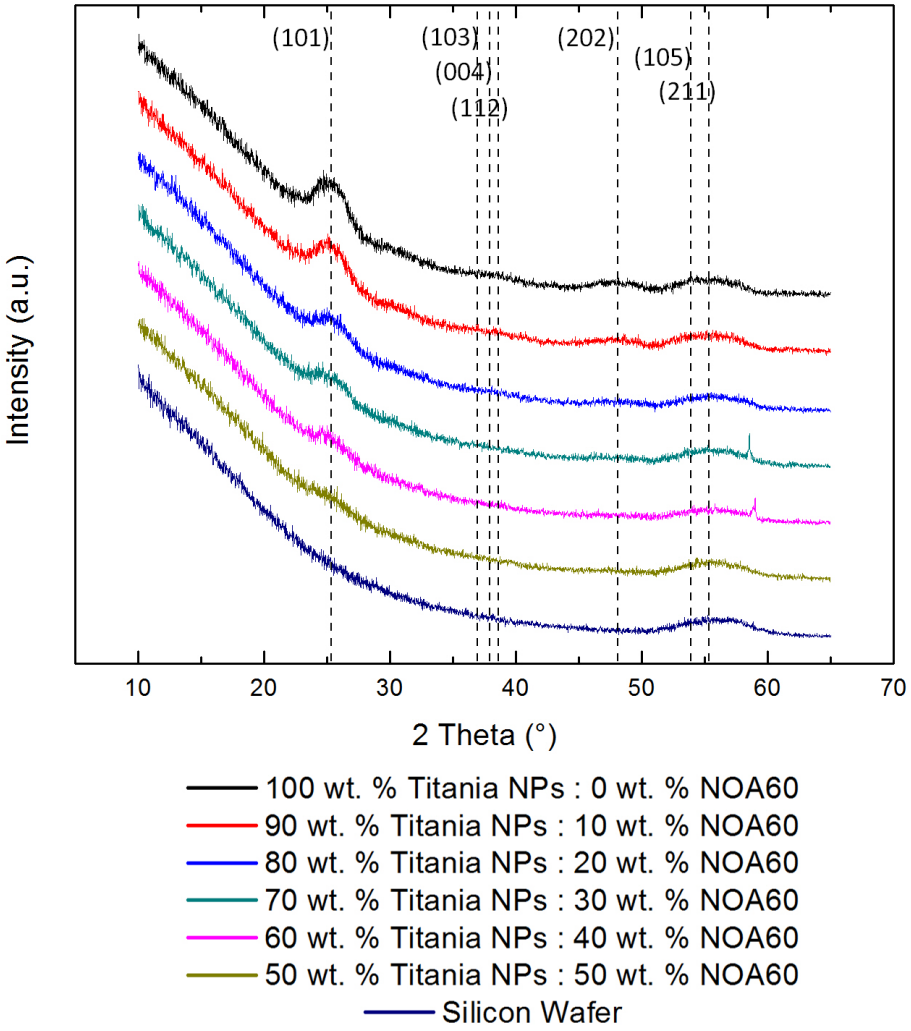

Figure 5.2. XRD of composite materials with various amounts of crystalline titanium dioxide nanoparticles, anatase phase, and NOA60.

The trend observed from XRD was that as more of the crystalline titanium dioxide nanoparticles were incorporated within the composite material, the more prevalent the diffraction peaks for the anatase phase of titanium dioxide became, which was the expected trend.

The photocatalytic properties associated with crystalline titanium dioxide, specifically anatase phase, upon exposure to ultraviolet (UV) light is well known[24].

During the fabrication of composite materials, it was realized that making composites containing organic matter and titanium dioxide nanoparticles, there may be a possibility of photocatalytic degradation of the organic material. To determine if the organic material was present after exposure to 365 nm UV-light, grazing angle attenuated total reflectance Fourier transform infrared (GATR-FT-IR) spectroscopy was performed for the composite materials with varying amounts of titanium dioxide nanoparticles after exposure to 365 nm UV-light for an energy per area of 11.43 J/cm^2 (irradiance power of 12.7 mW/cm^2 for 900 seconds). The proposed chemical structure of the active components for NOA60 materials is provided in Figure 5.3[25–27]. The GATR-FT-IR spectra, provided in Figure 5.4, showed the presence of a carbonyl (C=O) stretching vibration at 1738 cm^{-1} and an ether (C-O) stretching vibration in the 1148 cm^{-1} to 1154 cm^{-1} range, attributed to the NOA60 active components, throughout the composite materials with various concentrations of titanium dioxide nanoparticles.

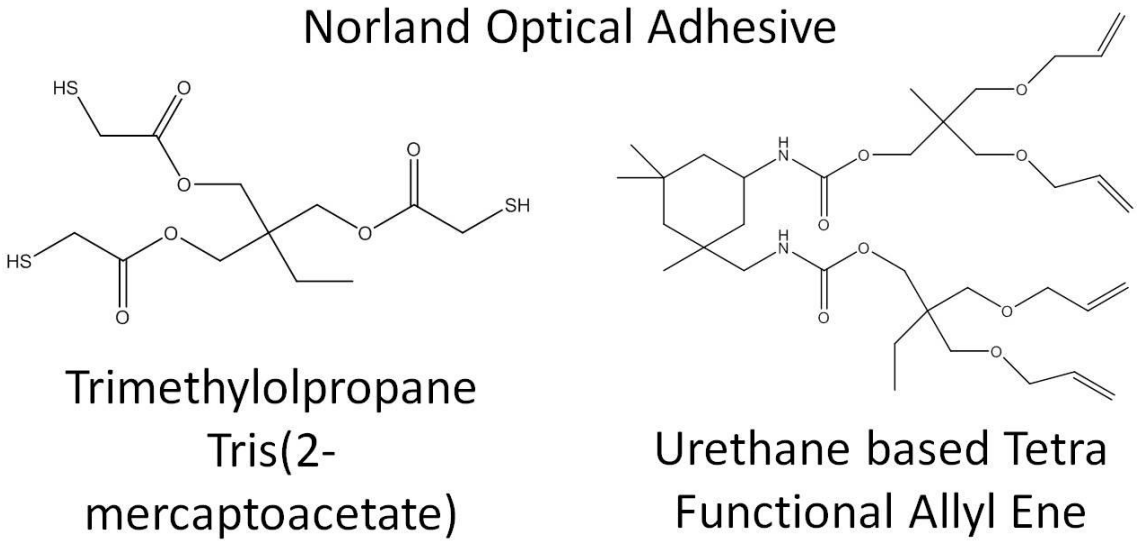

Figure 5.3. Proposed chemical structure of active components within NOA 60 materials.

When the NOA60 photoresist was absent from the composite material, i.e. only titanium dioxide nanoparticles were present, the GATR-FT-IR spectrum showed no sign of either the carbonyl or the ether stretching vibrations attributed to NOA60. The only infrared (IR) signals present for the titanium dioxide nanoparticles was the stretching vibration of the titanium-oxygen bond (Ti-O) at 700 cm^{-1}, carbonyl (C=O) stretching vibration at 1695 cm^{-1} due to acetic acid stabilizing the titanium dioxide nanoparticle, and the hydroxyl stretching vibration from the surface hydroxyl groups (Ti-OH) on the titanium dioxide nanoparticles and hydroxyl group of the acetic acid in the range of 3700 cm^{-1} to 2600 cm^{-1}. From the GATR-FT-IR, it was concluded that the organic photoresist was present throughout the composite film, even after irradiation from 365 nm UV-light, thus the titanium dioxide did not significantly degrade the organic material photocatalytically.

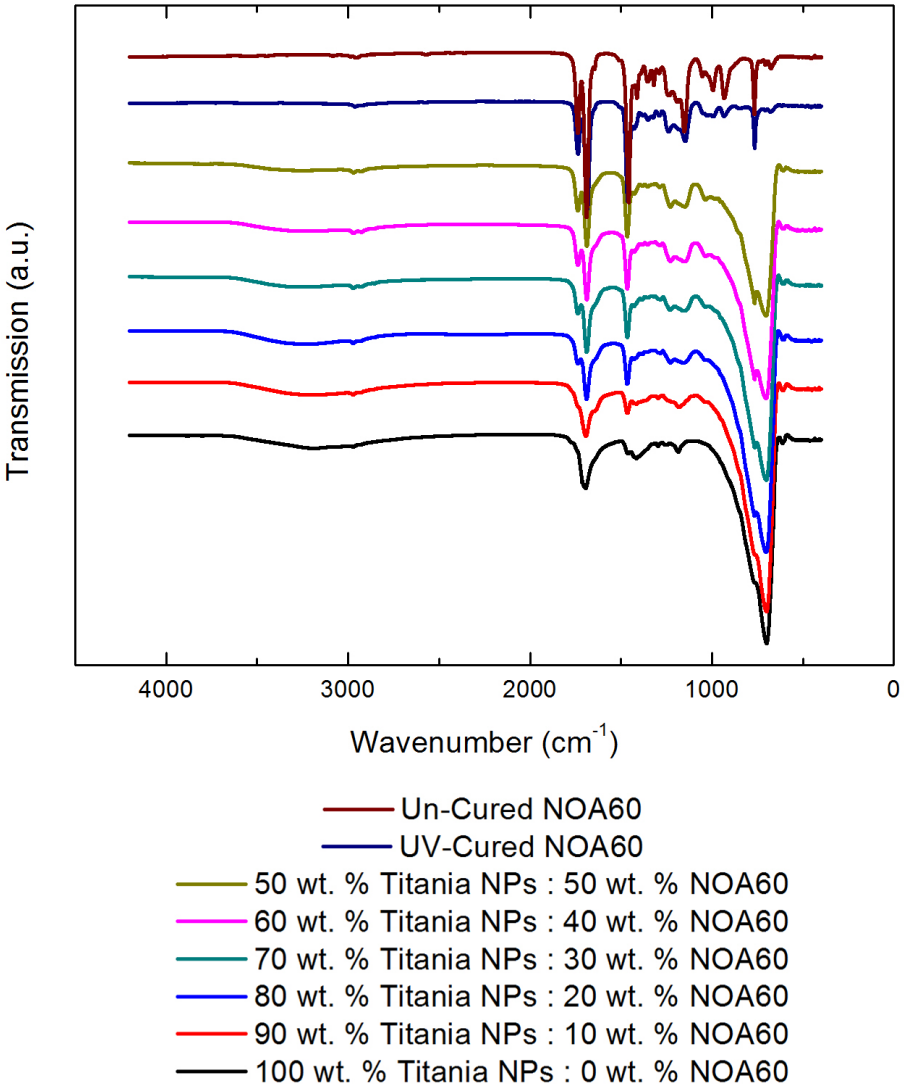

Figure 5.4. GATR-FT-IR spectra of composite materials with various loadings of titanium dioxide nanoparticles after exposure to 365 nm UV-light.

For titanium dioxide to exhibit photocatalytic activity at 365 nm UV-light, the titanium dioxide must absorb ultraviolet light within this region of the electromagnetic spectrum. To confirm the absorption and the transparency of the titanium dioxide / NOA60 composite materials, ultraviolet-visible (UV-Vis) spectroscopy was performed and is shown in Figure 5.5.

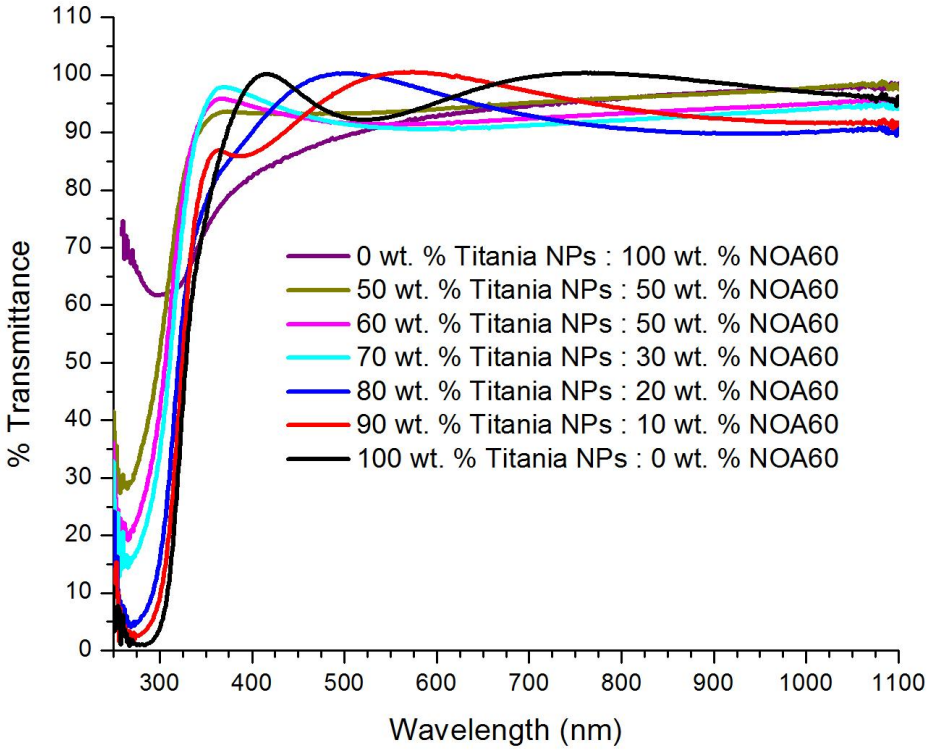

Figure 5.5. UV-Vis spectra for planar composite materials comprised of titanium dioxide and NOA 60 with various concentrations.

From the UV-Vis spectra, it was confirmed that there was a strong absorption of UV-light below 350 nm for the composite materials. As more of the NOA60 was incorporated into the composite material, the transparency below 350 nm improves, which would be expected due to NOA60 having a transparency greater than 60 % below 350 nm. It should be noted here that the variations present within the nanoparticle based composite materials arise due to the thickness variations of the planar films.

To ensure that the NOA60 photoresist was receiving a sufficient amount of 365 nm UV-radiation for crosslinking, photoDSC was performed and is shown in Figure 5.6, with a closer examination of the photoDSC provided in Figure 5.7.

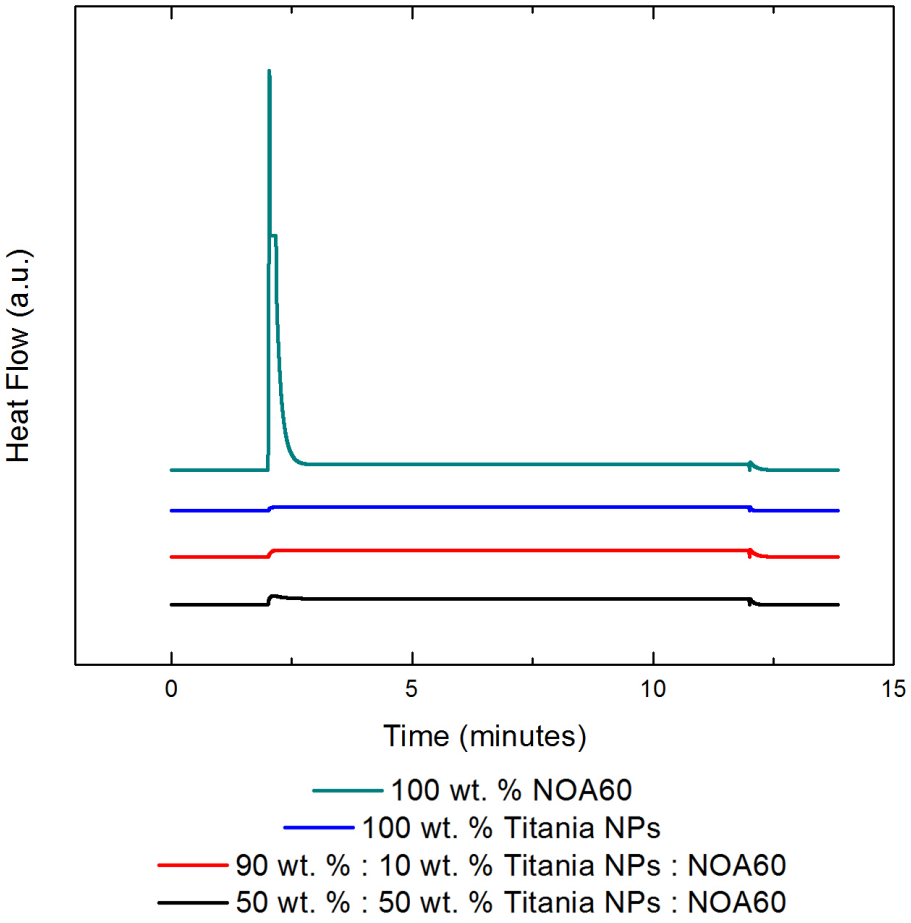

Figure 5.6. PhotoDSC data for composite materials containing titanium dioxide nanoparticles and NOA 60 photoresist.

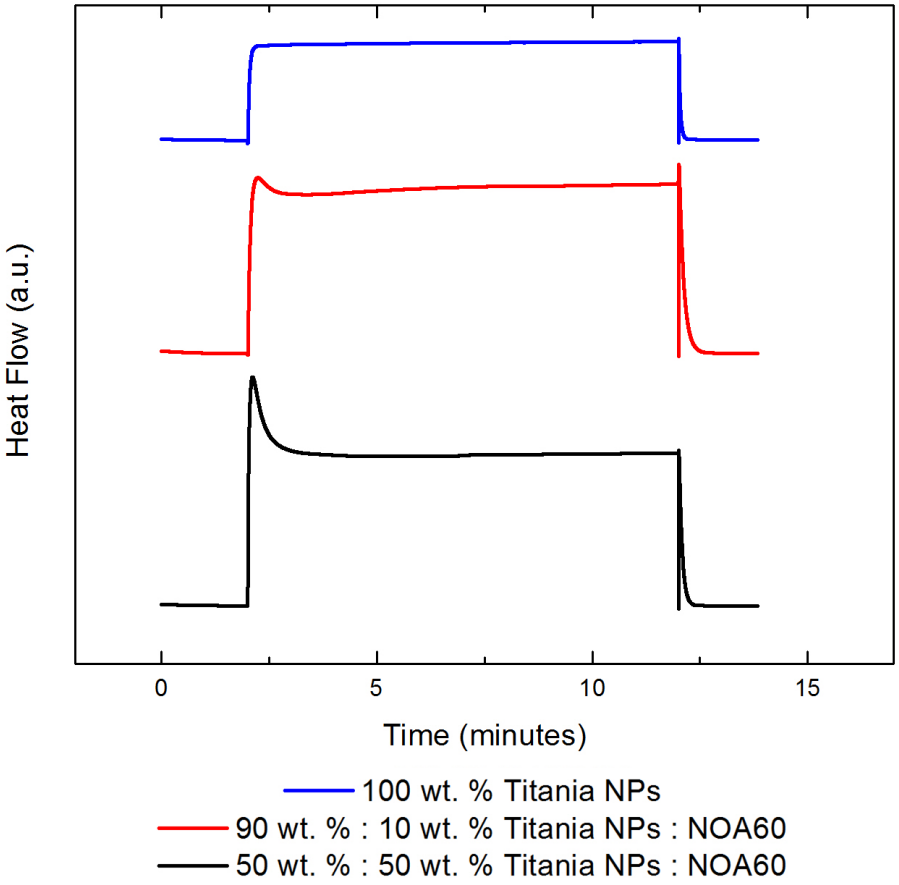

Figure 5.7. Closer examination of photoDSC data for composite materials containing titanium dioxide nanoparticles and NOA 60.

Table 5.2. Specific energy, as calculated from photoDSC, of composite materials containing various concentrations of NOA60.

Composite Material	Specific Energy (J/g)
100 wt. % titanium dioxide nanoparticles / 0 wt. % NOA 60	0.00
90 wt. % titanium dioxide nanoparticles / 10 wt. % NOA 60	1.56
50 wt. % titanium dioxide nanoparticles / 50 wt. % NOA 60	23.15
0 wt. % titanium dioxide nanoparticles / 100 wt. % NOA 60	229.90

From the photoDSC data, it appeared that the photocrosslinking reaction of the NOA60 photoresist was able to be performed, due to the exothermic reaction observed once the

UV-irradiation was initiated, while in the presence of the titanium dioxide nanoparticles, as shown by the specific energies reported in Table 5.2. The heat of reaction, as measured by the photoDSC, showed that as more of the NOA60 was incorporated into the composite material, a greater extent of reaction was observed. As expected, the titanium dioxide nanoparticles, without the NOA60 as a binder material, showed no response to being irradiated by 365 nm UV-light.

The final property that was evaluated for the planar nanoparticle composite materials was the refractive index by spectroscopic ellipsometry (SE), which is shown in Figure 5.8.

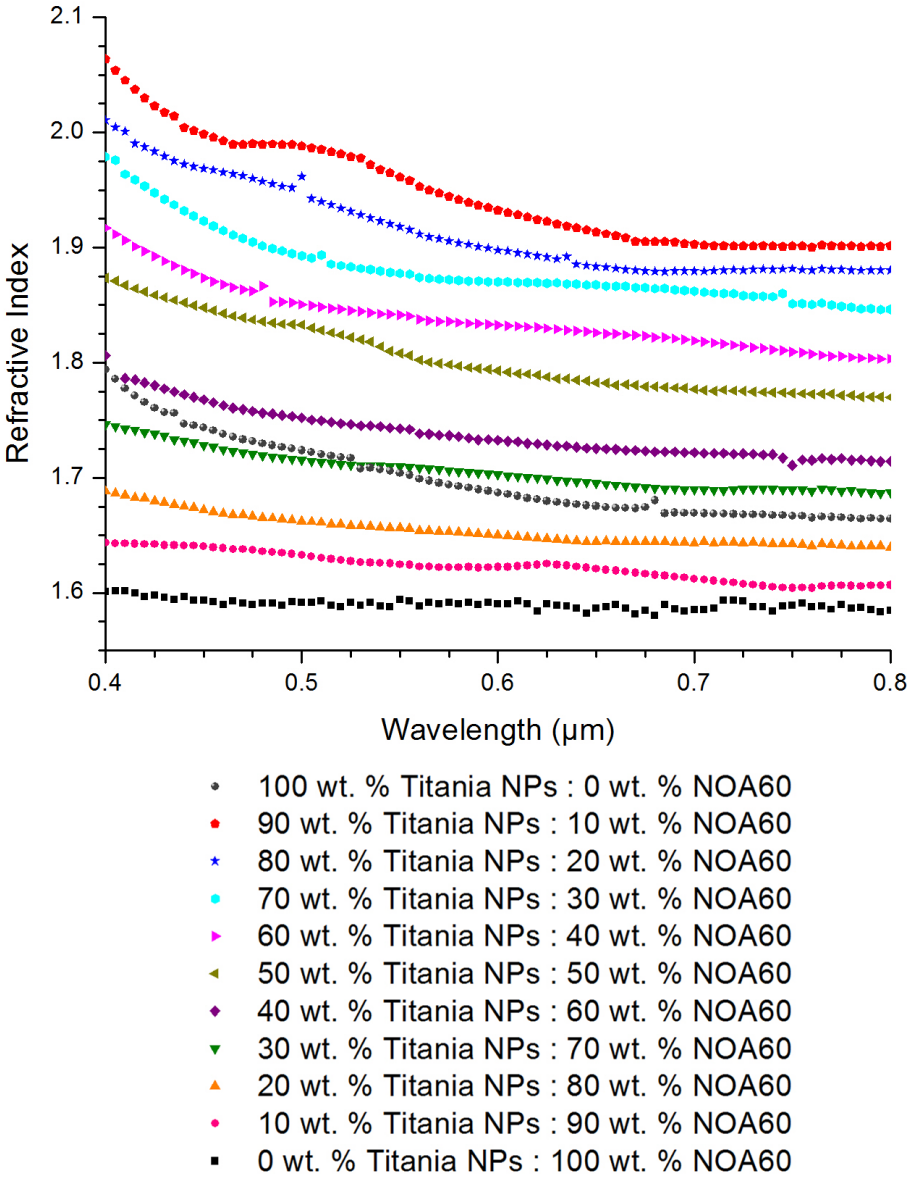

Figure 5.8. Refractive index of titanium dioxide nanoparticle composite materials with various loadings of titanium dioxide nanoparticles measured by spectroscopic ellipsometry.

By using the composite system of titanium dioxide nanoparticles and NOA60 photoresist, the refractive index, at a wavelength of 800 nm, may be tuned within the range of ~ 1.57 for the NOA60 photoresist to ~ 1.92 for the 90 wt. % titanium dioxide / 10 wt. % NOA60 composite material. For reference, the refractive index for pure anatase phase titanium

dioxide was reported as 2.49 at an assumed wavelength of 600 nm[28]. It should also be noted that the refractive index of most materials increases as the wavelength is blueshifted, i.e. a decrease in wavelength, within the visible spectrum. The 100 wt. % titanium dioxide nanoparticle showed a refractive index of 1.67 at 800 nm wavelength, which was lower than the composite material comprised of 90 wt. % titanium dioxide nanoparticles, which has a refractive index of 1.90 at 800 nm wavelength. The reduction in refractive index was due to the porosity of the 100 wt. % titanium dioxide composite material which has air, with a refractive index of ~ 1, as the binder/filler material. For the 90 wt. % titanium dioxide nanoparticle composite, the filler/binder material was 10 wt. % NOA60, which has a refractive index of 1.57 at a wavelength of 800 nm, which was filling the porosity present within the nanoparticle based composite film thus increasing the refractive index of the composite material. It should be noted here that the composite material comprised of 90 wt. % titanium dioxide nanoparticles has a volume fraction of ~ 66 %, which was slightly lower than the theoretical packing efficiency of ~ 68 volume %. There was also a distribution of titanium dioxide nanoparticle diameters, which would increase the packing efficiency of nanoparticles within the nanoparticle composite materials.

With all of the knowledge regarding the planar films for the composite materials containing titanium dioxide nanoparticles and NOA60 photoresist, nanopatterning via NIL was performed. The initial pattern that was used for evaluation of imprint lithography for the composite materials was a line array consisting of 500 nm line width (LW), 1.0 μm pitch (P), and 500 nm depth (D). The composites with varying concentrations of titanium dioxide nanoparticles were patterned and SEM images were

obtained, as shown in Figure 5.9. From the SEM images, the line arrays present appeared to be less than 500 nm in LW, which may arise due to the material properties of Sylgard 184 PDMS molds. With the use of soft mold Sylgard 184 PDMS molds, the residual solvent that remains within the composite thin film after spin-coating will swell the Sylgard 184 PDMS mold such that the original features of the silicon master mold were reproduced but with slight variations to the dimensions. The use of methanol and NMP was known to swell the Sylgard 184 PDMS slightly (2 % for methanol and 3 % for NMP)[29] which may partially account for the dimension variations present for the composite nanostructures.

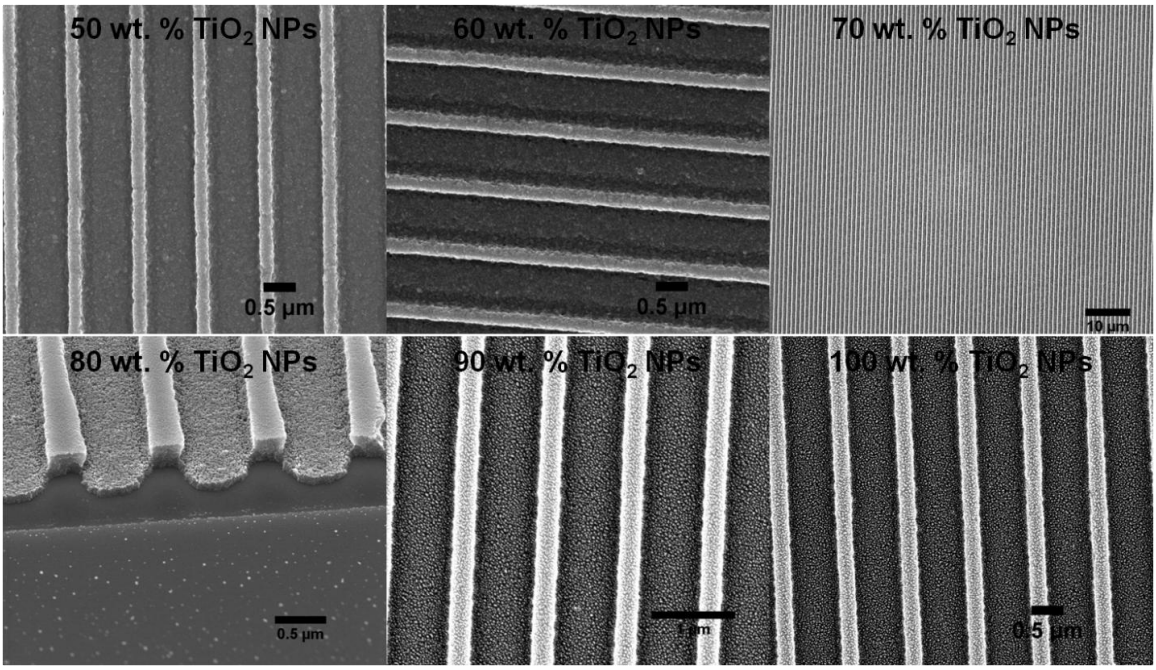

Figure 5.9. SEM evaluation of composite materials comprised of titanium dioxide nanoparticles and NOA 60 photoresist patterned through imprint lithography with a line array of 500 nm LW, 1.0 µm P, and 500 nm D.

The pattern formation of the composite material was not limited to just that of the line array but other nanostructures have been replicated such as line arrays of 500 nm LW, 1.0 µm P, and 100 nm D, line arrays of 800 nm LW, 1.6 µm P, and 500 nm D, line

arrays of 240 nm LW, 480 nm P, and 500 nm D, line arrays of 100 nm LW, 200 nm P, and 100 nm D, triangular grating structures of 135 nm top LW, 900 nm bottom LW, 1.0 μm P, and 900 nm D, as well as via structures, with rectangular or circular geometry, of varying critical dimensions and pitches.

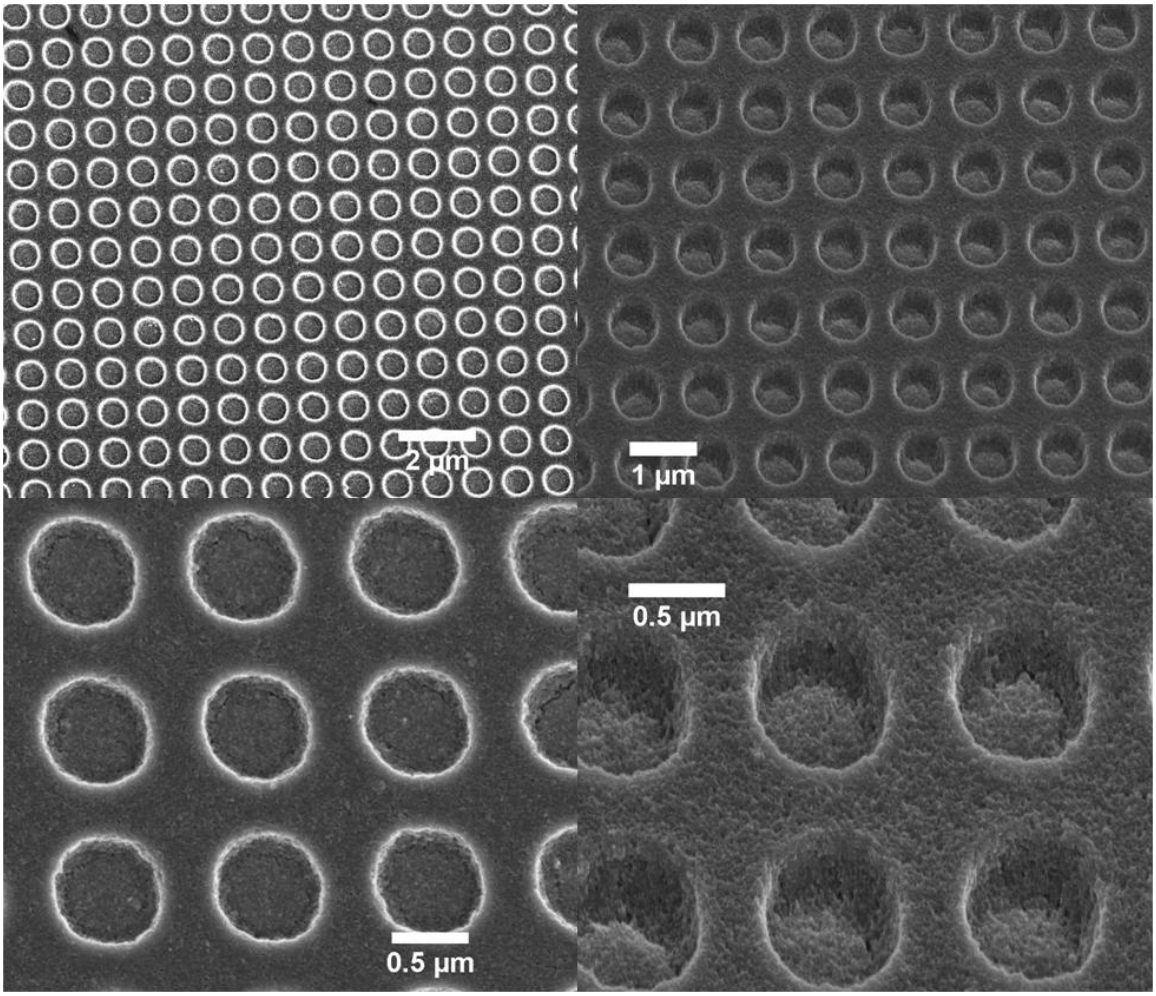

Figure 5.10. SEM evaluation of composite materials comprised of 90 wt. % titanium dioxide nanoparticles and 10 wt. % NOA 60 photoresist patterned through imprint lithography with a circular via structure. Top-down SEM images (top left and bottom left) and cross-sectional (50 ° tilt) images (top right and bottom right).

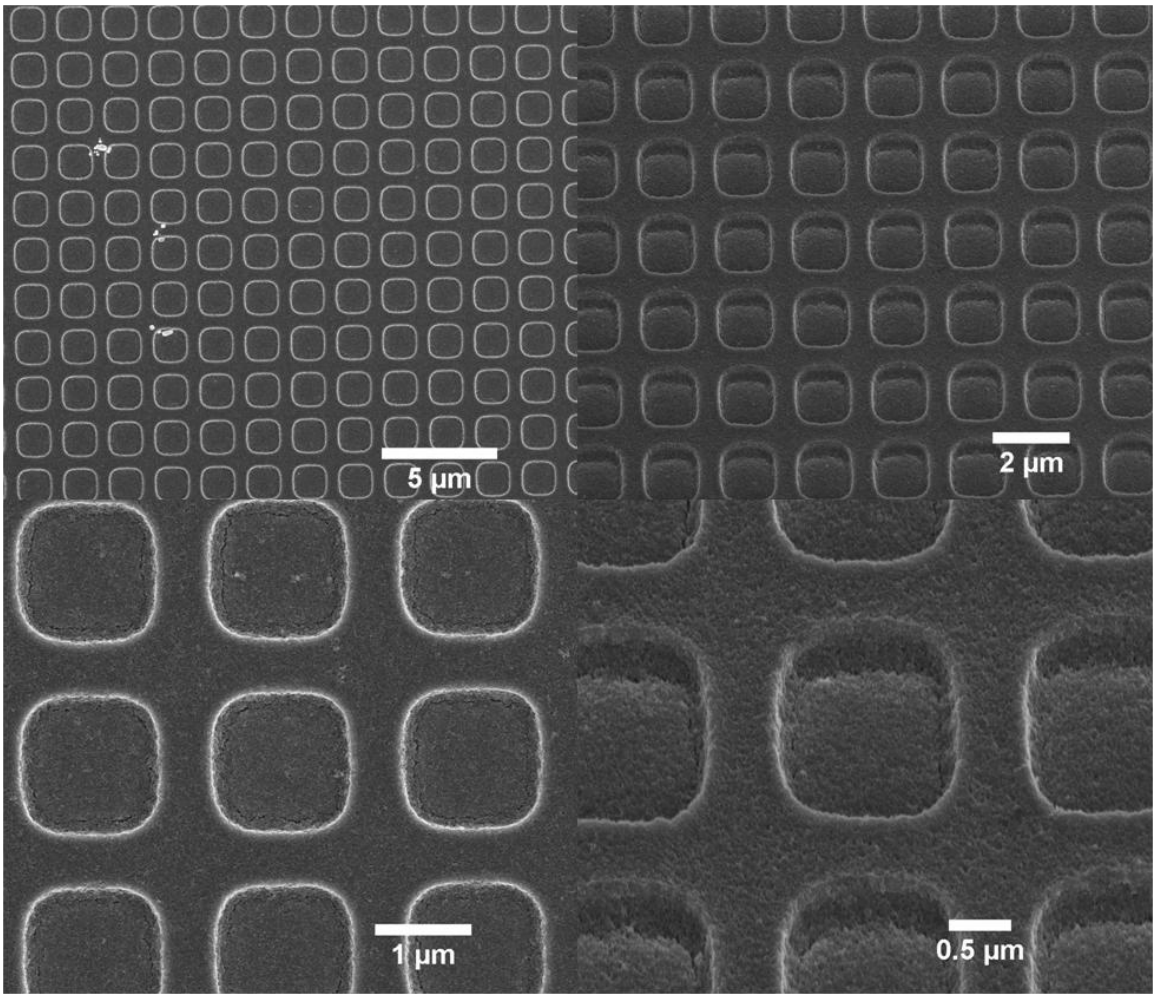

Figure 5.11. SEM evaluation of composite materials comprised of 90 wt. % titanium dioxide nanoparticles and 10 wt. % NOA 60 photoresist patterned through imprint lithography with a square via structure. Top-down SEM images (top left and bottom left) and cross-sectional (50 ° tilt) images (top right and bottom right).

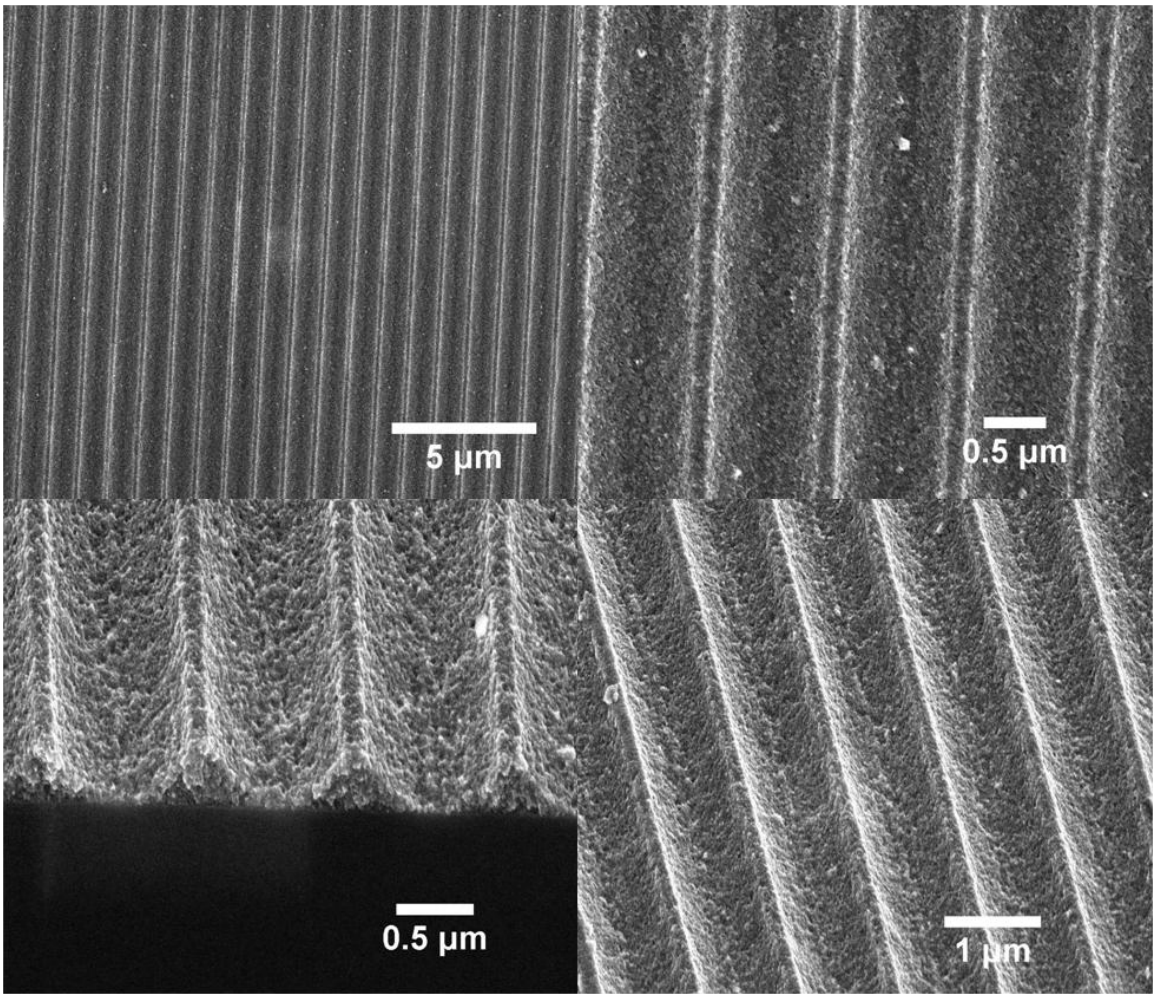

Figure 5.12. SEM evaluation of composite materials comprised of 90 wt. % titanium dioxide nanoparticles and 10 wt. % NOA 60 photoresist patterned through imprint lithography with a triangular grating structure. Top-down SEM images (top left and top right), cross-sectional (50 ° tilt) image (bottom left), and cross-sectional (50 ° tilt and rotation) image (bottom right).

The imprint lithography technique of patterning nanoparticle composite materials has solely focused on materials containing titanium dioxide nanoparticles thus far but the utility of this lithography technique is that any nanoparticle may be patterned. Other examples of nanoparticles that have been patterned through this technique are cerium dioxide, zirconium dioxide, iron oxide, and indium tin oxide to name several. The SEM images of the cerium dioxide nanoparticles patterned with the 500 nm LW, 1.0 µm P, 500

nm D line array are shown in Figure 5.13, which are accompanied by the X-ray diffraction (XRD) spectra.

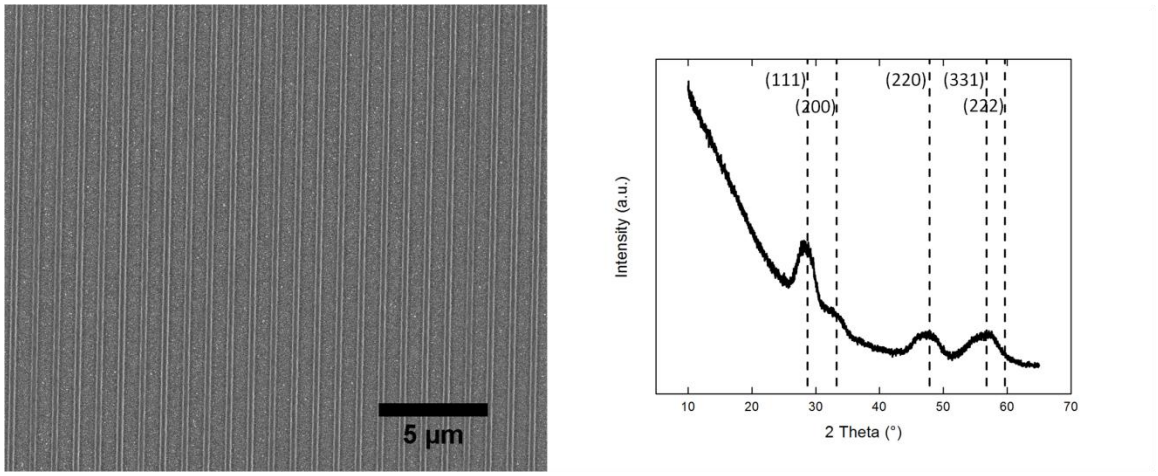

Figure 5.13. SEM image (left) and XRD spectra (right) of cerium dioxide nanoparticles

The nanoparticle composites that have been described thus far have involved the use of an organic filler/binder material to compliment the titanium dioxide nanoparticle. While the organic filler/binder material has advantages (ease of processability, suitable solubility within common solvents, photoactive at common UV-wavelengths), there are drawbacks such as inherent insulator properties, reduced operating temperatures due to thermal degradation, and reduced optical properties. The incorporation of an inorganic filler/binder would relieve such issues. To borrow a concept from the well-studied research topic of sol-gel chemistry, the use of sol-gel precursor materials as a filler/binder material would easily allow for further connectivity of the pre-synthesized nanoparticles without suffering from the drawbacks of the organic filler/binder materials. Literature has also established that common sol-gel precursors, consisting of β-diketonate ligands and combinations of β-diketonate stabilized metal alkoxides, are sensitive to electromagnetic radiation, specifically 365 nm UV-light, such that, when exposed under ambient conditions, hydrolysis and condensation of the sol-gel precursors will occur[30–33].

With knowledge of the previous results from literature, composite materials containing the titanium dioxide sol-gel precursor of titanium diisopropoxide bis(acetylacetonate) and titanium dioxide nanoparticles were generated and patterned with NIL. The SEM images of the patterned titanium dioxide sol-gel precursor and titanium dioxide nanoparticles composite materials are shown in Figure 5.14. From the SEM images, the line array comprised of 500 nm LW, 1.0 μm P, and 500 nm D was successfully replicated into the composite materials containing the inorganic filler/binder material. The pattern replication into the composite material comprised of the titanium dioxide sol-gel precursor and the titanium dioxide nanoparticles showed reduced dimensions of the line width, which was consistent with the observations from the composite materials comprised of titanium dioxide nanoparticles and the organic filler/binder material of NOA60.

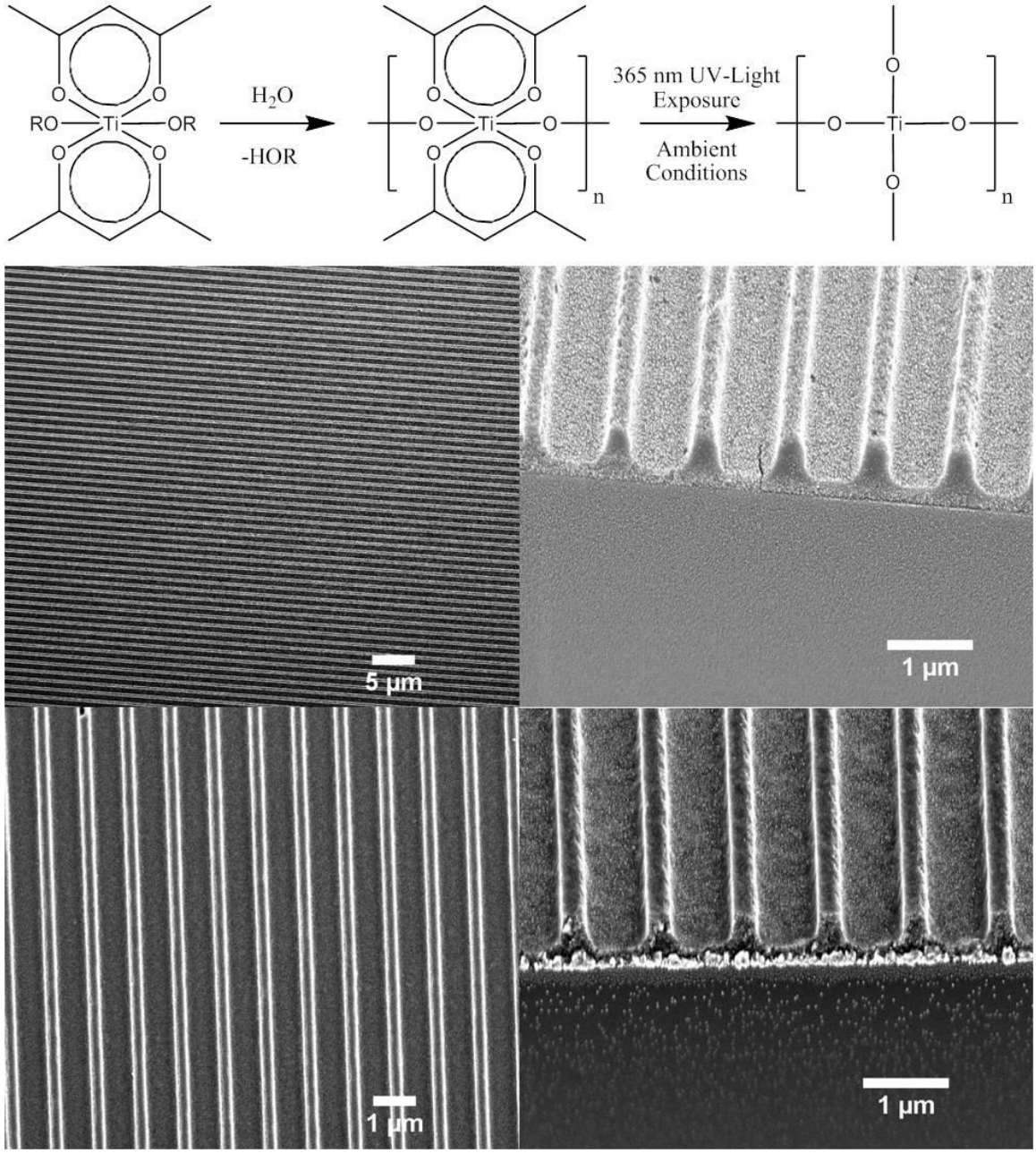

Figure 5.14. Schematic showing the condensation of β-diketonate stabilized titanium alkoxides upon exposure to 365 nm UV-light under ambient conditions. SEM images, top-down and cross-sectional (50 ° tilt) for 50 wt. % titanium dioxide sol-gel precursor / 50 wt. % titanium dioxide nanoparticle (top left (top-down) and top right (cross-sectional)) and 10 wt. % titanium dioxide sol / 90 wt. % titanium dioxide nanoparticles (bottom left (top-down) and bottom right (cross-sectional)).

To confirm the removal of the acetylacetonate ligand from the titanium dioxide sol-gel precursor, GATR-FT-IR was performed systematically, as shown in Figure 5.15.

From the GATR-FT-IR, the monitoring of the acetylacetonate ligand vibrations was observed within the IR region of 1700 cm^{-1} to 1200 cm^{-1} and the band assignments are provided in Table 5.3[34] along with an enlarged GATR-FT-IR spectrum for the acetylacetonate ligand region of interest, shown in Figure 5.16.

Table 5.3. Infrared band assignments and band positions for acetylacetonate ligands on the β-diketonate stabilized titanium alkoxide present with the titanium dioxide nanoparticles.

Band Assignment	Band Position (Ti - acac) (cm^{-1})
υ (C-O)	1285
δ (C-H) and υ (C-C)	1330 - 1470
υ (C=C-C)	1531
υ (C=O)	1591

What was observed in the exposure of the composite material containing the titanium dioxide sol-gel precursor upon prolonged exposure to 365 nm UV-light is that the acetylacetonate ligand was removed, while in the presence of the titanium dioxide nanoparticles, as shown in the GATR-FT-IR data, by the disappearance of the four infrared signals associated with the acetylacetonate ligand.

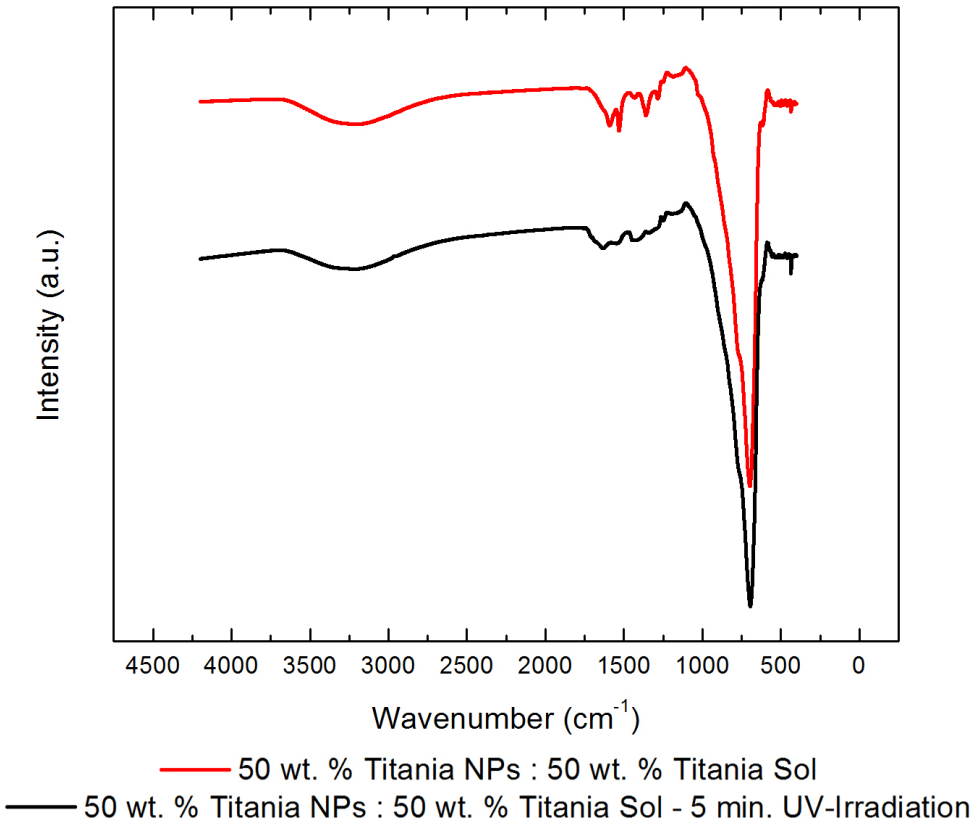

Figure 5.15. GATR-FT-IR spectra of composite materials containing titanium dioxide sol-gel precursor and titanium dioxide nanoparticles before and after exposure to 365 nm UV-light.

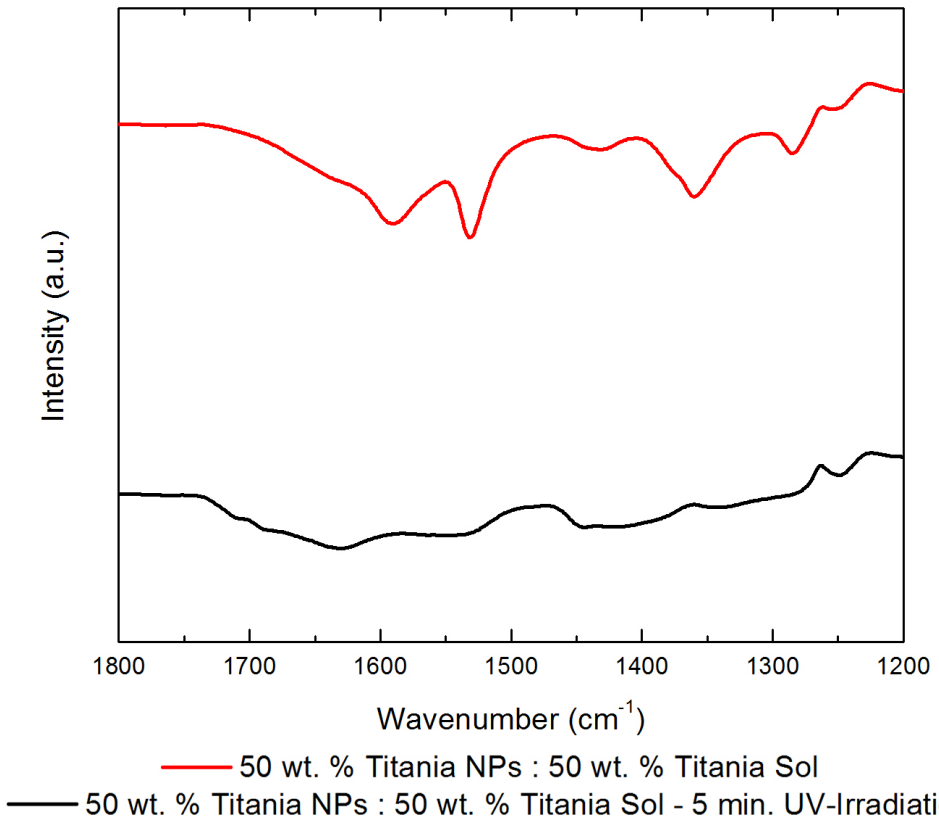

Figure 5.16. Enhanced spectra of GATR-FT-IR for the area of interest of the acetylacetonate ligand on the β-diketonate stabilized titanium alkoxide present with titanium dioxide nanoparticles.

To obtain a better understanding of the kinetics of the titanium dioxide sol-gel precursor transformation to titanium dioxide film, thin films of only the titanium dioxide sol-gel precursor were prepared on silicon wafers, via spin-coating, and exposed to various dosages of energy per area by varying the exposure time (0 seconds to 300 seconds), which is shown in Figure 5.17. The region of interest from the GATR-FT-IR spectrum for the acetylacetonate ligand, 1800 cm^{-1} to 1200 cm^{-1}, is shown in Figure 5.18 and the region of interest for the hydroxyl groups (4000 cm^{-1} to 2600 cm^{-1}) present after the removal of the acetylacetonate ligands is shown in Figure 5.19.

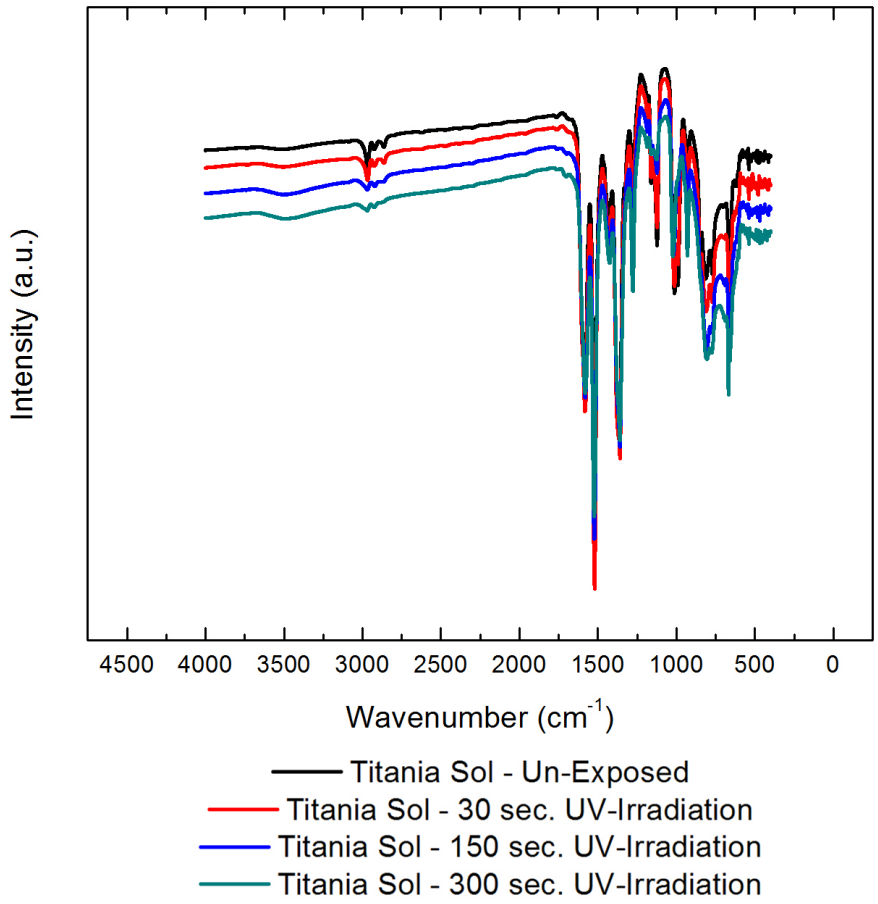

Figure 5.17. GATR-FT-IR spectra of titanium dioxide sol-gel precursor exposed to various times of 365 nm UV-irradiation.

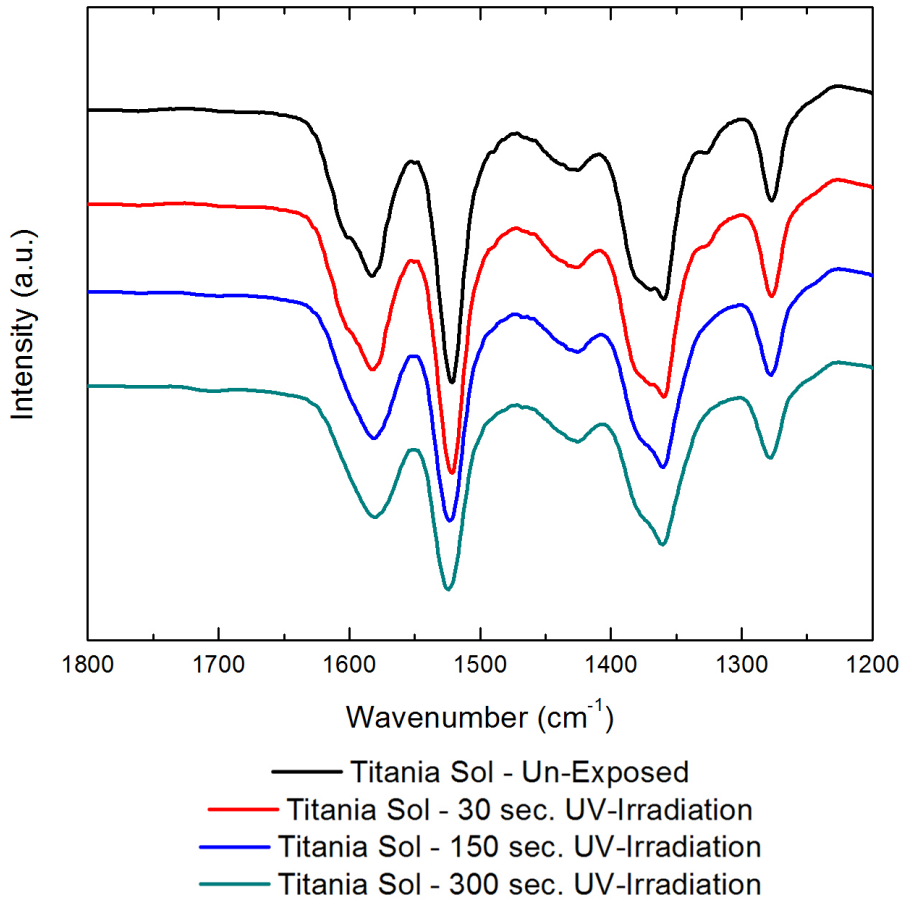

Figure 5.18. GATR-FT-IR spectra focused on the acetylacetonate ligand IR region of interest.

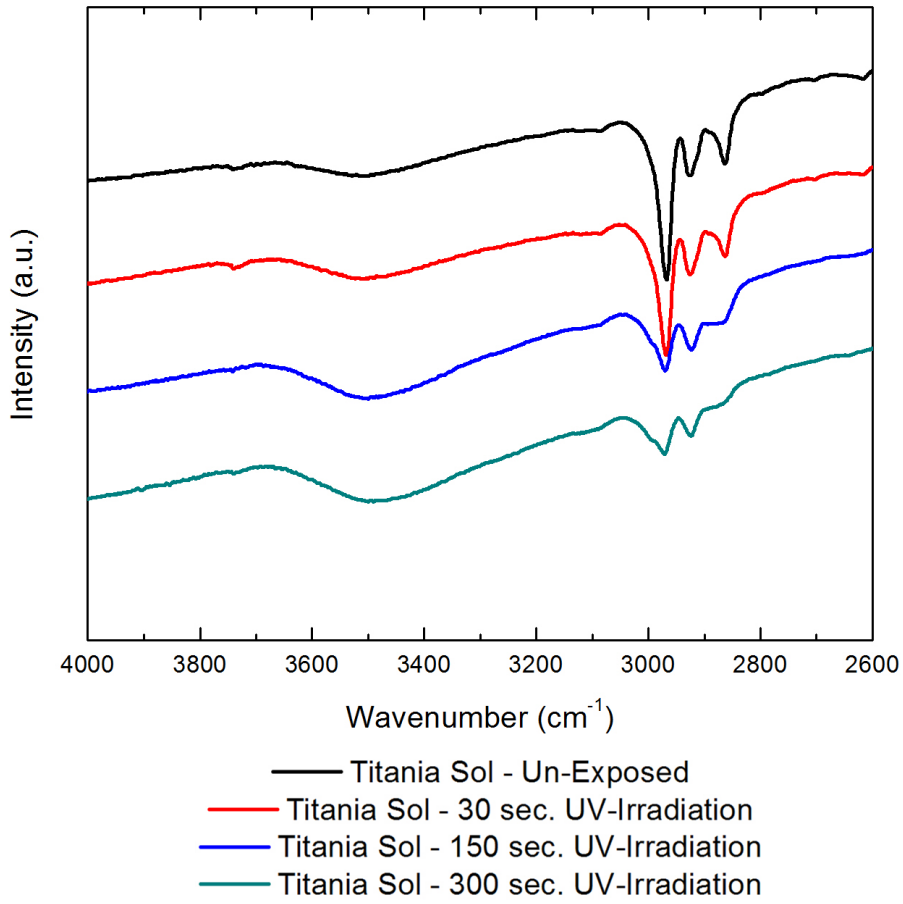

Figure 5.19. GATR-FT-IR spectra focused on the formation of titanium dioxide hydroxyl groups.

From the continuous exposure to the UV-irradiation, the titanium dioxide sol-gel precursor was quickly establishing the titanium dioxide matrix by dissociating and hydrolyzing the acetylacetonate ligand with atmospheric water as well as condensing the hydroxyl groups to form titanium-oxygen-titanium (Ti-O-Ti) bonds simultaneously. This was shown by the reduction in the IR signals for the acetylacetonate ligand within the wavenumber range of 1700 cm^{-1} to 1250 cm^{-1}. The appearance of the titanium dioxide hydroxyl group (Ti-OH), appearing between 3800 cm^{-1} and 3000 cm^{-1}, showed that the titanium dioxide matrix was being established through simultaneous hydrolysis and

condensation reactions. Another observation that the titanium dioxide matrix was being established was the reduction of tackiness of the titanium dioxide thin film on the silicon wafer after exposure to 365 nm UV-light. With prolonged exposure to the 365 nm UV-irradiation, the thin film appeared more robust, equating to the establishment of the titanium dioxide matrix.

The ability to crosslink nanoparticle composites, either with organic or inorganic binder materials, allows for a complete network to be established. With this capability, it was hypothesized that a nanoparticle composite material, which has undergone crosslinking, may be released from the substrate (silicon wafer or flexible material) where previous processing had occurred and floated onto a water surface through the correct utilization of a release layer. The ability to float crosslinked nanoparticle composite materials would allow for the fabrication of a true three-dimensional structure. Figure 5.20 shows the schematic of preparing a three-dimensional structure.

The initial release layer used was 20 k Mw poly(acrylic acid) (PAA) of ~ 300 nm in thickness. The use of PAA as the release layer allowed the structured nanoparticle composite material to be released onto the surface of water, which has sufficient surface tension to allow thin films to be floated upon. Due to the solubility of PAA in polar solvents, such as water, methanol, and NMP, a barrier layer was required to protect the release layer of PAA from prematurely dissolving from the solvents used for the nanoparticle composite materials, which was comprised of methanol and NMP. The initial barrier layer used was PS of 90 k Mw polystyrene (PS) and ~ 100 nm thickness, which provided enough solubility contrast between the PAA release layer and the

nanoparticle composite material, which consisted of a co-solvent of methanol and NMP, such that the release layer of PAA was not significantly hindered.

The nanoparticle composite used for the initial experiments consisted of 50 wt. % titanium dioxide nanoparticles and 50 wt. % NOA60 and the dimensions of the nanostructure were 500 nm LW, 1.0 μm P, and 500 nm D. The patterning of the nanoparticle composite material was performed with the same patterning process established for the patterning of nanoparticle composite materials on substrates without the additional release layer and barrier layer. With the patterned nanoparticle composite material on the stack structure of the release layer and the barrier layer, the substrate was brought into contact with a room temperature water bath, at low angles, such that the water would only contact the edges of the substrate and selectively dissolve the PAA release layer. The use of PAA as the release layer allowed for extremely quick dissolution in the water bath and resulted in the releasing of the nanostructured nanoparticle composite material to yield a free standing film. A pre-patterned substrate, consisting of identical composition and nanostructure dimensions, was submerged in the water bath containing the free standing nanostructured nanoparticle composite material film such that the direction of the pre-patterned substrate line array was placed orthogonal to the direction of the floating film line arrays. The directionality of the line array structure was confirmed by shining a laser perpendicularly on the nanostructured nanoparticle composite material, which, due to the dimensions and periodic nature of the line array, would produce diffraction spots perpendicular to the direction of the line array. This method of confirming the directionality of the line array may also have utility for accurate and precise alignment and placement of nanostructured nanoparticle composite

materials when required. The pre-patterned substrate was carefully brought into contact with the free standing film and allowed to dry for extended periods of time, at room temperature, to remove any residual water that may remain.

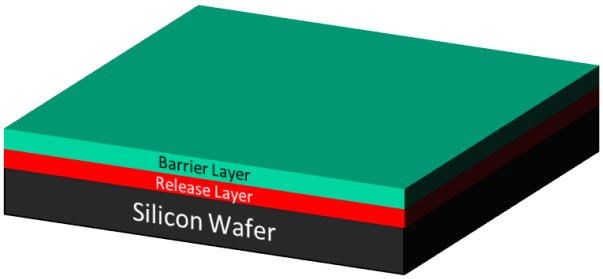

Spin-Coating, Patterning, and UV-Curing of TiO_2 Nanoparticle / Norland Optical Adhesive 60 Nanocomposite

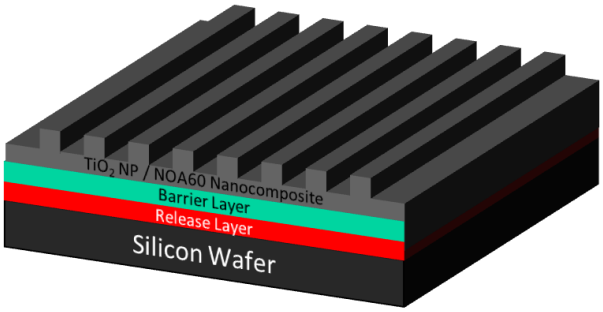

Release UV-Cured TiO_2 Nanoparticle / Norland Optical Adhesive 60 Nanocomposite Film in Water

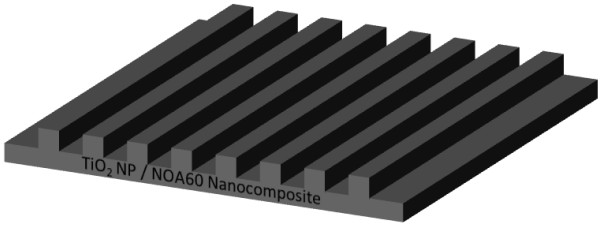

Free Standing UV-Cured TiO_2 Nanoparticle / Norland Optical Adhesive 60 Nanocomposite Film Collected by Pre-Patterned Film of TiO_2 NP / NOA60

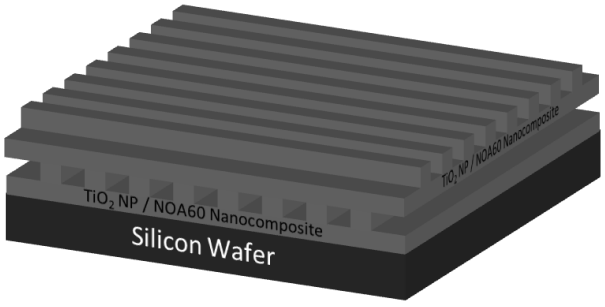

Figure 5.20. Schematic showing the fabrication of true three-dimensional structures.

From the SEM images provided in Figure 5.21, the free standing structured nanoparticle composite film was transported orthogonally to the pre-patterned nanoparticle composite film that was on a rigid substrate of silicon wafer to form a nanostructured bilayer film.

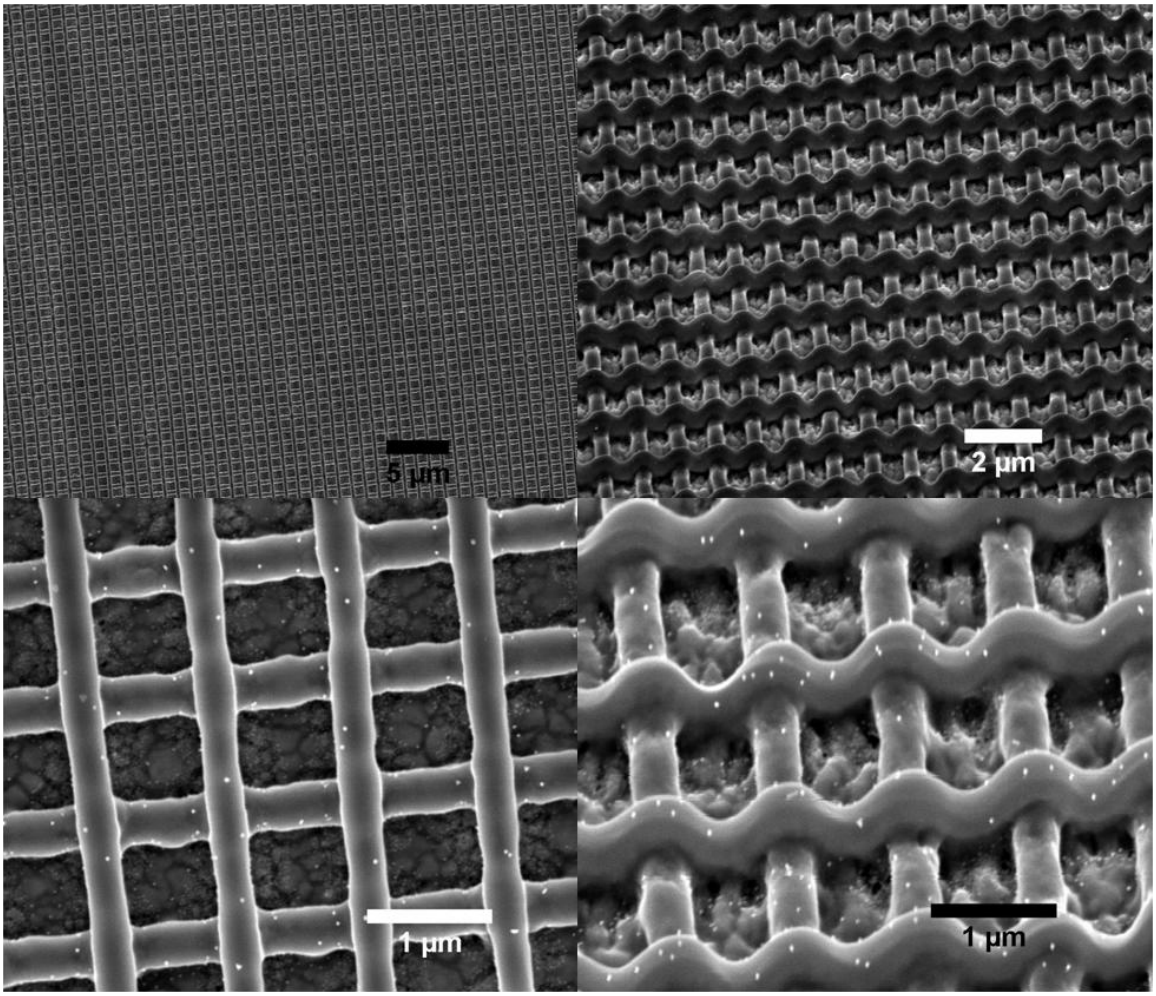

Figure 5.21. SEM images of three-dimensional structures of nanoparticle composite materials from top-down (top left and bottom left) and cross-sectional (top right and bottom right).

The coverage area of the bilayer structure was ~ 25 mm x 25 mm and has minimal defects present over that area. From the SEM analysis, the nanoparticle composite structures appeared to conform to the pre-patterned structure on the silicon wafer, i.e. the nanoparticle composite features appeared to be flexible. Multiple layers, two or greater,

of the nanoparticle composite films have been prepared orthogonal to each prior layer, as shown in Figure 5.22, which was a quad-layer of 50 wt. % titanium dioxide nanoparticles and 50 wt. % NOA60, and this fabrication method has emerged as a robust process for generating three-dimensional structures.

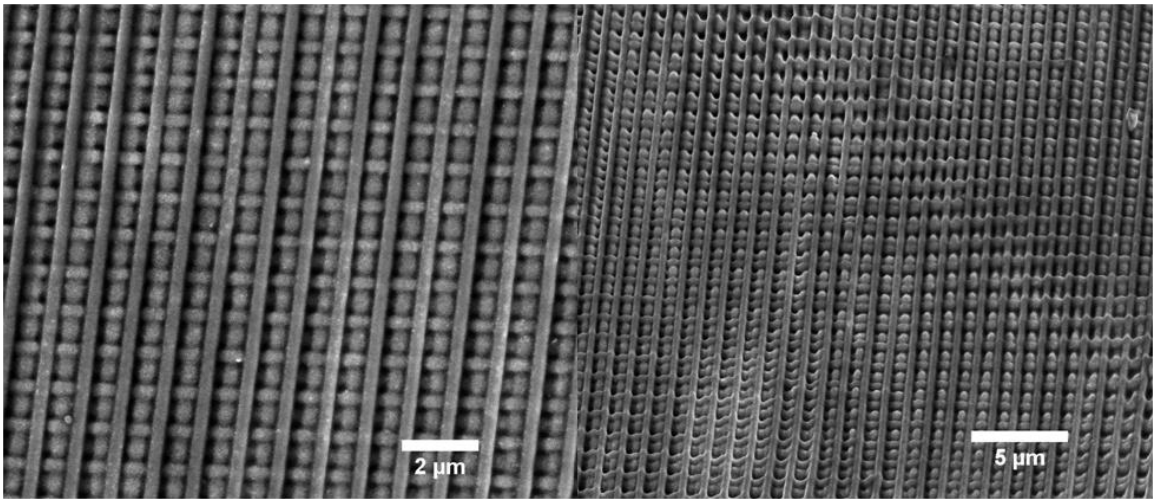

Figure 5.22. SEM images, top-down (left) and cross-sectional (right), of quad-layer, three-dimensional structures of nanoparticle composite materials containing 50 wt. % titanium dioxide nanoparticles and 50 wt. % NOA60.

It should be noted here that the use of PAA as the release layer and PS as the barrier layer has encountered several issues such as the premature dissolving of PAA during the spin-coating of the nanoparticle composite material. The PAA has been prematurely removed during the spin-coating due to the PAA layer swelling in the presence of the polar solvents used for the nanoparticle composite solutions which led to the barrier layer of PS cracking and prematurely dissolving the PAA layer. The low molecular weight of the initial PAA release layer was advantageous due to the quick and efficient solubility in water but was hindered by the sufficient amount of swelling in the presence of polar solvents. Optimization of the release layer and the barrier layer has been investigated by adjusting the following parameters: the molecular weight of PAA was varied within the

range of 1,800 to 2,000,000 Mw, the barrier layer material was adjusted such that the difference between the solubility parameter[35] of the barrier layer and that of the co-solvent of methanol and NMP would be great, and annealing conditions of both the release layer and the barrier layer. All of the aforementioned parameters have been thoroughly investigated but without much success. Just recently, the use of poly(vinyl alcohol) as a release layer has appeared to be the best candidate and has produced a fabrication method that was extremely reliable.

5.4. Conclusions

The use of commercially available, pre-synthesized nanoparticle dispersions have been successfully incorporated into sub-micron structures through the use of imprint lithography. The structures that are capable of being fabricated from this method are only limited by the dimensions of the nanoparticles and imprint lithography molds that are available. The primary nanoparticle of choice has consisted of crystalline metal oxide nanoparticles, specifically titanium dioxide, but the fabrication method has been extended to numerous metal oxide nanoparticles such as cerium dioxide, zirconium dioxide, and indium tin oxide. The use of binder/filler materials in the form of commercially available negative tone photoresists as well as photoactive inorganic sol-gel precursors have been successfully incorporated into the nanoparticle based composite material. Due to the establishment of a network through the crosslinking mechanism of the binder/filler matter, nanoparticle composite materials have been successfully released from substrates such that true three-dimensional structures have been formed. Initial three-dimensional structures have been fabricated from bi-layer and quad-layer structures. Several

applications are being pursued for the three-dimensional structures, one of which is a photonic bandgap crystal. Another application is creating such structures on a continuous procedure via roll-to-roll (R2R) processing due to the solution processability of the patterned nanoparticle composites.

5.5. Acknowledgements

The work presented within this dissertation chapter has been conducted in a true collaboration with Michael "Ruosty" Beaulieu, who equally contributed to this work, if not more, and will be continuing research on this project.

5.6. References

(1) Burda, C.; Chen, X.; Narayanan, R.; El-Sayed, M. A. *Chemical Reviews* **2005**, *105*, 1025-1102.

(2) Hanemann, T.; Szabó, D. V. *Materials* **2010**, *3*, 3468-3517.

(3) Jiguet, S.; Bertsch, A.; Hofmann, H.; Renaud, P. *Advanced Functional Materials* **2005**, *15*, 1511-1516.

(4) Damean, N.; Parviz, B. A.; Lee, J. N.; Odom, T.; Whitesides, G. M. *Journal of Micromechanics and Microengineering* **2005**, *15*, 29-34.

(5) Xu, J.; Wong, C. P. *Journal of Applied Polymer Science* **2007**, *103*, 1523-1528.

(6) Dawan, F.; Jin, Y.; Goettert, J.; Ibekwe, S. *Microsystem Technologies* **2008**, *14*, 1451-1459.

(7) Martiradonna, L.; Qualtieri, A.; Stomeo, T.; Carbone, L.; Cingolani, R.; Devittorio, M. *Sensors and Actuators B: Chemical* **2007**, *126*, 116-119.

(8) Pompa, P.; Martiradonna, L.; Torre, A.; Carbone, L.; Delmercato, L.; Manna, L.; Devittorio, M.; Calabi, F.; Cingolani, R.; Rinaldi, R. *Sensors and Actuators B: Chemical* **2007**, *126*, 187-192.

(9) Qualtieri, A.; Martiradonna, L.; Stomeo, T.; Todaro, M. T.; Cingolani, R.; Vittorio, M. D. *Microelectronic Engineering* **2009**, *86*, 1127-1130.

(10) Singh, A.; Kulkarni, S. K.; Khan-Malek, C. *Microelectronic Engineering* **2011**, *88*, 939-944.

(11) Tekin, E.; Smith, P. J.; Hoeppener, S.; van den Berg, A. M. J.; Susha, A. S.; Rogach, A. L.; Feldmann, J.; Schubert, U. S. *Advanced Functional Materials* **2007**, *17*, 23-28.

(12) Ko, S. H.; Park, I.; Pan, H.; Grigoropoulos, C. P.; Pisano, A. P.; Luscombe, C. K.; Fréchet, J. M. J. *Nano Letters* **2007**, *7*, 1869-1877.

(13) Loffredo, F.; Mauro, a. D. G. D.; Burrasca, G.; La Ferrara, V.; Quercia, L.; Massera, E.; Di Francia, G.; Sala, D. D. *Sensors and Actuators B: Chemical* **2009**, *143*, 421-429.

(14) Chou, S. Y.; Krauss, P. R.; Renstrom, P. J. *Applied Physics Letters* **1995**, *67*, 3114-3116.

(15) Chou, S. Y.; Krauss, P. R.; Renstrom, P. J. *Science* **1996**, *272*, 85-87.

(16) Chou, S. Y.; Krauss, P. R.; Zhang, W.; Guo, L.; Zhuang, L. *Journal of Vacuum Science & Technology B: Microelectronics and Nanometer Structures* **1997**, *15*, 2897-2904.

(17) Reboud, V.; Kehagias, N.; Sotomayor Torres, C. M.; Zelsmann, M.; Striccoli, M.; Curri, M. L.; Agostiano, A.; Tamborra, M.; Fink, M.; Reuther, F.; Gruetzner, G. *Applied Physics Letters* **2007**, *90*, 011115.

(18) Tamborra, M.; Striccoli, M.; Curri, M. L.; Alducin, J. A.; Mecerreyes, D.; Pomposo, J. A.; Kehagias, N.; Reboud, V.; Sotomayor Torres, C. M.; Agostiano, A. *Small* **2007**, *3*, 822-828.

(19) Ingrosso, C.; Fakhfouri, V.; Striccoli, M.; Agostiano, A.; Voigt, A.; Gruetzner, G.; Curri, M. L.; Brugger, J. *Advanced Functional Materials* **2007**, *17*, 2009-2017.

(20) Persano, L.; Molle, S.; Girardo, S.; Neves, A. A. R.; Camposeo, A.; Stabile, R.; Cingolani, R.; Pisignano, D. *Advanced Functional Materials* **2008**, *18*, 2692-2698.

(21) Park, O.-H.; Cheng, J. Y.; Hart, M.; Topuria, T.; Rice, P. M.; Krupp, L. E.; Miller, R. D.; Ito, H.; Kim, H.-C. *Advanced Materials* **2008**, *20*, 738-742.

(22) Choi, J.-H.; Lee, S.-W.; Jeong, J.-H.; Choi, D.-G.; Lee, E.-S. *Microelectronic Engineering* **2009**, *86*, 622-627.

(23) Kim, Y.; Kim, G.; Lee, J. *Microelectronic Engineering* **2010**, *87*, 839-842.

(24) Fujishima, A.; Honda, K. *Nature* **1972**, *238*, 37-38.

(25) Smith, G. W. *Molecular Crystals and Liquid Crystals* **1991**, *196*, 89-102.

(26) Pinto-Iguanero, B.; Olivares-Pérez, A.; Fuentes-Tapia, I. *Optical Materials* **2002**, *20*, 225-232.

(27) Moran, I. W.; Briseno, A. L.; Loser, S.; Carter, K. R. *Chemistry of Materials* **2008**, *20*, 4595-4601.

(28) Hanaor, D. A. H.; Sorrell, C. C. *Journal of Materials Science* **2010**, *46*, 855-874.

(29) Lee, J. N.; Park, C.; Whitesides, G. M. *Analytical Chemistry* **2003**, *75*, 6544-6554.

(30) Tohge, N.; Shinmou, K.; Minami, T. *Journal of Sol-Gel Science and Technology* **1994**, *2*, 581-585.

(31) Tohge, N.; Zhao, G.; Chiba, F. *Thin Solid Films* **1999**, *351*, 85-90.

(32) Tohge, N.; Hasegawa, M.; Noma, N.; Kintaka, K.; Nishii, J. *Journal of Sol-Gel Science and Technology* **2003**, *26*, 903-907.

(33) Saifullah, M. S. M.; Subramanian, K. R. V.; Tapley, E.; Kang, D.-J.; Welland, M. E.; Butler, M. *Nano Letters* **2003**, *3*, 1587-1591.

(34) Innocenzi, P.; Zub, Y. L.; Kessler, V. G. *Sol-Gel Methods for Materials Processing*; Innocenzi, P.; Zub, Y. L.; Kessler, V. G., Eds.; Springer Netherlands: Dordrecht, 2008.

(35) Zeng, W.; Du, Y.; Xue, Y.; Frisch, H. L. In *Physical Properties of Polymers Handbook*; 2007; pp. 289-303.

CHAPTER 6

CONCLUSIONS, FUTURE WORK, INITIATED RESEARCH PROJECTS, AND COLLABORATIVE RESEARCH PROJECTS

6.1. Conclusions

6.1.1. Formation of Hierarchical Silica Nanochannels through Nanoimprint Lithography

The combination of supercritical carbon dioxide ($scCO_2$) infusion processing and nanoimprint lithography (NIL) allowed for the fabrication of embedded nanochannels within a mesoporous silica thin film. The $scCO_2$ infusion processing yielded the mesoporous thin films with pore diameters of ~ 4 - 5 nm and morphologies of either spheres or cylinders while the NIL procedure generated sacrificial material templates for the embedded nanochannel structures. The hierarchical silica nanochannels were evaluated as low-k dielectric materials and a dielectric constant of 2.0 was reported. The utility of the fabrication procedure described within this dissertation chapter was the numerous hierarchical structures that could be generated from this procedure, i.e. the mesoporous thin film may have the diameter and morphology varied by simply adjusting the amphiphilic block copolymer used, while the embedded nanochannel dimensions were only dependent on the molds available for NIL processing.

6.1.2. Mesoporous Silica Doped with Functional Nanomaterials

Functional nanomaterials were successfully incorporated within thin films of mesoporous silica, which was generated from $scCO_2$ infusion processing, through selective hydrogen bonding between the functional nanomaterial and the hydrophilic

segment of an amphiphilic block copolymer. The functional nanomaterials investigated within this dissertation chapter were pre-synthesized gold nanoparticles, tris(malonic acid) fullerene derivatives, and polyhedral oligomeric silsesquioxane (POSS) molecules, all of which were decorated with hydrogen bond donating ligands. The properties afforded to the functional nanomaterials were imparted upon the mesoporous silica with the example of enhanced thermal and hydrothermal properties shown for the POSS doped mesoporous silica thin films. The research presented within this dissertation chapter provided the framework for doping functional nanomaterials within mesoporous silica thin films provided that the functional nanomaterials have the ability to interact favorably with the hydrophilic segment of an amphiphilic block copolymer.

6.1.3. Alternative Substrates for Mesoporous Silica

Hierarchically porous silica materials have been successfully fabricated from amphiphilic block copolymer coated cellulose filter paper and $scCO_2$ infusion processing. The cellulose filter paper provided a mesoporosity and macroporosity while the amphiphilic block copolymer provided an additional mesoporosity to afford a hierarchically porous silica material with tri-modal porosity. The use of $scCO_2$ infusion processing allowed for the transport of the silica precursor throughout the complex geometry of the cellulose filter paper to replicate the mesoporosity of the amphiphilic block copolymer as well as the bundles and strands of crystalline cellulose. The hierarchically porous silica material is an ideal candidate for applications of filtration and/or separation.

6.1.4. Patterned Nanoparticle Composite Structures

Composite materials, containing commercially available nanoparticle dispersions and binder/filler materials based on either organic or inorganic components, have been successfully patterned into sub-micron structures through imprint lithography. The nanoparticles of interest were crystalline metal oxide nanoparticles, specifically titanium dioxide nanoparticles, however, other nanoparticles have been used such as cerium dioxide nanoparticles. The organic binder/filler material consisted of negative tone photoresists while the inorganic binder/filler material was comprised of sol-gel precursors. Simple two-dimensional nanostructures have been created as well as true three-dimensional nanostructures, which relied on the use of release layers. Initial investigations utilizing the three-dimensional nanostructures have consisted of photonic bandgap crystals with future plans of processing the composite materials through roll-to-roll (R2R) manufacturing platforms.

6.2. Future Work

6.2.1. Formation of Hierarchical Silica Nanochannels through Nanoimprint Lithography

The hierarchical structure of silica, through the combination of airgap structures and mesopores, allowed for the reduction of capacitance for interlayer dielectric (ILD) materials, however, the dimensions used for the proof of concept were not applicable for microelectronics used currently. Nonetheless, to make the hierarchically porous silica more intriguing for microelectronics, the dimensions of the airgap structure must be less than 25 nm while the mesopore diameter and domain spacing must be less than 2 nm and 4 nm respectively. The criteria established here for the hierarchically porous silica structure is achievable through the fabrication method described within Chapter 2 of this

dissertation. Nanoimprint lithography (NIL) is capable of patterning sub-nanometer features while the $scCO_2$ infusion process is capable of producing mesopores with reduced dimensions by simply selecting an amphiphilic block copolymer with the required dimensions.

The hierarchical structure of embedded nanochannels within mesoporous silica is also an ideal candidate to study fluid flow behaviors for nano/microfluidic devices. The capability of patterning dual scale porosity within silica should allow for unique capabilities in nanofluidic and microfluidic devices. Such fluid flow properties are of interest to the microelectronics community for use in active on-boarding cooling as well as for applications of filtration and/or separation. There are also fundamental aspects of fluid flow properties that could be investigated as well with the hierarchically porous silica structures presented here.

6.2.2. Mesoporous Silica Doped with Functional Nanomaterials

The functional nanomaterials incorporated into the mesoporous silica afforded the composite material with properties that are not typically afforded to mesoporous silica, i.e. conductivity, activity upon exposure to specific electromagnetic radiation, and enhanced mechanical properties. The gold nanoparticle doped mesoporous silica may exhibit conductivity upon the additional incorporation of gold nanoparticles, however, the catalytic activity[1] afforded to gold nanoparticles, such as oxidation of carbon monoxide, alcohols, and aldehydes,[2] as well as epoxidation[3] and hydrogenation[4,5], is an advantageous property that should be researched further. The mesoporous silica structure, with open cylindrical mesopores, is an excellent host material for gold

nanoparticles and would allow easy access to the catalytic surface of the gold nanoparticles.

The original novelty of doping mesoporous silica with POSS molecule was to take advantage of the excellent mechanical strength exhibit by composite materials when POSS is incorporated. To make accurate mechanical measurements of mesoporous silica doped with POSS molecules, the thin films are required to have a minimum thickness of 500 nm, which was achieved, to be evaluated by nanoindentation. It is believed that the mesoporous silica thin films doped with POSS molecules would have enhanced hardness and modulus properties, which would be highly desired by the microelectronics community.

One dopant material that has yet to be considered for the mesoporous silica thin films is that of heteroatoms such as aluminum and cobalt. Previous research has shown that metal salts of cobalt have successfully phase separated into the poly(ethylene oxide) (PEO) segment of the Pluronic® block copolymer surfactants[6]. The research idea to incorporate metal salts, specifically aluminum salts, within the mesoporous silica was driven by the possibility of making aluminosilicate, i.e. zeolite, thin films. Aluminum salts with a counterion of nitrate, acetate, and acetylacetonate have been incorporated within the Pluronic® block copolymer surfactants and $scCO_2$ infusion processing has been performed with limited success. The research project currently requires additional research efforts in the $scCO_2$ infusion processing to maintain a well-ordered mesoporous structure, while incorporating the metal salt, which should be achievable.

6.2.3. Alternative Substrates for Mesoporous Silica

The fabrication of mesoporous silica on alternative substrates, such as cellulose filter paper, allows for direct application to filtration and/or separation. By incorporating the high surface areas afforded to mesoporous materials with the ease of handling afforded to cellulose filter paper, one may perform separations of heavy metal ions[7] without tedious collection procedures of the separation medium, as is the case when mesoporous silica nanoparticles are used. To make useful separation and filtration devices, the mesoporous silica requires modification through well known condensation chemistry between surface silanol groups and chloro or alkoxy functionalized silanes. The required end functionality of the silanes would be either amino or thiol to attract heavy metal ions such as mercury, copper, chromium, and nickel to name several.

The use of cellulose filter paper as the alternative substrate may limit the number of applications that would be advantageous for mesoporous silica generated on alternative substrates due to reduced operating temperatures and/or fragility. Other alternative substrates have been considered such as glass fiber, Kevlar®, Nylon, carbon fibers, and composites of the aforementioned, which would all be perfect candidates to host mesoporous silica due to the inherent hydrophilic nature of the substrates.

6.2.4. Patterned Nanoparticle Composite Structures

The focus of patterning nanoparticle composite materials has primarily been on titanium dioxide nanoparticles and photonic applications. One application that was evaluated extensively, but was not discussed within this dissertation, was hybrid solar cells, which were constructed from patterned titanium dioxide nanoparticles on indium tin oxide (ITO) substrates and poly(3-hexylthiophene) (P3HT). The hypothesis behind this research endeavor was that increasing the interfacial surface area between the

titanium dioxide and the P3HT would increase the efficiency of the hybrid solar cell. The initial hybrid solar cell devices suffered from electrical connection shorting between the two electrodes, i.e. shorting, but this issue was overcome by depositing a dense layer of titanium dioxide from a titanium dioxide sol-gel precursor[8] and a molybdenum oxide buffer layer for the anode. True p-n junction behavior, as would be expected for hybrid solar cells, was observed, however, a greater study is required.

The utility of patterning nanoparticle composites with imprint lithography is that any nanoparticle composite material may be structured with sub-micron features. Nanoparticle composite materials that would have applications to solid oxide fuel cells (SOFCs), i.e. zirconium dioxide, cerium dioxide, and yttria stablized zirconia (YSZ), have been evaluated but were not extensively discussed within this dissertation. The opportunity to pattern nanoparticle composite materials for use as electrodes and electrolytes in SOFCs is great due to the simplicity of the fabrication technique described within Chapter 5 of this dissertation. The ability to dope nanoparticle composite materials is also advantageous for SOFCs due to the enhanced performance from SOFCs doped with heteroatoms such as yttrium, gadolinium, and samarium to name several. Evaluation of nanoparticle composite materials for SOFCs is currently underway.

An important class of materials yet to be discussed is transparent conductive oxide (TCO) materials with the most common TCO material being indium tin oxide (ITO). TCO materials find use in applications ranging from transparent electrodes for solar cells to display panels for touch devices and televisions. The ability to generate a conductive three-dimensional network through the stacking of released nanoparticle

composite material thin films, as shown for the titanium dioxide nanoparticle composite materials, would be extremely attractive for display panels.

6.3. Initiated Research Projects

6.3.1. Mesoporous Carbon from Selective Hydrogen Bonding Interactions

Mesoporous carbon materials have gained increased research attention from the materials community due to the combination of properties that the materials possess such as conductivity, uniform pore sizes, and ease of doping, all of which are advantageous for applications such as energy storage, electrodes, and sensors. Mesoporous carbon materials may be synthesized via hard template routes[9] and soft template routes[10]. The hard template route for synthesizing mesoporous carbon consists of creating a hard mesoporous template (typically mesoporous silica) back filling of the hard mesoporous structure with a carbon precursor, carbonization of the carbon precursor, and finally removal of the hard template to generate the mesoporous carbon material. The soft template approach to mesoporous carbon is less burdensome then the hard template approach due to the simplicity of the technique, which only requires self-assembly of a carbon precursor with an amphiphilic block copolymer template and subsequent carbonization. The research project initiated here is an extension of the soft template approach to create mesoporous carbon materials through the use of furfuryl alcohol (FA) as the carbon precursor and Pluronic® block copolymer surfactants.

Recent research efforts from the Watkins' research group have focused on the additive driven self-assembly of block copolymer materials through enthalpically favorable interactions between the additive and the block copolymer template. The research idea hypothesized here was to make blends of FA and Pluronic® block

copolymer surfactants that would form well-ordered mesoporous structures due to the hydrogen bonding interaction between the FA and the hydrophilic segment of the Pluronic® template. To determine the ordering of the template, small angle X-ray scattering (SAXS) was employed as the characterization technique. The initial blends to be evaluated by SAXS were simple blends of FA and Pluronic® F127 and the SAXS profiles, recorded at 80 °C, are shown in Figure 6.1. From the SAXS data provided in Figure 6.1, long range ordering of the Pluronic® F127 template was not achieved.

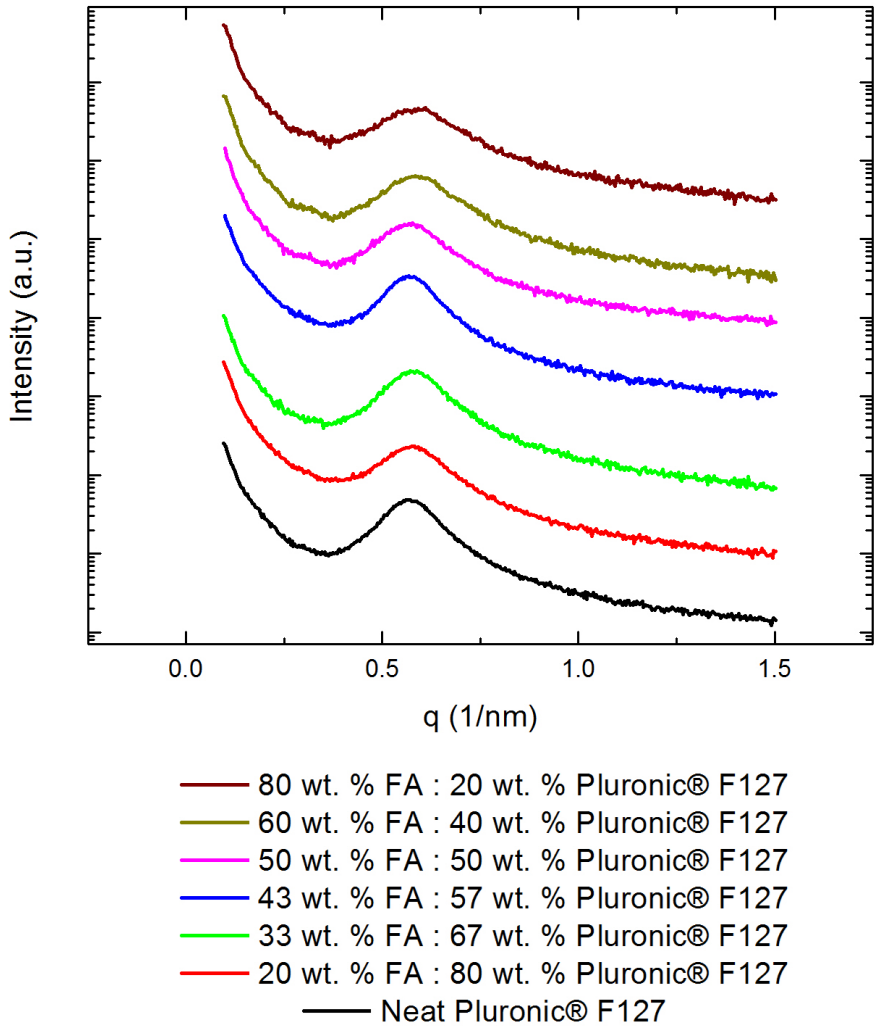

Figure 6.1. SAXS profiles of FA : Pluronic® F127 blends recorded at 80 °C.

To further enhance the long range order of the Pluronic® template through the incorporation of FA, an acid catalyst, in the form of para-toluene sulfonic acid (pTSA) was included into the blends of FA and Pluronic® F127. However, the incorporation of a strong organic acid prematurely polymerized the FA in solution[11], as observed by the dark brown color of the solutions in Figure 6.2. The dark brown color was also transferred to the drop casted films, which are shown in Figure 6.3.

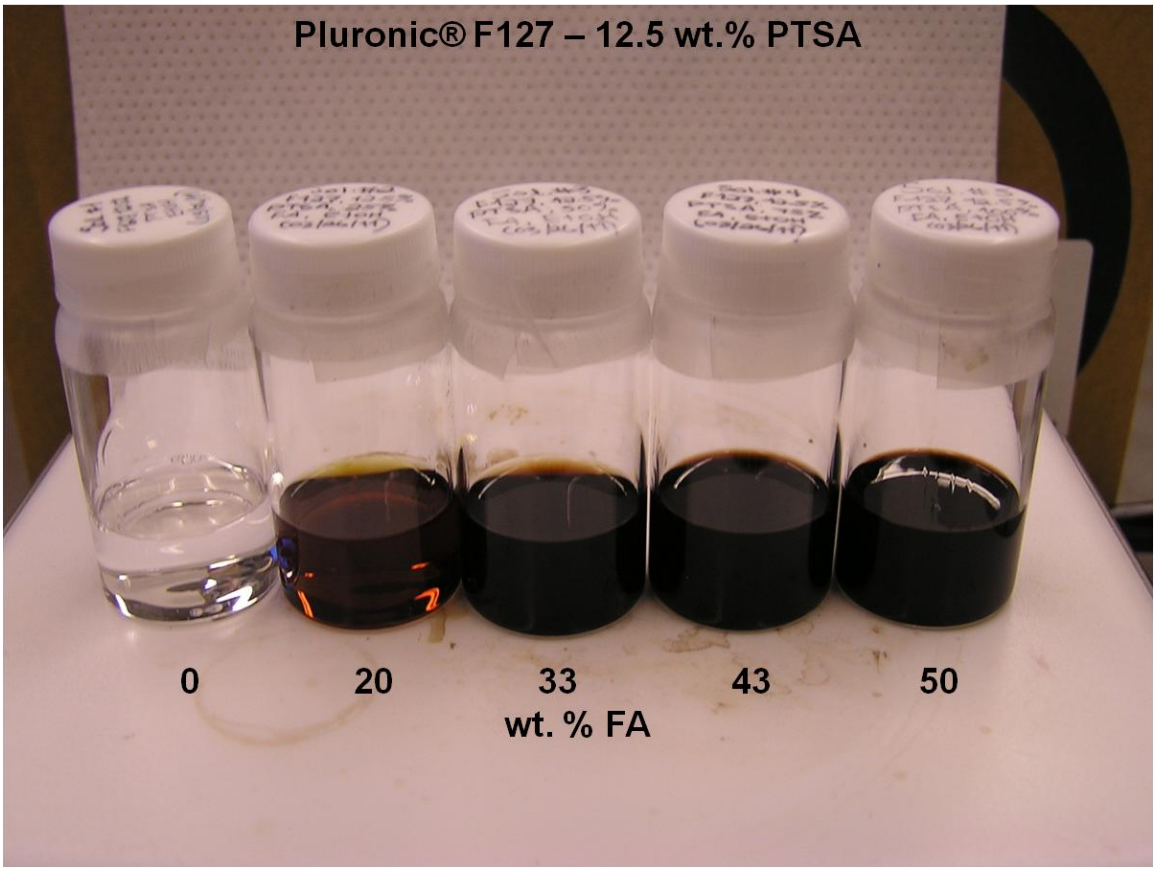

Figure 6.2. Solutions of various weight percentages of FA with Pluronic® F127.

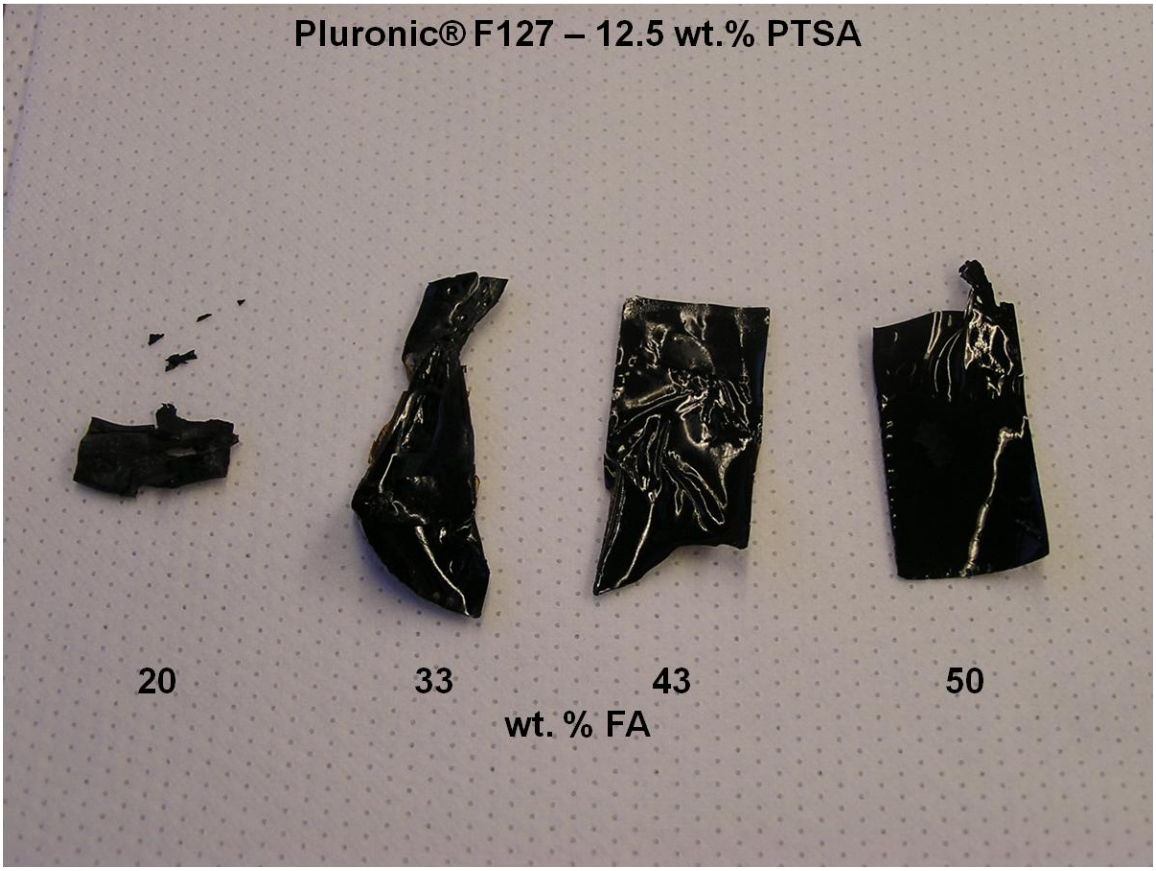

Figure 6.3. Drop cast films of various concentrations of FA and Pluronic® F127.

To avoid the premature polymerization of FA in solution, a photoacid generator (PAG), in the form of triphenylsulfonium triflate (TPST), was incorporated into the blends of FA and Pluronic® F127. The SAXS profiles for the blends of TPST, FA, and Pluronic® F127, recorded at 80 °C and provided in Figure 6.4, showed the narrowing of the full width at half maximum (FWHM) of the primary peak in the SAXS profile, which indicated the ordering of the Pluronic® F127 template, however, without the presence of higher order peaks.

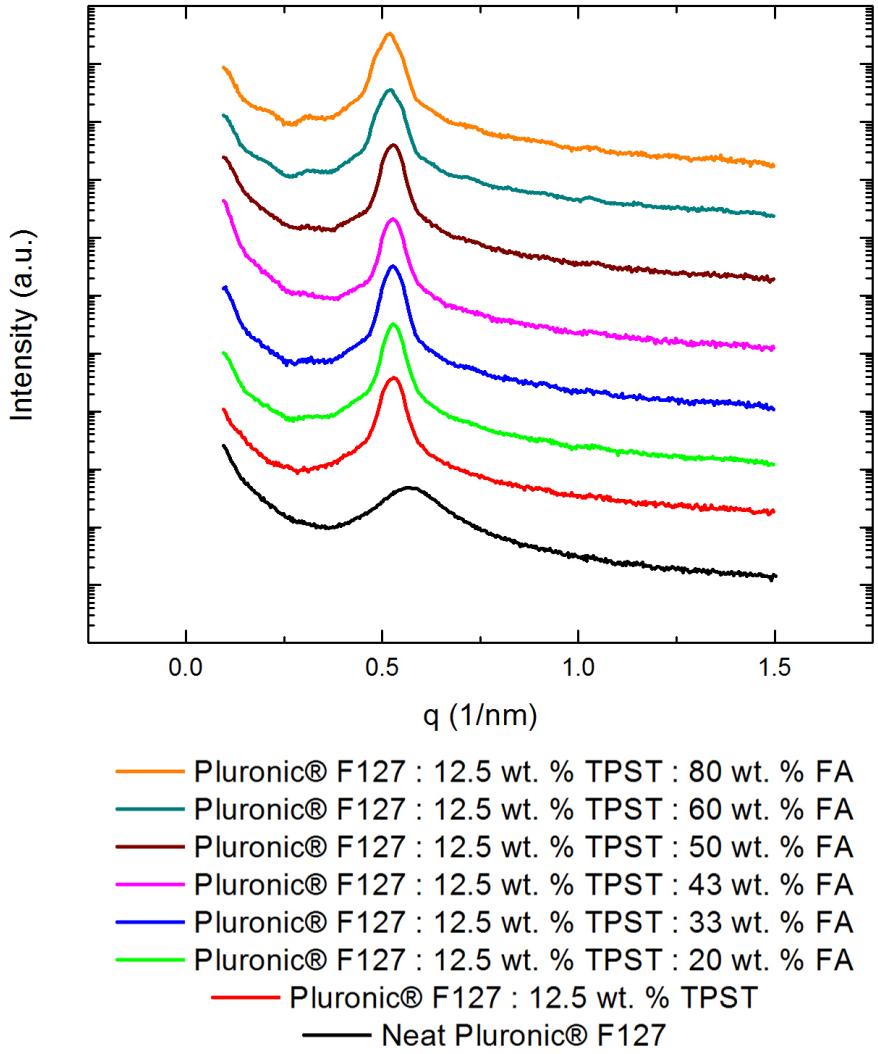

Figure 6.4. SAXS profiles of 12.5 wt. % TPST : FA : Pluronic® F127 blends recorded at 80 °C.

To generate the acid from the blends of TPST, FA, and Pluronic® F127, the drop cast films must be irradiated with 254 nm UV-light at elevated temperatures of 80 °C to avoid crystallization of the (PEO) segment of the Pluronic® F127 template. The SAXS profiles of the TPST, FA, and Pluronic® F127, provided in Figure 6.5, showed that ordering of the Pluronic® F127 template was present after irradiation at 254 nm UV-light due to the presence of the primary peak. The incorporation of additional FA did not alter

the domain spacing of the Pluronic® F127 template, even at loadings of 80 wt. % FA. It should be noted here that the SAXS profiles in Figure 6.5 were acquired prior to the SAXS instrument being repaired and the SAXS detector being rebuilt, which may explain the signal to noise issue present in Figure 6.5.

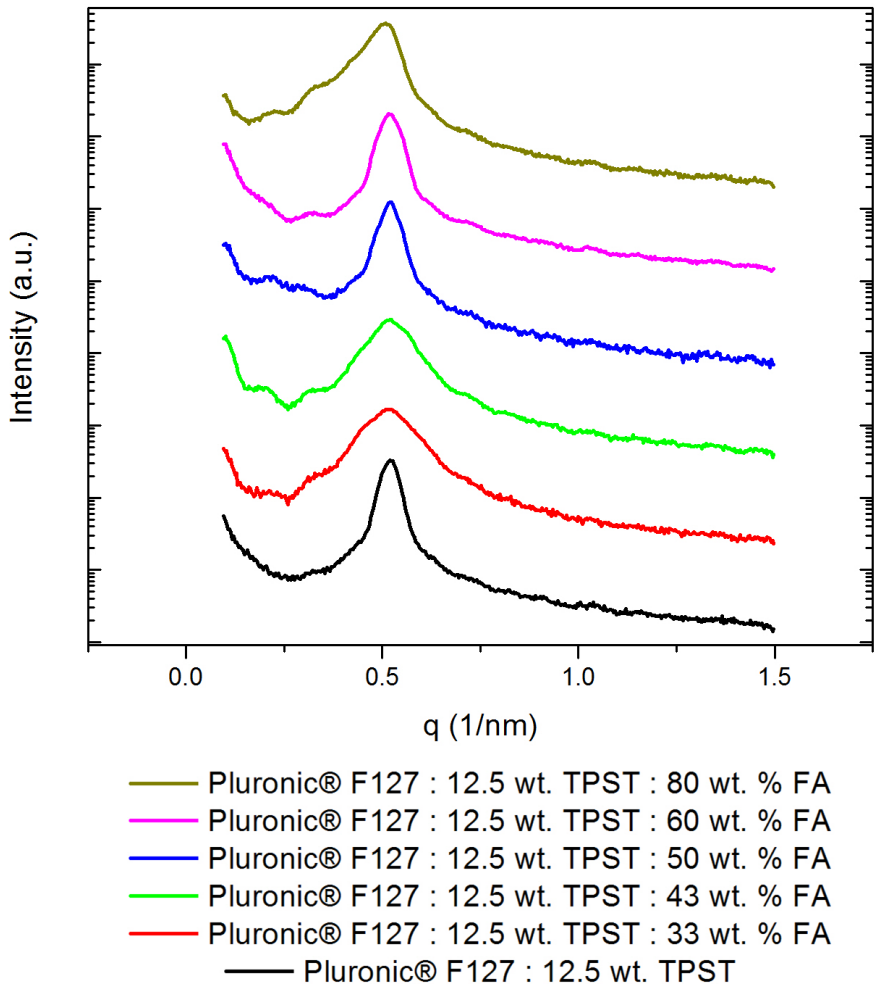

Figure 6.5. SAXS profiles of 12.5 wt. % TPST : FA : Pluronic® F127 blends, after irradiation of 254 nm UV-light, recorded at 80 °C.

Even though there is more research to be performed on this research project, such as confirmation of the FA selectively incorporating into the PEO segment of the Pluronic® template (confirmed through suppression of PEO crystallization as determined

by differential scanning calorimetry (DSC)) and Fourier transform infrared (FT-IR) spectroscopy to confirm the polymerization of FA, the initial research performed here appears promising. The next logical research endeavors for this research project would be the incorporation of dopant materials, in the form of metal oxide nanoparticles and/or precursors, to increase the electrochemical storage capacity as well as the patterning of the blend materials through UV-assisted nanoimprint lithography (UV-NIL).

6.3.2. Patterning of Solid Oxide Fuel Cell Electrodes

The need for electrochemical energy conversion and storage devices such as fuel cells, batteries, and capacitors has never been greater. The interest in electrochemical energy systems comes from advantages over traditional energy conversion systems such as increased energy efficiencies, increased volumetric energy densities, and reduced pollution generation[12–14]. Fuel cells have generated a tremendous amount of interest for applications such as transportation vehicles, mobile and stationary power generation units, and portable electronic devices[13,14]. Fuel cells come in a variety of types and are typically application dependent due to the form of electrolyte used, operation temperature range, and type of fuel required. Several types of fuel cells currently available are polymer electrolyte or proton exchange membrane fuel cells (PEMFC), direct methanol fuel cells (DMFC), alkaline fuel cells (AFC), phosphoric acid fuel cells (PAFC), molten carbonate fuel cells (MCFC), and, of particular interest to this dissertation section, solid oxide fuel cells (SOFC)[15].

The basic structure of a SOFC consists of two electrodes, anode and cathode, that are connected by an electrolyte, typically a non-porous ceramic material, to complete the

circuit and transfer electrons. The construction of a typical electrochemical cell is shown in Figure 6.6.

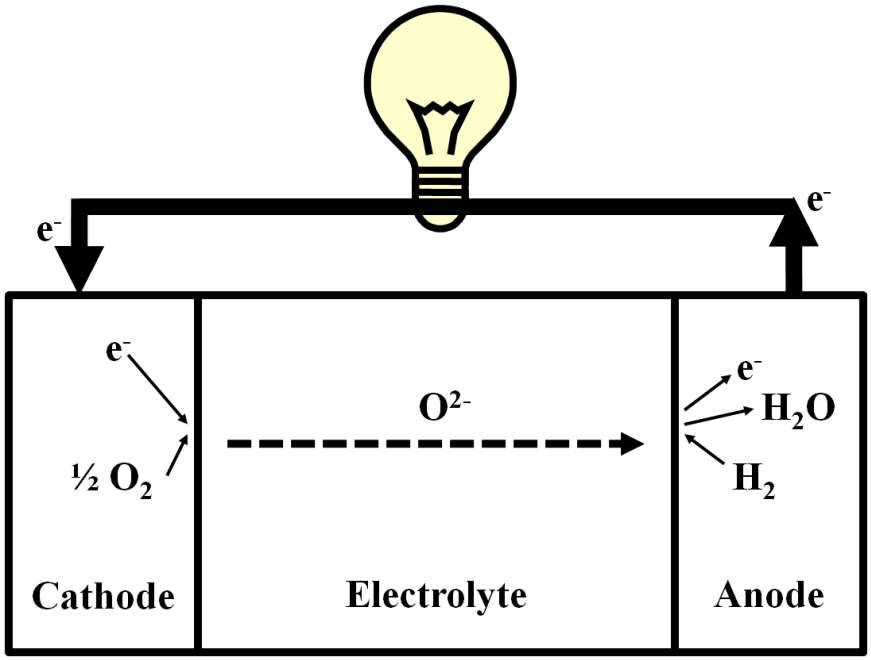

Figure 6.6. Schematic diagram of standard operation for a SOFC.

Over the last decade, much effort has been put forth to reduce the overall structural dimension of SOFCs through microfabrication techniques. The term micro solid oxide fuel cell (μ-SOFCs) is often used when SOFCs are produced with microfabrication techniques. This reduction in magnitude has potential to achieve reduced ohmic and transport losses, increase the volumetric energy and power densities, improve energy conversion efficiency, reduce operation temperature, and unlock new applications[12]. There is also interest in developing well-defined, geometry controlled, nanostructured electrodes and electrolyte materials to improve performance and provide electrodes for modeling of parameters such as oxygen reduction, diffusion length, and nano-ionic effects[16–18]. Patterning the interface created between the electrode and the electrolyte material in μ-SOFCs with nanoscopic features, achievable with NIL, is of

interest. The use of NIL would allow well-defined, dense features to be generated as electrode structures as well as providing enhanced control over the cathode electrolyte interface, surface area, and conduction path length.

Previous research performed on patterning the interface between the electrode and the electrolyte has been conducted by photolithography methods to yield structures on the order of 5 μm to 100 μm in size[19–23]. Through this patterning of the electrodes, improved conductivities have been observed that are in direct relation to the pattern size of the interdigitated electrode[17]. NIL has previously been used to pattern the electrode of micro fuel cell devices, by Guo et al. in 2007, but this study did not include any work for μ-SOFCs[16]. It is believed that if electrode patterning on the micron scale has increased the conductivity, the patterning of electrodes on the nanometer scale should drastically increase the conductivity of μ-SOFCs. The goal of this research project is to further elaborate on this research by applying NIL techniques to generate patterned electrodes for μ-SOFCs.

The initial effort for this research project was to generate an interdigitated electrode mold for NIL, with sub-micron features, by electron beam lithography (EBL). A significant amount of effort was dedicated to the making of an interdigitated electrode mold for NIL but was deemed inappropriate due to the amount of time and cost it was requiring. An alternative approach to measure the conductivity of the μ-SOFC was taken that did not require an interdigitated electrode design but rather only a line array[19]. A standard bi-layer lift-off NIL process was used such that the lift-off layer was poly(2-hydroxyethyl methacrylate) (pHEMA) and the imprint layer was Norland Optical Adhesive 60 (NOA60). The pHEMA was spin-coated first followed by the spin-coating

of NOA60. The NOA60 was then patterned through a process called easy soft imprint nanolithography (ESINL)[24] which was followed by sufficient reactive ion etch (RIE) processing with oxygen (O_2) plasma to expose the underlying substrate. The metal of choice, i.e. platinum, was then deposited, typically through electron beam evaporation, to a specific thickness and the patterned metal deposited sample was placed in a solvent, i.e. methanol at elevated temperatures, to remove the lift-off layer of pHEMA while simultaneously experiencing ultrasonication. The substrate of intereset was the YSZ electrolyte and several YSZ substrates were used for the patterning of platinum electrodes with the difference being surface roughness. The patterning of platinum electrodes on rough YSZ, shown in Figure 6.7, did not allow for uniform lift-off of the deposited platinum metal, as shown in the optical microscopy image where the dark regions represent the areas where platinum was not removed. When the substrate was switched to polished YSZ, the deposited platinum metal was capable of complete lift-off to yield a patterned platinum electrode YSZ substrate, shown in Figure 6.8.

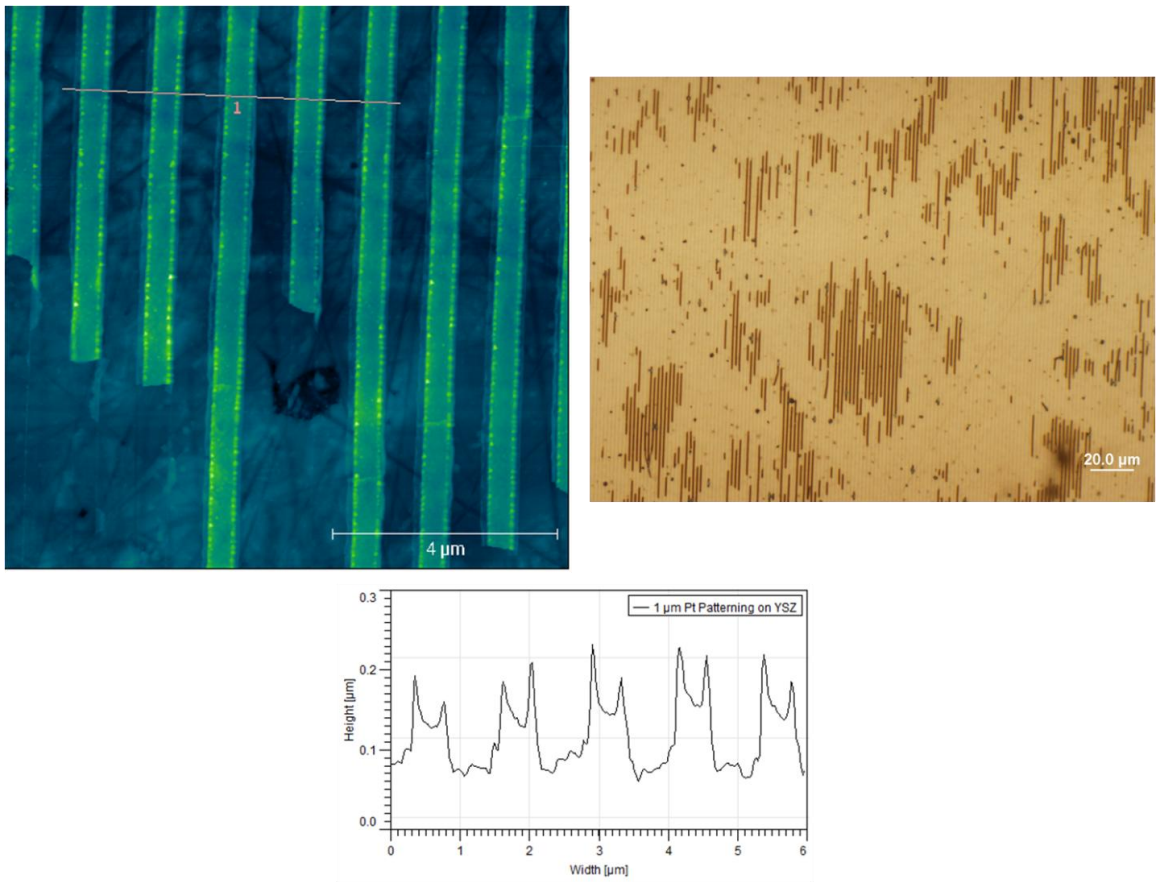

Figure 6.7. Lift-off of platinum electrode on rough YSZ substrate. AFM image (top left) and height profile (bottom) with optical microscopy image (top right).

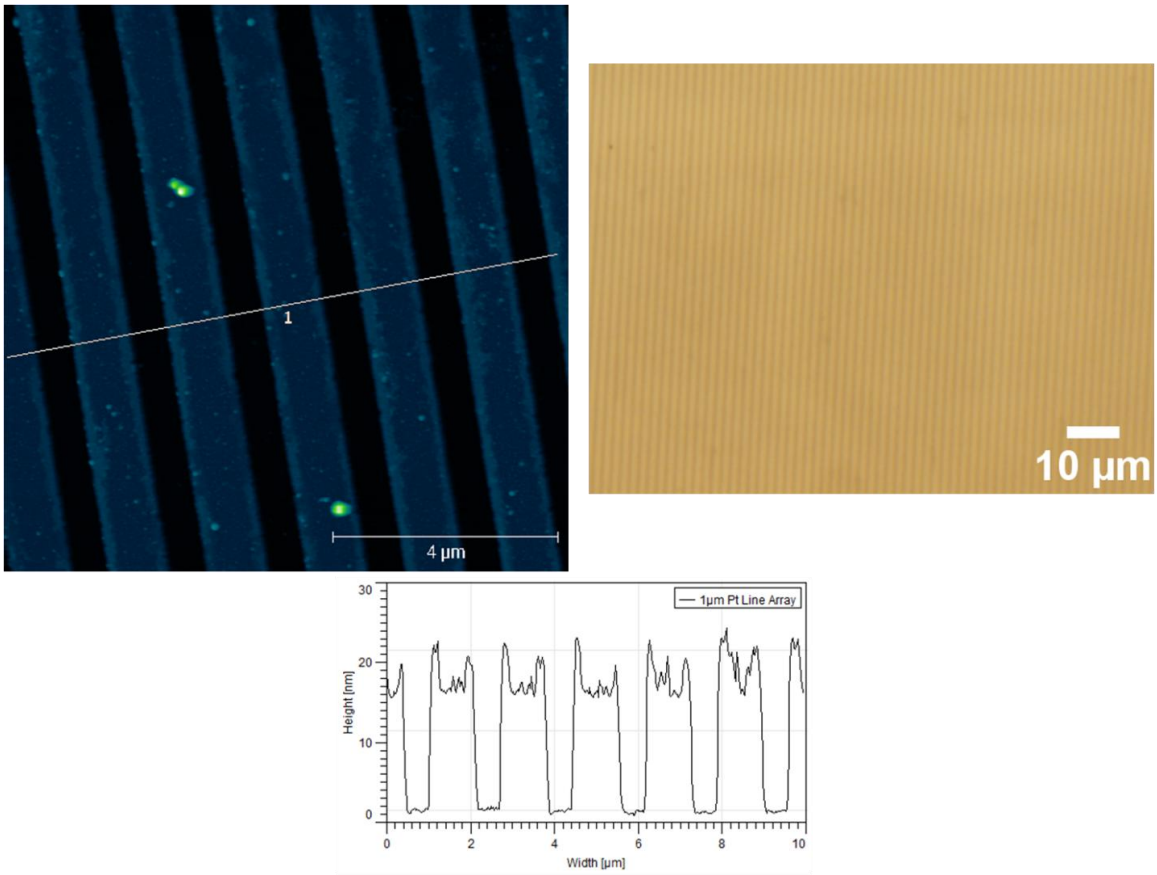

Figure 6.8. Lift-off of platinum electrode on polished YSZ substrate. AFM image (top left) and height profile (bottom) with optical microscopy image (top right).

This research project shows imminent promise with the next step for this research being the conductivity measurements of the reduced dimension platinum electrodes. The research could continue on with endeavors into various SOFC electrode materials, further reduced dimensions of the electrode, and perhaps structuring of the YSZ electrolyte material rather than the electrode to increase the surface area and the triple phase boundary.

The research presented here regarding the patterning of SOFC electrodes was done in collaboration with David Mesguich and Quentin Le Trequesser of Dr. Cyril Aymonier's research group at the Institut de Chimie de la Matière Condensée de

Bordeaux (ICMCB), a Centre National de la Recherche Scientifique (National Center for Scientific Research) in Bordeaux, France.

6.4. Collaborative Research Projects

6.4.1. Construction of Titanium Dioxide Nanochannels Using Nanoimprint Lithography and Supercritical Fluid Deposition

Early in the twentieth century, the primary role of titanium dioxide materials was for use as a pigment[25,26] for applications varying from paints to sunscreens. The discovery by Fujishima and Honda in 1972[27] that titanium dioxide materials were capable of photocatalytically splitting water, while under irradiation of UV-light, has lead to a tremendous amount of research interest over the last several decades. To further enhance the photoactivity of titanium dioxide, a significant amount of research has been performed, via various synthetic strategies[28,29], to create unique and tunable nanomaterial morphologies, such as nanoparticles, nanorods[30], and nanoplatelets[31], as well as various nanostructures such as nanotubes. Titanium dioxide has also been extensively researched in the form of thin films. Thin films of titanium dioxide are capable of being produced by numerous methods such as chemical vapor deposition (CVD), physical vapor deposition (PVD), atomic layer deposition (ALD), plasma enhanced chemical vapor deposition (PECVD), sputtering, ion beam, dip-coating, spin-coating, and evaporation, to just name several.

To further extend the capability of deposition techniques to deposit titanium dioxide thin films, a technique known as supercritical fluid deposition (SFD) was developed by Watkins et al.[32,33] SFD utilizes a supercritical fluid, typically $scCO_2$ due to the easily accessible supercritical parameters, as the reaction medium to perform surface

selective, conformal depositions of titanium dioxide thin films. SFD is not limited to the deposition of only titanium dioxide thin films but has been shown to produce thin films of metals[32,33], metal oxides[34,35], and alloys as well as doped metals and metal oxides[36]. To add an additional function to the SFD deposition of titanium dioxide thin films, the fabrication of titanium dioxide nanochannels, thorugh the combination of SFD and nanoimprint lithography (NIL), as depicted in Figure 6.9, was attempted and will be further elaborated upon within this dissertation section.

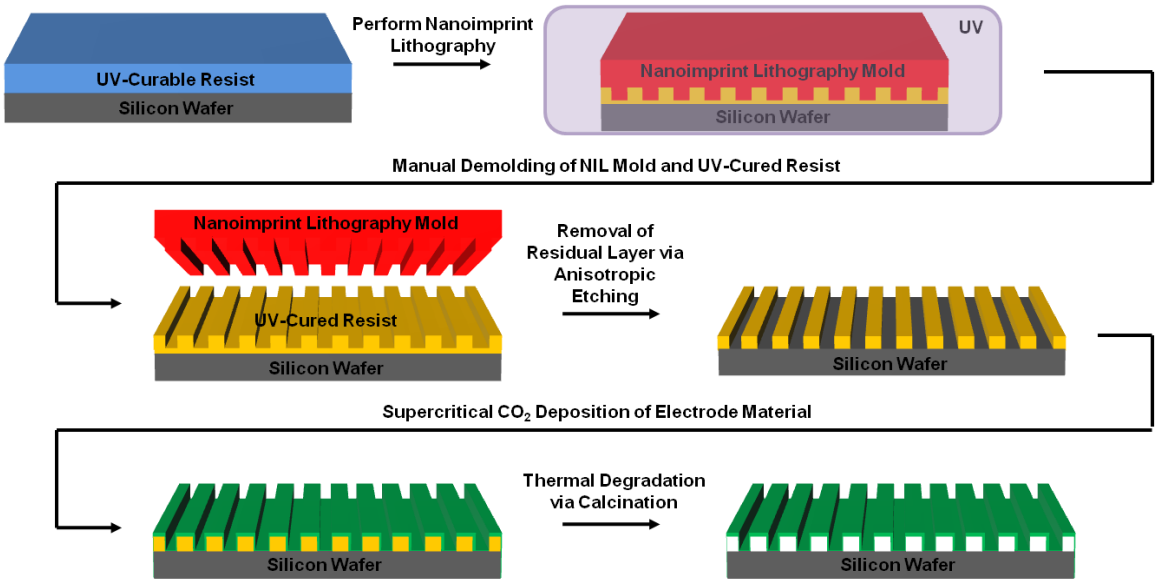

Figure 6.9. Schematic depicting the fabrication procedure of titanium dioxide nanochannels through the combination of SFD and NIL.

To begin the fabrication of titanium dioxide nanochannels through the combination of SFD and NIL, the deposition conditions of titanium dioxide from SFD needed to be well understood. To successfully create a titanium dioxide matrix, water was required to perform the hydrolysis of the titanium dioxide precursor of titanium diisopropoxide bis(2,2,6,6-tetramethyl-3,5-heptanedionato), (Ti (O^iPr)$_2$(tmhd)$_2$). For the SFD deposition of titanium dioxide, Coleman grade carbon dioxide (CO_2) was used,

which has a reported water impurity of less than 10 ppm, and has previously been shown to successfully deposit titanium dioxide thin films from SFD[34].

The SFD of titanium dioxide thin films required elevated temperatures, typically greater than 150 °C, to generate dense titanium dioxide thin films. To successfully deposit titanium dioxide from SFD on patterned polymer templates from NIL, the thermal properties of the photopolymer were investigated. Thermogravimetric analysis (TGA) was performed to confirm that the crosslinked photopolymer of choice (NOA60) would withstand the deposition temperatures, as high as 250 °C, used for SFD. From the TGA graph, Figure 6.10, only a 5 % mass lose was observed for NOA60. However, the elevated temperatures of the SFD processing imparted mobility to the crosslinked photopolymer, as shown in the differential scanning calorimetry (DSC), Figure 6.11, such that the edges of the NIL features were slightly rounded, as shown in scanning electron microscopy (SEM) images, Figure 6.12.

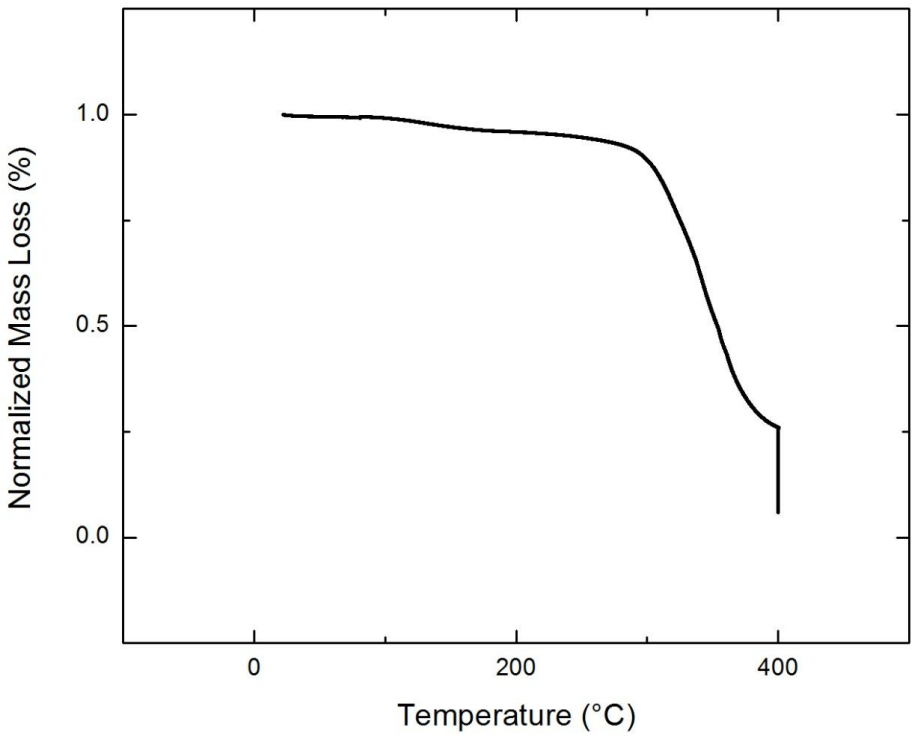

Figure 6.10. TGA of NOA60 photopolymer after UV-irradiation at 365 nm UV-light (13 mW/cm^2) for 15 minutes. TGA data shows that only ~ 5 % mass loss at 250 °C.

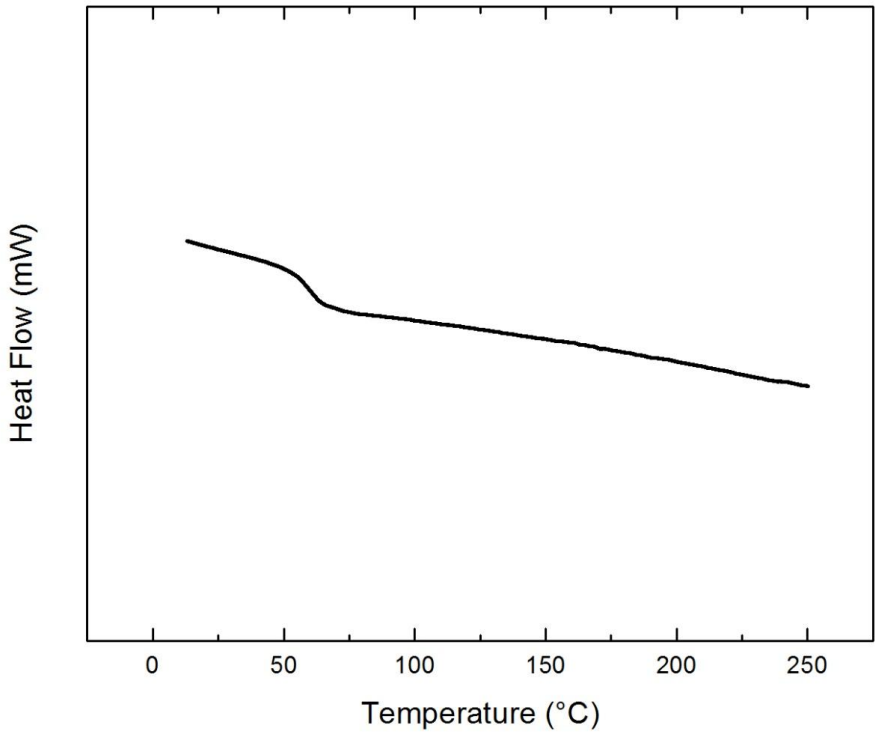

Figure 6.11. DSC of NOA60 after UV-irradiation at 365 nm UV-light (13 mW/cm^2) for 15 minutes.

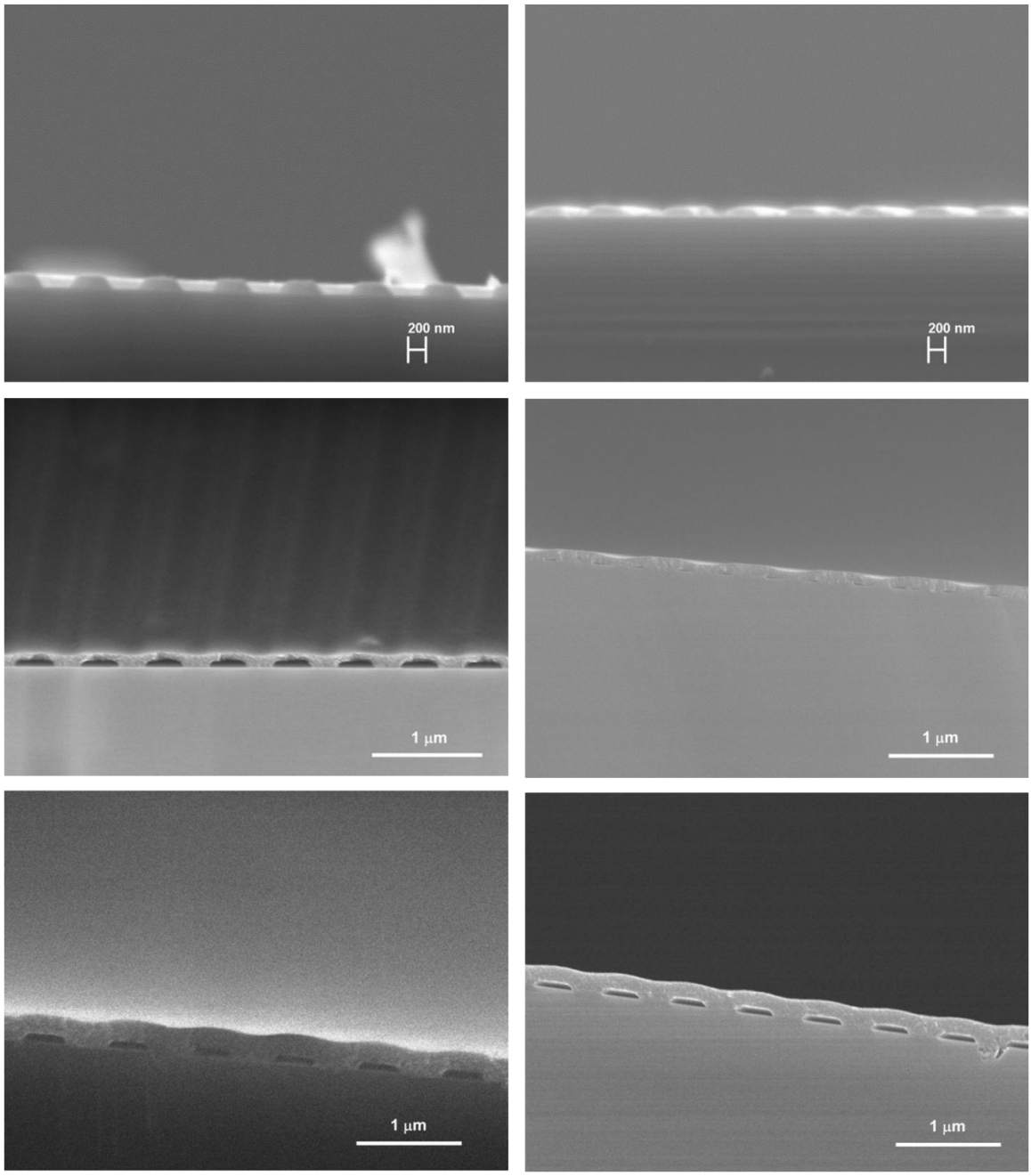

Figure 6.12. Cross-sectional SEM images for patterned NOA60 (top left), patterned NOA60 after experiencing SFD without titanium dioxide precursor (top right), SFD deposited titanium dioxide on patterned NOA60 (middle left), calcination of SFD deposited titanium dioxide on patterned NOA60 (middle right), hydrothermally treated SFD deposited titanium dioxide on patterned NOA60 (bottom left), and calcination of hydrothermally treated SFD deposited titanium dioxide on patterned NOA60 (bottom right).

After deposition of the titanium dioxide thin film from SFD, the crosslinked NOA60 must be removed to generate the nanochannel structure. From the TGA data in Figure 6.10, the crosslinked NOA60 was completely removed at 400 °C under ambient conditions. Based on the TGA data, a thermally degradation, i.e. calcination, procedure, of 1.56 °C/minute ramp rate to a final temperature of 400 °C, hold for 6 hours at 400 °C, and 1.56 °C/minute ramp rate to room temperature was used to thermally degrade the crosslinked NOA60. After calcination of the titanium dioxide deposited on the NOA60 NIL templates, the cross-sectional SEM images, Figure 6.12, showed that the nanochannels were collapsing, resulting in irregularly shaped nanochannels underneath the titanium dioxide thin film. The loss of integrity to the nanochannel structure may arise from to two competing processes during the calcination; the thermal degradation of the crosslinked NOA60 and the densification and/or crystallization of the amorphous titanium dioxide thin film. During the calcination process, it was observed that the titanium dioxide thin films became thinner, which was a result from the densification of the titanium dioxide at elevated temperatures.

To prevent the titanium dioxide nanochannels from collapsing at elevated temperatures, a hydrothermal crystallization step was added to the fabrication process prior to the calcination procedure. With the hydrothermal treatment, the amorphous titanium dioxide thin film was exposed to a superheated water vapor, which allowed the titanium dioxide thin film to densify and crystallize before removing the sacrificial support structure of the crosslinked NOA60. Once the titanium dioxide thin film had undergone the hydrothermal treatment procedure, the crosslinked NOA60 was removed by calcination, which further condensed the titanium dioxide matrix to yield a free

standing titanium dioxide nanochannel. To confirm that the amorphous titanium dioxide was experiencing crystallization, X-ray diffraction (XRD), shown in Figure 6.13, was performed. The as deposited titanium dioxide thin film from SFD was initially amorphous, however, after the hydrothermal treatment, the titanium dioxide thin film crystallized into the anatase phase of titanium dioxide, according to the literature (titanium dioxide, anatase phase, 00-021-1272). When the hydrothermally treated titanium dioxide thin film underwent the calcination procedure, the anatase crystalline phase remained[37].

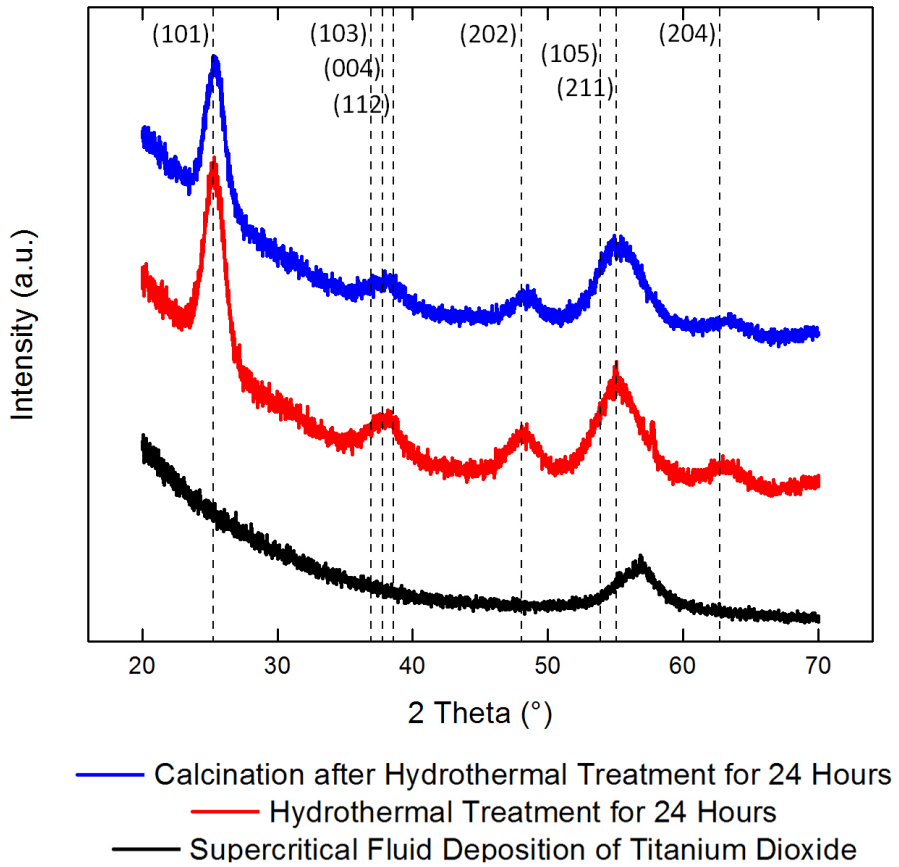

Figure 6.13. XRD patterns for the fabrication of titanium dioxide nanochannels.

To study the chemical composition of the titanium dioxide thin film throughout the fabrication procedure, X-ray photoelectron spectroscopy (XPS) sputter depth profiling was performed. The carbon content of the titanium dioxide nanochannels, after the calcination procedure, was negligible, regardless if the hydrothermal treatment was performed or not, which supports that the titanium dioxide nanochannels were free of NOA60 template. The XPS sputter depth profiling of the hydrothermally treated titanium dioxide nanochannels, shown in Figure 6.14, indicated that silicon was incorporated within the bulk of the titanium dioxide thin film. It is shown that the silicon incorporation occurred during the hydrothermal treatment procedure because XPS sputter depth profiling of the as deposited titanium dioxide from SFD as well as the titanium dioxide after calcination showed no silicon incorporation.

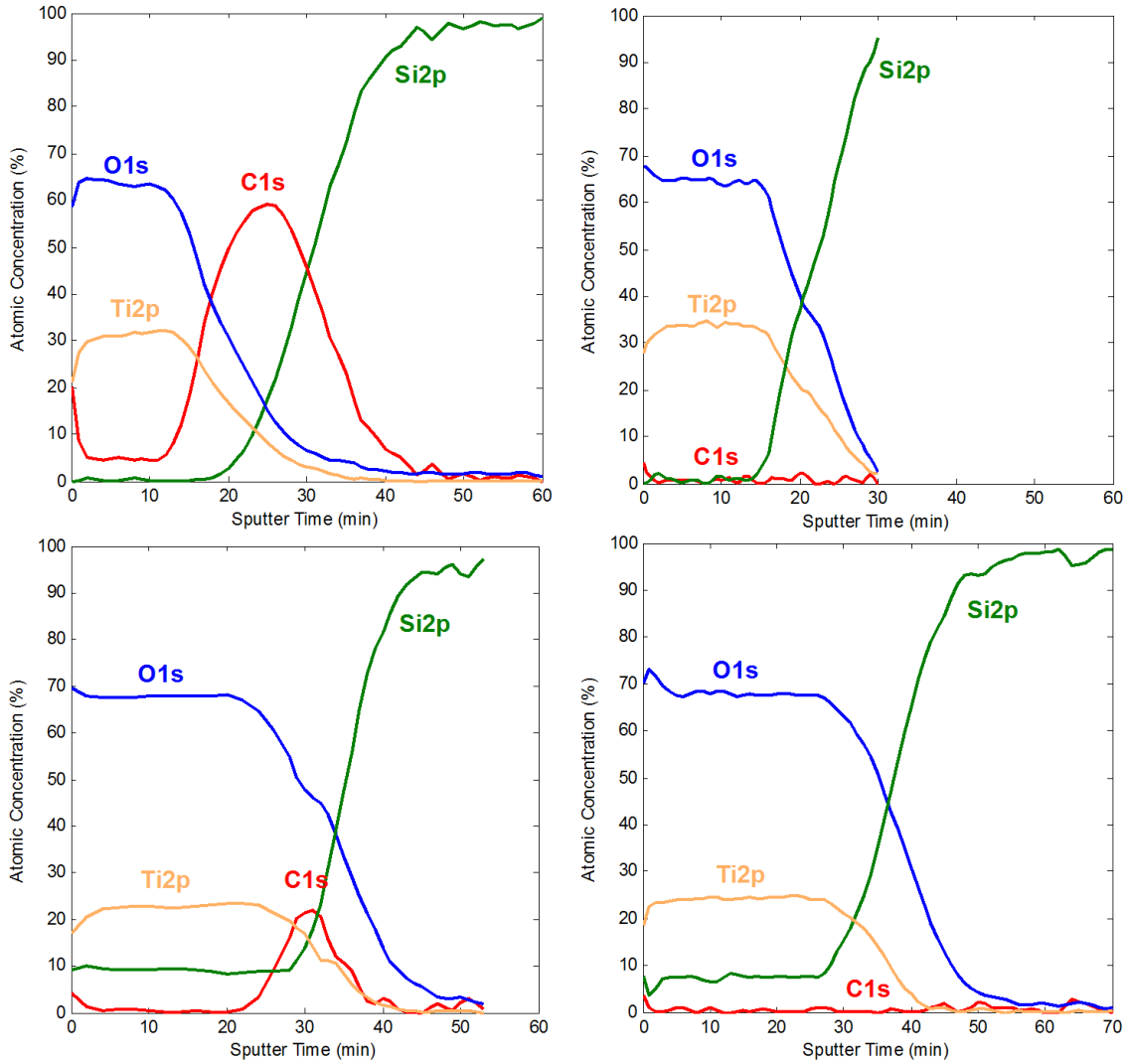

Figure 6.14. XPS sputter depth profiling of the SFD deposited titanium dioxide thin film (top left), calcination of SFD deposited titanium dioxide thin film (top right), hydrothermally treated SFD deposited titanium dioxide thin film (bottom left), and calcination of hydrothermally treated SFD deposited titanium dioxide thin film.

From the hydrothermal treatment, not only did the crystallization of titanium dioxide thin film occur, the silicon wafer appeared to be oxidizing as well. It is well known in the microelectronics field that the thermal oxidation of silicon is easily achieved by heating the wafer to a high temperature, typically 900 °C to 1200 °C, in an atmosphere containing either pure oxygen or water vapor. As silicon is consumed with the oxide growth, the resulting oxide layer grows in thickness. However, given the fact that the hydrothermal

treatment performed at 120 °C was performed within a confined and high-pressure environment, the oxidation of silicon may still have occurred seeing that the titanium dioxide thin film was crystallized to the anatase phase at temperatures several hundred degrees Celsius lower than the anticipated crystallization temperature of 450 °C. Figure 6.15 shows the XPS spectra of the silicon 2p region for the titanium dioxide film after argon (Ar^+) sputtering for different periods of time. From the XPS sputter depth profile, the silicon in the titanium dioxide thin film formed an oxidized version of silicon of either silicate or silica. From Figure 6.15, the XPS sputter depth profile showed that the silicon oxide layer migrated into the titanium dioxide thin film after experiencing the hydrothermal treatment.

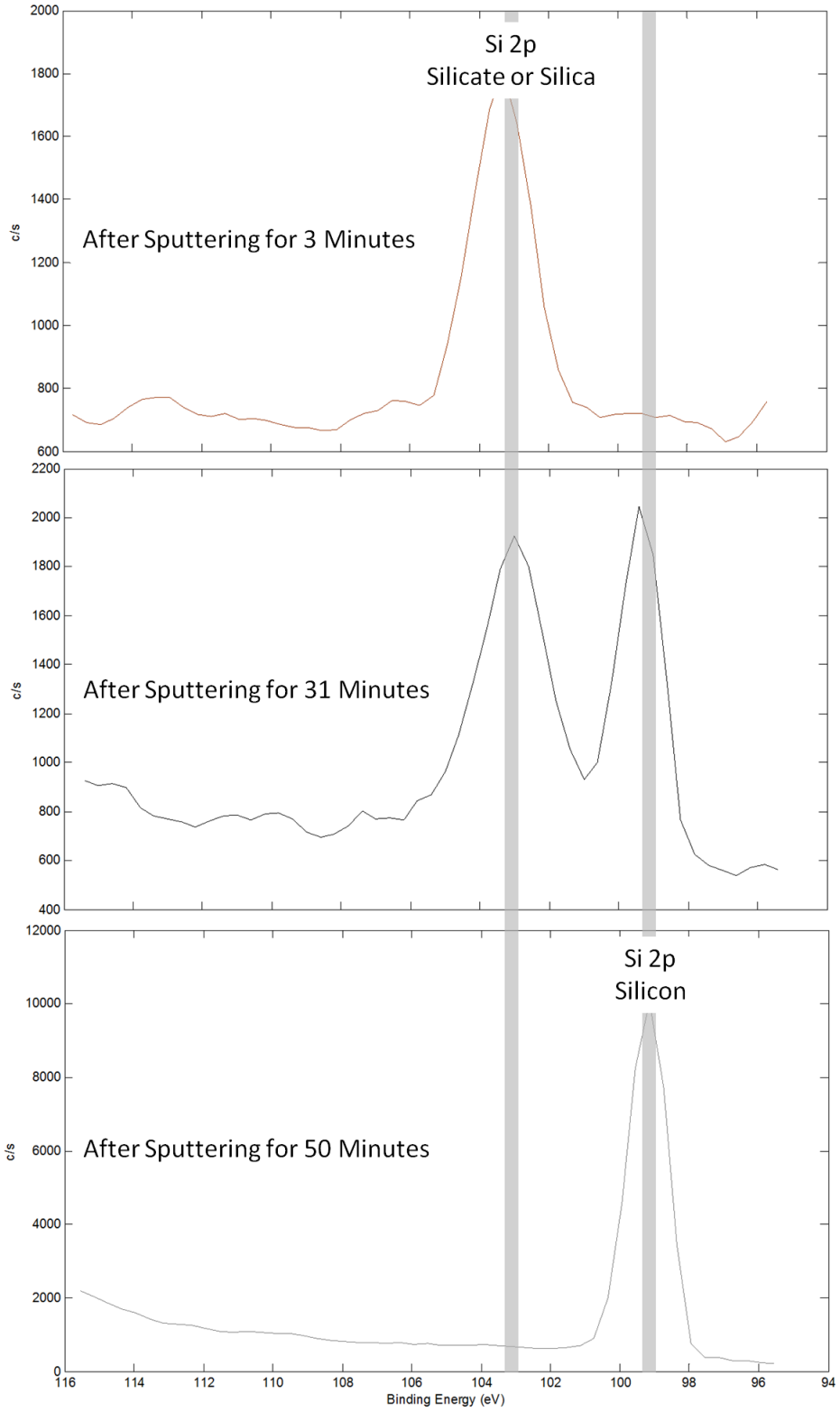

Figure 6.15. XPS spectra of the silicon regions for various sputtering times.

To confirm the removal of the crosslinked photopolymer, GATR-FT-IR was utilized systematically after each fabrication step and is shown in Figure 6.16. The infrared (IR) signal for the titanium dioxide thin film framework, i.e. Ti-O-Ti, was expected between 900 cm^{-1} and 500 cm^{-1}, which was observed, and without the presence of any organic material from the NOA60, which was observed as well. Two additional comments regarding Figure 6.16, the degree of condensation from the hydrothermal treatment was immense due to the intensity of the Ti-O-Ti peaks as well as the lack of intensity for the titanium hydroxyl peak between 3800 cm^{-1} and 3000 cm^{-1}.

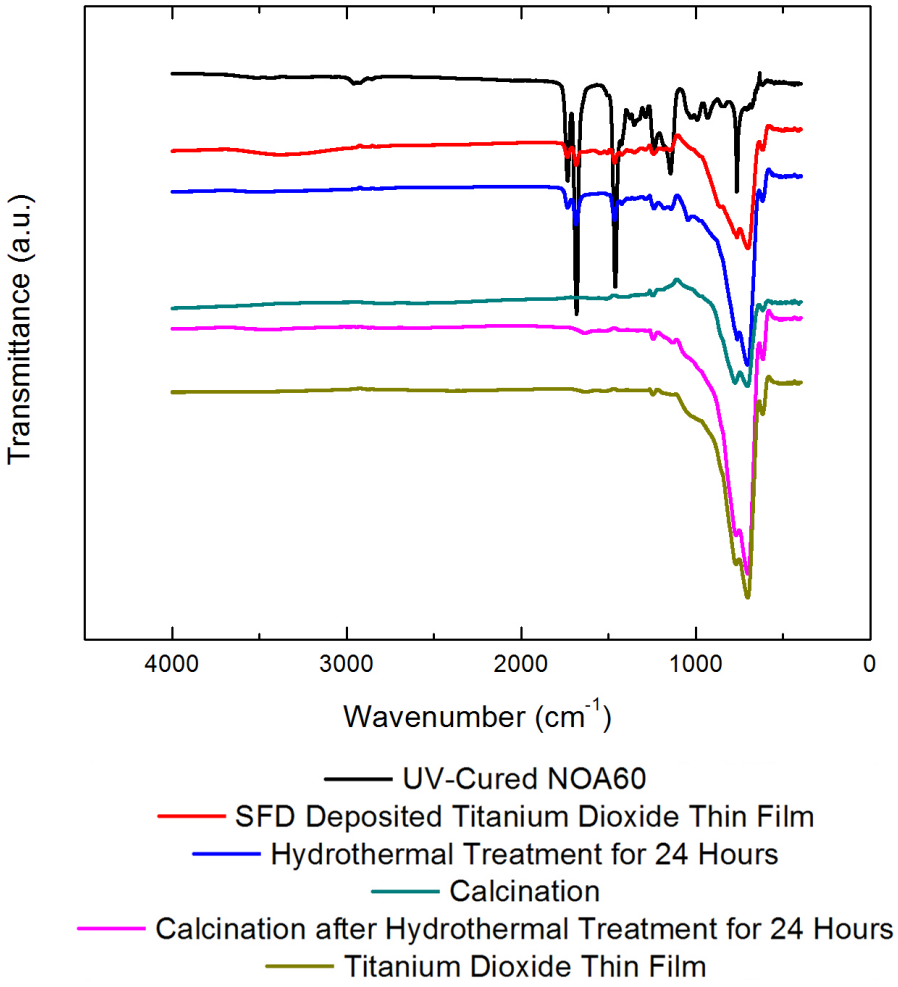

Figure 6.16. GATR-FT-IR spectra of titanium dioxide nanochannels through the various processing steps.

In conclusion, the combination of SFD with NIL enabled a unique preparation for nanochannel arrays embedded within the titanium dioxide matrix. The geometries and dimensions afforded to the NIL technique allow for adaptation to multiple application platforms, especially when coupled with SFD, which allows for various metal oxides as well as metals to be deposited in an efficient manner. With the flexibility afforded to SFD, i.e. capable of depositing materials at relatively low temperatures and with

moderate deposition rates, and NIL, i.e. geometries and dimensions depending only on the mold, there are numerous combinations of nanochannel structures that could be created.

The research presented within this dissertation section was performed in collaboration with Eun Young You of James J. Watkins' research group.

6.4.2. Continuous Processing of Porous Metal Oxide Films with Plasma Enhanced Rapid Expansion of Supercritical Solutions / Supercritical Solution Precursor Plasma Spraying

Nanostructured films of metal oxides are an important class of materials for applications that require high surface areas such as energy harvesting and catalysis. The metal oxide materials of interest for such applications are titanium dioxide, iron oxide, and cerium oxide, while the nanostructure of interest is that of a porous dendritic structures which provide high surface areas while supported on a substrate. Within the research group of James J. Watkins, a procedure called plasma enhanced rapid expansion of supercritical solutions (PRESS) or supercritical solution precursor plasma spraying (scSPPS) is capable of producing dendritic structures of metal oxide materials. For more information regarding PRESS/scSPPS, please refer to the dissertations of Christos F. Karanikas and Eun Young You.

The research presented within this dissertation section was a continuation of the initial research efforts for PRESS/scSPPS in which the process is altered from a batch process to a continuous process. The general schematic for the continuous processing of porous metal oxide films from PRESS/scSPPS is shown in Figure 6.17. The principle of the PRESS/scSPPS continuous process was to have separate lines for the supercritical fluid, i.e. scCO_2 and the precursor solution, i.e. saturated alcohol solutions of metal salts.

The $scCO_2$ and precursor met within a mixing chamber to allow for sufficient combination to create a saturated $scCO_2$ precursor solution which travelled through metering valves to expand across a nozzle and into a plasma field.

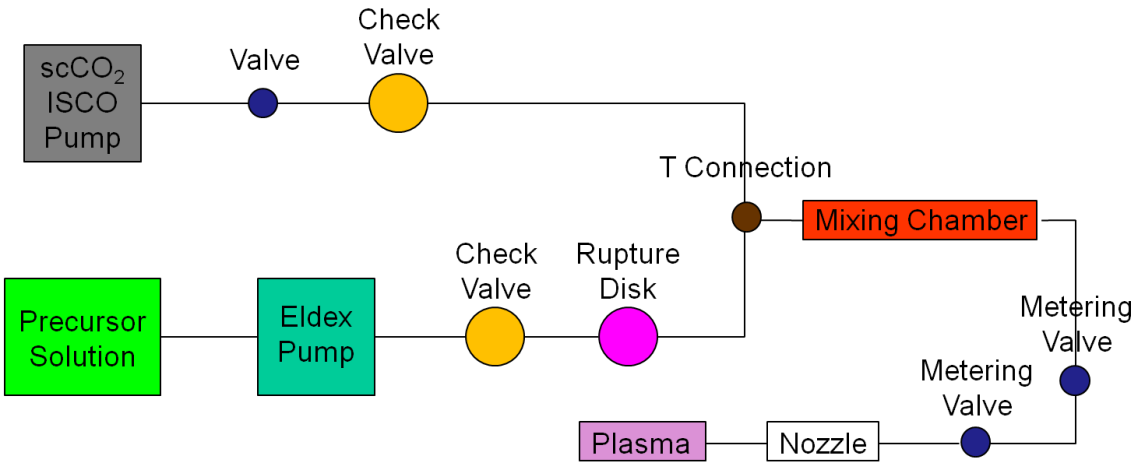

Figure 6.17. General schematic for the continuous processing of porous metal oxide films from PRESS/scSPPS.

The materials of interest for the continuous processing of PRESS/scSPPS were that of cerium oxide, iron oxide, and cobalt oxide. Dendritic structures of each of the aforementioned metal oxides were successfully fabricated, as shown by the cross-sectional SEM images in Figure 6.18.

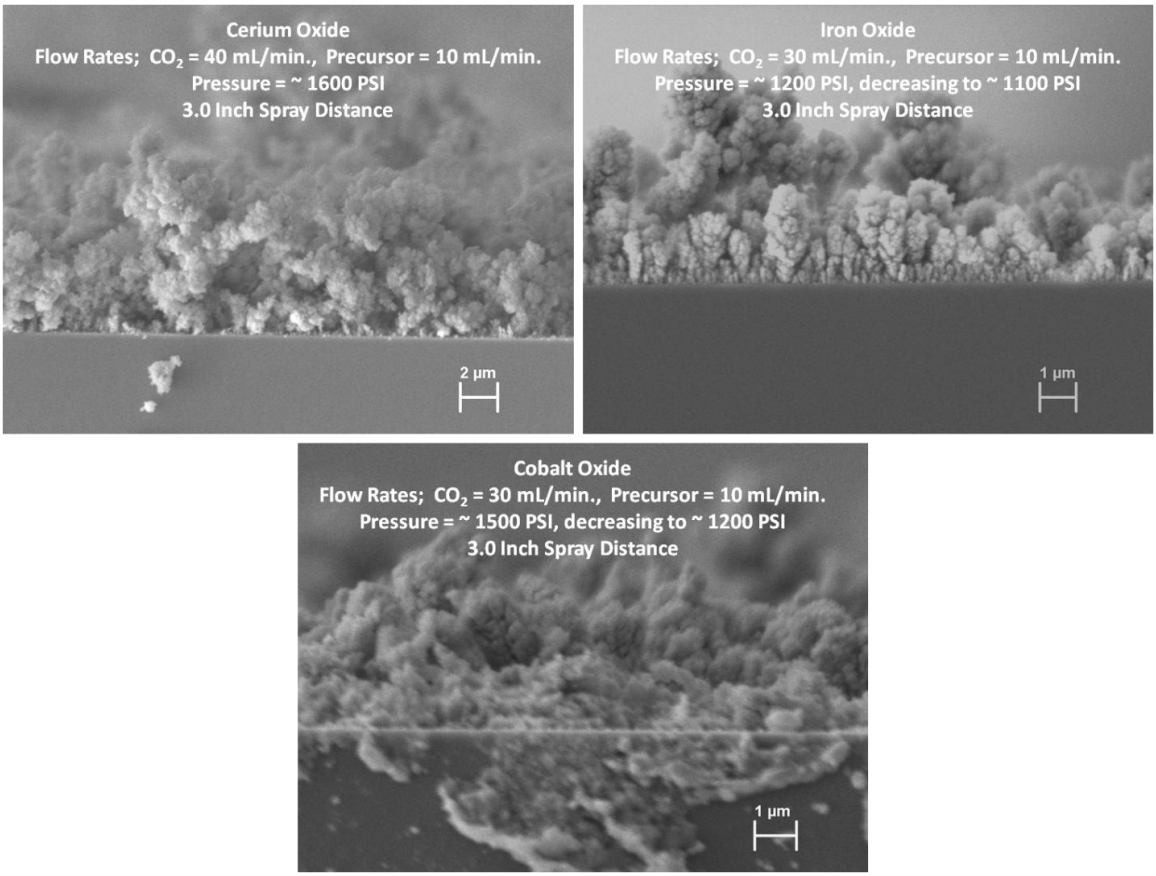

Figure 6.18. Cross-sectional SEM images of continuous processing of PRESS/scSPPS for cerium oxide (top left), iron oxide (top right), and cobalt oxide (bottom).

The initial proof of concept experiments showed that the batch processing of PRESS/scSPPS could be applied to a continuous process while yielding dendritic structures of metal oxide films. Further research endeavors for this research project would have focused on evaluating the continuous processing conditions, such as flow rates of both $scCO_2$ and precursor solution, ratios of $scCO_2$ to precursor, and overall flow rate of the saturated $scCO_2$ precursor solution. With a better understanding of the continuous processing parameters, the focus would have then shifted to the applications of photocatalytic water splitting, photocatalytic degradation of organic materials, solid oxide fuel cell electrolytes, and dye-sensitized solar cells.

The research presented within this dissertation section was performed in collaboration with Eun Young You of James J. Watkins' research group.

6.5. References

(1) Haruta, M.; Kobayashi, T.; Sano, H.; Yamada, N. *Chemistry Letters* **1987**, 405–408.

(2) Budroni, G.; Corma, A. *Angewandte Chemie International Edition* **2006**, *45*, 3328–31.

(3) Hayashi, T.; Tanaka, K.; Haruta, M. *Journal of Catalysis* **1998**, *178*, 566–575.

(4) Mukherjee, P.; Patra, C. R.; Ghosh, A.; Kumar, R.; Sastry, M. *Chemistry of Materials* **2002**, *14*, 1678–1684.

(5) Mohr, C.; Hofmeister, H.; Radnik, J.; Claus, P. *Journal of the American Chemical Society* **2003**, *125*, 1905–1911.

(6) Romang, A. H. Ordered Nanomaterials and Supercritical CO2: Mechanically Enhanced Low-K Dielectric Materials and Ordered Block Copolymer Surfactant Systems, 2012.

(7) Liu, A. M.; Hidajat, K.; Kawi, S.; Zhao, D. Y. *Chemical Communications* **2000**, *15*, 1145–1146.

(8) Malibert, C.; Bach, S. *Thin Solid Films* **2002**, *418*, 79–84.

(9) Ryoo, R.; Joo, S. H.; Jun, S. *The Journal of Physical Chemistry B* **1999**, *103*, 7743–7746.

(10) Meng, Y.; Gu, D.; Zhang, F.; Shi, Y.; Yang, H.; Li, Z.; Yu, C.; Tu, B.; Zhao, D. *Angewandte Chemie International Edition* **2005**, *44*, 7053–9.

(11) Principe, M.; Martínez, R.; Ortiz, P.; Rieumont, J. *Polímeros* **2000**, *10*, 8–14.

(12) O', G. J. L.; In, H. J.; Crumlin, E.; Barbastathis, G. *International Journal of Energy Research* **2007**, *31*, 548–575.

(13) Litzelman, S. J.; Hertz, J. L.; Jung, W.; Tuller, H. L. *Fuel Cells* **2008**, *8*, 294–302.

(14) Brett, D. J. L.; Atkinson, A.; Brandon, N. P.; Skinner, S. J. *Chemical Society Reviews* **2008**, *37*, 1568–78.

(15) Carrette, L.; Friedrich, K. A.; Stimming, U. *ChemPhysChem* **2000**, *1*, 162–193.

(16) Taylor, A.; Lucas, B.; Guo, L.; Thompson, L. *Journal of Power Sources* **2007**, *171*, 218–223.

(17) Beckel, D.; Bieberle-Hütter, A.; Harvey, A.; Infortuna, A.; Muecke, U. P.; Prestat, M.; Rupp, J. L. M.; Gauckler, L. J. *Journal of Power Sources* **2007**, *173*, 325–345.

(18) Tietz, F.; Mai, A.; Stöver, D. *Solid State Ionics* **2008**, *179*, 1509–1515.

(19) Bieberle, A.; Meier, L. P.; Gauckler, L. J. *Journal of The Electrochemical Society* **2001**, *148*, A646.

(20) Hertz, J. L.; Tuller, H. L. *Journal of Electroceramics* **2004**, *13*, 663–668.

(21) Rothschild, A.; Litzelman, S. J.; Tuller, H. L.; Menesklou, W.; Schneider, T.; Ivers-Tiffée, E. *Sensors and Actuators B: Chemical* **2005**, *108*, 223–230.

(22) Bieberle-Hütter, A.; Sogaard, M.; Tuller, H. *Solid State Ionics* **2006**, *177*, 1969–1975.

(23) Hertz, J. L.; Rothschild, A.; Tuller, H. L. *Journal of Electroceramics* **2009**, *22*, 428–435.

(24) Moran, I. W.; Briseno, A. L.; Loser, S.; Carter, K. R. *Chemistry of Materials* **2008**, *20*, 4595–4601.

(25) Braun, J. H. *Journal of Coatings Technology* **1997**, *69*, 59–72.

(26) Pfaff, G.; Reynders, P. *Chemical Reviews* **1999**, *99*, 1963–1982.

(27) Fujishima, A.; Honda, K. *Nature* **1972**, *238*, 37–38.

(28) Chen, X.; Mao, S. S. *Journal of Nanoscience and Nanotechnology* **2006**, *6*, 906–925.

(29) Chen, X.; Mao, S. S. *Chemical Reviews* **2007**, *107*, 2891–2959.

(30) Cozzoli, P. D.; Kornowski, A.; Weller, H. *Journal of the American Chemical Society* **2003**, *125*, 14539–48.

(31) Shan, G.-B.; Demopoulos, G. P. *Nanotechnology* **2010**, *21*, 025604.

(32) Watkins, J. J.; Blackburn, J. M.; McCarthy, T. J. *Chemistry of Materials* **1999**, *11*, 213–215.

(33) Blackburn, J. M.; Long, D. P.; Cabanas, A.; Watkins, J. J. *Science* **2001**, *294*, 141–5.

(34) O'Neil, A.; Watkins, J. J. *Chemistry of Materials* **2007**, *19*, 5460–5466.

(35) Mesguich, D.; Aymonier, C.; Bassat, J.-M.; Mauvy, F.; You, E.; Watkins, J. J. *Chemistry of Materials* **2011**, *23*, 5323–5330.

(36) Le Trequesser, Q.; Mesguich, D.; You, E.; Aymonier, C.; Watkins, J. J. *The Journal of Supercritical Fluids* **2011**, *66*, 328–332.

(37) Hanaor, D. A. H.; Sorrell, C. C. *Journal of Materials Science* **2010**, *46*, 855–874.

APPENDIX I

THERMAL AND HYDROTHERMAL STABILITY OF MESOPOROUS SILICA DOPED WITH POSS-OAA

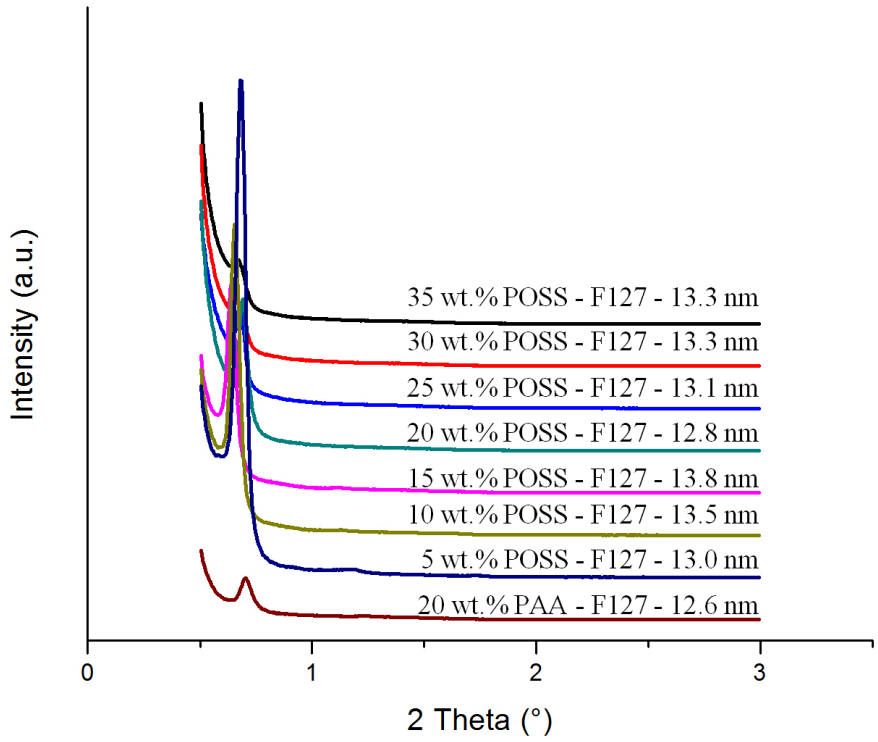

Figure S3.1. Infused, i.e. polymeric template present, mesoporous silica samples from the Pluronic® F127 template with various concentrations of POSS-OAA. D-spacing values shown.

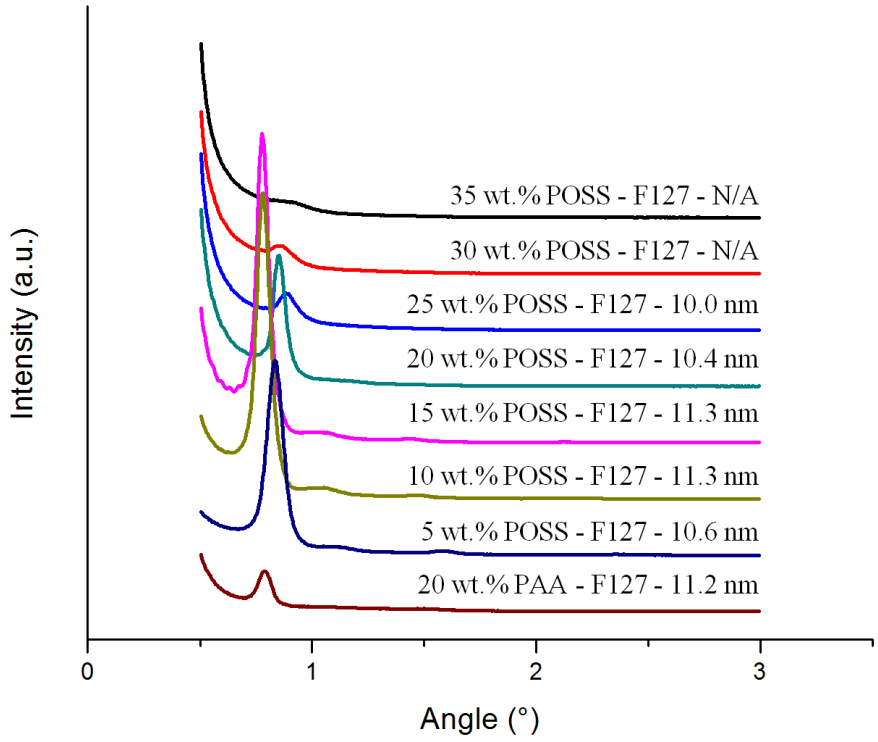

Figure S3.2. Mesoporous silica samples from the Pluronic® F127 template with various concentrations of POSS-OAA calcined, i.e. polymeric template absent, at 400 °C in air. D-spacing values shown.

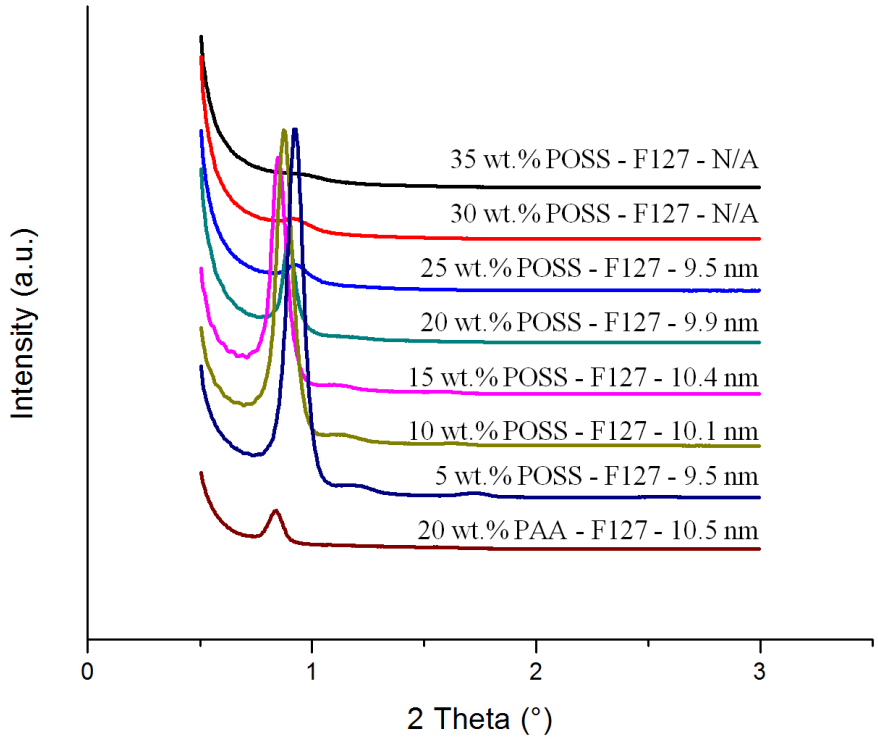

Figure S3.3. Mesoporous silica samples from the Pluronic® F127 template with various concentrations of POSS-OAA calcined, i.e. polymeric template absent, at 500 °C in air. D-spacing values shown.

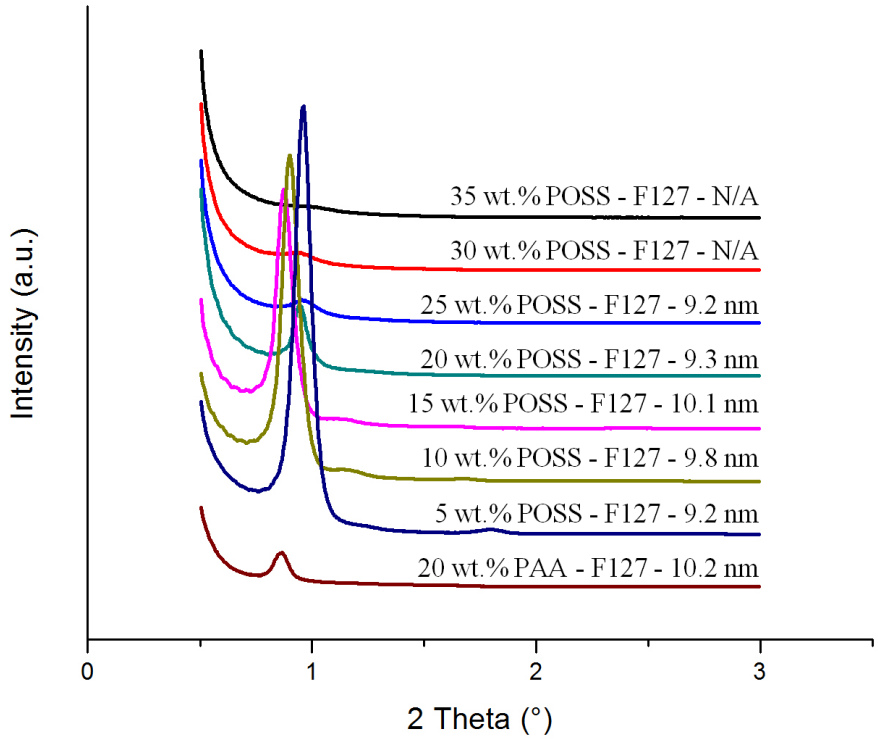

Figure S3.4. Mesoporous silica samples from the Pluronic® F127 template with various concentrations of POSS-OAA calcined, i.e. polymeric template absent, at 600 °C in air. D-spacing values shown.

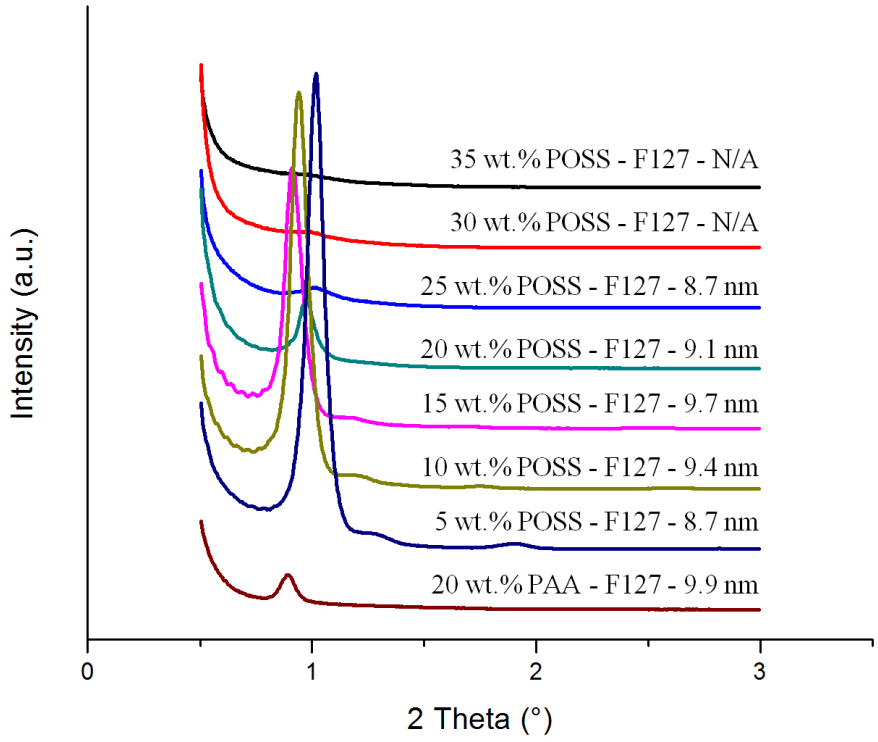

Figure S3.5. Mesoporous silica samples from the Pluronic® F127 template with various concentrations of POSS-OAA calcined, i.e. polymeric template absent, at 700 °C in air. D-spacing values shown.

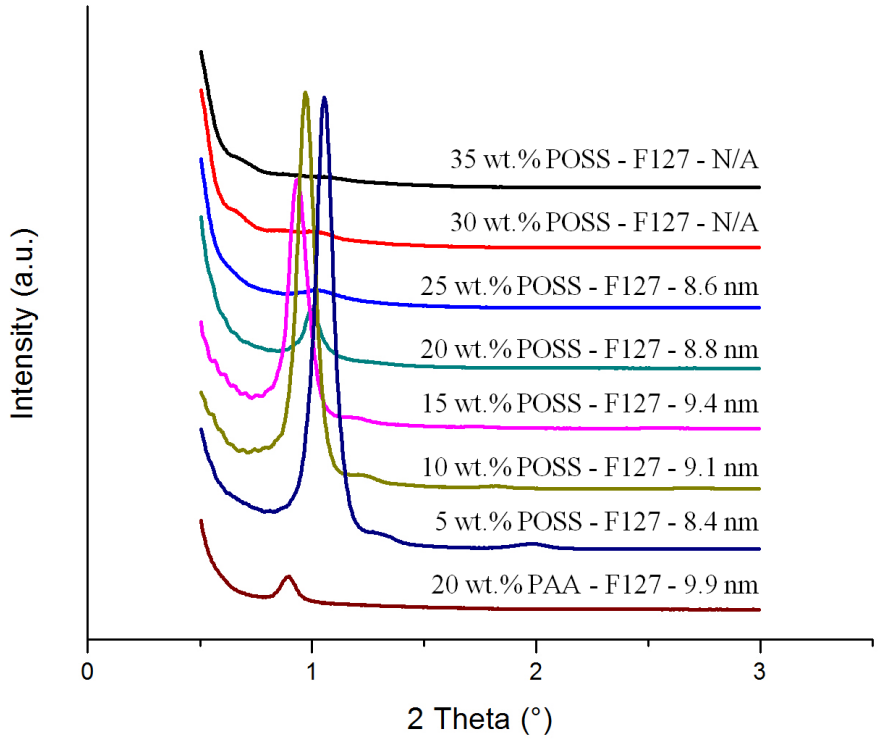

Figure S3.6. Mesoporous silica samples from the Pluronic® F127 template with various concentrations of POSS-OAA calcined, i.e. polymeric template absent, at 800 °C in air. D-spacing values shown.

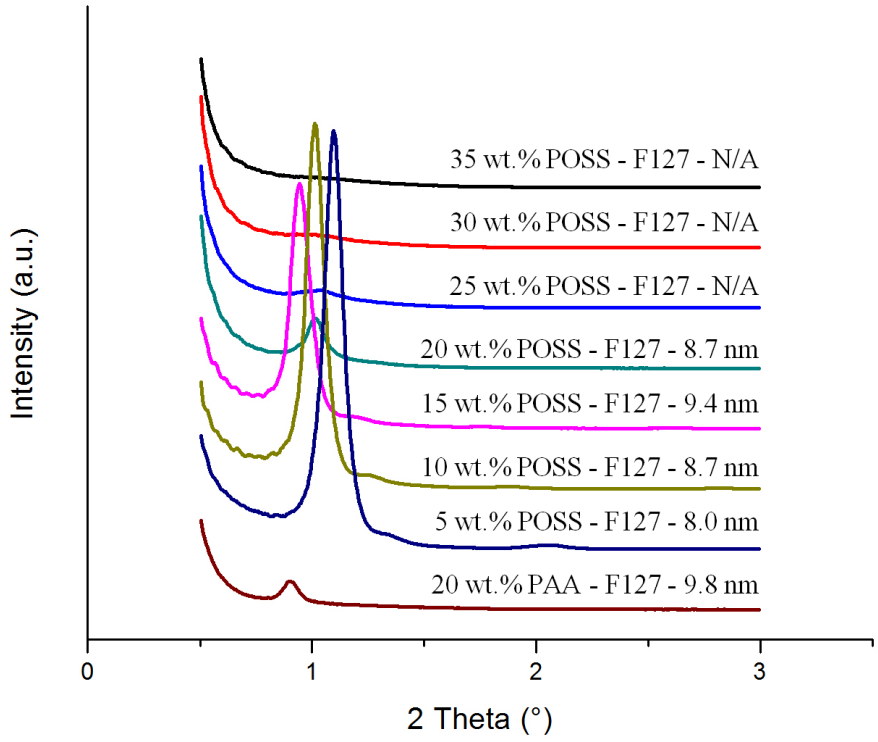

Figure S3.7. Mesoporous silica samples from the Pluronic® F127 template with various concentrations of POSS-OAA calcined, i.e. polymeric template absent, at 900 °C in air. D-spacing values shown.

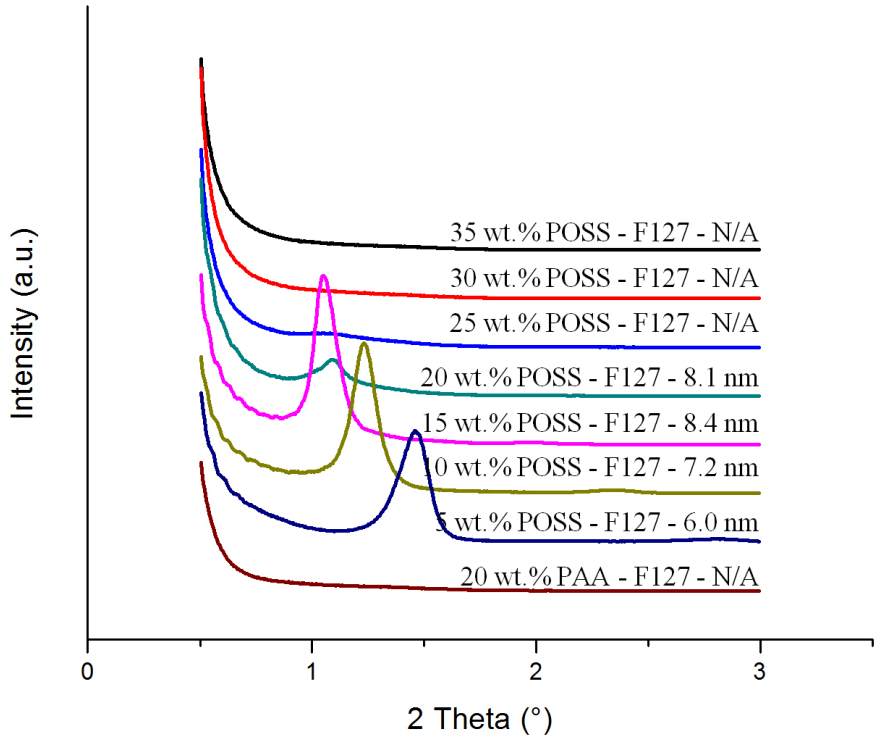

Figure S3.8. Mesoporous silica samples from the Pluronic® F127 template with various concentrations of POSS-OAA calcined, i.e. polymeric template absent, at 1000 °C in air. D-spacing values shown.

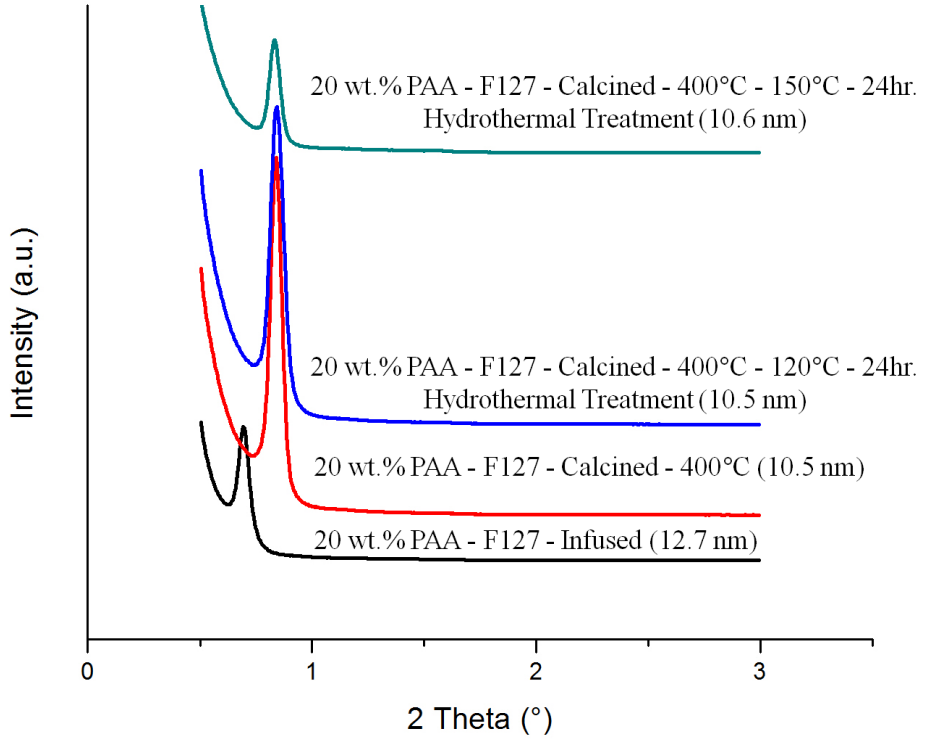

Figure S3.9. Mesoporous silica samples from Pluronic® F127 templates with 20 wt. % 1.8 k Mw PAA experiencing various hydrothermal treatments after calcination, i.e. polymer template absent, at 400 °C in air. D-spacing values shown.

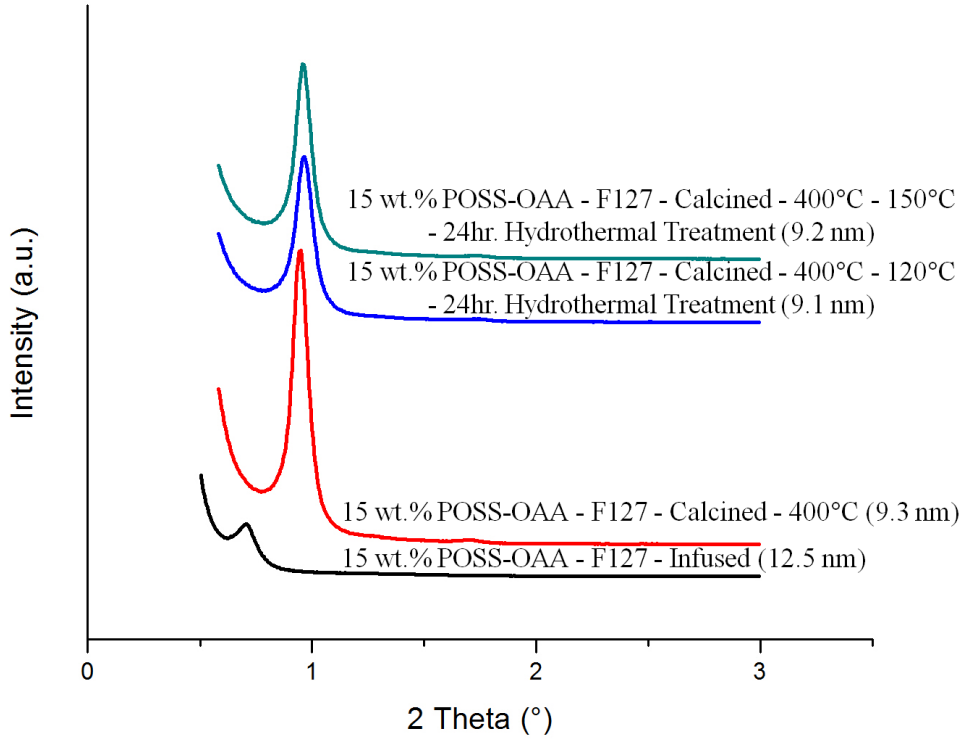

Figure S3.10. Mesoporous silica samples from Pluronic® F127 templates doped with 15 wt. % POSS-OAA experiencing various hydrothermal treatments after calcination, i.e. polymeric template absent, at 400 °C in air. D-spacing values shown.

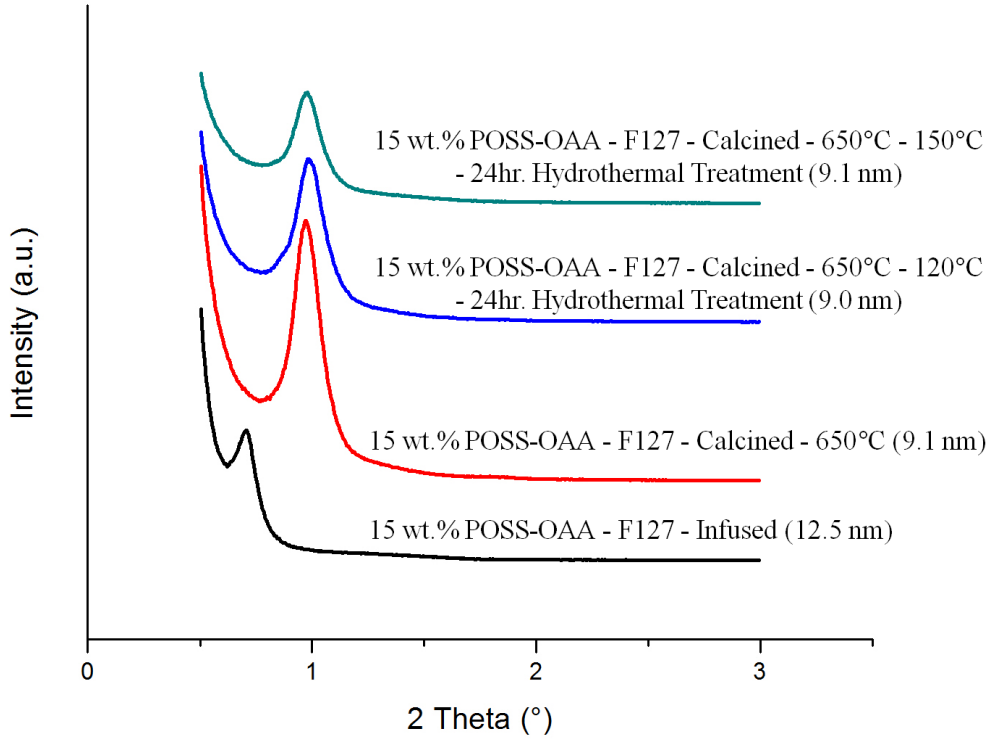

Figure S3.11. Mesoporous silica samples from Pluronic® F127 templates doped with 15 wt. % POSS-OAA experiencing various hydrothermal treatments after calcination, i.e. polymeric template absent, at 650 °C in air. D-spacing values shown.

APPENDIX II

AFM IMAGES OF VARIOUS NANOPARTICLE COMPOSITES

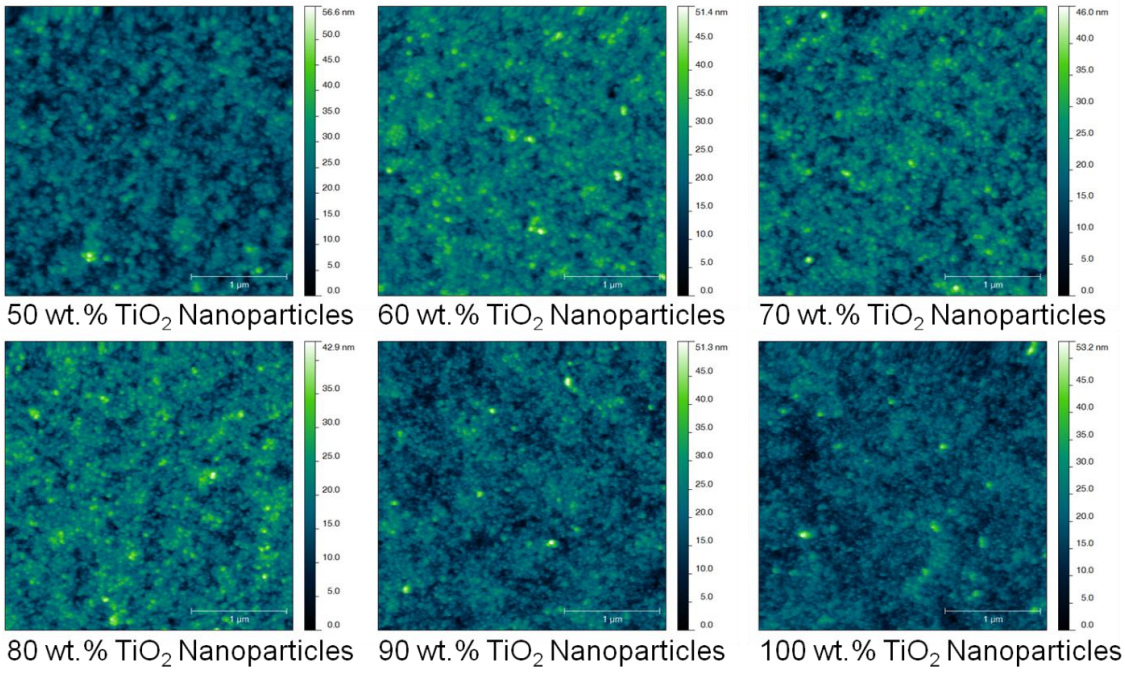

Figure S5.1. AFM images of planar composite material compositions containing various concentration of titanium dioxide nanoparticles with NOA60 as the binder/filler material.

BIBLIOGRAPHY

Anderson, E. R., Daga, V. K., Gido, S. P., & Watkins, J. J. (n.d.). Hydrogen Bond Mediated Self-Assembly of Two Diblock Copolymers. *Submitted*.

Antonietti, M., Berton, B., Göltner, C., & Hentze, H.-P. (1998). Synthesis of Mesoporous Silica with Large Pores and Bimodal Pore Size Distribution by Templating of Polymer Latices. *Advanced Materials*, *10*(2), 154–159.

Atkins, P., & de Paula, J. (2002). *Physical Chemistry* (7th ed.). New York: W. H. Freeman and Company.

Bagshaw, S. A. (1999). Bimodal pore systems in non-ionically templated [Si]-MSU-X mesoporous silica through biomimetic synthesis in weakly ionic solutions. *Chemical Communications*, (18), 1785–1786.

Bagshaw, S. A., Prouzet, E., & Pinnavaia, T. J. (1995). Templating of mesoporous molecular sieves by nonionic polyethylene oxide surfactants. *Science*, *269*(5228), 1242–1244.

Bahadur, P., & Sastry, N. V. (2002). *Principles of Polymer Science* (1st ed.). Pangbourne, England: Alpha Science International Ltd.

Bai, Y., Yang, H., Yang, W., Li, Y., & Sun, C. (2007). Gold nanoparticles-mesoporous silica composite used as an enzyme immobilization matrix for amperometric glucose biosensor construction. *Sensors and Actuators B: Chemical*, *124*(1), 179–186.

Baskaran, S., Liu, J., Domansky, K., Kohler, N., Li, X., Coyle, C., Fryxell, G. E., et al. (2000). Low Dielectric Constant Mesoporous Silica Films Through Molecularly Templated Synthesis. *Advanced Materials*, *12*(4), 291–294.

Bates, F S, & Fredrickson, G. H. (1990). Block copolymer thermodynamics: theory and experiment. *Annual Review of Physical Chemistry*, *41*, 525–57.

Bates, Frank S., & Fredrickson, G. H. (1999). Block Copolymers—Designer Soft Materials. *Physics Today*, *52*(2), 32.

Beck, J S, Vartuli, J. C., Roth, W. J., Leonowicz, M. E., Kresge, C. T., Schmitt, K. D., Chu, C. T. W., et al. (1992). A new family of mesoporous molecular sieves prepared with liquid crystal templates. *Journal of the American Chemical Society*, *114*(27), 10834–10843.

Beck, Jeffrey S. (1991). Method for Synthesizing Mesoporous Crystalline Material. *US 5057296*, 20.

Beckel, D., Bieberle-Hütter, A., Harvey, A., Infortuna, A., Muecke, U. P., Prestat, M., Rupp, J. L. M., et al. (2007). Thin films for micro solid oxide fuel cells. *Journal of Power Sources*, *173*(1), 325–345.

Bentivegna, F., Canva, M., Georges, P., Brun, A., Chaput, F., Malier, L., & Boilot, J.-P. (1993). Reverse saturable absorption in solid xerogel matrices. *Applied Physics Letters*, *62*(15), 1721.

Bieberle, A., Meier, L. P., & Gauckler, L. J. (2001). The Electrochemistry of Ni Pattern Anodes Used as Solid Oxide Fuel Cell Model Electrodes. *Journal of The Electrochemical Society*, *148*(6), A646.

Bieberle-Hütter, A., Sogaard, M., & Tuller, H. (2006). Electrical and electrochemical characterization of microstructured thin film La1−xSrxCoO3 electrodes. *Solid State Ionics*, *177*(19-25), 1969–1975.

Blackburn, J. M., Long, D. P., Cabanas, A., & Watkins, J. J. (2001). Deposition of conformal copper and nickel films from supercritical carbon dioxide. *Science*, *294*(5540), 141–5.

Borodin, V. I., & Trukhacheva, V. A. (2004). Thermal stability of fullerenes. *Technical Physics Letters*, *30*(7), 598–599.

Braun, J. H. (1997). Titanium dioxide--a review. *Journal of Coatings Technology*, *69*(868), 59–72.

Brett, D. J. L., Atkinson, A., Brandon, N. P., & Skinner, S. J. (2008). Intermediate temperature solid oxide fuel cells. *Chemical Society Reviews*, *37*(8), 1568–78.

Brinker, C. J., & Scherer, G. W. (1990). *Sol-Gel Science: The Physics and Chemistry of Sol-Gel Processing*. San Diego: Academic Press.

Brusatin, G., Guglielmi, M., Bozio, R., Meneghetti, M., Signorini, R., Maggini, M., Scorrano, G., et al. (1997). Preparation and Characterization of Fullerenes Containing Sol-Gel Glass. *Journal of Sol-Gel Science and Technology*, *8*, 609–613.

Brust, M., Fink, J., Bethell, D., Schiffrin, D. J., & Kiely, C. (1995). Synthesis and reactions of functionalised gold nanoparticles. *Journal of the Chemical Society, Chemical Communications*, (16), 1655.

Budroni, G., & Corma, A. (2006). Gold-organic-inorganic high-surface-area materials as precursors of highly active catalysts. *Angewandte Chemie International Edition*, *45*(20), 3328–31.

Burda, C., Chen, X., Narayanan, R., & El-Sayed, M. A. (2005). Chemistry and properties of nanocrystals of different shapes. *Chemical Reviews*, *105*(4), 1025–1102.

Cao, H., Yu, Z., Wang, J., Tegenfeldt, J. O., Austin, R. H., Chen, E., Wu, W., et al. (2002). Fabrication of 10 nm enclosed nanofluidic channels. *Applied Physics Letters*, *81*(1), 174–176.

Carn, F., Colin, A., Achard, M.-F., Deleuze, H., Sellier, E., Birot, M., & Backov, R. (2004). Inorganic monoliths hierarchically textured via concentrated direct emulsion and micellar templates. *Journal of Materials Chemistry*, *14*(9), 1370–1376.

Carrette, L., Friedrich, K. A., & Stimming, U. (2000). Fuel Cells: Principles, Types, Fuels, and Applications. *ChemPhysChem*, *1*(4), 162–193.

Caruso, R. A., & Antonietti, M. (2002). Silica Films with Bimodal Pore Structure Prepared by Using Membranes as Templates and Amphiphiles as Porogens. *Advanced Functional Materials*, *12*(4), 307–312.

Cassiers, K., Linssen, T., Mathieu, M., Benjelloun, M., Schrijnemakers, K., Van Der Voort, P., Cool, P., et al. (2002). A Detailed Study of Thermal, Hydrothermal, and Mechanical Stabilities of a Wide Range of Surfactant Assembled Mesoporous Silicas. *Chemistry of Materials*, *14*(5), 2317–2324.

Chen, H.-T., Crosby, T. A., Park, M.-H., Nagarajan, S., Rotello, V. M., & Watkins, J. J. (2009). Accessibility of cylindrical channels within patterned mesoporous silica films using nanoparticle diffusion. *Journal of Materials Chemistry*, *19*(1), 70.

Chen, X., & Mao, S. S. (2006). Synthesis of Titanium Dioxide (TiO2) Nanomaterials. *Journal of Nanoscience and Nanotechnology*, *6*(4), 906–925.

Chen, X., & Mao, S. S. (2007). Titanium dioxide nanomaterials: synthesis, properties, modifications, and applications. *Chemical Reviews*, *107*(7), 2891–2959.

Chiola, V., Ritsko, J. E., & Vanderpool, C. D. (1971). Process for Producing Low-Bulk Density Silica. *US 3556725*, 3.

Choi, J.-H., Lee, S.-W., Jeong, J.-H., Choi, D.-G., & Lee, E.-S. (2009). Direct imprint of conductive silver patterns using nanosilver particles and UV curable resin. *Microelectronic Engineering*, *86*(4-6), 622–627.

Chou, S. Y., Krauss, P. R., & Renstrom, P. J. (1996). Imprint Lithography with 25-Nanometer Resolution. *Science*, *272*(5258), 85–87.

Chou, S.Y., Krauss, P. R., Zhang, W., Guo, L., & Zhuang, L. (1997). Sub-10 nm imprint lithography and applications. *Journal of Vacuum Science & Technology B: Microelectronics and Nanometer Structures*, *15*(6), 2897–2904.

Chou, Stephen Y., Krauss, P. R., & Renstrom, P. J. (1995). Imprint of sub-25 nm vias and trenches in polymers. *Applied Physics Letters*, *67*(21), 3114–3116.

Colburn, M., Johnson, S., Stewart, M., Damle, S., Bailey, T., Choi, B., Wedlake, M., et al. (1999). Step and Flash Imprint Lithography : A New Approach to High-Resolution Patterning. *Proceedings of SPIE*, *3676*, 379–389.

Corma, A. (1997). From Microporous to Mesoporous Molecular Sieve Materials and Their Use in Catalysis. *Chemical Reviews*, *97*(6), 2373–2420.

Coustel, N., Di Renzo, F., & Fajula, F. (1994). Improved stability of MCM-41 through textural control. *Journal of the Chemical Society, Chemical Communications*, *41*(8), 967–968.

Cozzoli, P. D., Kornowski, A., & Weller, H. (2003). Low-temperature synthesis of soluble and processable organic-capped anatase TiO2 nanorods. *Journal of the American Chemical Society*, *125*(47), 14539–48.

Daga, V. K., Anderson, E. R., Gido, S. P., & Watkins, J. J. (2011). Hydrogen Bond Assisted Assembly of Well-Ordered Polyhedral Oligomeric Silsesquioxane–Block Copolymer Composites. *Macromolecules*, *44*(17), 6793–6799.

Daga, V. K., & Watkins, J. J. (2010). Hydrogen-Bond-Mediated Phase Behavior of Complexes of Small Molecule Additives with Poly(ethylene oxide- b -propylene oxide- b -ethylene oxide) Triblock Copolymer Surfactants. *Macromolecules*, *43*(23), 9990–9997.

Damean, N., Parviz, B. A., Lee, J. N., Odom, T., & Whitesides, G. M. (2005). Composite ferromagnetic photoresist for the fabrication of microelectromechanical systems. *Journal of Micromechanics and Microengineering*, *15*(1), 29–34.

Daniel, M.-C., & Astruc, D. (2004). Gold nanoparticles: assembly, supramolecular chemistry, quantum-size-related properties, and applications toward biology, catalysis, and nanotechnology. *Chemical Reviews*, *104*(1), 293–346.

Das, D., Tsai, C.-M., & Cheng, S. (1999). Improvement of hydrothermal stability of MCM-41 mesoporous molecular sieve. *Chemical Communications*, (5), 473–474.

Davis, S. A., Burkett, S. L., Mendelson, N. H., & Mann, S. (1997). Bacterial templating of ordered macrostructures in silica and silica-surfactant mesophases. *Nature*, *385*(6615), 420–423.

Dawan, F., Jin, Y., Goettert, J., & Ibekwe, S. (2008). High functionality of a polymer nanocomposite material for MEMS applications. *Microsystem Technologies*, *14*(9-11), 1451–1459.

Dong, A., Wang, Y., Tang, Y., Zhang, Y., Ren, N., & Gao, Z. (2002). Mechanically Stable Zeolite Monoliths with Three-Dimensional Ordered Macropores by the Transformation of Mesoporous Silica Spheres. *Advanced Materials*, *14*(20), 1506–1510.

Dugan, L. L., Turetsky, D. M., Du, C., Lobner, D., Wheeler, M., Almli, C. R., Shen, C. K., et al. (1997). Carboxyfullerenes as neuroprotective agents. *Proceedings of the National Academy of Sciences of the United States of America*, *94*(17), 9434–9.

El Haskouri, J., Ortiz de Zárate, D., Guillem, C., Latorre, J., Caldés, M., Beltrán, A., Beltrán, D., et al. (2002). Silica-based powders and monoliths with bimodal pore systems. *Chemical Communications*, (4), 330–331.

Ell, J. R., Crosby, T. A., Peterson, J. J., Carter, K. R., & Watkins, J. J. (2010). Formation of SiO 2 Air-Gap Patterns Through scCO 2 Infusion of NIL Patterned PHEMA. *Chemistry of Materials*, *22*(4), 1445–1451.

Fardad, M. A. (2000). Catalysts and the structure of SiO 2 sol-gel films. *Journal of Materials Science*, *35*, 1835–1841.

Fujishima, A., & Honda, K. (1972). Electrochemical Photolysis of Water at a Semiconductor Electrode. *Nature*, *238*(5358), 37–38.

Fukushima, Y., & Wakayama, H. (1999). Nanoscale Casting Using Supercritical Fluid. *The Journal of Physical Chemistry B*, *103*(16), 3062–3064.

Fullerene Applications. (n.d.).

Gabaldon, J. P., Bore, M., & Datye, A. K. (2007). Mesoporous silica supports for improved thermal stability in supported Au catalysts. *Topics in Catalysis*, *44*(1-2), 253–262.

Galarneau, A., Barodawalla, A., & Pinnavaia, T. J. (1995). Porous clay heterostructures formed by gallery-templated synthesis. *Nature*, *374*(6522), 529–531.

Garves, K. (1988). Acid Catalyzed Degradation of Cellulose in Alcohols. *Journal of Wood Chemistry and Technology*, *8*(1), 121–134.

Ghosh, G. (1999). Dispersion-equation coefficients for the refractive index and birefringence of calcite and quartz crystals. *Optics Communications*, *163*(1-3), 95–102.

Giunta, P. R., Washington, R. P., Campbell, T. D., Steinbock, O., & Stiegman, A. E. (2004). Preparation of mesoporous silica monoliths with ordered arrays of macrochannels templated from electric-field-oriented hydrogels. *Angewandte Chemie*, *43*(12), 1505–1507.

Goldstein, J., Newbury, D. E., Joy, D. C., Lyman, C. E., Echlin, P., Lifshin, E., Sawyer, L., et al. (2003). *Scanning Electron Microscopy and X-Ray Microanalysis* (3rd ed.). New York: Springer.

Graham, T. (1864). On the properties of silicic acid and other analogous colloidal substances. *Journal of the Chemical Society*, *17*, 318–327.

Gunji, T., Ozawa, M., Abe, Y., & West, R. (2001). Preparation of C 60 – Silica Hybrid Monolith by Sol-Gel Process. *Journal of Sol-Gel Science and Technology*, *22*, 219–224.

Guo, L. J., Cheng, X., & Chou, C.-F. (2004). Fabrication of Size-Controllable Nanofluidic Channels by Nanoimprinting and Its Application for DNA Stretching. *Nano Letters*, *4*(1), 69–73.

Gupta, G., Shah, P. S., Zhang, X., Saunders, A. E., Korgel, B. A., & Johnston, K. P. (2005). Enhanced Infusion of Gold Nanocrystals into Mesoporous Silica with Supercritical Carbon Dioxide. *Chemistry of Materials*, *17*(26), 6728–6738.

Gupta, R. R., RamachandraRao, V. S., & Watkins, J. J. (2003). Measurement of Probe Diffusion in CO 2 -Swollen Polystyrene Using in Situ Fluorescence Nonradiative Energy Transfer. *Macromolecules*, *36*(4), 1295–1303.

Gupta, S., Zhang, Q., Emrick, T., Balazs, A. C., & Russell, T. P. (2006). Entropy-driven segregation of nanoparticles to cracks in multilayered composite polymer structures. *Nature Materials*, *5*(3), 229–233.

Gupta, S., Zhang, Q., Emrick, T., & Russell, T. P. (2006). "Self-corralling" nanorods under an applied electric field. *Nano Letters*, *6*(9), 2066–2069.

Gvishi, R., Bhawalker, J. D., Kumar, N. D., Ruland, G., Narang, U., Prasad, P. N., & Reinhardt, B. A. (1995). Multiphasic Nanostructured Composites for Photonics: Fullerene-Doped Monolith Glass. *Chemistry of Materials*, *7*(11), 2199–2202.

Haisma, J., Verheijen, M., van den Heuvel, K., & van den Berg, J. (1996). Mold-assisted nanolithography: A process for reliable pattern replication. *Journal of Vacuum Science & Technology B: Microelectronics and Nanometer Structures*, *14*(6), 4124–4128.

Hanaor, D. A. H., & Sorrell, C. C. (2010). Review of the anatase to rutile phase transformation. *Journal of Materials Science*, *46*(4), 855–874.

Hanemann, T., & Szabó, D. V. (2010). Polymer-Nanoparticle Composites: From Synthesis to Modern Applications. *Materials*, *3*(6), 3468–3517.

Haruta, M., Kobayashi, T., Sano, H., & Yamada, N. (1987). Novel Gold Catalysts for the Oxidation of Carbon Monoxide at a Temperature far Below 0 °C. *Chemistry Letters*, 405–408.

Haruta, M., Tsubota, S., Kobayashi, T., Kageyama, H., Genet, M. J., & Delmon, B. (1993). Low-Temperature Oxidation of CO over Gold Supported on TiO2, α-Fe2O3, and Co3O4. *Journal of Catalysis*, *144*(1), 175–192.

Hasegawa, I., & Nonomura, S. (2000). Annealing Temperature Dependence of the Size of C 60 Clusters in C 60 -Doped Silicon Oxide Films. *Journal of Sol-Gel Science and Technology*, *19*, 297–300.

Hasegawa, I., Shibusa, K., Kobayashi, S., Nonomura, S., & Nitta, S. (1997). Facile fabrication procedure for C-60-doped silicon oxide thin films. *Chemistry Letters*, (10), 995–996.

Hayashi, T., Tanaka, K., & Haruta, M. (1998). Selective Vapor-Phase Epoxidation of Propylene over Au/TiO2Catalysts in the Presence of Oxygen and Hydrogen. *Journal of Catalysis*, *178*(2), 566–575.

Hedrick, J. L., Miller, R. D., Hawker, C. J., Carter, K. R., Volksen, W., Yoon, D. Y., & Trollsås, M. (1998). Templating Nanoporosity in Thin-Film Dielectric Insulators. *Advanced Materials*, *10*(13), 1049–1053.

Hendricks, N. R., Watkins, J. J., & Carter, K. R. (2011). Formation of hierarchical silica nanochannels through nanoimprint lithography. *Journal of Materials Chemistry*, *21*, 14213–14218.

Hertz, J. L., & Tuller, H. L. (2004). Electrochemical Characterization of Thin Films for a Micro-Solid Oxide Fuel Cell. *Journal of Electroceramics*, *13*(1-3), 663–668.

Hertz, Joshua L., Rothschild, A., & Tuller, H. L. (2009). Highly enhanced electrochemical performance of silicon-free platinum–yttria stabilized zirconia interfaces. *Journal of Electroceramics*, *22*(4), 428–435.

Holland, B. T., Abrams, L., & Stein, A. (1999). Dual Templating of Macroporous Silicates with Zeolitic Microporous Frameworks. *Journal of the American Chemical Society*, *121*(17), 4308–4309.

Holland, B. T., Blanford, C. F., Do, T., & Stein, A. (1999). Synthesis of Highly Ordered, Three-Dimensional, Macroporous Structures of Amorphous or Crystalline Inorganic Oxides, Phosphates, and Hybrid Composites. *Chemistry of Materials*, *11*(3), 795–805.

Hoofman, R., Caluwaerts, R., Michelon, J., Herrerobernabe, P., Gueneaudemussy, J., Bruynseraede, C., Lee, J., et al. (2006). Self-aligned multi-level air gap integration. *Microelectronic Engineering*, *83*(11-12), 2150–2154.

Huang, L., Wang, Z., Sun, J., Miao, L., Li, Q., Yan, Y., & Zhao, D. (2000). Fabrication of Ordered Porous Structures by Self-Assembly of Zeolite Nanocrystals. *Journal of the American Chemical Society*, *122*(14), 3530–3531.

Huerta, L., Guillem, C., Latorre, J., Beltrán, A., Beltrán, D., & Amorós, P. (2003). Large monolithic silica-based macrocellular foams with trimodal pore system. *Chemical Communications*, (12), 1448–1449.

Huo, Q., Margolese, D. I., Ciesla, U., Feng, P., Gier, T. E., Sieger, P., Leon, R., et al. (1994). Generalized synthesis of periodic surfactant/inorganic composite materials. *Nature*, *368*(6469), 317–321.

Inagaki, S., Fukushima, Y., & Kuroda, K. (1993). Synthesis of highly ordered mesoporous materials from a layered polysilicate. *Journal of the Chemical Society, Chemical Communications*, (8), 680–682.

Ingrosso, C., Fakhfouri, V., Striccoli, M., Agostiano, A., Voigt, A., Gruetzner, G., Curri, M. L., et al. (2007). An Epoxy Photoresist Modified by Luminescent Nanocrystals for the Fabrication of 3D High-Aspect-Ratio Microstructures. *Advanced Functional Materials*, *17*(13), 2009–2017.

Innocenzi, P., Martucci, A., Guglielmi, M., Bearzotti, A., & Traversa, E. (2001). Electrical and structural characterisation of mesoporous silica thin films as humidity sensors. *Sensors and Actuators B: Chemical*, *76*(1-3), 299–303.

Innocenzi, P., Martucci, A., Guglielmi, M., Bearzotti, A., Traversa, E., & Pivin, J. C. (2001). Mesoporous silica thin films for alcohol sensors. *Journal of the European Ceramic Society*, *21*(10-11), 1985–1988.

Innocenzi, P., Zub, Y. L., & Kessler, V. G. (2008). *Sol-Gel Methods for Materials Processing*. (P. Innocenzi, Y. L. Zub, & V. G. Kessler, Eds.). Dordrecht: Springer Netherlands.

Jiguet, S., Bertsch, A., Hofmann, H., & Renaud, P. (2005). Conductive SU8 Photoresist for Microfabrication. *Advanced Functional Materials*, *15*(9), 1511–1516.

Jun, S., Kim, J. M., Ryoo, R., Ahn, Y.-S., & Han, M.-H. (2000). Hydrothermal stability of MCM-48 improved by post-synthesis restructuring in salt solution. *Microporous and Mesoporous Materials*, *41*(1-3), 119–127.

Kim, J. M., Jun, S., & Ryoo, R. (1999). Improvement of Hydrothermal Stability of Mesoporous Silica Using Salts: Reinvestigation for Time-Dependent Effects. *The Journal of Physical Chemistry B*, *103*(30), 6200–6205.

Kim, Y., Kim, G., & Lee, J. (2010). Fabrication of a conductive nanoscale electrode for functional devices using nanoimprint lithography with printable metallic nanoink. *Microelectronic Engineering*, *87*(5-8), 839–842.

Klocek, J., Henkel, K., Kolanek, K., Broczkowska, K., Schmeisser, D., Miller, M., & Zschech, E. (2012). Studies of the chemical and electrical properties of fullerene and 3-aminopropyltrimethoxysilane based low-k materials. *Thin Solid Films*, *520*(7), 2498–2504.

Ko, S. H., Park, I., Pan, H., Grigoropoulos, C. P., Pisano, A. P., Luscombe, C. K., & Fréchet, J. M. J. (2007). Direct nanoimprinting of metal nanoparticles for nanoscale electronics fabrication. *Nano Letters*, *7*(7), 1869–1877.

Kojima, Y., Usuki, A., Kawasumi, M., Okada, A., Fukushima, Y., Kurauchi, T., & Kamigaito, O. (1993). Mechanical properties of nylon 6-clay hybrid. *Journal of Materials Research*, *8*(5), 1185–1189.

Kordatos, K., Prato, M., Menna, E., Scorrano, G., & Maggini, M. (2001). Synthesis of Fullerene Derivatives for Incorporation in Sol-Gel Glasses. *Journal of Sol-Gel Science and Technology*, *22*, 237–244.

Kost, A., Tutt, L., Klein, M. B., Dougherty, T. K., & Elias, W. E. (1993). Optical limiting with C(60) in polymethyl methacrylate. *Optics Letters*, *18*(5), 334–336.

Koyano, K. A., Tatsumi, T., Tanaka, Y., & Nakata, S. (1997). Stabilization of Mesoporous Molecular Sieves by Trimethylsilylation. *The Journal of Physical Chemistry B*, *101*(46), 9436–9440.

Kresge, C. T., Leonowicz, M. E., Roth, W. J., Vartuli, J. C., & Beck, J. S. (1992). Ordered mesoporous molecular sieves synthesized by a liquid-crystal template mechanism. *Nature*, *359*(6397), 710–712.

Kroto, H. W., Heath, J. R., O'Brien, S. C., Curl, R. F., & Smalley, R. E. (1985). C60: Buckminsterfullerene. *Nature*, *318*(6042), 162–163.

Kyriakopoulos, J., Tzirakis, M. D., Panagiotou, G. D., Alberti, M. N., Triantafyllidis, K. S., Giannakaki, S., Bourikas, K., et al. (2012). Highly active catalysts for the photooxidation of organic compounds by deposition of [60] fullerene onto the MCM-41 surface: A green approach for the synthesis of fine chemicals. *Applied Catalysis B: Environmental*, *117-118*, 36–48.

Kónya, Z., Puntes, V. F., Kiricsi, I., Zhu, J., Ager, J. W., Ko, M. K., Frei, H., et al. (2003). Synthetic Insertion of Gold Nanoparticles into Mesoporous Silica. *Chemistry of Materials*, *15*(6), 1242–1248.

Lamparth, I., & Hirsch, A. (1994). Water-soluble malonic acid derivatives of C60 with a defined three-dimensional structure. *Journal of the Chemical Society, Chemical Communications*, *7*(14), 1727.

Le Page, M., Beau, R., & Duchene, J. (1970). Porous Silica Particles Containing a Crystallized Phase and Method. *US 3493341*, 3.

Le Trequesser, Q., Mesguich, D., You, E., Aymonier, C., & Watkins, J. J. (2011). Supercritical fluid deposition of compositionally uniform yttria stabilized zirconia films. *The Journal of Supercritical Fluids*, *66*, 328–332.

Lee, J. N., Park, C., & Whitesides, G. M. (2003). Solvent compatibility of poly(dimethylsiloxane)-based microfluidic devices. *Analytical Chemistry*, *75*(23), 6544–6554.

Lee, J.-Y., Zhang, Q., Emrick, T., & Crosby, A. J. (2006). Nanoparticle Alignment and Repulsion during Failure of Glassy Polymer Nanocomposites. *Macromolecules*, *39*(21), 7392–7396.

Leifer, S., Goodwin, D., Anderson, M., & Anderson, J. (1995). Thermal decomposition of a fullerene mix. *Physical Review B*, *51*(15), 9973–9978.

Li, Q., He, J., Glogowski, E., Li, X., Wang, J., Emrick, T., & Russell, T. P. (2008). Responsive Assemblies: Gold Nanoparticles with Mixed Ligands in Microphase Separated Block Copolymers. *Advanced Materials*, *20*(8), 1462–1466.

Li, W., Tegenfeldt, J. O., Chen, L., Austin, R. H., Chou, S. Y., Kohl, P. A., Krotine, J., et al. (2003). Sacrificial polymers for nanofluidic channels in biological applications. *Nanotechnology*, *14*(6), 578–583.

Liang, X., Morton, K. J., Austin, R. H., & Chou, S. Y. (2007). Single sub-20 nm wide, centimeter-long nanofluidic channel fabricated by novel nanoimprint mold fabrication and direct imprinting. *Nano Letters*, *7*(12), 3774–80.

Lin, Y., Daga, V. K., Anderson, E. R., Gido, S. P., & Watkins, J. J. (2011). Nanoparticle-driven assembly of block copolymers: a simple route to ordered hybrid materials. *Journal of the American Chemical Society*, *133*(17), 6513–6516.

Lin, Y., Lim, J. A., Wei, Q., Mannsfeld, S. C. B., Briseno, A. L., & Watkins, J. J. (2012). Cooperative Assembly of Hydrogen-Bonded Diblock Copolythiophene/Fullerene Blends for Photovoltaic Devices with Well-Defined Morphologies and Enhanced Stability. *Chemistry of Materials*, *24*(3), 622–632.

Linstrom, P. J., & Mallard, W. G. (n.d.). National Institute of Standards and Technology Chemistry WebBook.

Litzelman, S. J., Hertz, J. L., Jung, W., & Tuller, H. L. (2008). Opportunities and Challenges in Materials Development for Thin Film Solid Oxide Fuel Cells. *Fuel Cells*, *8*(5), 294–302.

Liu, A. M., Hidajat, K., Kawi, S., & Zhao, D. Y. (2000). A new class of hybrid mesoporous materials with functionalized organic monolayers for selective adsorption of heavy metal ions. *Chemical Communications*, *15*(13), 1145–1146.

Liu, J., Tanaka, T., Sivula, K., Alivisatos, A. P., & Fréchet, J. M. J. (2004). Employing end-functional polythiophene to control the morphology of nanocrystal-polymer composites in hybrid solar cells. *Journal of the American Chemical Society*, *126*(21), 6550–6551.

Loffredo, F., Mauro, a. D. G. D., Burrasca, G., La Ferrara, V., Quercia, L., Massera, E., Di Francia, G., et al. (2009). Ink-jet printing technique in polymer/carbon black sensing device fabrication. *Sensors and Actuators B: Chemical*, *143*(1), 421–429.

Lu, Q., Cui, F., Dong, C., Hua, Z., & Shi, J. (2011). Gold nanoparticles incorporated mesoporous silica thin films of varied gold contents and their well-tuned third-order optical nonlinearities. *Optical Materials*, *33*(8), 1266–1271.

Maekawa, H., Esquena, J., Bishop, S., Solans, C., & Chmelka, B. F. (2003). Meso/Macroporous Inorganic Oxide Monoliths from Polymer Foams. *Advanced Materials*, *15*(78), 591–596.

Malibert, C., & Bach, S. (2002). Elaboration and characterization of thin films of TiO 2 prepared by sol – gel process. *Thin Solid Films*, *418*, 79–84.

Martiradonna, L., Qualtieri, A., Stomeo, T., Carbone, L., Cingolani, R., & Devittorio, M. (2007). Lithographic nano-patterning of colloidal nanocrystal emitters for the fabrication of waveguide photonic devices. *Sensors and Actuators B: Chemical*, *126*(1), 116–119.

McBranch, D. W., Mattes, B. R., Koskelo, A., Robinson, J. M., & Love, S. P. (1994). C60-doped silicon dioxide sonogels for optical limiting. *Proceedings of SPIE*, *2284*, 15–20.

McCullen, S. B., & Vartuli, J. C. (1992). Method for Stabilizing Synthetic Mesoporous Crystalline Material.

Meng, Y., Gu, D., Zhang, F., Shi, Y., Yang, H., Li, Z., Yu, C., et al. (2005). Ordered mesoporous polymers and homologous carbon frameworks: amphiphilic surfactant templating and direct transformation. *Angewandte Chemie International Edition*, *44*(43), 7053–9.

Mesguich, D., Aymonier, C., Bassat, J.-M., Mauvy, F., You, E., & Watkins, J. J. (2011). Low-Temperature Deposition of Undoped Ceria Thin Films in scCO 2 As Improved Interlayers for IT-SOFC. *Chemistry of Materials*, *23*(24), 5323–5330.

Mohr, C., Hofmeister, H., Radnik, J., & Claus, P. (2003). Identification of active sites in gold-catalyzed hydrogenation of acrolein. *Journal of the American Chemical Society*, *125*(7), 1905–1911.

Mok, W. S.-L., Antal, M. J., & Varhegyi, G. (1992). Productive and parasitic pathways in dilute acid-catalyzed hydrolysis of cellulose. *Industrial & Engineering Chemistry Research*, *31*(1), 94–100.

Moran, I. W., Briseno, A. L., Loser, S., & Carter, K. R. (2008). Device Fabrication by Easy Soft Imprint Nano-Lithography. *Chemistry of Materials*, *20*(14), 4595–4601.

Mukherjee, P., Patra, C. R., Ghosh, A., Kumar, R., & Sastry, M. (2002). Characterization and Catalytic Activity of Gold Nanoparticles Synthesized by Autoreduction of Aqueous Chloroaurate Ions with Fumed Silica. *Chemistry of Materials*, *14*(4), 1678–1684.

Nagarajan, S., Li, M., Pai, R. A., Bosworth, J. K., Busch, P., Smilgies, D.-M., Ober, C. K., et al. (2008). An Efficient Route to Mesoporous Silica Films with Perpendicular Nanochannels. *Advanced Materials*, *20*(2), 246–251.

Nagarajan, Sivakumar, Bosworth, J. K., Ober, C. K., Russell, T. P., & Watkins, J. J. (2008). Simple Fabrication of Micropatterned Mesoporous Silica Films Using Photoacid Generators in Block Copolymers. *Chemistry of Materials*, *20*(3), 604–606.

Nguyen, C. V., Carter, K. R., Hawker, C. J., Hedrick, J. L., Jaffe, R. L., Miller, R. D., Remenar, J. F., et al. (1999). Low-Dielectric, Nanoporous Organosilicate Films Prepared via Inorganic/Organic Polymer Hybrid Templates. *Chemistry of Materials*, *11*(11), 3080–3085.

Noguchi, J., Sato, K., Konishi, N., Uno, S., Oshima, T., Ishikawa, K., Ashihara, H., et al. (2005). Process and Reliability of Air-Gap Cu Interconnect Using 90-nm Node Technology. *IEEE Transactions on Electron Devices*, *52*(3), 352–359.

Odian, G. (2004). *Principles of Polymerization* (4th ed.). Hoboken, New Jersey: John Wiley & Sons, Inc.

Okabe, A., Niki, M., Fukushima, T., & Aida, T. (2005). A simple route to bimodal mesoporous silica via tetrafluoroborate ion-mediated hydrophobic transformation of template micellar surface. *Journal of Materials Chemistry*, *15*(13), 1329.

O', G. J. L., In, H. J., Crumlin, E., & Barbastathis, G. (2007). Recent advances in microdevices for electrochemical energy conversion and storage. *International Journal of Energy Research*, *31*, 548–575.

O'Neil, A., & Watkins, J. J. (2007). Reactive Deposition of Conformal Metal Oxide Films from Supercritical Carbon Dioxide. *Chemistry of Materials*, *19*(23), 5460–5466.

Pai, R. A., Humayun, R., Schulberg, M. T., Sengupta, A., Sun, J.-N., & Watkins, J. J. (2004). Mesoporous silicates prepared using preorganized templates in supercritical fluids. *Science*, *303*(5657), 507–510.

Panagiotou, G. D., Tzirakis, M. D., Vakros, J., Loukatzikou, L., Orfanopoulos, M., Kordulis, C., & Lycourghiotis, A. (2010). Development of [60] fullerene supported on silica catalysts for the photo-oxidation of alkenes. *Applied Catalysis A: General*, *372*(1), 16–25.

Pantouvaki, M., Humbert, A., Vanbesien, E., Camerotto, E., Travaly, Y., Richard, O., Willegems, M., et al. (2008). Air gap formation by UV-assisted decomposition of CVD material. *Microelectronic Engineering*, *85*(10), 2071–2074.

Park, O.-H., Cheng, J. Y., Hart, M., Topuria, T., Rice, P. M., Krupp, L. E., Miller, R. D., et al. (2008). High Aspect-Ratio Cylindrical Nanopore Arrays and Their Use for Templating Titania Nanoposts. *Advanced Materials*, *20*(4), 738–742.

Perry, J. L., & Kandlikar, S. G. (2005). Review of fabrication of nanochannels for single phase liquid flow. *Microfluidics and Nanofluidics*, *2*(3), 185–193.

Persano, L., Molle, S., Girardo, S., Neves, A. A. R., Camposeo, A., Stabile, R., Cingolani, R., et al. (2008). Soft Nanopatterning on Light-Emitting Inorganic-Organic Composites. *Advanced Functional Materials*, *18*(18), 2692–2698.

Pfaff, G., & Reynders, P. (1999). Angle-Dependent Optical Effects Deriving from Submicron Structures of Films and Pigments. *Chemical Reviews*, *99*(7), 1963–1982.

Philip, D. (2008). Synthesis and spectroscopic characterization of gold nanoparticles. *Spectrochimica Acta. Part A, Molecular and Biomolecular Spectroscopy*, *71*(1), 80–85.

Pinto-Iguanero, B., Olivares-Pérez, A., & Fuentes-Tapia, I. (2002). Holographic material film composed by Norland NOA 65® adhesive. *Optical Materials*, *20*(3), 225–232.

Pompa, P., Martiradonna, L., Torre, A., Carbone, L., Delmercato, L., Manna, L., Devittorio, M., et al. (2007). Fluorescence enhancement in colloidal semiconductor nanocrystals by metallic nanopatterns. *Sensors and Actuators B: Chemical*, *126*(1), 187–192.

Prato, M. (1997). [60]Fullerene chemistry for materials science applications. *Journal of Materials Chemistry*, *7*(7), 1097–1109.

Principe, M., Martínez, R., Ortiz, P., & Rieumont, J. (2000). The polymerization of furfuryl alcohol with p-toluenesulfonic acid: photocross-linkeable feature of the polymer. *Polímeros*, *10*(1), 8–14.

Pérez-Pariente, J., Díaz, I., & Agúndez, J. (2005). Organising disordered matter: strategies for ordering the network of mesoporous materials. *Comptes Rendus Chimie*, *8*(3-4), 569–578.

Qualtieri, A., Martiradonna, L., Stomeo, T., Todaro, M. T., Cingolani, R., & Vittorio, M. D. (2009). Multicolored devices fabricated by direct lithography of colloidal nanocrystals. *Microelectronic Engineering*, *86*(4-6), 1127–1130.

Reboud, V., Kehagias, N., Sotomayor Torres, C. M., Zelsmann, M., Striccoli, M., Curri, M. L., Agostiano, A., et al. (2007). Spontaneous emission control of colloidal nanocrystals using nanoimprinted photonic crystals. *Applied Physics Letters*, *90*(1), 011115.

Romang, A. H. (2012). *Ordered Nanomaterials and Supercritical CO2: Mechanically Enhanced Low-K Dielectric Materials and Ordered Block Copolymer Surfactant Systems*.

Rothschild, A., Litzelman, S. J., Tuller, H. L., Menesklou, W., Schneider, T., & Ivers-Tiffée, E. (2005). Temperature-independent resistive oxygen sensors based on SrTi1−xFexO3−δ solid solutions. *Sensors and Actuators B: Chemical*, *108*(1-2), 223–230.

Ryan, K. M., Mastroianni, A., Stancil, K. A., Liu, H., & Alivisatos, A. P. (2006). Electric-field-assisted assembly of perpendicularly oriented nanorod superlattices. *Nano Letters*, *6*(7), 1479–1482.

Ryoo, R., Joo, S. H., & Jun, S. (1999). Synthesis of Highly Ordered Carbon Molecular Sieves via Template-Mediated Structural Transformation. *The Journal of Physical Chemistry B*, *103*(37), 7743–7746.

Ryoo, R., & Jun, S. (1997). Improvement of Hydrothermal Stability of MCM-41 Using Salt Effects during the Crystallization Process. *The Journal of Physical Chemistry B*, *101*(3), 317–320.

Ryoo, R., Kim, J. M., Ko, C. H., & Shin, C. H. (1996). Disordered Molecular Sieve with Branched Mesoporous Channel Network. *The Journal of Physical Chemistry*, *100*(45), 17718–17721.

Saifullah, M. S. M., Subramanian, K. R. V., Tapley, E., Kang, D.-J., Welland, M. E., & Butler, M. (2003). Sub-10 nm Electron Beam Nanolithography Using Spin-Coatable TiO 2 Resists. *Nano Letters*, *3*(11), 1587–1591.

Schell, J., Brinkmann, D., Ohlmann, D., Hönerlage, B., Levy, R., Joucla, M., Rehspringer, J. L., et al. (1998). Optical limiting properties and dynamics of induced absorption in C[sub 60]-doped solid xerogel matrices. *The Journal of Chemical Physics*, *108*(20), 8599.

Schell, J., Ohlmann, D., Brinkmann, D., Lévy, R., Joucla, M., Rehspringer, J. L., & Hönerlage, B. (1999). Reverse saturable absorption in C[sub 60]-doped porous glasses studied by single- and double-pulse pump–probe experiments. *The Journal of Chemical Physics*, *111*(13), 5929.

Schell, J., Ohlmann, D., Hönerlage, B., Levy, R., Joucla, M., Rehspringer, J. L., Serughetti, J., et al. (1998). Induced absorption in fullerene-doped solid xerogel matrices. *Carbon*, *36*(5-6), 671–674.

Schubert, U. (2009). Preparation of metal oxide or metal nanoparticles in silica via metal coordination to organofunctional trialkoxysilanes. *Polymer International*, *58*(3), 317–322.

Seidel, H., Csepregi, L., Heuberger, A., & Baumgäterl, H. (1990a). Anisotropic Etching of Crystalline Silicon in Alkaline Solutions. *Journal of The Electrochemical Society*, *137*(11), 3612–3626.

Seidel, H., Csepregi, L., Heuberger, A., & Baumgäterl, H. (1990b). Anisotropic Etching of Crystalline Silicon in Alkaline Solutions. *Journal of The Electrochemical Society*, *137*(11), 3626–3632.

Sen, T, Tiddy, G. J. T., Casci, J. L., & Anderson, M. W. (2003). Macro-cellular silica foams: synthesis during the natural creaming process of an oil-in-water emulsion. *Chemical Communications*, (17), 2182–2183.

Sen, T., Tiddy, G. J. T., Casci, J. L., & Anderson, M. W. (2005). Meso-cellular silica foams, macro-cellular silica foams and mesoporous solids: a study of emulsion-mediated synthesis. *Microporous and Mesoporous Materials*, *78*(2-3), 255–263.

Sen, Tapasi, Jana, S., Koner, S., & Patra, A. (2010). Energy Transfer between Confined Dye and Surface Attached Au Nanoparticles of Mesoporous Silica. *The Journal of Physical Chemistry C*, *114*(2), 707–714.

Shan, G.-B., & Demopoulos, G. P. (2010). The synthesis of aqueous-dispersible anatase TiO2 nanoplatelets. *Nanotechnology*, *21*(2), 025604.

Silverstein, R. M., Webster, F. X., & Kiemle, D. J. (2005). *Spectrometric Identification of Organic Compounds*. Hoboken, New Jersey: John Wiley & Sons, Inc.

Singh, A., Kulkarni, S. K., & Khan-Malek, C. (2011). Patterning of SiO2 nanoparticle–PMMA polymer composite microstructures based on soft lithographic techniques. *Microelectronic Engineering*, *88*(6), 939–944.

Sinha, A. K., Seelan, S., Tsubota, S., & Haruta, M. (2004). A three-dimensional mesoporous titanosilicate support for gold nanoparticles: vapor-phase epoxidation of propene with high conversion. *Angewandte Chemie International Edition*, *43*(12), 1546–1548.

Smith, G. W. (1991). Cure Parameters and Phase Behavior of An Ultraviolet-Cured Polymer-Dispersed Liquid Crystal. *Molecular Crystals and Liquid Crystals*, *196*(1), 89–102.

Stein, A. (2003). Advances in Microporous and Mesoporous Solids—Highlights of Recent Progress. *Advanced Materials*, *15*(10), 763–775.

Sun, J., Shan, Z., Maschmeyer, T., Moulijn, J. A., & Coppens, M.-O. (2001). Synthesis of tailored bimodal mesoporous materials with independent control of the dual pore size distribution. *Chemical Communications*, (24), 2670–2671.

Tamborra, M., Striccoli, M., Curri, M. L., Alducin, J. A., Mecerreyes, D., Pomposo, J. A., Kehagias, N., et al. (2007). Nanocrystal-based luminescent composites for nanoimprinting lithography. *Small*, *3*(5), 822–828.

Tanev, P T, Chibwe, M., & Pinnavaia, T. J. (1994). Titanium-containing mesoporous molecular sieves for catalytic oxidation of aromatic compounds. *Nature*, *368*(6469), 321–323.

Tanev, Peter T., & Pinnavaia, T. J. (1995). A Neutral Templating Route to Mesoporous Molecular Sieves. *Science*, *267*(5199), 865–867.

Taylor, A., Lucas, B., Guo, L., & Thompson, L. (2007). Nanoimprinted electrodes for micro-fuel cell applications. *Journal of Power Sources*, *171*(1), 218–223.

Tekin, E., Smith, P. J., Hoeppener, S., van den Berg, A. M. J., Susha, A. S., Rogach, A. L., Feldmann, J., et al. (2007). Inkjet Printing of Luminescent CdTe Nanocrystal–Polymer Composites. *Advanced Functional Materials*, *17*(1), 23–28.

The Project on Emerging Nanotechnologies. (n.d.).

Tietz, F., Mai, A., & Stöver, D. (2008). From powder properties to fuel cell performance – A holistic approach for SOFC cathode development. *Solid State Ionics*, *179*(27-32), 1509–1515.

Tirumala, V. R., Daga, V., Bosse, A. W., Romang, A., Ilavsky, J., Lin, E. K., & Watkins, J. J. (2008). Well-Ordered Polymer Melts with 5 nm Lamellar Domains from Blends of a Disordered Block Copolymer and a Selectively Associating Homopolymer of Low or High Molar Mass. *Macromolecules*, *41*(21), 7978–7985.

Tirumala, V. R., Pai, R. A., Agarwal, S., Testa, J. J., Bhatnagar, G., Romang, A. H., Chandler, C., et al. (2007). Mesoporous Silica Films with Long-Range Order Prepared from Strongly Segregated Block Copolymer/Homopolymer Blend Templates. *Chemistry of Materials*, *19*(24), 5868–5874.

Tirumala, V. R., Romang, A., Agarwal, S., Lin, E. K., & Watkins, J. J. (2008). Well Ordered Polymer Melts from Blends of Disordered Triblock Copolymer Surfactants and Functional Homopolymers. *Advanced Materials*, *20*(9), 1603–1608.

Tohge, N, Zhao, G., & Chiba, F. (1999). Photosensitive gel films prepared by the chemical modification and their application to surface-relief gratings. *Thin Solid Films*, *351*, 85–90.

Tohge, N., Shinmou, K., & Minami, T. (1994). Effects of UV-irradiation on the formation of oxide thin films from chemically modified metal-alkoxides. *Journal of Sol-Gel Science and Technology*, *2*(1-3), 581–585.

Tohge, Noboru, Hasegawa, M., Noma, N., Kintaka, K., & Nishii, J. (2003). Fabrication of Two-Dimensional Gratings Using Photosensitive Gel Films and Their Characterization. *Journal of Sol-Gel Science and Technology*, *26*, 903–907.

Tomkins, H. G. (1992). *A User's Guide to Ellipsometry* (1st ed.). San Diego: Academic Press.

Tomkins, H. G., & McGahan, W. A. (1999). *Spectroscopic Ellipsometry and Reflectometry*. New York: John Wiley & Sons, Inc.

Tsubaki, N., Zhang, Y., Sun, S., Mori, H., Yoneyama, Y., Li, X., & Fujimoto, K. (2001). A new method of bimodal support preparation and its application in Fischer–Tropsch synthesis. *Catalysis Communications*, *2*(10), 311–315.

Usuki, A., Kojima, Y., Kawasumi, M., Okada, A., Fukushima, Y., Kurauchi, T., & Kamigaito, O. (1993). Synthesis of nylon 6-clay hybrid. *Journal of Materials Research*, *8*(5), 1179–1184.

Vaudreuil, S., Bousmina, M., Kaliaguine, S., & Bonneviot, L. (2001). Synthesis of Macrostructured Silica by Sedimentation–Aggregation. *Advanced Materials*, *13*(17), 1310–1312.

Velev, O. D., Jede, T. A., Lobo, R. F., & Lenhoff, A. M. (1998). Microstructured Porous Silica Obtained via Colloidal Crystal Templates. *Chemistry of Materials*, *10*(11), 3597–3602.

Vogt, B. D. (2003). *Diblock Copolymers Swollen with Compressible Fluids: Fundamentals and Applications*.

Vogt, B. D., Pai, R. A., Lee, H.-J., Hedden, R. C., Soles, C. L., Wu, W., Lin, E. K., et al. (2005). Characterization of Ordered Mesoporous Silica Films Using Small-Angle Neutron Scattering and X-ray Porosimetry. *Chemistry of Materials*, *17*(6), 1398–1408.

Wakayama, H., & Fukushima, Y. (1999). Porous platinum fibers synthesized using supercritical fluid. *Chemical Communications*, (4), 391–392.

Wakayama, H., & Fukushima, Y. (2000). Nanoporous Silica Prepared with Activated Carbon Molds Using Supercritical CO 2. *Chemistry of Materials*, *12*(3), 756–761.

Wakayama, H., Itahara, H., Tatsuda, N., Inagaki, S., & Fukushima, Y. (2001). Nanoporous Metal Oxides Synthesized by the Nanoscale Casting Process Using Supercritical Fluids. *Chemistry of Materials*, *13*(7), 2392–2396.

Wang, L., Wang, H., Hapala, P., Zhu, L., Ren, L., Meng, X., Lewis, J. P., et al. (2011). Superior catalytic properties in aerobic oxidation of olefins over Au nanoparticles on pyrrolidone-modified SBA-15. *Journal of Catalysis*, *281*(1), 30–39.

Wang, X., Dou, T., & Xiao, Y. (1998). Synthesis of double-mesopore silica using aqueous ammonia as catalyst. *Chemical Communications*, (9), 1035–1036.

Wang, Y. J., Tang, Y., Ni, Z., Hua, W. M., Yang, W. L., Wang, X. D., Tao, W. C., et al. (2000). Synthesis of Macroporous Materials with Zeolitic Microporous Frameworks by Self-Assembly of Colloidal Zeolites. *Chemistry Letters*, (5), 510–511.

Watkins, J. J., Blackburn, J. M., & McCarthy, T. J. (1999). Chemical Fluid Deposition: Reactive Deposition of Platinum Metal from Carbon Dioxide Solution. *Chemistry of Materials*, *11*(2), 213–215.

White, R. (1964). *Handbook of Industrial Infrared Analysis* (1st ed.). New York: Plenum Press.

Wirnsberger, G., Yang, P., Scott, B. J., Chmelka, B. F., & Stucky, G. D. (2001). Mesostructured materials for optical applications: from low-k dielectrics to sensors and lasers. *Spectrochimica Acta. Part A, Molecular and Biomolecular Spectroscopy*, *57*(10), 2049–60.

Wu, H., Lin, Y., Tang, J., Gao, D., Cai, R., & Zhao, D. (2007). Monodispersed Fullerene Derivatives Introduced into the Channels of Mesoporous Silica via Chemical Bond Interactions. *Bulletin of the Chemical Society of Japan*, *80*(5), 994–998.

Xia, D., Gamble, T. C., Mendoza, E. A., Koch, S. J., He, X., Lopez, G. P., & Brueck, S. R. J. (2008). DNA transport in hierarchically-structured colloidal-nanoparticle porous-wall nanochannels. *Nano Letters*, *8*(6), 1610–8.

Xia, Q.-H., Hidajat, K., & Kawi, S. (2000). Improvement of the hydrothermal stability of fluorinated MCM-41 material. *Materials Letters*, *42*(1-2), 102–107.

Xiao, F.-S. (2004). Hydrothermally Stable and Catalytically Active Ordered Mesoporous Materials Assembled from Preformed Zeolite Nanoclusters. *Catalysis Surveys from Asia*, *8*(3), 151–159.

Xu, J., & Wong, C. P. (2007). High dielectric constant SU8 composite photoresist for embedded capacitors. *Journal of Applied Polymer Science*, *103*(3), 1523–1528.

Yang, P., Deng, T., Zhao, D., Feng, P., Pine, D., Chmelka, B. F., Whitesides, G. M., et al. (1998). Hierarchically Ordered Oxides. *Science*, *282*(5397), 2244–2246.

Yuan, Z.-Y., Blin, J.-L., & Su, B.-L. (2002). Design of bimodal mesoporous silicas with interconnected pore systems by ammonia post-hydrothermal treatment in the mild-temperature range. *Chemical Communications*, (5), 504–505.

Zanella, R., Giorgio, S., Henry, C. R., & Louis, C. (2002). Alternative Methods for the Preparation of Gold Nanoparticles Supported on TiO 2. *The Journal of Physical Chemistry B*, *106*(31), 7634–7642.

Zeng, W., Du, Y., Xue, Y., & Frisch, H. L. (2007). Solubility Parameters. *Physical Properties of Polymers Handbook* (pp. 289–303).

Zhang, H., Hardy, G. C., Rosseinsky, M. J., & Cooper, A. I. (2003). Uniform Emulsion-Templated Silica Beads with High Pore Volume and Hierarchical Porosity. *Advanced Materials*, *15*(1), 78–81.

Zhang, Y., Liu, X., & Huang, J. (2011). Hierarchical mesoporous silica nanotubes derived from natural cellulose substance. *ACS Applied Materials & Interfaces*, *3*(9), 3272–3275.

Zhao, D., Feng, J., Huo, Q., Melosh, N., Fredrickson, G. H., Chmelka, B. F., & Stucky, G. D. (1998). Triblock Copolymer Syntheses of Mesoporous Silica with Periodic 50 to 300 Angstrom Pores. *Science*, *279*(5350), 548–552.

Zhao, Dongyuan, Huo, Q., Feng, J., Chmelka, B. F., & Stucky, G. D. (1998). Nonionic Triblock and Star Diblock Copolymer and Oligomeric Surfactant Syntheses of Highly Ordered, Hydrothermally Stable, Mesoporous Silica Structures. *Journal of the American Chemical Society*, *120*(24), 6024–6036.

Zhao, Dongyuan, Yang, P., Chmelka, B. F., & Stucky, G. D. (1999). Multiphase Assembly of Mesoporous−Macroporous Membranes. *Chemistry of Materials*, *11*(5), 1174–1178.

Zhao, X. S., & Lu, G. Q. (1998). Modification of MCM-41 by Surface Silylation with Trimethylchlorosilane and Adsorption Study. *The Journal of Physical Chemistry B*, *102*(9), 1556–1561.

Zhu, L., Li, Y., Wang, J., & Shen, J. (1995). Structural and optical characteristics of fullerenes incorporated inside porous silica aerogel. *Chemical Physics Letters*, *239*, 393–398.

Ziolo, R. F., Giannelis, E. P., Weinstein, B. A., O'Horo, M. P., Ganguly, B. N., Mehrotra, V., Russell, M. W., et al. (1992). Matrix-Mediated Synthesis of Nanocrystalline ggr-Fe2O3: A New Optically Transparent Magnetic Material. *Science*, *257*(5067), 219–223.

de Boer, M. J., Tjerkstra, R. W., Berenschot, J. W., Jansen, H. V., Burger, G. J., Gardeniers, J. G. E., Elwenspoek, M., et al. (2000). Micromachining of buried micro channels in silicon. *Journal of Microelectromechanical Systems*, *9*(1), 94–103.